

University of Dundee

DOCTOR OF PHILOSOPHY

Resonance Tracking and Vibration Stabilisation of Ultrasonic Surgical Instruments

Kuang, Yang

*Award date:*  
2014

[Link to publication](#)

**General rights**

Copyright and moral rights for the publications made accessible in the public portal are retained by the authors and/or other copyright owners and it is a condition of accessing publications that users recognise and abide by the legal requirements associated with these rights.

- Users may download and print one copy of any publication from the public portal for the purpose of private study or research.
- You may not further distribute the material or use it for any profit-making activity or commercial gain
- You may freely distribute the URL identifying the publication in the public portal

**Take down policy**

If you believe that this document breaches copyright please contact us providing details, and we will remove access to the work immediately and investigate your claim.

DOCTOR OF PHILOSOPHY

# Resonance Tracking and Vibration Stabilisation of Ultrasonic Surgical Instruments

Yang Kuang

2014

University of Dundee

## Conditions for Use and Duplication

Copyright of this work belongs to the author unless otherwise identified in the body of the thesis. It is permitted to use and duplicate this work only for personal and non-commercial research, study or criticism/review. You must obtain prior written consent from the author for any other use. Any quotation from this thesis must be acknowledged using the normal academic conventions. It is not permitted to supply the whole or part of this thesis to any other person or to post the same on any website or other online location without the prior written consent of the author. Contact the Discovery team ([discovery@dundee.ac.uk](mailto:discovery@dundee.ac.uk)) with any queries about the use or acknowledgement of this work.

# **Resonance Tracking and Vibration Stabilisation of Ultrasonic Surgical Instruments**

**By**

**Yang Kuang**



Doctoral thesis submitted in fulfilment of requirements for degree of  
Doctor of Philosophy (PhD) to School of Engineering, Physics and  
Mathematics, University of Dundee  
Dundee, Scotland, UK

©Copyright by Yang Kuang  
May, 2014

## **ABSTRACT**

Ultrasonic surgical instruments actuated by piezoelectric transducers are usually driven at relatively high power levels to generate high vibration amplitude at the probe, which interact with biological tissues to achieve the desired effects. In operation, the high power level introduces nonlinearities into the behaviours of the piezoelectric transducer and the biological tissues place a load onto the transducer. Both the nonlinearities and the load result in variations in resonant frequency and electric impedance, which negatively affect the performance of the ultrasonic surgical instrument. The aim of this work was to develop an adaptive driving system to address the issue of the resonant frequency shift and impedance variation and to study its effectiveness in optimising the performance of ultrasonic surgical instruments.

An ultrasonic planar tool based on piezocrystal PMN-PT was designed with various configurations as an alternative to the existing ultrasonic scalpels. To address the problem of resonant frequency shift and impedance variation observed on the planar tools in characterisation stage, an adaptive driving system was developed to track the resonant frequency and stabilise the vibration velocity. The system was carefully calibrated, and its effectiveness in optimising the performance of unloaded transducers in a broad frequency range was validated. The performance variation of the planar tool under the combined influence of high power level and external tissue loads was then investigated. The capacity of the adaptive driving system to optimise the performance of the planar tool under such conditions was then accessed by performing soft tissue penetrating test. Furthermore, a needle actuating device was designed to increase the visibility of medical needles in ultrasound guided percutaneous procedures. Its modal behaviour was studied in finite element analysis and verified by experimental characterisation. The ability of the adaptive driving system to improve the performance of the needle actuating device was accessed in pre-clinical trials.

The results demonstrate that the adaptive driving system developed can track the resonant frequency and stabilise the vibration velocity of ultrasonic surgical instruments in frequency up to 5 MHz and power up to 300 W. By using the adaptive driving system, optimal performance of the planar tool and needle actuating device can be achieved in both unloaded and loaded conditions. The ultrasonic planar tool with PMN-PT is potentially useful in surgical operations. However, its performance is limited by the intensive heat generated in the joint area and the low Curie point of PMN-PT. The needle actuating device can increase the visibility of standard medical needles in colour Doppler imaging.

## **DECLARATION**

I hereby declare that this thesis entitled, “Resonance Tracking and Vibration Stabilisation of Ultrasonic Surgical Instruments”, submitted in partial fulfilment of the requirements of the University of Dundee for the degree of Doctor of Philosophy represents my own work. No part of the work referred to in this thesis has been supported in application of another degree or qualification of this university or any other university or institute of learning.

.....  
Yang Kuang

## **CERTIFICATE**

This is to certify that Yang Kuang has done this research under my supervision and that he has fulfilled the conditions of Ordinance 39 of the University of Dundee, so that he is qualified to submit for the Degree of Doctor of Philosophy.

.....

Dr Zhihong Huang

## **COPYRIGHT**

Attention is drawn to the fact that copyright of this thesis rests with its author. This copy of the thesis has been supplied on the condition that anyone who consults it is understood to recognise that its copyright rests with the author and that no quotation from this thesis and no information derived from it may be published, without prior written consent of the author.

This thesis may not be consulted, photocopied or lent by any library without permission of the author for a period of three year from the date of acceptance of the thesis.



# ACKNOWLEDGEMENTS

First and foremost, I would like to thank the China Scholarship Council and University of Dundee for offering me financial support to commence my PhD project. Then I would like to express my deepest gratitude to my supervisors Dr Zhihong Huang and Professor Sandy Cochran for their support, enthusiasm and expertise. I'd like to highlight their tremendous effort for a well-organized and inspiring research environment and atmosphere. Thanks to my colleague Mr Muhammad Sadiq for his guidance in device fabrication and characterisation, particularly at the initial stage of my PhD. Thanks must also go to Mr Yongqiang Qiu for his help in silicon and titanium dicing. I must also take this opportunity to express my appreciation to technicians in the workshop. I'm deeply indebted to my former and present colleagues: Yunwei Jin, Andre Hilgers, Xiaochun Liao, Xiaoxu Lei and Xiaojia Xie for their assistance in the development of this research work.

Last but not least, I am especially grateful to my whole family – my wife and my parents, for their love, encouragement and support.

## TABLE OF CONTENTS

ABSTRACT .....	II
DECLARATION .....	IV
CERTIFICATE .....	V
COPYRIGHT .....	VI
ACKNOWLEDGEMENTS .....	VII
TABLE OF CONTENTS .....	VIII
LIST OF FIGURES .....	XIII
LIST OF TABLES .....	XXII
GLOSSARY OF TERMS .....	XXIII
1 Introduction.....	1
1.1 Background.....	1
1.2 Objectives .....	2
1.3 Content of thesis.....	3
1.4 Publication arising from this work.....	4
2 TECHNICAL BACKGROUND .....	6
2.1 High Power Ultrasonics in Medical Applications.....	6
2.1.1 Soft Tissue Dissection .....	7
2.1.2 Bone Cutting .....	10

2.1.3 Tissue Fragmentation and Aspiration.....	12
2.1.4 Performance Variation of Ultrasonic Surgical Instruments.....	13
2.2 High Power Ultrasonic System.....	14
2.2.1 Piezoelectricity .....	15
2.2.2 Piezoelectric Transducer.....	18
2.2.3 Acoustic horns.....	25
2.3 Nonlinearities of Piezoelectric Transducers .....	27
2.3.1 Nonlinear behaviour .....	28
2.3.2 Nonlinear Characterisation of Piezoelectric Transducers.....	33
2.4 Driving Systems for High Power Ultrasonics.....	37
2.4.1 Feedback Signals.....	37
2.4.2 Control Strategies .....	38
2.5 Discussion and Conclusion.....	42
<b>3 DESIGN AND CHARACTERISATION OF ULTRASONIC PLANAR TOOLS</b>	<b>44</b>
3.1 Design.....	45
3.1.1 Schematic.....	45
3.1.2 Design Considerations .....	45
3.2 Finite Element Analysis .....	51
3.2.1 PMN-PT piezocrystal .....	51
3.2.2 Blades .....	53

3.2.3 Ultrasonic Planar tools.....	55
3.3 Fabrication .....	56
3.3.1 Thin film gold deposition .....	57
3.3.2 Assemble the tools.....	59
3.4 Characterisation .....	61
3.4.1 Methods .....	61
3.4.2 Results.....	62
3.5 Discussion and Conclusion.....	69
4 ADAPTIVE DRIVING SYSTEM.....	71
4.1 Dynamic behaviour of piezoelectric transducers .....	71
4.1.1 Electrical model of the transducer.....	71
4.1.2 Dynamic tuning of the transducer .....	73
4.2 Adaptive Driving System Configuration.....	76
4.2.1 Layout and hardware .....	76
4.2.2 Current measurement.....	77
4.2.3 Impedance calculation .....	79
4.2.4 Control module.....	82
4.2.5 Software programming .....	87
4.3 Experimental validation.....	89
4.3.1 Impedance measurement.....	90

4.3.2 Resonance tracking and vibration stabilization.....	93
4.4 Discussion and Conclusions .....	98
5 EFFECTS OF POWER LEVELS AND SOFT TISSUE LOADS .....	101
5.1 High Power Characterisation .....	101
5.1.1 Experimental Arrangements .....	102
5.1.2 Experimental Results .....	104
5.2 Soft Tissue Penetrating Test .....	115
5.2.1 Experimental Arrangements .....	115
5.2.3 Experimental Results .....	117
5.3 Discussion and conclusion.....	122
6 CASE STUDY-NEEDLE ACTUATING DEVICE .....	124
6.1 Percutaneous Needle Procedures .....	124
6.2 Needle Actuating Device Design .....	126
6.3 Finite Element Analysis of the Needle Actuating Device .....	127
6.3.1 Piezoelectric Transducers .....	127
6.3.2 Standard Needles .....	130
6.3.3 Needle Actuating Device .....	133
6.4 Fabrication .....	138
6.5 Characterisation .....	139
6.5.1 Piezoelectric Transducers .....	139

## TABLE OF CONTENTS

---

6.5.2 Needle Actuating Device .....	140
6.6 Needle Visibility Test.....	146
6.6.1 Experimental arrangement .....	146
6.6.2 Experimental results .....	148
6.7 Discussion and conclusion.....	156
7 CONCLUSIONS AND FUTURE WORK.....	159
7.1 Conclusions.....	159
7.2 Future Work.....	162
7.2.1 Adaptive Driving System.....	162
7.2.2 Ultrasonic Planar Tool.....	162
7.2.3 Needle Actuating Device .....	163
REFERENCES .....	164
Appendix A- Labview program for resonance tracking and vibration stablisation .....	175
Appendix B- Labview program for impedance measurement .....	178

## LIST OF FIGURES

Figure 2-1 Ultrasonic scalpels (a) Ethicon Harmonic Synergy blade (b) Ethicon Harmonic ACE <sup>®</sup> Shear (c) cutting and coagulation of a vessel by a harmonic shear .....	8
Figure 2-2 Ethicon Harmonic Synergy blades with complicated geometrical features....	9
Figure 2-3 (a) Handpiece of the Mectron piezosurgery ultrasonic device (b) different inserts can be screwed on the top of the handpiece [32].....	11
Figure 2-4 Schematic of a basic ultrasonic surgical aspirator [7] .....	12
Figure 2-5 Schematic configuration of a high power ultrasonic system .....	14
Figure 2-6 Schematic diagrams of the direct and converse piezoelectric effect: (a) inverse piezoelectric effect, where an electric field applied to the material changes its shape (b) direct piezoelectric effect, where a stress on the material yields an electric field across it.....	16
Figure 2-7 Vibration modes of piezoelectric material: $d_{31}$ (plate) and $d_{33}$ (bar) .....	16
Figure 2-8 Sandwich piezoelectric transducer .....	18
Figure 2-9 Three-port model representing a piezoelectric transducer [49].....	19
Figure 2-10 Mason 1-D model of a piezoelectric plate excited in thickness expansion mode [49] .....	20
Figure 2-11 Butterworth-Van Dyke model of a piezoelectric transducer operating near resonance [11] .....	21
Figure 2-12 Electrical input impedance and admittance of piezoelectric transducer (a) impedance versus frequency plot (b) conductance versus susceptance plot.....	23

Figure 2-13 Profiles of the commonly used ultrasonic horns: (a) conical (b) exponential (c) catenary (d) stepped.....	26
Figure 2-14 Hysteresis phenomenon of a piezoelectric transducer [105].....	33
Figure 2-15 Transient response of the piezoelectric transducer during burst excitation [111].....	36
Figure 2-16 Functional block diagram of driving system based on PLL[11] .....	39
Figure 2-17 Schematic diagram of autoresonant ultrasonic cutting system [127] .....	41
Figure 3-1 Schematic of the ultrasonic planar tool.....	45
Figure 3-2 Profiles of the blades (a) conical blade with flange (b) conical blade (c) exponential blade .....	46
Figure 3-3 Clamps for the planar tools (a) clamp 1 (b) clamp 2 .....	50
Figure 3-4 Longitudinal mode of the PMN-PT plate .....	53
Figure 3-5 Longitudinal vibration mode of Si blade .....	54
Figure 3-6 Longitudinal vibration modes of the silicon planar tool: (a) single-sided configuration (b) double-sided configuration.....	55
Figure 3-7 Longitudinal mode shape of the silicon planar tool with position error in length direction (a) position of the piezocrystal plates (b) longitudinal mode.....	56
Figure 3-8 Longitudinal mode shape of the silicon tool with position error in width direction (a) position of the piezocrystal plates (b) longitudinal mode .....	56
Figure 3-9 Schematic of DC sputtering process.....	58
Figure 3-10 Gold evaporation process (a) schematic (b) gold wire mounted on evaporation boat .....	59



Figure 3-11 Blades with electrodes deposited (a) Si blade (b) AlN blade.....	59
Figure 3-12 Bespoke jig for alignment (a) individual components (b) assembly .....	60
Figure 3-13 Fabricated planar tools (a) stainless steel tool (b) Ti tool (c) Si tool.....	61
Figure 3-14 Setup to measure the displacement of ultrasonic planar tools.....	62
Figure 3-15 Electrical impedance of PMN-PT (Sample 5) and Ti planar tool with Sample 5 attached (a) magnitude (b) phase .....	63
Figure 3-16 Electrical impedance and vibration response of the Ti tool (a) impedance magnitude (b) impedance phase (c) displacement response at 5 V .....	64
Figure 3-17 Electrical impedance of the planar tools (a) stainless steel tool (b) Si tool (c) AlN conical tool (d) AlN exponential tool.....	66
Figure 3-18 Vibration velocity of the ultrasonic planar tools at different voltage (a) AlN tools in conical and exponential profiles (b) conical profiles in different blade materials .....	68
Figure 3-19 Resonant frequency of the Ti tool at different voltage .....	69
Figure 4-1 Electric model for an unloaded piezoelectric transducer operating near resonance .....	71
Figure 4-2 Locus diagram of admittance .....	73
Figure 4-3 Admittance locus of Ti tool under loaded and unloaded conditions (a) unloaded (b) loaded by poultry breast tissue.....	74
Figure 4-4 Electrical model of an unloaded transducer with a shunted inductor .....	75
Figure 4-5 Admittance locus of Ti tool with and without electrical matching (a) unloaded (b) loaded by poultry breast tissue.....	75

Figure 4-6 Schematic of the adaptive driving system for high power ultrasonic transducers.....	77
Figure 4-7 Current measurement circuit .....	78
Figure 4-8 Schematic of the orthogonal correlation method.....	79
Figure 4-9 Schematic of the improved phase calculation algorithm .....	81
Figure 4-10 Block diagram of a PID controller.....	83
Figure 4-11 Schematic diagram of the control module .....	84
Figure 4-12 The adaptive driving system with LDV .....	90
Figure 4-13 Impedance of a standard resistor measured by HP 4194A impedance analyser and the adaptive driving system from 20 kHz to 5 MHz (a) magnitude (b) phase .....	91
Figure 4-14 Impedance phase between 20 and 100 kHz measured by the adaptive driving system and the commercial impedance analyser .....	92
Figure 4-15 Electrical impedance of a commercial transducer measured by HP 4194A impedance analyser and the adaptive driving system: (a) magnitude (b) phase .....	93
Figure 4-16 Parameters of the Ti planar tool driven by the adaptive driving system: (a) current; (b) resonant frequency; (c) impedance phase; (d) impedance magnitude; (e) voltage; and (f) vibration velocity .....	94
Figure 4-17 Vibration velocity of the Ti planar tool during a swept-sine test and a continuous driving test at different current amplitudes .....	96
Figure 4-18 Two piezoelectric sandwich transducers used in the experiment (a) 35.3 kHz (b) 34.25 kHz .....	97
Figure 4-19 Vibration velocity of the 35.3 kHz transducer driven by the three driving systems .....	97

Figure 4-20 Vibration velocity of the 34.25 kHz transducer (a) comparison between the adaptive driving system and the Vibra Cell (b) comparison between the adaptive driving system and the non-adaptive circuit.....	98
Figure 5-1 LDV and infrared camera used to characterise the Ti planar tool in unloaded characterisation.....	103
Figure 5-2 (a) Experimental setup for loaded characterisation (b) a diagram of the loaded characterisation.....	104
Figure 5-3 (a) Typical thermograph of the Ti tool captured by the infrared camera (b) detailed view of the Ti tool .....	105
Figure 5-4 Steady state temperature of the Ti tool at different current amplitudes.....	105
Figure 5-5 Thermal graph of PMN-PT piezocrystal with a dummy epoxy bump under continuous driving .....	107
Figure 5-6 Resonant frequency shift of the planar tool (a) time profile at 0.07A (b) resonant frequency shift measured at the beginning and the steady state of the driving processes .....	108
Figure 5-7 Profile of $\Delta T$ in the ‘bottom epoxy’ when the planar tool is driven at 0.07A .....	109
Figure 5-8 (a) Time profiles of $\Delta T$ and $\Delta f$ measured at 0.07A (b) Estimated time constants $\tau_f$ and $\tau_T$ .....	110
Figure 5-9 Electric impedance of the planar tool at different current amplitudes.....	111
Figure 5-10 Vibration velocity of the planar tool at different current amplitudes .....	111
Figure 5-11 Electrical impedance and resonant frequency of the planar tool in soft tissue loaded condition (a) electrical impedance (b) resonant frequency .....	112

Figure 5-12 BVD model for the loaded ultrasonic planar tool operating near resonance .....	113
Figure 5-13 Radiation resistance of the planar tool at different insertion depths and different current amplitudes .....	114
Figure 5-14 Temperature rise of the planar tool in soft tissue loaded condition.....	115
Figure 5-15 A diagram of the soft tissue penetrating experiment .....	116
Figure 5-16 Cutting force versus cutting depth at different power level and vibration velocity (a) 0.02A & 0.5 m/s (b) 0.05A & 1.25 m/s (c) 0.1 A & 2.500 m/s .....	118
Figure 5-17 Parameters of the planar tool monitored during an penetrating test at 0.1A (a) impedance phase (b) resonant frequency (c) impedance magnitude (d) current.....	119
Figure 5-18 Cutting force versus cutting depth with and without using adaptive driving system.....	120
Figure 5-19 impedance phase of the planar tool with and without using the adaptive driving system during the soft tissue penetrating test.....	121
Figure 5-20 Effects of vertical cutting velocity on the cutting force and work required (a) force reduction in percentage (b) work reduction in percentage .....	122
Figure 6-1 Schematic CAD model of the needle actuating device.....	126
Figure 6-2 Longitudinal vibration mode of the transducer .....	129
Figure 6-3 Longitudinal vibration mode of the transducer with the outer collet assembled .....	129
Figure 6-4 3D model of a standard needle .....	130
Figure 6-5 Typical vibration modes of a needle (a) flexural mode at 10.4 kHz (b) torsional mode at 15.9 kHz (c) longitudinal mode at 25.2 kHz .....	131

Figure 6-6 Longitudinal displacement along the G21×100 mm needle in the first and second longitudinal vibration modes .....	132
Figure 6-7 Longitudinal resonant frequencies of standard needle of different lengths	132
Figure 6-8 Longitudinal vibration modes of Needle Actuating Device: (a) 21.7 kHz (b) 26.7 kHz (c) 52.1 kHz.....	133
Figure 6-9 Displacement profile on the G21×100 mm needle at the needle's resonance modes: the needle is clamped by the transducer at 45 mm from needle tip.....	134
Figure 6-10 Displacement profiles of the needle actuating device at different clamping positions .....	136
Figure 6-11 Comparison of displacement profiles: the transducer's resonant mode of the needle actuating device and the second longitudinal vibration mode of a free vibration needle .....	137
Figure 6-12 Transducer's resonant mode of the needle actuating device working with a G21×120 mm needle.....	138
Figure 6-13 Components prepared for transducer fabrication .....	139
Figure 6-14 (a) fabricated piezoelectric transducer (b) needle actuating device.....	139
Figure 6-15 Electric impedance of the piezoelectric transducer (a) magnitude (b) phase .....	140
Figure 6-16 (a) Longitudinal displacement response and (b) electric impedance of the needle actuating device: a G21 ×120 mm needle is clamped by the transducer at 45 mm from tip.....	141
Figure 6-17 Resonant frequencies of needle's resonant mode: (a) resonant frequencies of a G21 ×120 mm needle and a G21 ×100 mm needle at different clamping positions (b) comparison of the experiment results with the FEA results on a G21 ×100 mm needle .....	142

Figure 6-18 Resonant frequencies of the transducer's mode with a G21 ×120 mm needle and a G21 ×100 mm needle at different clamping positions .....	143
Figure 6-19 Longitudinal and lateral vibration at the tip of a G21 ×100 needle clamped by the transducer at 45 mm .....	143
Figure 6-20 Electric impedance of the needle actuating device working with a G21×120 mm needle before and after impedance matching (a) magnitude (b) phase.....	145
Figure 6-21 Electric impedance of the needle actuating device measured in air and in tissue (a) magnitude (b) phase .....	145
Figure 6-22 Vibration velocity of the needle actuating device at needle tip .....	146
Figure 6-23 Experimental setup .....	147
Figure 6-24 Comparison of the needle actuating device observed under grey scale ultrasound imaging and colour Doppler imaging (a) grey scale (b) colour Doppler....	149
Figure 6-25 Colour Doppler imaging of the needle actuating device by tuning the frequency manually.....	149
Figure 6-26 Colour Doppler imaging of the needle actuating device during needle advancing (a) 0 s (b) 2s (c) 4s (d) 6s (e) 8s (f) 10s (g) 12s (h) 14s .....	151
Figure 6-27 Colour Doppler images of the needle actuating device under different excitation current: in plane approach (a) 0.025A (b) 0.0375A (c) 0.05A (d) 0.0625A	152
Figure 6-28 Colour Doppler images of the needle actuating device under different driving voltage: out of plane approach (a) 0.0125A (b) 0.025A (c) 0.0375A (d) 0.05A .....	153
Figure 6-29 Colour Doppler imaging of the needle at different insertion angles: (a) 30° (b) 40° (c) 50° (d) 60° .....	155

Figure 6-30 Colour Doppler imaging of the needle actuating device working at its  
needle's resonance mode at different current amplitudes: (a) 0.025A (b) 0.0375A (c)  
0.05A (d) 0.0625A..... 156

## LIST OF TABLES

Table 2-1 Formulas of horn profiles .....	27
Table 3-1 Mechanical properties of materials [39, 138] .....	49
Table 3-2 Resonant frequencies of PMN-PT plate samples .....	50
Table 3-3 Material properties of PMN-29%PT [141] .....	52
Table 3-4 Mechanical properties of (100) Si wafer in <110> direction [142] .....	53
Table 3-5 Characteristics of the designed blades .....	54
Table 3-6 Properties of the Ti tool during fabrication .....	63
Table 3-7 Properties of the Ti tool.....	65
Table 3-8 Measured properties of the planar tools .....	67
Table 5-1 Averaged force and work reduction at different current amplitudes .....	118
Table 6-1 Mechanical properties of aluminium and stainless steel .....	128
Table 6-2 Material properties of PZ 26.....	128
Table 6-3 Mechanical properties of surgical stainless steel.....	130
Table 6-4 The first longitudinal resonant frequencies of the needle's resonance modes at different tip part lengths .....	135



## GLOSSARY OF TERMS

$ Z $	Magnitude of electrical input impedance
$\Delta f$	Frequency shift value
$\Delta T$	Temperature rise
$B$	Susceptance
BVD	Butterworth-Van Dyke model
$C_0$	Clamped capacitance of BVD model
$C_1$	Capacitance of BVD model
$d$	Matrix of piezoelectric constants
$D$	Vector of electric displacement
$E$	Vector of applied electric field
$f$	Frequency
$f_a$	Anti-resonant frequency
FEA	Finite element analysis
$f_m$	Maximum admittance frequency
$F_{max}$	Force
$f_n$	Minimum admittance frequency
$f_p$	Parallel frequency
$f_r$	Resonant frequency with zero phase
$f_s$	Serial resonant frequency/mechanical resonant frequency
$I$	Current through the transducer
$I_0$	Current through $C_0$
$I_1$	Current through the mechanical arm
$I_t$	Target current amplitude
$K_a$	Displacement amplification of an acoustic horn
$K_{df}$	Derivative constant of the PID controller for frequency tracking
$k_{eff}$	Electromechanical coupling coefficient
$K_{if}$	Integral constant of the PID controller for frequency tracking
$K_{pf}$	Proportional constant of the PID controller for frequency tracking

$L_0$	Inductance shunted to tune out C0
$L_I$	Inductance of BVD model
LDV	Laser Doppler Vibrometer
PID	Proportional, Integral and Derivative controller
PMN-PT	Lead Magnesium Niobate-Lead Titanate
PZT	Lead Zirconate Titanate
$Q_M$	Mechanical quality factor
$R_0$	Dielectric loss resistance
$R_I$	Resistance of BVD model
$R_r$	Radiation resistance
$R_{ref}$	Reference resistance
$s$	Matrix of compliance coefficient
$\tan \delta_e$	Dielectric loss
$U$	Voltage
$u$	Displacement amplitude
$v$	Velocity amplitude
$W$	Work
$X_r$	Radiation reactance
$Y$	Complex electric input admittance
$Z$	Complex electric input impedance
$\delta$	Stress vector
$\varepsilon$	Strain vector
$\zeta$	Permittivity
$\theta$	Phase of electrical input impedance
$\theta_I$	Phase of current
$\theta_t$	Target phase
$\theta_U$	Phase of voltage
$\omega$	Angular frequency

# 1 INTRODUCTION

## 1.1 Background

Ultrasonic surgical instruments are widely used in surgical operations for biological tissue dissection [1], ablation [2] or fragmentation [3], because of the advantages including less bleeding, less postoperative complications [4], less thermal damage, and precise, fast operation using relatively low forces [5]. These devices usually consist of a piezoelectric transducer to generate high frequency vibration (20-100 kHz), an acoustic horn to boost the vibration amplitude (up to 300  $\mu\text{m}$ ) and a probe to interact with tissues. The oscillation of the probe leads to the desired physical or chemical changes in the target biological tissues through cavitation, direct mechanical or thermal effects [6, 7].

The ultrasonic surgical instruments are inherently desirable to be driven at the resonant frequency because of optimum power conversion and vibration response. The vibration amplitude at the probe tip is also expected to be stable so that the clinical outcome is consistent and repeatable, therefore, safe to patients. However, the characteristics of ultrasonic surgical instruments suffer from significant variations in operation, resulting from high excitation power required and physical loads from tissue. The high excitation power introduces nonlinear behaviours into the piezoelectric transducers and thus changes their working characteristics [8]. These nonlinearities include resonant frequency shift, increase in mechanical losses, temperature rise in piezoelectric material and hysteresis phenomenon, which negatively affect the transducer's performance. The biological tissues contacting with the ultrasonic probe act as physical loads onto it, changing its resonant frequency and electrical input impedance [9, 10].

Driving piezoelectric transducer at frequencies other than resonance results in low power conversion, and consequently poor vibration response. The problem is exacerbated when the mechanical quality factor of the transducer,  $Q_M$ , is high, which is usually the case for high power ultrasonic transducers, as the electrical impedance changes rapidly at frequencies near its resonance [11]. Even if the resonance of the transducer is maintained, the electric impedance still varies with power levels and

external physical loads, leading to unstable electrical input power and consequently unstable vibration amplitude [12].

Thus, to drive the ultrasonic surgical instruments in an efficient way and achieve repeatable and controllable effects in operation, the driving system should be able to track the resonant frequency of the instruments and provide stable vibration amplitude despite the variations in working characteristics. The traditional driving systems with such abilities are based on analogue integrated circuits [13, 14]. The tuneable range of these circuits is limited by the characteristics of the analogue components. The development of such a system usually involves designing a power amplifier, which makes the process complicated and tedious. Although commercial ultrasonic driving systems for high power ultrasonics are available, each driving system is matched to only limited, specific transducers and changes in the transducers require complicated calibration procedure by the supplier.

### **1.2 Objectives**

The aim of this research is to develop an adaptive driving system with high flexibility for high power ultrasonic surgical instruments and to study its ability to improve the performance of these devices. The driving system, first of all, is capable of tracking the resonant frequency of the instruments and providing stable vibration velocity despite power and load variations. Secondly, the system should be flexible in terms of tuneable range and function, which covers the essential needs of both research and applications. Within the framework of this project, the following specific objectives were set.

1. To design simple ultrasonic tools and to investigate their performance variation under high power levels and external loads placed by biological tissues.
2. To develop an adaptive driving system to track the resonant frequency and stabilise the vibration amplitude of ultrasonic instruments.
3. To validate the ability of the driving system to improve the performance of ultrasonic tools.

4. To study the ability of the adaptive driving system to optimize the performance of a needle actuating device.

### **1.3 Content of thesis**

The content of this thesis is organised as following.

Chapter 2 reviews the background literatures relating to high power ultrasonic surgical instruments. The clinical applications of ultrasonic surgical instruments are described while the challenges associated with these procedures are also reported. Following a detailed description of the high power ultrasonic systems, the nonlinear behaviour and its characterisation methods are presented. Finally, the current solutions to address the challenges of ultrasonic surgical instruments are provided.

Chapter 3 details the design, fabrication and characterisation of ultrasonic planar tools with piezoelectric single crystal PMN-PT (Lead Magnesium Niobate/Lead Titanate). It investigates the characteristics of the planar tools with blades in different materials and different profiles by using a non-adaptive driving circuit. The nonlinear behaviour observed on the planar tools under high power demonstrates the need of an adaptive driving system.

Chapter 4 presents the development of an adaptive driving system with combined analogue-digital configuration to address the issue of resonant frequency shift and impedance variation in operation. It is capable of tracking the resonant frequency of transducers and providing stable vibration velocity despite changes in power levels and loading conditions. The system can also be used as an impedance analyser to characterise the performance of ultrasonic transducers at low/high power levels.

Chapter 5 investigates the ability of the adaptive driving system to improve the performance of ultrasonic planar tools under both high power levels and soft tissue loads. The influences of power levels and soft tissue loads on the working characteristics of ultrasonic planar tools are studied first, and the working limits are identified. Then the ultrasonic planar tools are used to penetrate soft animal tissue

driven by the adaptive driving system. The cutting force required is recorded to analyse the contribution of ultrasonic excitation.

Chapter 6 provides a case study of the theory and methods established in the previous Chapters. A needle actuating device is designed, fabricated and characterised, targeting to increase needle visibility under ultrasound imaging by inducing ultrasonic vibration to a standard regional anaesthesia needle. The adaptive driving system is used to enhance the performance of the needle actuating device during pre-clinical condition tests.

A summary of the findings and recommendations for future work is given in Chapter 7.

## **1.4 Publication arising from this work**

### **Journal Publications**

- (1) **Y. Kuang**, Y. Jin, S. Cochran and Z. Huang. *Resonance Tracking and Vibration Stabilization for High Power Ultrasonic Transducers*. Ultrasonics. 2014:54 (1). Pp: 187-194.
- (2) M. Sadiq, **Y. Kuang**, S. Cochran and Z. Huang. *High Performance Planar Ultrasonic Tool Based on d31-mode piezocrystal*. Ultrasonics, Ferroelectrics and Frequency Control, IEEE Transactions on, accepted for publication 2014, subject to revisions.
- (3) **Y. Kuang**, S. Cochran and Z. Huang. *Effects of High Power Levels and Soft Tissue Loads on Ultrasonic Planar Tools Driven by d<sub>31</sub>-mode PMN-PT*. Ultrasonics, Ferroelectrics and Frequency Control, IEEE Transactions on (Under review).

### **Conference Proceedings**

1. **Y.Kuang**, M.Sadiq, S. Cochran and Z. Huang. *Effects of High Power Level and Soft Tissue Loads on Ultrasonic Devices*. IEEE Ultrasonic Symposium (IUS), Prague, Czech Republic, 2013

2. **Y.Kuang**, M.Sadiq, S. Cochran and Z. Huang. *Ultrasonic Cutting with Resonance Tracking and Vibration Stabilization*. IEEE Ultrasonic Symposium (IUS), Dresden, Germany, 2012.
3. **Y.Kuang**, M.Sadiq, S. Cochran and Z. Huang. *Design and Characterisation of Ultrasonic Surgical Tool Using  $d_{31}$  PMN-PT plate*. Ultrasonic Industry Association Symposium (UIA), 2011 40<sup>th</sup> Annual.
4. M.Sadiq, **Y.Kuang**, S. Cochran and Z. Huang. *High Performance Planar Ultrasonic Tool based on  $d_{31}$ -mode Piezocrystal*. IEEE Ultrasonic Symposium (IUS), America, 2011
5. M.Sadiq, **Y.Kuang**, S. Cochran and Z. Huang. *High Performance Ultrasonic Tool for Tissue Cutting*. 4th International Conference on Biomedical Engineering and Informatics (MBEI), 2011

## 2 TECHNICAL BACKGROUND

In this chapter, Section 2.1 presents the current status of high power ultrasonics in medical applications. Section 2.2 introduces the components of high power ultrasonic systems and then gives a general description of piezoelectric material, piezoelectric transducer and acoustic horns. Section 2.3 presents the nonlinear behaviours of piezoelectric transducer at high power levels and the characterisation methods. Section 2.4 introduces the current status of the adaptive driving system for high power ultrasonic instruments. Discussion and conclusion of this chapter are given in Section 2.5.

### 2.1 High Power Ultrasonics in Medical Applications

Ultrasound is an oscillating sound pressure wave with frequency greater than the upper limit of the human hearing range. Although this limit varies from person to person, 20 kHz is often regarded as an acceptable lower limit in describing ultrasound.

The application of ultrasound is often referred to as ultrasonics. It is used in a wide range of applications that have historically been divided into two categories: low power high frequency ultrasound and high power low frequency ultrasound [15]. The former is usually concerned with the generation of waves at frequencies above several hundred kHz and used in ultrasound diagnostic imaging and ultrasonic physical therapy. In ultrasound diagnostic imaging, ultrasonic waves (typically 3-5 MHz) with power intensity in  $0.1\text{-}0.5\text{ W/cm}^2$  range are transmitted into the body. As it travels through the body, the ultrasound interacts with the tissues, creating a series of echoes, which can be detected by a probe and processed to produce information about the patient's anatomy [16]. If an ultrasound beam is focused down to a small size on the target tissue, the power intensity becomes very large and significant thermal energy could be absorbed from the beam by the tissue, resulting in heat. Such hyperthermia has been traditionally employed in physical therapy to warm tissue, in drug delivery to melt drug-containing liposomes, and in medical treatment to kill or ablate tissue [17].



Unlike low power ultrasonics, high power ultrasound in the medical field usually targets permanent physical or chemical change in the target tissue. It is characterised by low ultrasonic frequency (usually in the 20-100 kHz range) and the requirement of high power (usually in the 10-300 W/cm<sup>2</sup>) [7]. With high power applied to the ultrasound transducer, high vibration amplitude is generated at the tip of the ultrasound actuated surgical instruments, which interacts with tissue and achieves the desired effects in the target tissue.

High power ultrasonics is currently used in a wide variety of medical procedures and applications, which are described in the following.

### 2.1.1 Soft Tissue Dissection

Ultrasonically actuated scalpels that cut and coagulate tissues have been increasingly used in both open and endoscopic surgery [18]. Figure 2-1 shows ultrasonic scalpels from Ethicon (Ethicon Endo-Surgery, Inc. United States). Other examples of currently available ultrasonic devices include the Autosonix (Covidien), SonoSurg (Olympus) and so on. The general design of these devices is similar. They consist of a piezoelectric transducer housed in the handpiece and a function probe. The transducer, usually in the sandwich configuration, converts electrical energy into mechanical vibration (around 55 kHz). The mechanical vibration (maximum amplitude ranging from 80 to 200  $\mu$ m) is conducted by an extending rod to a function probe [19].

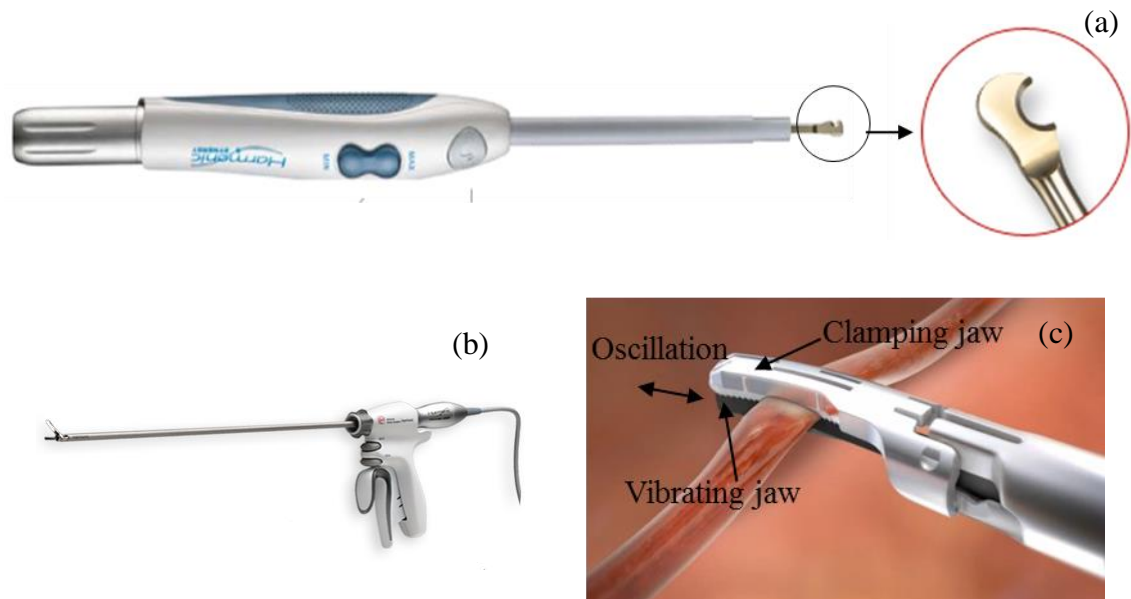


Figure 2-1 Ultrasonic scalpels (a) Ethicon Harmonic Synergy blade (b) Ethicon Harmonic ACE® Shear (c) cutting and coagulation of a vessel by a harmonic shear

The ultrasonic tissue dissection occurs as a result of a saw mechanism between the vibrating probe and tissue. Due to the friction, the cutting process is accompanied by high temperatures (60-80°C) at the interface between the probe and tissue, which are directly proportional to the power setting and activation time [20] [21]. The tissue changes its chemical structure primarily as a result of protein denaturation under high temperature. The increased viscosity and the adhesion properties of the sectioned tissue provide closing of vascular structures and bleeding control, and support the cutting process [22, 23]. If the probe comes into contact with liquid in tissue, cavitation occurs, which further supports the denaturation of the proteins and the cutting process [18].

The coagulating and cutting capacities of an ultrasonic scalpel can be controlled by the geometry of the probe and the power settings. Using a blunt probe in sufficient sizes, coagulation can be induced without the cutting option. In contrast, when a sharp edge blade is used, cutting occurs before coagulation and as a result, coagulation effect is poor [24]. For this reason, the geometry of a blade can be complicated such that different functions can be achieved by using the different part of the blade, as illustrated in Figure 2-2. Each blade is a multifunctional instrument, which provides both cutting and coagulating abilities. At high power settings, the probe vibrates at relatively high vibration amplitudes and is suitable for rapid tissue dissection. Lateral thermal spread is

less within this mode, but the haemostatic potential is poor. At low power settings, the probe vibrates at smaller amplitude. In such a mode, the cutting process is slow and is ideal for vessel sealing [25, 26]. However there is an increased risk of lateral thermal spread with this mode.

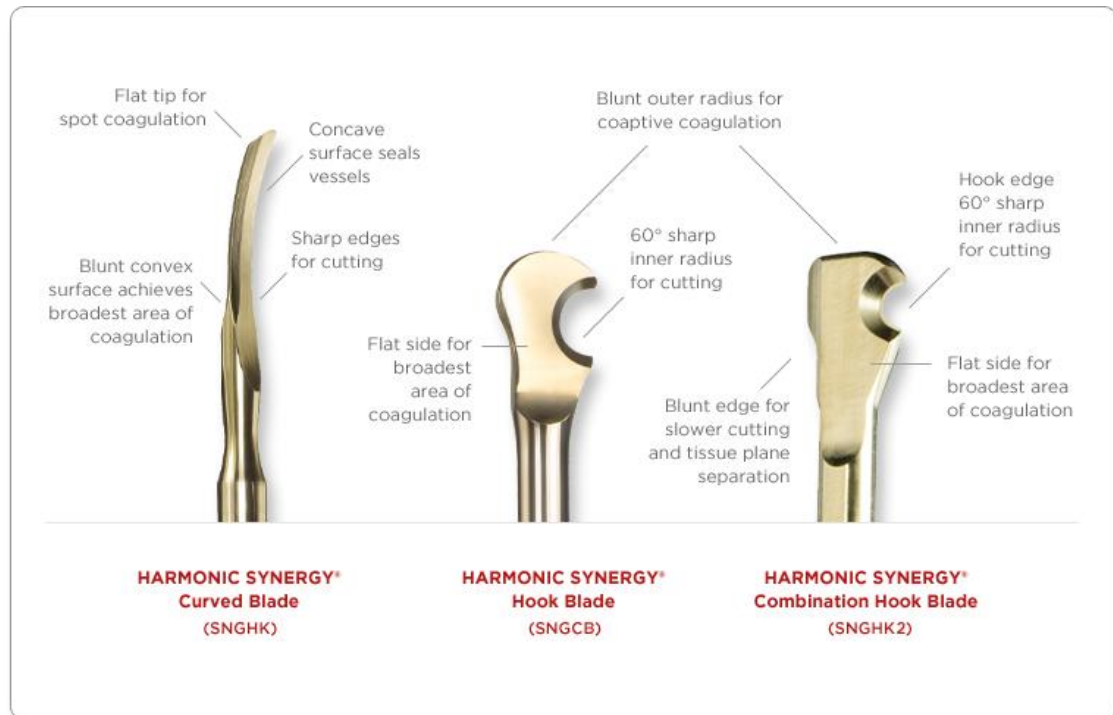


Figure 2-2 Ethicon Harmonic Synergy blades with complicated geometrical features

Ultrasonic scalpels provide precise dissection, excellent haemostasis and strong, durable seals for vessels up to 5 mm [27]. Compared with other dissection techniques such as laser surgery and high-frequency electrosurgery, ultrasonic scalpels hold advantages including less lateral thermal damage, less tissue sticking during use, and no current transmission. Ultrasonic dissection system works at a temperature below 80 °C, compared with 100 °C for electrosurgery. As a result, there is less risk of thermal damage to adjacent organs [19]. Thermal damage to the lateral tissue is also minimized [22]. The lack of current transmission allows coagulation of vessels very close to the stomach, bowel, or biliary tract without the risks inherent in HF electrosurgery. The smoke-free operation ensures better visibility in an endoscopic surgery and may also contribute to the reduction of postoperative adhesions [19].

The activation time for vessel sealing is subjective because there is no tissue impedance/temperature cut-off or audio signal (available with advanced electrosurgery devices [26]) to inform the surgeon when the vessel sealing is complete. Despite the lower working temperature with ultrasonic scalpels, there are still reports about thermal complications during applications [28, 29]. Ultrasonic scalpels can only seal vessels smaller than 5 mm [26]. Sealing larger vessels requires longer operation time, which might result in more significant lateral thermal effect. Thus, haemostasis of large vessels still requires suture ligations [30], which tie around the blood vessels to shut them off.

### 2.1.2 Bone Cutting

Ultrasonic osteotomy was developed in response to the need for precision and safety in bone surgery than was available with other manual and motorised instruments [31]. Clinical applications have been reported in a wide range of surgeries, including oral surgery, maxillofacial surgery, otological surgery, neurosurgery and orthopaedic surgery [32].

Figure 2-3 shows the ultrasonic bone cutting device, piezosurgery® (Mectron, Carasco, Italy). The piezoelectric transducer housed in the handpiece is tuned to produce longitudinal vibration in conjunction with a variety of different cutting inserts. The vibration mode of the inserts can be either longitudinal or in a combined longitudinal-flexural. The width, the thickness and the angle of the inserts vary in relation to the power that is applied, the bone density and the surgical techniques that they are used for [33]. A frequency of 25-29 kHz is used because the vibration at low frequency cut only mineralised tissue while higher frequencies have a propensity for separating soft tissue. [34]. The device also consists of a peristaltic pump for cooling with a jet of solution that discharges from the insert and removes debris from the cutting site.

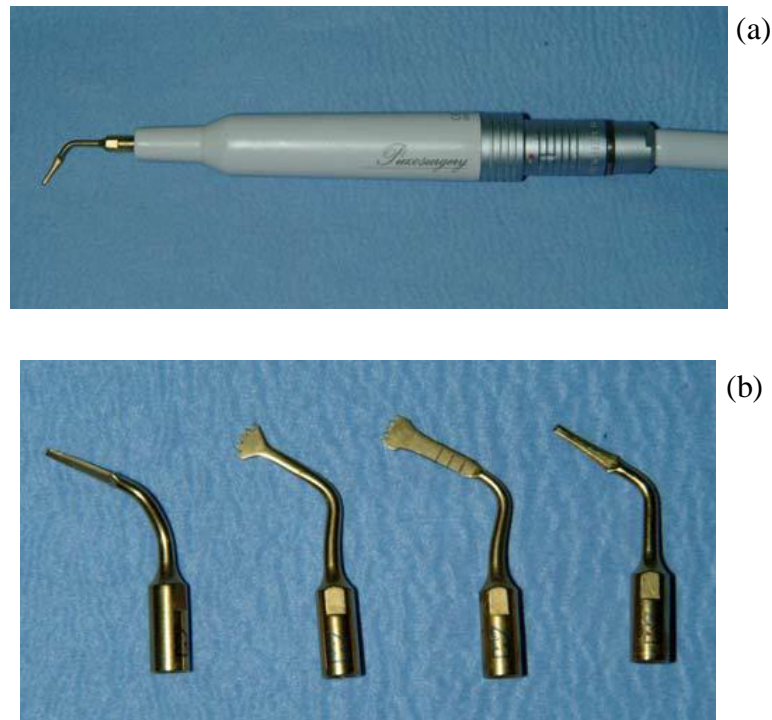


Figure 2-3 (a) Handpiece of the Mectron piezosurgery ultrasonic device (b) different inserts can be screwed on the top of the handpiece [32]

The conventional instruments performing osteotomies are drills and saws. They offer a higher cutting rate than ultrasonic instruments [35]. However, they may also cut the soft tissues below or beside the bone because a rotating tip or a sawing blade usually does not stop on contact with structures of different density [33]. In contrast, ultrasonic bone cutting devices are selective for bone. Even though the blade of instruments may touch soft tissue during operation, no wound is generated unless enough pressure is applied [36]. Because the proper use of the piezoelectric device calls for application of limited pressure, the safety margins are high, allowing it to perform an osteotomy in proximity to the nerve. The vibration of the piezoelectric bone surgery ensures a precise cutting action, and at the same time maintains a blood free operative area secondary to the cavitation effect from the irrigation solution [37]. Moreover, histological examinations performed on the cut surfaces have confirmed the lack of necrosis by ultrasonic osteotomy, thus increasing the presence of live osteocytes and reducing healing time [37].

Limitations were also witnessed on ultrasonic bone cutting. Cooling systems are needed to prevent the bone from overheating, which deliver water or saline solution to the cut site. However, they lead to an additional problem of cross-contamination [38, 39] and deep incisions in bone are still greatly restricted by the high temperature [40] .

### 2.1.3 Tissue Fragmentation and Aspiration

Ultrasonic surgical devices have been used for tissue fragmentation and removal since the 1960s [3]. In procedures using such devices, a hard vibrating tip is used to cut or emulsify soft tissue. In some instruments, tissue fragmentation is achieved using a hollow tool, which also provides suction at the interaction site for debris removal (aspiration) [19]. A schematic of a basic ultrasonic surgical aspirator is shown in Figure 2-4.

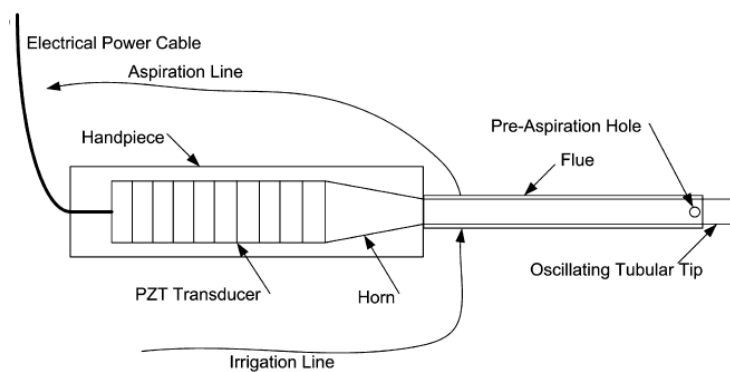


Figure 2-4 Schematic of a basic ultrasonic surgical aspirator [7]

The transducer works at 20-30 kHz and the vibration amplitude generated at the tip is around 100  $\mu\text{m}$ . The debris is removed by a suction path up the centre of the hollow tip. A source of irrigation fluid is usually included to cool the tip and also provide fluid to create a tissue slurry which helps prevent clogging in the aspirant line [7]. The purpose of the aspiration is claimed to be twofold. Firstly, it functions to aspirate fragmented debris via the hollow lumen and secondly, to counteract the positive acoustic pressure close to the tip of the ultrasonic device [41]. In the absence of the negative pressure, tissue moves away from the vibrating probe, and no fragmentation occurs. When the negative pressure is present, the aspiration pressure draws the tissue into or against the probe end-effector for ablation or fragmentation.

The vibrating metal probe is believed to break the tissue into emulsion through three classes of interaction for ultrasound with tissue: cavitation, thermal effect and direct mechanical effect [41, 42]. The peak-to-peak displacement and suction are the two most significant parameters that affect the rate of tissue fragmentation [41]. The reported clinical applications of ultrasonic assisted fragmentation and aspiration are phaco-emulsification (emulsification of cataracts), neurosurgery (fragmentation and aspiration of brain tumours), and lipoplasty (fragmentation and aspiration of fatty tissues) [43].

#### 2.1.4 Performance Variation of Ultrasonic Surgical Instruments

In applications mentioned above, the desired physical or chemical benefits are achieved through cavitation, direct mechanical impact or thermal effects. However, the mechanisms of these effects are not fully understood yet [18]. At the same time, the tissue interacting with the probe acts as physical loads to the resonant system. It manifests itself as additional mass to the system and changes the system's stiffness. Consequently, the resonant frequency varies. When the probe contacts with the tissue, the ultrasound wave transmits into the tissue, resulting in energy losses of the resonant system. The energy losses are reflected as an increase in the electric impedance of the system. Both frequency variation and impedance increase result in decrease of vibration amplitude generated by the transducer and consequently the efficiency of the ultrasonic instruments.

The variation of the working characteristics of ultrasonic surgical instruments was first observed clinically by Aro et al. [44] who noted that an ultrasonic scalpel needed to be regulated at the generator to maintain optimal vibratory frequency. Ying et al. [9] demonstrated that soft tissue such as fat, muscle, liver shifted the resonant frequency of an ultrasonic probe to lower working frequency compared to unloaded operation in air. Conversely, resonant frequency shifted to higher frequency when the probe was loaded in cancellous or cortical bone. In addition, both soft and hard tissue increases the electric impedance of the ultrasonic probe.

Apart from the probe-tissue interaction, the high excitation level during applications also induces nonlinearities to the piezoelectric transducer and thus changes its working characteristics. This will be discussed in detail in Section 2.3.

## 2.2 High Power Ultrasonic System

Typically, a high power ultrasonic system consists of a driving system, a transducer/convertor, a horn/booster/concentrator and an operating tip/probe, as shown in Figure 2-5.

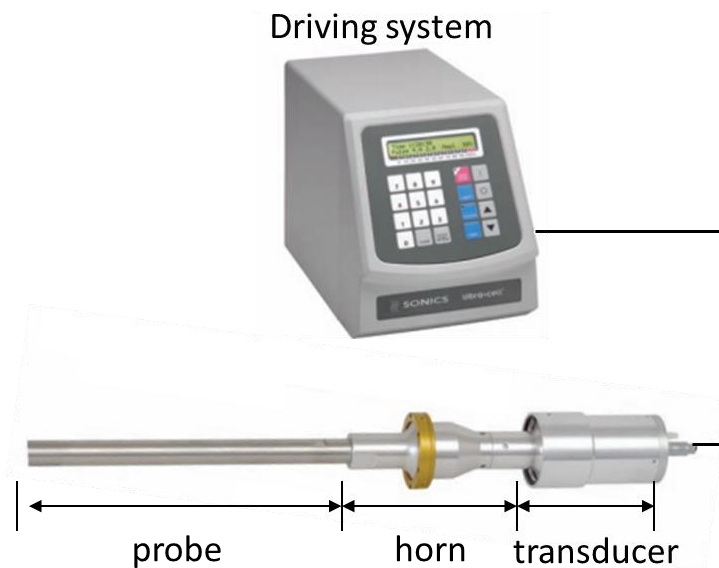


Figure 2-5 Schematic configuration of a high power ultrasonic system

The ultrasonic generator is the power supply of the transducer. It converts the main electricity into a specific high frequency electric signal (20-100 kHz) and gives the output power as required.

Ultrasound transducer converts a particular type of source energy into acoustic energy. The source energy can be either mechanical (mechanical transducer) or electrical (electromechanical transducer). At present, electromechanical transducers based on magnetostrictive or piezoelectric effects are most widely used [45]. Magnetostrictive effect refers to the phenomenon where a material changes shape due to a change in its magnetic state. In contrast, a piezoelectric material changes its mechanical dimensions when an electric field is applied. Conversely, an electric field is generated on a piezoelectric material that is strained.



Historically magnetostrictive transducers were the first to be used on an industrial scale to generate high power ultrasound. They are of extremely robust and durable construction and provide very large driving force. However, there are two disadvantages. Firstly the upper limit to the frequency range is 100 kHz, beyond which the metal cannot respond fast enough to the magnetostrictive effect. Secondly the electric efficiency is less than 60% with significant losses emerging as heat [46]. In contrast, the piezoelectric transducers are more efficient and can operate over a wide frequency range, thus becoming the most common types of ultrasound transducers today.

The vibration amplitude generated by the transducer is usually in the range of 2-10  $\mu\text{m}$ , which is magnified by a horn and then transmitted to the distal probe. The horn and distal probe are commonly tuned to a specific mode of vibration, usually longitudinal but sometimes torsional, lateral or combinations of these, at the required excitation frequency [47].

The following subsections introduce the technical background of piezoelectric material, piezoelectric transducer and acoustic horn. The driving system will be discussed in Section 2.4. The geometries and dimension of the distal probe are highly dependent on application and beyond the scope of this thesis.

### 2.2.1 Piezoelectricity

Piezoelectric material is the most important part of a piezoelectric transducer which employs converse piezoelectric effect to convert electrical energy into mechanical energy. Piezoelectric effect was found on certain crystalline materials by Curie brothers in 1880. These materials have the ability to develop an electric charge proportional to a mechanical stress, which is called the direct piezoelectric effect. Soon it was realized that materials showing this phenomenon must also show the converse piezoelectric effect: a geometric strain/deformation proportional to an applied voltage [48]. A schematic diagram for illustration of direct and converse piezoelectric effect is shown in Figure 2-6.

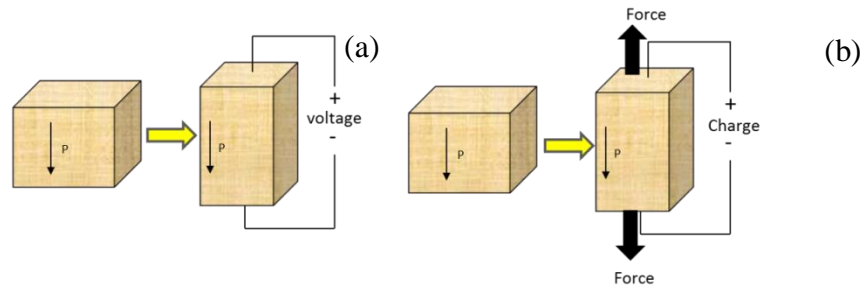


Figure 2-6 Schematic diagrams of the direct and converse piezoelectric effect: (a) inverse piezoelectric effect, where an electric field applied to the material changes its shape (b) direct piezoelectric effect, where a stress on the material yields an electric field across it

Piezoelectric materials can operate in different vibration modes depending on how they are cut. Figure 2-7 shows two most commonly used vibration modes in ultrasound transducers:  $d_{31}$  mode (plate) and  $d_{33}$  mode (bar). In  $d_{31}$  mode, the piezoelectric material is poled in  $[001]$ , i.e. the electric field is applied along the axis  $[001]$ , whereas the vibration direction is along the axis  $[100]$ . In  $d_{33}$  mode, both the poling direction and the vibration direction are along the axis  $[001]$ .

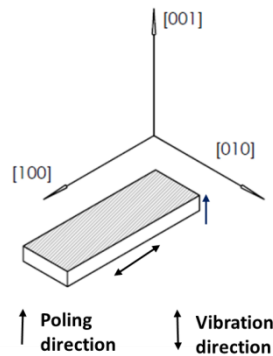


Figure 2-7 Vibration modes of piezoelectric material:  $d_{31}$  (plate) and  $d_{33}$  (bar)

Quartz was the first piezoelectric material used to generate ultrasound [49]. Along with tourmaline and Rochelle salt, these piezoelectric crystals were used in some piezoelectric devices such as sonars. However, the traditional single crystal materials suffer from some disadvantages which limit their use to some extent. For example, they mostly exhibit only a weak piezoelectric effect and low mechanical strength. Some are very sensitive to moisture, and their operating temperature range is often limited [48].

In 1946, piezoelectricity was observed in a new ferroelectric material consisting of barium titanate ( $\text{BaTiO}_3$ ) in polycrystalline ceramic form [49]. Since that time, the piezoelectric ceramics (piezoceramic) have been widely used in the major ultrasound transducer industries including naval, non-destructive valuation and medical applications. In 1954, strong piezoelectric effects were discovered in lead zirconate and lead titanate solid solutions [50]. This led to the development of a wide variety of polycrystalline lead zirconate titanate ceramics that are generally referred as PZT. The electromechanical properties of PZT can be controlled through the addition of small amounts of dopants to meet the requirements of different applications. These dopants results in a number of compositions. Electromechanical coupling coefficient measures the effectiveness with which a piezoelectric material converts electric energy into mechanical energy or coverts mechanical energy into electric energy. In certain compositions of PZT, the electromechanical coupling factor can be as high as 0.75 [51] . As a result, PZT began to dominate the piezoceramic commercial market. The most common piezoceramic materials available for high power applications are PZT-4 and PZT-8.

In 1981, Kuwata et al. [52] reported that single crystals of the solid solution of lead-zinc-niobate and lead titanate possessed a electromechanical coupling factor of greater than 0.9. Because the highest value is typically around 0.75 for PZT ceramics, the value above 0.9 attained in single crystal relaxors (piezocrystals) represents a major improvement. About 1992, the potential advantages of using single crystal relaxors for ultrasound imaging arrays were recognised, as evidenced by a patent application assigned to Toshiba [53]. Since then, interest has grown rapidly. Other single crystal relaxor-based ferroelectrics such as the solid solutions of lead-zirconium-niobate/lead titanate and lead-magnesium-niobate/lead titanate (PMN-PT) also exhibit piezoelectric coupling factors of greater than 0.9 [49].

Compared with piezoceramics, piezocrystals offer increased bandwidth, sensitivity and sources levels due to ultrahigh electromechanical coupling factors ( $k_{33}>0.94$ ) and high piezoelectric coefficients [51, 54, 55]. These promising material properties make it an exciting possibility for transducer, sensor and actuator technologies. On the negative side, the lower clamped dielectric constant results in reduced capacitance and higher

electrical impedance. This gives negative effects on transducer impedance matching with the power delivery system. Moreover, the Curie point of piezocrystals is 130-170 °C, compared with 300 °C of PZT. As the piezoelectric material only exhibits piezoelectric effect below the Curie point, the low Curie point of piezocrystals restricts their acceptance in numerous applications [49].

### 2.2.2 Piezoelectric Transducer

The configuration of a piezoelectric ultrasound transducer can take many forms depending on its application and operation frequency. In high-power ultrasonics and underwater acoustics, the sandwich type piezoelectric transducer is widely used, as shown in Figure 2-8.

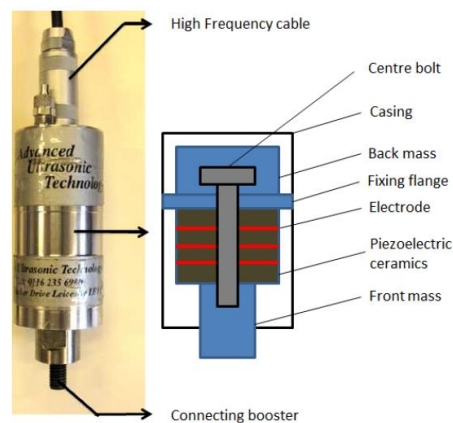


Figure 2-8 Sandwich piezoelectric transducer

It is composed of piezoelectric ceramic elements in  $d_{33}$  operating mode, sandwiched between two metal blocks: the front mass and the back mass. The metal blocks lower the resonant frequency of the transducer and increase the mechanical quality factor. The neighbouring piezoelectric elements are polarized oppositely. The outer electrodes contacting the metal masses are grounded and the central washer is charged. Although piezoelectric ceramic are fragile under large tensile stress, the clamping bolt imposes a compressive stress on the piezoelectric element, avoiding the tensile stress in operation. So, the transducer can operate at high power levels. The front mass is approximately matched to the medium by use of a matching material with intermediate impedance,

such as aluminium and magnesium. The material of the back mass, often steel or tungsten is used to block or reduce the motion of the rear surface [56].

### (1) Electrical Models

A piezoelectric transducer is part acoustic as its moving surface is in contact with the acoustic medium, part mechanical as a moving body controlled by forces, and part electrical as a current controlled by voltage [49]. Thus, electric equivalent circuits representing the acoustic and mechanical parts make possible an electric simulation of the whole transducer. There are several approaches to model the piezoelectric behaviour of piezoelectric elements and the interaction between the piezoelectric elements and the mechanical structure in terms of an electrical equivalent circuit.

A piezoelectric transducer is considered as a three-port device: one electric port and two acoustic ports. The electric port consist of the current ( $I$ ) and voltage ( $V$ ) between two metallized surfaces, while the acoustic port parameters consist of the force ( $F_1$  and  $F_2$ ) and particle velocity ( $v_1$  and  $v_2$ ) on each surface, as shown in Figure 2-9.

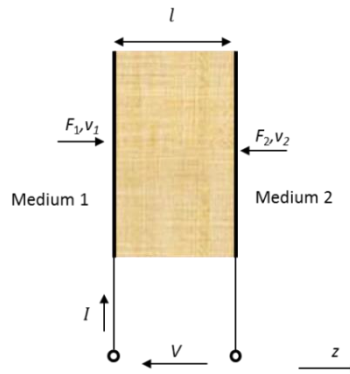


Figure 2-9 Three-port model representing a piezoelectric transducer [49]

The terminal behaviour of the three-port transducer can be characterised as

$$\begin{aligned}
 \begin{bmatrix} F_1 \\ F_2 \\ V \end{bmatrix} &= \begin{bmatrix} Z_{11} & Z_{12} & Z_{13} \\ Z_{21} & Z_{22} & Z_{23} \\ Z_{31} & Z_{32} & Z_{33} \end{bmatrix} \begin{bmatrix} v_1 \\ v_2 \\ I \end{bmatrix} \\
 &= -j \begin{bmatrix} Z_a \cot(\beta l) & Z_a \operatorname{cosec}(\beta l) & h/\omega \\ Z_a \operatorname{cosec}(\beta l) & Z_a \cot(\beta l) & h/\omega \\ h/\omega & h/\omega & 1/(\omega C_0) \end{bmatrix} \begin{bmatrix} v_1 \\ v_2 \\ I \end{bmatrix}
 \end{aligned} \tag{2-1}$$

$\beta$  is the wave number (propagation constant);  $\omega$  the angular frequency;  $l$  thickness of the piezoelectric element;  $h$  piezoelectric charge-stress constants;  $Z_a$  acoustic impedance;  $C_0$  the clamped (zero strain) capacitance of the transducer. The basis of this model is a solution a 1-D wave equation for propagation in direction of polarization. It assumes that the lateral transducer dimensions are much larger than the thickness and that the behaviour is linear [49].

In 1948, Mason [57] proposed the circuit model shown in Figure 2-10, whose terminal equations are identical to equation (2-4).  $\Psi$  is the transformation turns ratio.  $Z_1$ ,  $Z_2$  and  $Z_3$  are frequency-dependent impedances whose physical interpretation is not immediately evident.

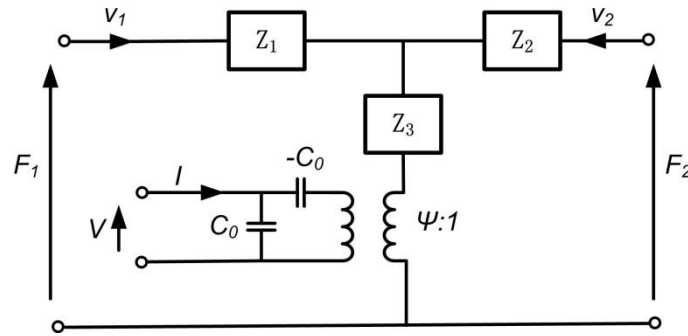


Figure 2-10 Mason 1-D model of a piezoelectric plate excited in thickness expansion mode [49]

$$Z_1 = Z_2 = Z_{11} - Z_{12} = jZ_a \tan(\beta l/2) \tag{2-2}$$

$$Z_3 = Z_{12} = -jZ_a \operatorname{cosec} \beta l \tag{2-3}$$

The electrical port is coupled, through an ideal transformer to a T-network which represents the acoustic propagation in the piezoelectric material (the first  $2 \times 2$  sub-matrix). Mason's model has also given rise to a variety of alternative formulations, such as Redwood equivalent circuit and KLM (developed by Krimholtz, Leedom and Matthaei) model. These models are usually termed as 'distributed models' because the mass and stiffness are distributed continuously throughout the structure.

In contrast, a piezoelectric transducer can also be represented as a lumped parameter model, where the mass is specified at a small number of points. A lumped model for piezoelectric transducer operating near resonance is presented in Figure 2-11, referred to as Butterworth-Van Dyke (BVD) model [58]. It is based on the analogies between a RLC (Resistor, Inductor and Capacitor) circuit and mechanical resonator.  $R_0$  and  $C_0$  are the dielectric loss resistance and the capacitance of the clamped transducer, which constitute the electric arm.  $M$ ,  $C_m$  and  $R_m$  are the effective mass, compliance and effective mechanical resistance of the transducer, which constitute the mechanical arm. The electric arm is coupled to the mechanical arm through a transformer. The mechanical arm can be further represented by a serial RLC circuit, as shown in the right circuit.  $L_1$ ,  $C_1$  and  $R_1$  are the inductor, capacitor and resistor of the RLC circuit. In this model, analogies can be made of force to voltage ( $F:V$ ), velocity to current ( $v:I$ ), compliance to capacitance ( $C_m:C_1$ ), mass to inductance ( $M:L_1$ ), and resistance to resistor ( $R_m:R_1$ ) [59].

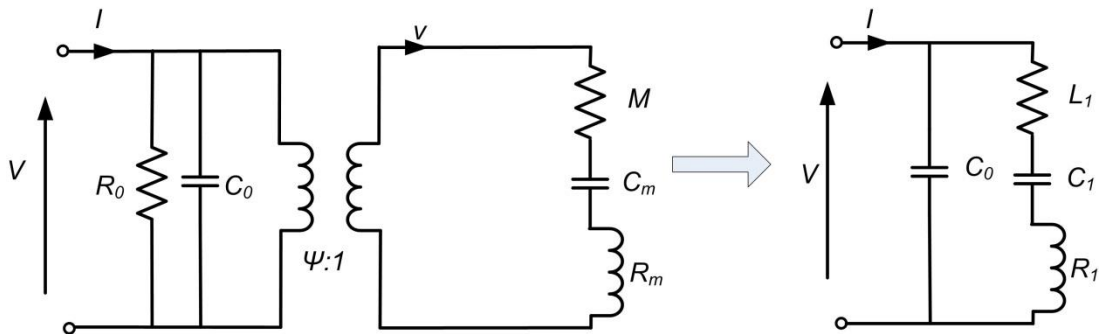


Figure 2-11 Butterworth-Van Dyke model of a piezoelectric transducer operating near resonance [11]

The input parameters of the distributed models include the transducer's physical parameters such as size and thickness, and the properties of the bonding layer.

Therefore, these models are more suitable for the mechanical design of the transducer [60]. The parameters of the BVD model can be determined from the measured impedance or admittance of the transducer without knowing the physical details. It is useful for understanding and evaluating the electromechanical resonance characteristics of piezoelectric transducers. However, it should be noted that the validity of the BVD model is limited to transducers close to the resonant frequency. It has limited accuracy and does not predict higher order resonant modes [59].

## (2) Transducer Characteristics

Since a piezoelectric transducer can be modelled as equivalent circuits, its electrical input impedance or admittance can be characterised. Both impedance and admittance are frequency-dependent. The impedance  $Z$  is a complex vector which can be broken down into its real and imaginary components, resistance  $R$  and reactance  $X$ . The inverse of impedance is the admittance  $Y$  of the transducer. This may also be broken into its real and imaginary parts, conductance  $G$  and susceptance  $B$ .

$$Z = \frac{V}{I} = R + jX \quad (2-4)$$

$$Y = \frac{I}{V} = G + jB \quad (2-5)$$

The electrical impedance or admittance measurement is a common and standard method for calibration and valuation of piezoelectric transducer. A range of performance parameters can be derived from the impedance/admittance versus frequency curves. Some of the important characteristics of piezoelectric transducers are briefly described in the following.

### **Resonant frequency**

A typical electric impedance and admittance plots near resonance of a high power ultrasonic transducer is shown in Figure 2-12.



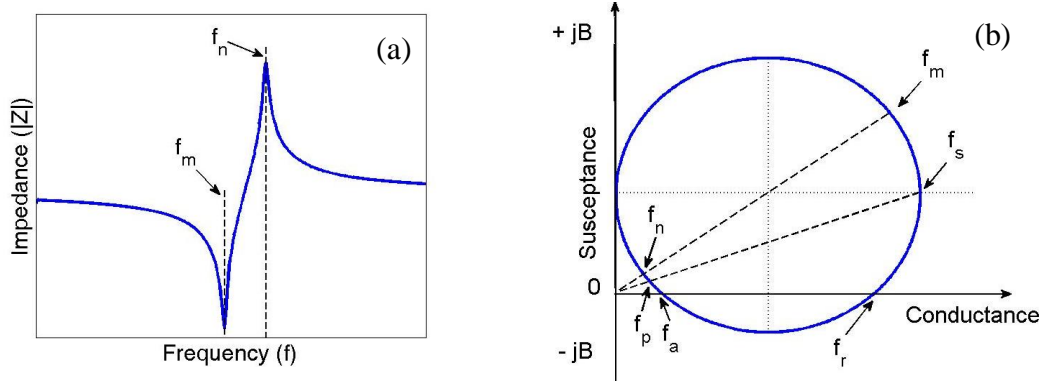


Figure 2-12 Electrical input impedance and admittance of piezoelectric transducer (a) impedance versus frequency plot (b) conductance versus susceptance plot

When exposed to an AC electric field a transducer changes dimension cyclically at the cycling frequency of the field. For each single vibration mode, six distinctive frequencies can be identified from the impedance/admittance plots. The serial resonant frequency, or the mechanical resonant frequency  $= f_s =$  frequency of the maximum conductance,  $f_m =$  frequency of the minimum impedance (the maximum admittance) and resonant frequency  $f_r =$  frequency of zero susceptance (zero impedance/admittance phase). The parallel resonant frequency  $= f_p =$  frequency of maximum resistance, anti-resonant frequency  $= f_a =$  frequency of zero susceptance, and  $f_n =$  frequency of maximum impedance (minimum admittance). For lossless piezoelectric transducers,  $f_m = f_s = f_r$  and  $f_a = f_p = f_n$ . In contrast, in lossy transducers,  $f_m < f_s < f_r$  and  $f_a < f_p < f_n$  [61].

### Mechanical Quality Factor $Q_M$

Mechanical quality factor,  $Q_M$  is a dimensionless parameter that describes how damped a transducer is. It is defined in terms of the ratio of energy stored in the transducer to the energy supplied by a generator, per cycle, to keep signal amplitude constant, at the resonant frequency:

$$Q_M = 2\pi \times \frac{\text{Energy stored}}{\text{Energy dissipated per cycle}} = \frac{f_s}{f_2 - f_1} \quad (2-6)$$

Where  $f_s$  is the serial resonant frequency with maximum conductance  $G_m$ ;  $f_1$  and  $f_2$  are the frequencies where the value of conductance is half of  $G_m$  on both the lower and upper sides of  $f_s$ . Also note that the  $Q_M^{-1}$  is defined as the mechanical loss  $\tan \delta_m$ .

$Q_M$  characterises the energy loss of a piezoelectric transducer and describes the transducer's bandwidth to its centre frequency. Higher  $Q_M$  indicates a lower rate of energy loss relative to the stored energy of the transducer and a narrower bandwidth. The vibration amplitude at an off-resonance frequency is amplified by a factor proportional to  $Q_M$  at the resonant frequency. Therefore, higher  $Q_M$  leads to a higher vibration amplitude at a constant voltage applied [59]. For some applications such as ultrasonic cutting and welding where high vibration amplitude is required, transducers with high  $Q_M$  and narrow bandwidth are preferable. Conversely, some applications such as acoustic emission detection and medical imaging require the transducer to work at a broad bandwidth. In such applications, transducers with broad bandwidth and consequently low  $Q_M$  are desirable[60] .

#### **Dielectric Loss, $\tan \delta_e$**

In practice, a piezoelectric material behaves like an imperfect capacitor, losing a fraction of its stored energy for each cycle of the applied field. Such losses are also valid for transducers and are denoted by  $\tan \delta_e$ , representing the losses per cycle of the applied field. It is determined by the ratio of the effective conductance to the effective susceptance measured at low frequency, typically 1 kHz [62].

The power dissipated by dielectric loss [63] can be described as

$$Power = 2\pi f C_0 \tan \delta_e V^2 \quad (2-7)$$

Where  $f$  is the frequency,  $C_0$  the capacitance,  $V$  applied voltage.

#### **Electromechanical Coupling Coefficient $K_{eff}$**

The electromechanical coupling coefficient,  $k_{eff}$ , is an indicator of the effectiveness with which a piezoelectric material or transducer converts electrical energy into mechanical

energy, or converts mechanical energy into electrical energy [64]. It can be determined from an electrical impedance or admittance plot by using equation (2-11), where  $f_s$  and  $f_p$  are the serial and parallel resonant frequencies, respectively.

$$K_{eff}^2 = 1 - \left(\frac{f_s}{f_p}\right)^2 \quad (2-8)$$

A high  $k_{eff}$  is usually desirable for efficient energy conversion. However, coupling coefficient is inversely proportional to  $Q_M$ , leading to a trade-off between the two parameters in transducer design.

### 2.2.3 Acoustic horns

Ultrasonic transmission line using horn structures has been widely used to boost the vibration amplitude generated by transducers. The basic principle is to concentrate the energy generated by a transducer at a larger cross section into a smaller cross section. Subsequently, high vibration amplitude or energy density is sustained at the smaller cross section [65]. The horns are usually tuned to resonate at the same frequency as the transducer. Although acoustic horns with longitudinal-torsional [47, 66] and flexural modes [67] have also gained wide applications in areas such as ultrasonic cutting, ultrasonic motor and ultrasonic welding, only ultrasonic horns in longitudinal mode are concerned in this work and discussed here.

The primary parameter of a horn is the amplification coefficient  $k_a$  equal to the ratio of the displacement or vibrational velocity at the horn ends and the area coefficient  $N$  equal to square of area ratio at horn ends [45]

$$k_a = \frac{u_l}{u_0} = \frac{v_l}{v_0} \quad (2-9)$$

$$N = \sqrt{S_l/S_0} \quad (2-10)$$

Here  $u_0$ ,  $v_0$  and  $S_0$  are the displacement, velocity and cross section area of the input surface of a horn, whereas  $u_l$ ,  $v_l$  and  $S_l$  are the displacement, velocity and cross section area of the output surface of a horn.

The most commonly used horn profiles are conical, exponential, stepped and catenary, as shown in Figure 2-13. The formulas of these four profiles are presented in Table 2-1, where  $k$  is the wavenumber. Conical horn is simple, easy to design and fabricate but the amplification coefficient is low. Exponential horns show low amplification coefficients as well but are advantageous in smooth stress distribution [68]. Stepped horns possess the maximum amplification coefficients and ease of fabrication. However, an abrupt change in the cross section of a stepped horn occurring in its nodal plane leads to high local stresses, overheating, and eventually to horn fracture. The amplification of catenary horn is greater than that of conical or exponential ones and less than that of stepped horns [45].

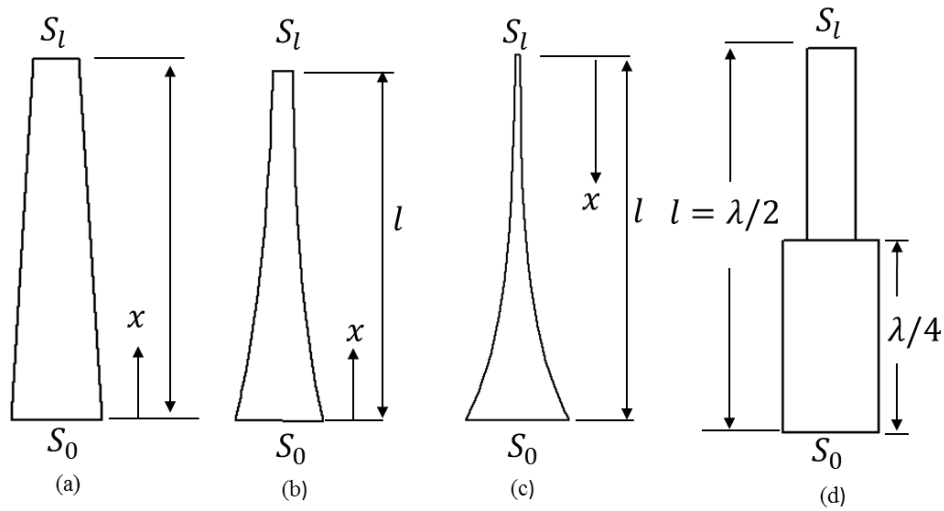


Figure 2-13 Profiles of the commonly used ultrasonic horns: (a) conical (b) exponential (c) catenary (d) stepped

Table 2-1 Formulas of horn profiles

Horn type	Cross section function	Amplification factor $k_a$
Conical	$S(x) = S_0(1 - bx)^2$ $b = (N - 1)/Nl$	$k_a = N(\cos kl - \frac{N - 1}{Nkl} \sin kl)$
Exponential	$S(x) = s_0 e^{-bx}$ $b = 2 \ln N / l$	$k_a = N$
Catenary	$S(x) = S_l \cosh^2 \frac{2x}{d_l}$	$k_a = \frac{N}{\cos(\sqrt{k^2 - \gamma^2}l)}$
Stepped	$S(x) = S_0 \quad 0 \leq x \leq \lambda/4$ $S(x) = S_l \quad \lambda/4 \ll x \ll \lambda/2$	$k_a = N^2$

Besides the horns mentioned above, horn profiles in other geometries have also been developed and widely used. These include Gaussian [69], Fourier, Bezier [68], sinusoidal [70] and wedge-shaped horns [71]. With the development in computing and finite element method (FEM), more complex horn profiles can be designed for particular applications and optimised for specific objectives.

### 2.3 Nonlinearities of Piezoelectric Transducers

When piezoelectric devices are used at resonance, if the excitation signal is elevated, as happens in the high power ultrasonics, nonlinear phenomena appear. The nonlinear behaviour of a piezoelectric transducer can result from structure features [72]. However, the main cause is the nonlinear elastic and electromechanical characteristics of the piezoelectric element under high electric field and high strain [73].

From the first use of piezoceramics such as PZT in ultrasonic devices during the 1950s, the nonlinear behaviour when excited above a certain threshold had been reported [74]. The physical origin of nonlinear behaviour of piezoelectric material is believed to be related to the extrinsic piezoelectric effect [62, 75-77]. Piezoelectric effect consists of two parts, the intrinsic and the extrinsic effects. The intrinsic effect refers to the lattice deformation caused by the electric field, and the extrinsic effect represents the elastic deformation caused by the motions domain walls and the interphase interfaces [76, 78]. Piezoelectric effect of a ferroelectric material comes mainly from extrinsic contributions. Intensive investigations [77, 79] have observed that the nonlinearities of piezoelectric material are mainly caused by the nonlinear motion of domain walls under high electric field or stress.

Under low electric field and stress, the behaviour of piezoelectric material is linear. The dielectric, elastic and piezoelectric constants are independent of the electric field strength and mechanical stress. Their relationships are described well by the standard piezoelectric constitutive equations. When the electric field strength and mechanical stress are above a certain threshold, nonlinear behaviour is observed and the dielectric, elastic and piezoelectric constants become field and stress-dependent [76, 80]. From piezoelectric transducer's point of view, the nonlinearities in the piezoelectric material can lead to several phenomena when a transducer is excited in high power level. These phenomena include increase of mechanical losses, temperature rise, resonant frequency shift, and appearance of frequency hysteresis [81, 82]. These phenomena have been intensively investigated because they negatively affect the performance of the transducer and its working limits.

### 2.3.1 Nonlinear behaviour

#### (1) Increase in Mechanical losses

Mechanical loss of a piezoelectric transducer can be indicated by the mechanical dissipation factor (mechanical loss tangent)  $\tan \delta_m$ , which equals  $Q_M^{-1}$  [83]. Alternatively, it can be denoted by the mechanical resistor  $R_1$  [8], as described in the BVD model previously.  $Q_M$  was observed to keep almost constant at small electric field

and vibration velocity, but reduce dramatically above a certain electrical field or vibration velocity [84-86].

The decrease of the mechanical quality factor by the increase in losses is a serious problem for high power ultrasonic devices because, at high electrical or stress level, this quality factor is several times lower [8, 87]. According to K. Uchino [88], the maximum vibration displacement of a piezoceramic plate in  $d_{31}$  operation mode is

$$u_{max} = \left(\frac{8}{\pi^2}\right) d_{31} E_z L Q_M \quad (2-11)$$

Where  $d_{31}$  is the piezoelectric constant,  $E_z$  the electric field in poling direction and  $L$  the length of the plate. Thus, the reduction in  $Q_M$  degrades the vibration amplitude of the ultrasonic transducer.

Further, as  $Q_M$  decreases with electrical or stress level, the efficiency of the transducer decreases and the energy dissipated rises. Takahashi [73] described the relationship between the dissipated vibration energy and mechanical quality factor as

$$\omega_0 W = \frac{1}{2} M V_0^2 \omega_0 Q_m^{-1} \quad (2-12)$$

Where  $M$  is the mass;  $V_0$  is the effective vibration velocity, and  $\omega_0$  is the resonant angular frequency. The dissipated vibration energy per second  $\omega_0 W$  is inversely proportional to  $Q_M$ . Part of the dissipated energy is converted into heat, leading to temperature rise of the piezoelectric material and consequently limiting the power and vibration level [89, 90].

## (2) Self-heating

Self-heating of piezoelectric material is a critical issue in high power ultrasonics and attracts intensive investigations. The reason behind is primarily because depolarization of piezoelectric material may occur if the temperature exceeds the Curie point, leading to a complete loss of piezoelectricity. Even below the Curie point, the elastic and electromechanical properties of the piezoelectric transducer undergo significant change

due to temperature increase, resulting in degradations in performance [91]. For instance, PMN-PT single crystals exhibit Curie temperature between 150 and 200 °C; however, a decrease of piezoelectricity was observed at temperatures much lower than the Curie temperature [92]. The temperature increase resulting from self-heating can significantly limit the maximum power and vibration amplitude of the transducer.

The heat sources in a piezoelectric transducer are mainly the mechanical and dielectric losses from piezoelectric element [88, 93]. The mechanical losses in other elements of a transducer are of less importance [91]. The dielectric energy loss is proportional to dielectric loss  $\tan \delta_e$  times the square of the electric field, as presented in Equation (2-7) previously, whereas the mechanical energy loss is proportional to the mechanical loss  $Q_M^{-1}$  times the square of the strain or velocity, as described by Equation (2-12). It is accepted that, at off resonance, dielectric losses are the dominate source of heat generation since the vibration velocity is low.

At resonance, the mechanical losses dominate the heating effect of piezoelectric material [86, 88, 93, 94]. The heat generation caused by mechanical loss is spatially dependent at resonance, considering the non-uniform strain distribution. This is a key difference between heat generated by mechanical losses and dielectric losses, where in the latter, the internal heat generation is assumed uniform throughout the volume [95]. Sherit [86] shown that for a plate sample of thickness,  $L$  and area  $A$ , with  $x=0$  at centre, the power distribution as a function of distance  $x$  was given by

$$P(x) = 2P_m \cos^2\left(\frac{\pi x}{L}\right) \quad (2-13)$$

$P_m$  is the mean power level. The cosine squared variation of temperature in a resonating piezoelectric device was confirmed by Tashiro [94]. Several workers [96, 97] have modelled and measured temperature profiles of piezoelectric transformers driven at resonance, and shown that hot spots coincide with regions of high strain.

However, Hirose et al [84, 98] suggested that when a piezoelectric vibrator was driven at resonance point, the main contribution to the total loss is from mechanical loss under small vibration velocity level. The contribution from the dielectric loss increased



dramatically above a certain critical vibration velocity such as 0.2-0.3 m/s, where the actual heat generation started to be observed. According to Kielczynski [91], minor impact of mechanical stress on the losses of a transducer in resonance was observed and the temperature of the piezoelectric element did not strictly depend on its position in relation to the nodal position.

Despite the controversial mechanism of self-heating of piezoelectric transducer, the temperature rise in the piezoelectric material or transducer is affected by both self-heating and heat dissipation conditions. Temperature rise of piezoelectric material increases with velocity and sharply goes up when the velocity reaches a certain value that depends on material composition [99]. The temperature rise is approximately proportional to the dissipated-vibration energy [73]. Zheng [89] found the heat generation depended on both driving frequency and electric field while the temperature rise was approximately proportional to the value  $v_e/A$  ( $v_e$  is the effective volume and  $A$  is the total surface area of the piezoelectric material). Li [83] reported that for a given actuator, as the vibration velocity/stress increased, the temperature raised. For different actuators, the higher frequency one (shorter length) produced larger temperature rise. The proper positioning of the heat source and appropriate choice of materials enable optimum removal of heat and also lowering the temperature of the source [56, 91].

### (3) Resonant frequency shift

When piezoelectric transducers are driven at high electric field, frequency softening effect is observed, i.e. the resonant frequency shifts to lower values at higher electric field [8, 82, 100]. As a high power piezoelectric transducer is desirable to driven at resonance to achieve the highest efficiency and generate the largest vibration amplitude, this softening effect, however, results in uncertainty in resonant frequency and thus reduces the performance of the transducer. This is particularly an issue for transducers with high  $Q_M$ , because the performance reduces rapidly at frequencies near the resonance [11].

For a piezoelectric material in plate shape, the resonant frequency can be expressed as

$$f_s = \frac{1}{2L} \sqrt{\frac{1}{\rho s_{11}^E}} \quad (2-14)$$

$L$ ,  $\rho$  and  $s_{11}^E$  are length, density and elastic compliance of the piezoelectric material.

The elastic compliance of a piezoelectric material is dependent on both the temperature and the stress level, making the resonant frequency shift with temperature and stress. It was observed that the elastic compliance increased with temperature. Thus, the resonant frequency shifted to lower values with increasing temperature [101]. The compliance of a material usually keeps constant at small strain/stress level and, yet increases with strain at large strain/stress level, referred as nonlinear elastic property [87]. There is no exception for piezoelectric material. Increase of compliance [101] or reduction of Young's modulus [73] is observed when the vibration velocity is above a certain value. At each vibration velocity, higher compliance was observed at higher temperature. Therefore, the fall of resonant frequency at high electric field and vibration velocity is caused by the decrease of compliance, since the length and density are considered to be almost constant.

#### (4) Hysteresis phenomenon

The nonlinear effects for a piezoelectric transducer are not the same for different frequencies around resonance; hence the resonance peak is no longer symmetrical [100]. When the electric field is high enough, the resonant frequency shift is very high, and hysteretic phenomenon appears. For each applied voltage, there is a frequency range for which there are two different stable steady state solutions, one or the other being reached depending on the initial conditions [102, 103]. When a frequency sweep is made in decreasing frequencies at a constant voltage high enough, the response drops discontinuously at a certain frequency. In contrast, if the frequency sweep is carried out in increasing frequencies, the response jumps up discontinuously at another frequency [82, 101, 104]. The response can be electrical input impedance/admittance, vibration velocity and current. These two characteristic frequencies cause a hysteresis region as shown in Figure 2-14.

The location of the jumping is between points II and III while the location of dropping is between V and IV, creating a hysteresis region and bifurcation, a point at which there may be a number of solutions rather than a unique one. A transducer working between the frequencies of the jumping and dropping will show unstable characteristics as the amplitude of the vibration alternates between high and low amplitudes of vibration. However, if the transducer is exited away from the hysteresis region, the system will remain stable [105].

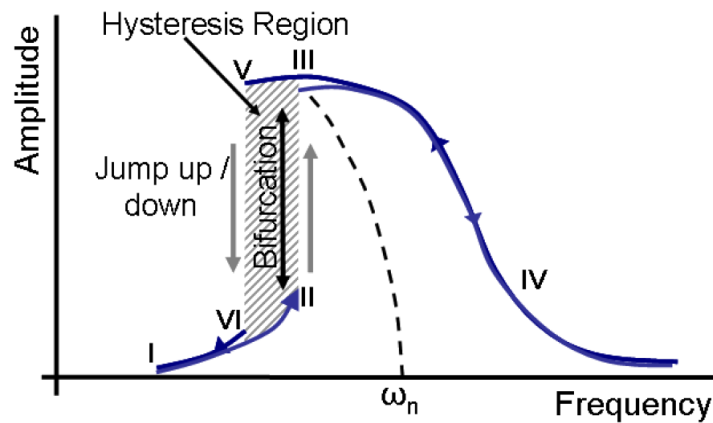


Figure 2-14 Hysteresis phenomenon of a piezoelectric transducer [105]

The hysteresis phenomenon of a piezoelectric transducer is attributed to the elastic compliance variation under different stress level [101, 106]. It was found that the compliance of hard PZT is proportional to the square of stress while the compliance of soft PZT is proportional to stress [8, 82, 99]. Further, the stress is believed to be proportional to the motional current through the transducer [82]. When a frequency sweep at constant voltage is taken around resonance, the current at different frequencies is different. Consequently, different stress is expected at different frequencies, resulting in different nonlinear effects.

### 2.3.2 Nonlinear Characterisation of Piezoelectric Transducers

Piezoelectric transducers suffer from serious nonlinear behaviours under high electric field and stress, as discussed above. These nonlinear behaviours reduce the performance of piezoelectric transducers significantly. It is thus necessary to characterise the nonlinearities of transducers at high power level to understand the mechanism and

determine the working limits [107]. To date, several techniques to characterise the nonlinearities of piezoelectric transducers have been proposed, including frequency sweep at constant voltage, frequency sweep at constant current, amplitude sweep at constant frequency and pulse drive method.

#### (1) Frequency Sweep at Constant Voltage

Frequency sweep at constant voltage is the conventional method to characterise the non-linear behaviour of ultrasonic devices and have been widely used [86, 108, 109]. It uses a network analyser and power amplifier to conduct frequency sweeps at different voltage amplitude levels, obtaining the electric impedance characteristics at the interest frequency range [82, 109]. The properties such as mechanical loss values and resonant frequency can be determined from the electric impedance characteristics [58]. Usually, the measurement of the motional current is necessary to estimate the mean strain undergoing in the ultrasonic devices[84].

The limitation of this method is, with increasing vibration velocity the electric impedance versus frequency curve distorts significantly, sometimes exhibiting large hysteresis or a jump of the peak curve upon uprising and falling driving frequency [84, 108]. This spectrum distortion makes it difficult to determine the properties of the device. It is thus necessary to make the frequency sweep only in decreasing frequencies, in order to make sure the resonance is always reached, even if the hysteresis phenomenon appears [82]. Another problem is that multiple frequency sweeps are required as one complete frequency sweep can only obtain one point on the nonlinear characterisation curve. Moreover, self-heating cannot be fully eliminated during the test [101].

#### (2) Frequency Sweep at Constant Current

Frequency sweep at constant current was proposed by Hirose [85, 102] to avoid the jump phenomenon during the high power characterisation. In this method, the vibration velocity of the specimen is held constant by varying the applied field as the frequency is swept through the natural resonance mode of the specimen. As the vibration velocity of the ultrasonic transducer is linearly proportional to the motional current, a feedback

electric system was employed to keep the current through the transducer constant after compensating the electric capacitance of the transducer. With the constant vibration velocity, asymmetries or hysteresis jumps in the admittance spectrum can be avoided. However, as the electric impedance of the transducer is usually very high off resonance, the frequency sweep can only be conducted in a very small region around resonance. A profile fitting technology is required to obtain a complete electric impedance or admittance spectrum.

This method provides a complete symmetric impedance peak spectrum without hysteresis or jump phenomenon up to a high vibration velocity level. The drawback of this system is the use of rather sophisticated, nonstandard generator. The main problem of this system is that the power applied to resonator is always high, resulting in significant self-heating effect [82, 109].

### (3) Amplitude Sweep at Constant Frequency

Another measurement method developed in [8, 110] consists of making an amplitude sweep at constant frequency. The measurements of resistance and reactance increase for the nonlinear characterisation depend only on the motional current and not on the frequency. In this system, an amplitude sweep is carried out for a fixed frequency near the resonance, and the measurement of the resistance  $R$ , reactance  $X$  and the current  $I$  are made in order to obtain the resonator nonlinear characterisation. This amplitude sweep is repeated at another close frequency to verify that the nonlinear characterisation is similar.

The results obtained from the system together with the mathematical model of nonlinear behaviour explain well the nonlinear response of piezoelectric material due to elastic nonlinearities [8, 110]. The drawback of this method is that not all impedance analyser allows these measurements. Some have no amplitude sweep ability available even if it allows the necessary measurement of  $R$ ,  $X$  and  $I$ .

### (4) Burst Excitation

In order to discriminate the effect of temperature rise from that of other factors during high power characterisation, Umeda [111] proposed a burst excitation method to

measure the electric transient response of the piezoelectric transducer. The harmonic AC voltage was applied to the piezoelectric transducer for only  $n$  cycles until the vibration velocity rises to a sufficient high amplitude level. After that, the electric terminal was short circuited, and the piezoelectric transducer experienced free vibration. Figure 2-15 shows the waveforms generated by the drive. The exponential decay curves of the current  $i$  and the vibration velocity  $v$  are analysed to determine the constants of the piezoelectric transducers.

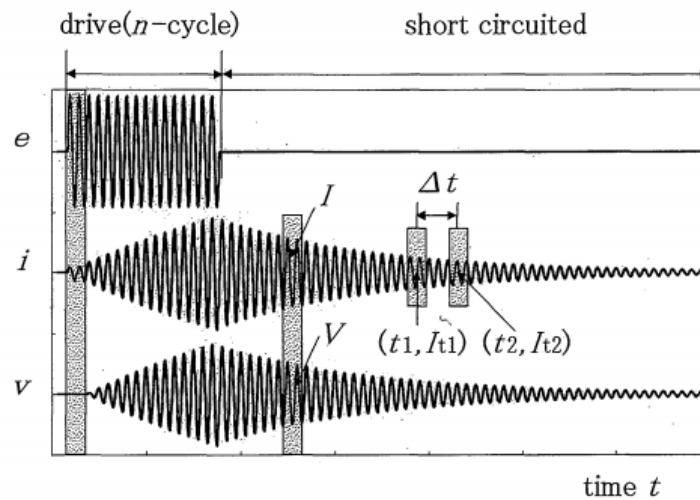


Figure 2-15 Transient response of the piezoelectric transducer during burst excitation [111]

This method has been successfully used to characterise transducers with a high mechanical quality factor, working at the first resonance mode, which is at the lowest frequency [82, 112, 113]. The main advantage is its ability to estimate the various constants of the piezoelectric transducer and clarify the mechanism of loss increase at high power range being free from the temperature change [114]. However, serious measurement difficulties have been found when it was used to characterise 3-1 composites [115, 116]. The beat phenomenon may easily occur due to close proximity and excitation of different modal frequencies associated with thickness and lateral modes. This beat effect makes the correct time constant measurement difficult [117].

## 2.4 Driving Systems for High Power Ultrasonics

Performance of ultrasonic surgical instruments suffers from significant variation in operation. This variation is partly resulted from the nonlinearities in transducers caused by the high operating power, and partly resulted from the physical loads placed by biological tissues. Particularly, the resonant frequency shift attracts the most attention in designing the driving system, because high power ultrasound transducers often possess high  $Q_M$  and thus very narrow bandwidth. Even a slight frequency shift can potentially results in significant performance reduction. Thus, to excite a piezoelectric transducer efficiently at high power, optimally, the driving system first of all should be capable of adjusting the frequency output to match that of the transducer. The electric impedance of the transducer may vary in operation, caused by the increasing mechanical loss and physical loads. When the electric impedance rises, the driving system should deliver more power to the transducer to keep the current through the transducer constant so that the vibration velocity is constant.

Therefore, to excite a piezoelectric transducer efficiently at high power levels, the driving system must be adaptive in driving frequency and voltage. This is usually achieved by using closed control loops. In a closed control loop, feedback signals obtained from the performance sensor are fed back to a controller, which, according to certain algorithm, calculates the driving frequency and voltage of the driving system.

### 2.4.1 Feedback Signals

The feedback signal in a control system should be able to reflect the performance of the plant. For a piezoelectric transducer, the feedback signals can be either mechanical or electrical [12] . Electrical feedback signals are the signals for electrical sensors measuring the electrical characteristics of a piezoelectric transducer, including voltage, current and power. In contrast, mechanical feedback signals are the signals from sensors measuring the mechanical characteristics of the oscillations, including vibration displacement, velocity and acceleration.

In a mechanical feedback system, sensors are placed near the cutting area at the end of the concentrator or the tip of the function probe to monitor the vibration velocity or

acceleration. Therefore, it directly reflects the oscillations of the ultrasonic system. By controlling the signal from this sensor, the actual state of vibration can be controlled [118] . However, it is inconvenient to use this arrangement in industrial conditions, since it is difficult to fix a sensor permanently because of the prolonged high frequency vibration. Additional wiring to the control system is a disadvantage as well, as the sensor is located in the cutting area. Laser vibrometer was found to provide signals with high precision and very low harmonic distortion, but too expensive and not intended for use within the industrial environment [119].

In an electrical feedback system, the sensors such as current probe and voltage probe can operate remotely. They do not need to be placed in the cutting area, which makes them convenient to use in practical conditions. However, this sensor reflects the oscillations of the system in an indirect way via the current or power in the piezoelectric transducer. This can cause problems when the transducer enters hysteresis region at high power levels, because the transducer has at least two steady state vibration amplitudes depending on the driving history [120]. In such a case, the current cannot reflect the actual vibration amplitude.

In terms of ultrasonic surgical instruments, electric feedback is preferred to mechanical feedback. This is not just because the installing of a sensor in the probe tip is not convenient, but also because the sensor installed on the probe tip requires sterilisation to work in the surgical site, which might be complicated in practice. In contrast, the electric feedback uses sensors operating remotely, thus no sterilisation is required.

#### 2.4.2 Control Strategies

A variety of control methods has been developed to track the resonant frequency and control the vibration amplitude of the transducers in high power applications. Fernandez [11] et al. proposed an automatically control system based on phase lock loop (PLL), as shown in Figure 2-16. In this system, the clamped capacitance of the transducer was tuned out by a shunted conductance so that the resonant frequency could be indicated by zero phase of the impedance. The voltage across and current through the transducer were measured, and their phases were compared. The phase difference served as a feedback to a proportional controller, which controlled the input of a voltage-controlled



oscillator (VCO). A VCO is an electronic oscillator whose oscillation frequency is controlled by a voltage input. By using the VCO, the driving frequency was adjusted by the phase difference, which was finally locked in zero.

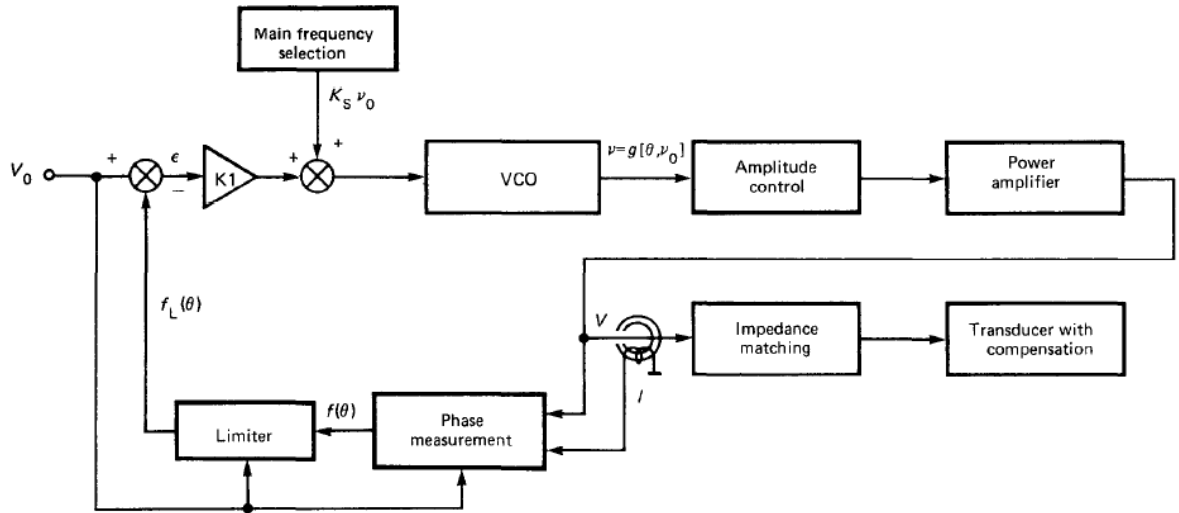


Figure 2-16 Functional block diagram of driving system based on PLL[11]

This PLL based on VCO has been widely used in other driving systems for ultrasonic transducers to track the resonant frequency shift [13, 121-123]. All these systems used the impedance phase as the feedback and a VCO to generate the driving signals at desired frequencies. In cases when the frequency range of VCO was higher than that of the transducer, a pair of flip-flops was used to count down the frequency [123]. The signal generated by VCO was basic driving signal, requiring magnification to drive the high power transducers. The amplitude of the driving signal was controlled to keep the current through the transducer stable so that the vibration velocity stayed at the desired levels [121, 124]. A significant part of these studies focused on optimizing the performance of the power amplifier in terms of efficiency and linearity through proper electronic circuit configuration [125] and power-converter control methods [13, 122].

The fundamental problem of PLL concerns the relationship between phase and resonance. If the clamped capacitance is not tuned out by a matching inductor, then the zero phase frequency  $f_r$  is different from the mechanical resonant frequency  $f_s$ . In some cases, the zero phase frequency even doesn't exist. If the matching conductor is used, then the zero phase frequency  $f_r$  equals to the mechanical resonant frequency  $f_s$ .

However, in practice, the matching conductor will only be correct at one resonant frequency.

Considering the problem of PLL, B. Mortimer [14] proposed a driving system, which track the frequency shift by admittance locking. It was based on the principle that the maximum power transfer from the transducer to the medium occurs when the transducer is at the maximum admittance. The current through the transducer was measured, based on which the slope of admittance curve,  $dG/df$ , was calculated.  $dG/df$  was forwarded to a VCO through a PI controller. The VCO adjusted the frequency so that  $dG/df$  was zero, i.e. maximum admittance was achieved. The advantage of this system is that only current has to be measured compared with PLL, where both voltage and current signal are essential. However, the system can only work at frequency below 25 kHz while the frequencies of high power ultrasound transducers vary between 20 to 100 kHz.

A resonant frequency tracking system for high-intensity ultrasound (HIFU) applicators was developed by Martin et al. [126] through minimizing the reflected voltage. An impedance matching network converted the transducer impedance to 50  $\Omega$  to match the transmitter output impedance. As the resonance of the applicators shifted, a mismatch between the transmitter and matching network occurred, causing an increase in the reflected voltage. The reflected voltage was sensed by a directional coupler and applied to a frequency adjust circuitry. When the reflected voltage increased to a special level, the signal output of the frequency adjusting circuitry would exceed a threshold and then controlled a frequency generator to produce a frequency variation of 100 Hz. In this way, the signal from the directional coupler provided feedback for changing the frequency as the applicator heated up in order to maintain it optimally matched. However, it was found that the negative swing at the output of the frequency adjust circuitry was limited in range, so tracking the need to increase the frequency operates only over a narrow span. This was attributed to the harmonics present in the drive signal resulting from the Class-D power transmitter used.

Babitsky [12, 118, 119, 127] developed an adaptive driving system for ultrasonic machining devices using the concept of autoresonant control. Autoresonant control is a method based on phase control, which maintains the resonant regime of oscillation

automatically by means of positive feedback using transformation and amplification of the signal from a sensor. It is based on the fact that during resonance the phase lag between the vibration of the working element and the excitation force applied is constant [120]. A schematic of the autoresonant control system designed for ultrasonic machining is shown in Figure 2-17 [127].

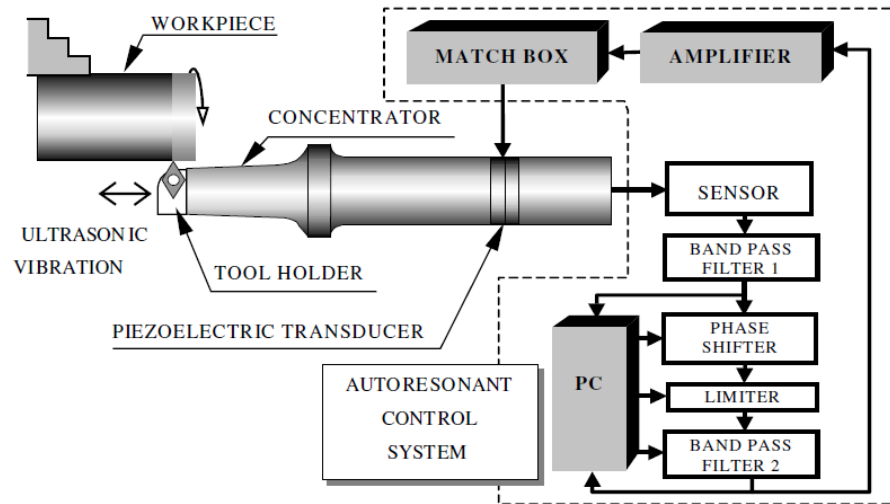


Figure 2-17 Schematic diagram of autoresonant ultrasonic cutting system [127]

The control system generated a control signal by means of shifting the phase of the signal from the sensor and changing its amplitude. This control signal was then supplied to the piezoelectric actuator to produce an excitation for the vibrating system. The sensors could be a current probe, an accelerometer or an ultrasonic microphone [118]. For every control cycle the phase shift value was changed by the phase shifter to the direction resulting in the maximum RMS value of the sensor signal. Thus, the control system always aimed at the most efficient autoresonant state. The vibration amplitude was kept at the desired levels by adjusting the threshold of the limiter. The control algorithms of these systems were implemented in software on a PC, which allowed various configurations of the autoresonant control system. However, the frequency range of the phase shifter was between 15 and 25 kHz. This also limited the working frequency range of the whole system.

## 2.5 Discussion and Conclusion

Ultrasonic surgical instruments have been widely used in surgical operations for biological tissue dissection, fragmentation and ablation, because of their well-documented benefits. These benefits are believed to result from cavitation, direct mechanism and thermal effects, although there is still an incomplete understanding of these mechanisms [7]. The ultrasonic surgical instruments are inherently desirable to be driven at the resonant frequency because optimal power conversion and vibration response are available. The vibration amplitude at the probe tip is also expected to be stable so that the clinical outcome is consistent and repeatable. However, the performance of the ultrasonic surgical instruments vary significantly in operation, resulting from nonlinearities induced by high driving power, and physical loads placed by biological tissues. This arouses the need for an adaptive driving system.

To drive the ultrasonic surgical instruments in an efficient way and achieve repeatable and controllable effects in operation, the driving system should be able to track the resonant frequency of the instruments and provide stable vibration amplitude despite the variations in operation conditions. Driving systems based on mechanical feedback signals were proved to be more efficient than systems based on electrical feedback signals. However, the installation of sensors on the probe of the instruments is difficult and not appropriate for medical applications. Among the systems using electrical feedback signals, phase lock loop (PLL) is the most widely used control strategies due to its effectiveness. The PLL systems reported are based on analogue integrated circuits. The tuneable range of the circuits is limited by the characteristics of the analogue intergraded circuits. Moreover, the development of such a system usually involves designing a power amplifier, which makes the process complicated and tedious.

In this thesis, simple ultrasonic devices for soft tissue cutting are designed and characterised. The devices are based on piezocrystals other than traditional PZT. An adaptive driving system is developed to track the resonant frequency and stabilise the vibration velocity of these devices. The system takes the advantage of using combined analogue-digital configuration, which improves its flexibility in function and tuneable range. The performance variations of these devices under high power levels and

external loads are investigated. The ability of the adaptive driving system to improve the performance is studied.

### 3 DESIGN AND CHARACTERISATION OF ULTRASONIC PLANAR TOOLS

Sandwich piezoelectric transducers based on piezoelectric materials in  $d_{33}$  mode have been widely used as actuators for ultrasonic surgical instruments because of their low resonant frequency, large power capacity and high electromechanical efficiency [128]. Simple and lightweight devices are desired in the medical industry. An alternative approach is to sandwich a blade between two piezoelectric plates in  $d_{31}$  mode, referred as ultrasonic planar tool in this thesis.

This design concept of ultrasonic planar tool was first proposed by Lal [129, 130] through bonding two PZT plates onto a silicon (Si) blade as a surgical tool for operations such as cataractous lens dissection. Friedrich [131] *et al* developed a micro-cutter based on the similar configuration and demonstrated its cutting ability on chicken tissue. Lee [69] adopted this design for generating controlled stress on thin films for accelerated stress testing. C. Tsai [132, 133] designed silicon-based ultrasonic nozzles to generate micrometre-sized droplets. In all the applications reported, piezoceramics PZT in  $d_{31}$  operation mode were used as the piezoelectric element. The planar tool design concept showed significant advantages, such as lightweight, simplicity, high vibration amplitude and low driving voltage required.

In this Chapter, ultrasonic planar tools based on PMN-PT piezocrystal operating in  $d_{31}$  mode are designed. The ultrasonic planar tools are distinguished by blade material and profiles. Stainless steel, titanium alloy, silicon and aluminium nitride are used as the blade materials while conical and exponential blade profiles are employed. The design process is carried out through finite element analysis (FEA) package Abaqus (Dassault Systemes, Vélizy-Villacoublay, France) to ensure their longitudinal vibration modes. Experimental characterisation is conducted by using impedance analyser and laser Doppler vibrometer (LDV) after fabrication process.

### 3.1 Design

#### 3.1.1 Schematic

The schematic of the ultrasonic planar tool is shown in Figure 3-1.

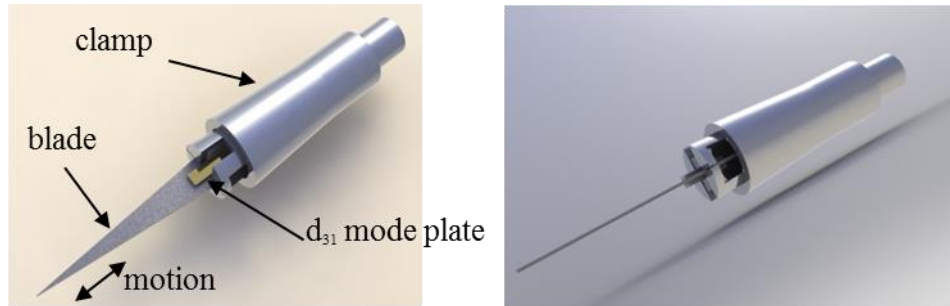


Figure 3-1 Schematic of the ultrasonic planar tool

Two piezoelectric plates are attached to a blade symmetrically to form a bimorph. The piezoelectric plates work in  $d_{31}$  operation mode, opposed to  $d_{33}$  mode of the piezoelectric material in sandwich transducers. They are electrically connected in parallel. When excited by alternate voltage, they convert the electrical energy into mechanical vibration in the longitudinal direction. The sharp and diminishing shape of the blade concentrates the energy and boosts the vibration amplitude at the tip.

#### 3.1.2 Design Considerations

##### (1) Blade Profiles

Normally, three factors are considered when designing planar horns. They are displacement amplification, mechanical strength and manufacturing complexity. Displacement amplification  $k_a$  is the ratio of vibration amplitude at the input end to the output end. It determines the vibration energy distribution on the horn. Higher displacement amplification concentrates more energy on the output face of the horn and subsequently makes it work more efficiently [68]. Stress concentration should be avoided as it limits the highest vibration amplitude that can be achieved before the horn fails mechanically [130]. Horns with complex profiles such as Fourier horns can

provide satisfactory performance in terms of displacement amplification and mechanical strength, their manufacturing are also complicated[132, 133].

In this design, blades in three profiles were considered, as shown in Figure 3-2. Each blade is composed of two sections: one with uniform and the other with variable cross section. The profiles of the variable cross section are conical in (a) and (b), and exponential in (c). The conical blade provides low displacement amplification but ease of manufacturing. It can be engineered by a dicing saw, which is available in our lab. The exponential blade offers both satisfactory displacement amplification and stress distribution. However, its manufacture requires laser cutting, and is thus more complicated than conical blade.

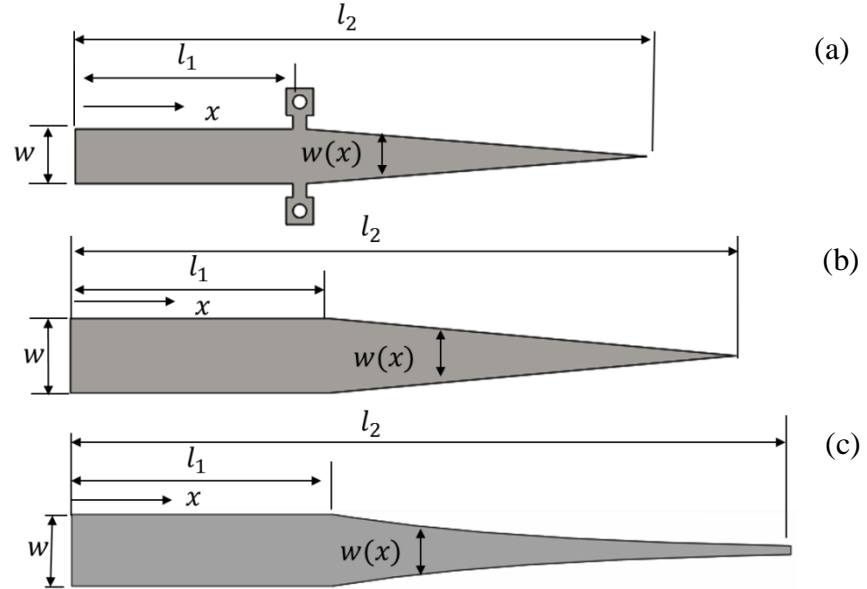


Figure 3-2 Profiles of the blades (a) conical blade with flange (b) conical blade (c) exponential blade

Blades in Figure 3-2 (a) and (b) are featuring in conical profiles and can be described as

$$\begin{aligned}
 w(x) &= w \quad 0 \ll x \ll l_1 \\
 w(x) &= \frac{w(l_2 - x)}{l_2 - l_1} \quad l_1 \ll x \ll l_2
 \end{aligned}
 \tag{3-1}$$



The profile of blade in Figure 3-2 (c) is exponential:

$$\begin{aligned} w(x) &= w \quad 0 \ll x \ll l_1 \\ w(x) &= we^{-\alpha(x-l_1)} \quad l_1 \ll x \ll l_2 \end{aligned} \tag{3-2}$$

$w(x)$  is the width of the blade at a distance  $x$  from the blunt side of the blade.  $l_1$  is the length of the blade with uniform cross section and  $l_2$  is the length of the blade with variable cross section.

## (2) Material of the blade

The choice of material for ultrasonic horns is critical in achieving maximum system efficiency. The horn material must have the lowest possible acoustic attenuation to maximise the energy transmitted. Acoustic attenuation or acoustic loss refers to the diminishing of intensity of the ultrasound wave front as it progresses through a material. The acoustic loss of a material can be accessed by the mechanical  $Q$  factor,  $Q_M$ . Low acoustic loss is associated with high  $Q_M$  value.

The ultrasonic horns are usually excited to work at high vibration velocity and subsequently, high dynamic stress is present with its distribution highly dependent on the geometry profiles of the horns. The peak stress undergoing in the ultrasonic horn should not be higher than the strength of the material, else the material will fracture. However, to ensure an acceptable safety in ultrasonic horns, the ultimate tensile strength of the material should be at least 30% higher than the peak stress experienced within the horn during operation [105].

The materials traditionally used for acoustic horns are stainless steel [68], Aluminium alloy (Al) and titanium alloy (Ti) [39]. Stainless steel actually has a relatively high acoustic loss that can result in high blade temperature if the instrument is operational for long periods of time [39]. The widespread use of stainless steel is probably because of its availability, low cost, high strength and ease of manufacturing. Al has lower acoustic loss than many steels however does not have the strength characteristics required for some applications. Ti is an ideal material for ultrasonic horns. It exhibits high stress

endurance limits combined with a very low acoustic loss. It is also highly resistant to wear.

For planar horns particularly, silicon wafer (Si) has been extensively used [69, 129, 131, 133, 134]. Si's material properties, together with established micromachining technology make it ideal for planar tools. Si possesses high acoustic velocity and low internal loss. It can be driven safely at much higher vibration amplitude than titanium alloy. Like other crystalline materials, Si is brittle. It is likely to crack more easily if stress concentrations beyond its yield stress are produced during use. Since cracks usually start from the surface of a structure, this problem can be avoided by surface toughening. This can be accomplished by depositing thin films of tougher materials like SiC and diamond.

Aluminium Nitride (AlN) Ceramic is a semiconductor material possessing even lower internal loss than Si [135]. It has gained wide application in piezoelectric devices, optoelectronics and other areas [136]. Even though AlN offers excellent acoustic properties, its usage as a horn material has not been reported, probably because of its brittle nature, material size availability and manufacturing difficulty.

For the planar tools, four materials were used to design and fabricate the blades. They were stainless steel, titanium alloy, silicon wafer and Aluminium Nitride Ceramic with key mechanical properties detailed in Table 3-1. The four materials selected offer different acoustic loss. Silicon and AlN have the lowest acoustic loss,  $Q^{-1}$ , which are followed by titanium alloy. Stainless steel has the highest acoustic loss. It is expected the material with lower acoustic loss will offer a higher vibration velocity under the same driving power. Thus, AlN and silicon are preferred to titanium alloy and stainless steel. However, AlN and silicon are also brittle, and are more likely to crack than titanium alloy and stainless steel. In this study, these four materials were selected to compare their performance for ultrasonic planar tools.

Table 3-1 Mechanical properties of materials [39, 137]

Material	Young's Modulus (GPa)	Density (kg/m <sup>3</sup> )	Ultimate Strength (MPa)	Acoustic loss $Q^{-1}$	Poisson's ratio
Stainless steel	193	8000	515	$\sim 3.8 \times 10^{-4}$	0.3
Titanium alloy	113	4430	950	$\sim 1.4 \times 10^{-4}$	0.34
Silicon	130-188	2320	7000	$\sim 10^{-5}$	0.28
AlN	320	3330	N/A	$\sim 10^{-5}$	0.24

### (3) Piezoelectric material

Compared with the piezoelectric ceramic material conventionally used, piezocrystals offer extremely high piezoelectric coefficients and high compliance, leading to a reduced stack length and subsequently reducing the overall size of a transducer and an ultrasonic device [138]. High vibration amplitude is also expected at low exciting voltage with piezocrystals. This newly developed material has been used in various applications such as SONA and ultrasound imaging [139].

The piezocrystal used in this work is PMN-29%PT (TRS Ceramics, USA; Shanghai SICCAS High Technology Corporation, China), which is categorised as the first generation of piezocrystal and is commercially available. The second and third generation of piezocrystals show lower losses and higher Curie temperature than PMN-PT. However, they are only explored in research, and only small amounts are available [140].

The PMN-PT was cut into plates in  $10 \times 3 \times 1 \text{ mm}^3$  and the resonant frequencies of these plates were characterised by an impedance analyser (HP 4194 Impedance/Gain-Phase Analyser, Agilent Technologies, USA). Because of the inconsistency associated with the properties of piezocrystal, the measured resonant frequencies of the PMN-PT plates varied from 66 kHz to 79 kHz. Five pairs of plates with close frequency were chosen for planar tools as shown in Table 3-2.

Table 3-2 Resonant frequencies of PMN-PT plate samples

Pair No.	Sample No.	f (kHz)	Pair No.	Sample No.	f(kHz)
I	1	73.1	II	3	74.1
	2	73.5		4	74.5
III	5	76.4	IV	7	69.1
	6	76.9		8	70.0
V	9	71.2			
	10	71.7			

#### (4) Jigs and Fixtures

Clamping of these planar tools is an important practical concern. To minimise losses due to the friction between the clamping structure and the planar tools, the clamp should be placed at the displacement node of planar tools, where the vibration amplitude is minimum. It is also wise to clamp the planar tools without contacting with the piezocrystal plates, because they can be easily chipped and seriously damped.

Two clamps were considered for the planar tools through the displacement node without touching the piezoelectric material, as shown in Figure 3-3. Clamp 1 was specially designed for the conical blade with flange. The flange of the blade was constrained by two M1 bolts. However, since machining of such flange was not possible with silicon and aluminium nitride because of their fragile nature, Clamp 2 was designed as shown in Figure (b). When the two bolts are tightened, the clamp applies a compression force onto the blade, and thus fixes it.

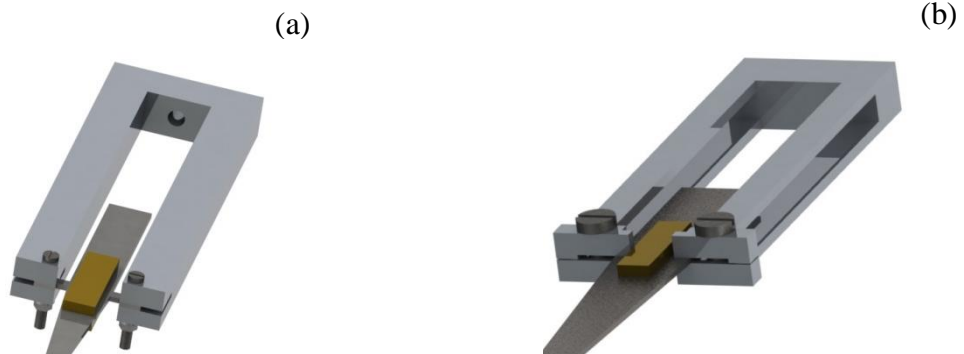


Figure 3-3 Clamps for the planar tools (a) clamp 1 (b) clamp 2

It should be noted that the contact area between the clamp and the planar tool should be as small as possible in order to reduce the losses, considering the limited width of the node plane. However, to ensure a secure clamp, the area should be large enough to provide enough friction force. So there is a trade-off in the designing of the clamp. In Clamp 2 and 3, width of the contact area in the length direction of the blade was 1 mm, determined experimentally, which was able to provide enough clamp force without damping the planar tools.

### **3.2 Finite Element Analysis**

Finite element analysis of the planar tools was carried out in Abaqus. The idea was to determine the dimensions of the blade and ensure its longitudinal resonance at the working frequency of PMN-PT piezocrystal.

#### **3.2.1 PMN-PT piezocrystal**

The frequency analysis of the PMN-PT piezocrystal in dimension of  $10 \times 3 \times 1 \text{ mm}^3$  was implemented in Abaqus. The frequency analysis procedure performs eigenvalue extraction to calculate the natural frequencies and the corresponding mode shapes of a system. The steps to perform a frequency analysis for piezoelectric material are detailed in the following:

- (a) Modelling. The physical model of the PMN-PT plate was created in Abaqus/CAE directly. For all work in simulation of this thesis, International System of units (SI) was employed and complied with.
- (b) Material Properties. Abaqus provides comprehensive coverage of linear and nonlinear, isotropic and anisotropic material behaviours. To define a material for frequency analysis, normally, the density, elastic modulus and Poisson's ratio are required to be specified. However, for a piezoelectric material, density, elastic constants, stress constants and permittivity properties are required. As an anisotropic material, the properties of the piezoelectric material are direction dependant, so the properties are in form of matrix and material orientation has to be assigned. The properties obtained from the supplier are listed in Table 3-3 [141].

- (c) Load and Boundary Conditions. Frequency analysis of a piezoelectric material in Abaqus can be performed with two electrodes to be both closed- and open-circuited. The closed-circuited cases are specified by setting the electric potentials on both electrodes to be zero. This situation yields the resonant frequencies. The open-circuited cases are specified by setting the potentials on only one electrode to zero, which allows a different potential to exist on the other electrode. This situation yields the antiresonant frequencies.

As only the resonant frequency and its corresponding mode shape are concerned in this work, the closed-circuited condition was specified. Both electrodes of the PMN-PT plate were assigned with uniformly distributed potential of zero.

- (d) Mesh. The mesh allows generating meshes on parts and assemblies within Abaqus/CAE and also assigning element type. To study the piezoelectric behaviours of the piezoelectric material, the element should be assigned to be piezoelectric family. For PMN-PT in this case, a 20-node quartic piezoelectric brick element from piezoelectric family (C3D20RE) was chosen.

Following the procedures above, the FE model of PMN-PT was created, and the resonant frequencies along with corresponding mode shape were solved. The longitudinal was found at 73.4 kHz as shown in Figure 3-4.

Table 3-3 Material properties of PMN-29%PT [141]

Elastic constants (GPa)	Stress constants (C/m <sup>2</sup> )	Permittivity (F/m)	Density (kg/m <sup>3</sup> )
D <sub>1111</sub> = 88.3	e <sub>311</sub> = -6.76	K <sub>11</sub> = 10.79E-9	7500
D <sub>1122</sub> = 75.1	e <sub>322</sub> = -6.76	K <sub>22</sub> = 10.79E-9	
D <sub>1133</sub> = 87.2	e <sub>333</sub> = 20.02	K <sub>33</sub> = 9.38E-9	
D <sub>2222</sub> = 88.3	e <sub>212</sub> = 8.8		
D <sub>2233</sub> = 87.2	e <sub>113</sub> = 8.8		
D <sub>3333</sub> = 110.5			
D <sub>1212</sub> = 68.9			
D <sub>1313</sub> = 68.9			
D <sub>2323</sub> = 20.9			

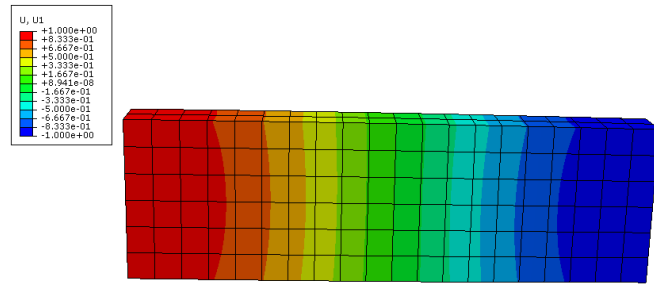


Figure 3-4 Longitudinal mode of the PMN-PT plate

### 3.2.2 Blades

The design process was based on the frequency analysis of the blade in Abaqus, which computed the first longitudinal resonant frequency of the blade. The dimension of the blade varied until the resonant frequency of the blade matched the resonant frequency of the piezoelectric materials. Stainless steel, AlN and Ti were defined as isotropic materials with density, elastic constant and Poisson's ratio specified in Abaqus, which were also listed in Table 3-1. However, Si is an anisotropic material, with elastic behaviour depending on the orientations of the structure as [142, 143]. In this case, (100) silicon wafer was used with complete mechanical properties listed in Table 3-4. The length direction of the silicon blade was parallel to the primary flat ([110]) of the wafer.

Table 3-4 Mechanical properties of (100) Si wafer in <110> direction [142]

Elastic constants (GPa)	Density (kg/m <sup>3</sup> )
$D_{1111} = 88.3$	2320
$D_{1122} = 75.1$	
$D_{1133} = 87.2$	
$D_{2222} = 88.3$	
$D_{2233} = 87.2$	
$D_{3333} = 110.5$	
$D_{1212} = 68.9$	
$D_{1313} = 68.9$	
$D_{2323} = 20.9$	

Table 3-5 presents the characteristics of the five blades. The resonant frequency of each blade matches to a pair of PMN-PT plates. The stainless steel blade is in conical profile with flange. The Ti and Si blades are in conical profiles. The two AlN blades are designed to be conical and exponential profiles, respectively. All the blades in conical profiles show about the same displacement amplification, 1.8 or 1.9. In contrast, exponential AlN blade gives a much higher value of 2.9. Higher displacement amplification means higher vibration amplitude at the tip, which is desirable for ultrasonic surgical operation.

Table 3-5 Characteristics of the designed blades

Materials	Profiles	$l_1$ (mm)	$l_2$ (mm)	w (mm)	$f_s$ (kHz)	$k_a$	Pair No. of PMN-PT
Stainless steel	Conical with flange	17	42	4	73.3	1.8	I
Titanium alloy	Conical	15	39	8	76.5	1.8	III
Silicon	Conical	28	72	8	74.6	1.9	II
AlN	Conical	30	88.8	8	69.5	1.9	IV
AlN	Exponential	30	82.8	8	71.5	2.9	V

Figure 3-5 shows a representative longitudinal modal shape of the blades. High vibration amplitude is seen at two ends, referred as displacement anti-node. Maximum vibration amplitude is always observed at tip of the blade. There also exists a plane where the vibration amplitude is minimum, referred as displacement node or nodal plane.

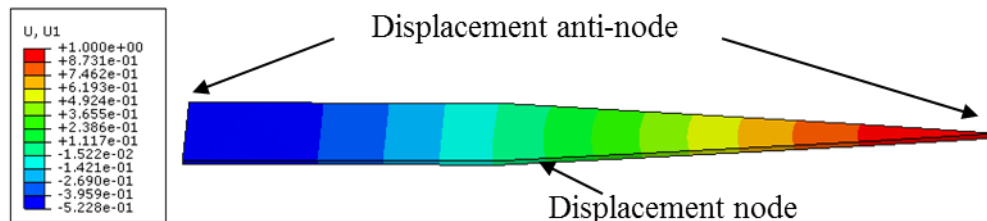


Figure 3-5 Longitudinal vibration mode of Si blade



### 3.2.3 Ultrasonic Planar tools

The ultrasonic planar tools were obtained by bonding PMN-PT piezocrystal plates onto the blades. The contact areas between different parts were constrained by ‘Tie constraint’. The ‘tie constraint’ in Abaqus ties two separate surfaces together so that there is no relative motion between them. This type of constraint allows fusing together two regions even though the meshes created on the surfaces of the regions may be dissimilar.

The effect of the adhesive epoxy was ignored in FEA. The nodal planes of the PMN-PT plates were aligned to that of the blade. Both electrodes of each plate were specified with zero potential so that the resonant frequencies of the planar tool could be solved.

It has been observed that for all the planar tools, with only one piezocrystal plate bonded onto the blade (single-sided configuration), serious flexural motion was coupled in the longitudinal mode, especially at the tip, as shown in Figure 3-6 (a). However, the coupled bending motion was avoided after the other piezocrystal was attached symmetrically (double-sided configuration), as shown in Figure 3-6 (b). This suggests the bending motion coupled in the longitudinal mode is mainly caused by the asymmetrical mass distribution when only one plate is bonded.

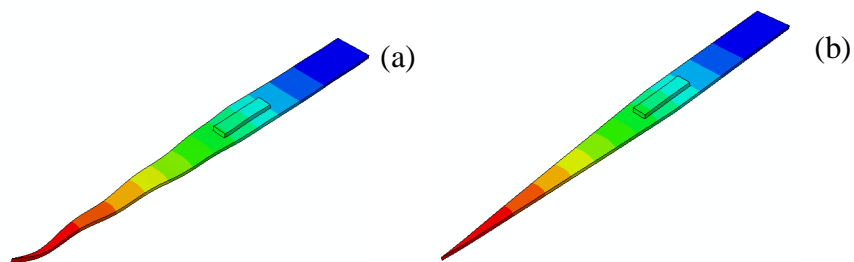


Figure 3-6 Longitudinal vibration modes of the silicon planar tool: (a) single-sided configuration (b) double-sided configuration

Even in the double-sided configuration, bending motion could also be observed if the placement of the two piezocrystal plates was not symmetric. Figure 3-7 shows the longitudinal vibration mode of the silicon planar tool when there is a position error of 1 mm in the longitudinal direction. Figure 3-8 shows the longitudinal vibration mode of the same tool when there is a position error of 0.5 mm in the width direction. As can be

seen from the figures, significant flexural motion is present in the longitudinal modes. This suggests extra caution should be taken during fabrication.

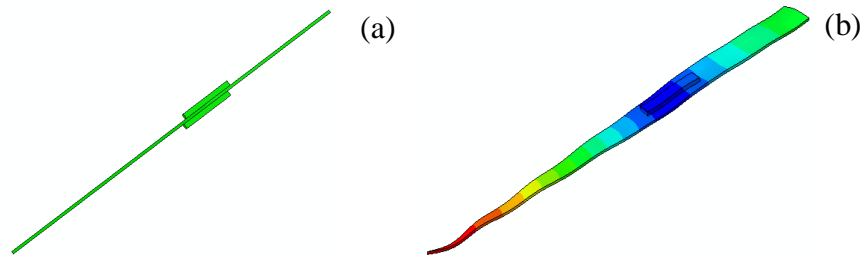


Figure 3-7 Longitudinal mode shape of the silicon planar tool with position error in length direction (a) position of the piezocrystal plates (b) longitudinal mode

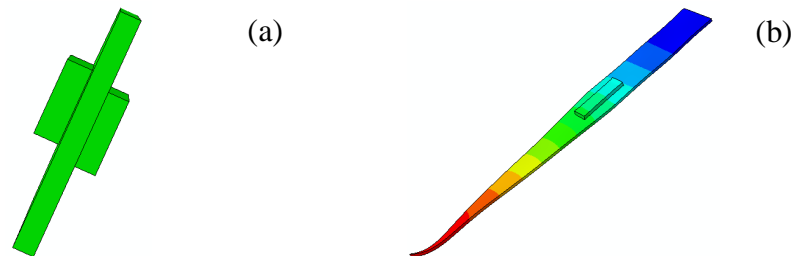


Figure 3-8 Longitudinal mode shape of the silicon tool with position error in width direction (a) position of the piezocrystal plates (b) longitudinal mode

### 3.3 Fabrication

The fabrication of planar tools involved machining the blades in different materials and shapes to accurate dimensions followed by the attachment of PMN-PT plates. The stainless steel blade with flange was cut by a laser cutter. The Si and Ti blades were manufactured by a wafer dicing saw (APD1, Logitech Ltd, Glasgow, UK). The AlN blades in conical and exponential profiles were provided by Ceramic Substrates & Components Limited (Ceramic Substrates & Components Limited, UK), considering the technology to manufacture an exponential AlN blade was not available in our lab. For the Si and AlN blades, surface toughening process, i.e. deposition of SiC, was not implemented at this stage.

### 3.3.1 Thin film gold deposition

Because Si and AlN are non-conductive materials, the Si and AlN blades were sputter-coated with Chromium (Cr, 25 nm) and then deposited with gold (Au, 75 nm) prior to the attachment of piezocrystal plates to serve as a ground connection. Cr was used to aid Au adhesion. The steps taken to carry out the gold evaporation is as follows:

#### **Cleaning**

Prior to the Cr sputtering, the Si and AlN blades were cleaned by acetone and isopropanol. This cleaning process is quite essential to ensure good adhesion of thin film of any metal or alloy. By using acetone and isopropanol solvent, organic and inorganic contaminants such as dust, oil and organic residues on the blades can be removed. These contaminants make the blades discoloured or smudged, and are mainly caused due to fingerprints, water spots, etc.

First, the blades were dipped into an acetone bath for 5 minutes. At this stage, most of the contaminants were cleaned. However, some solvents including acetone leave their own milky-white coloured residue. In order to clean the residue, the blades were dipped into an isopropanol bath twice for 2 minutes and wiped with soaked tissues in the interval between two baths. Finally, the blades were heated at 120 °C on a heat plate for 3-5 minutes to get rid of any water molecules which may present in molecular scale on the surface of the blades.

#### **Chromium deposition**

Before the gold evaporation, a thin film of Cr (25 nm) was deposited onto the surface of the blades through DC sputtering to aid the adhesion of gold film. DC sputtering is a physical vapour deposition process used for depositing materials onto a substrate, by ejecting atoms from such materials and condensing the ejected atoms onto a substrate in a high vacuum environment.

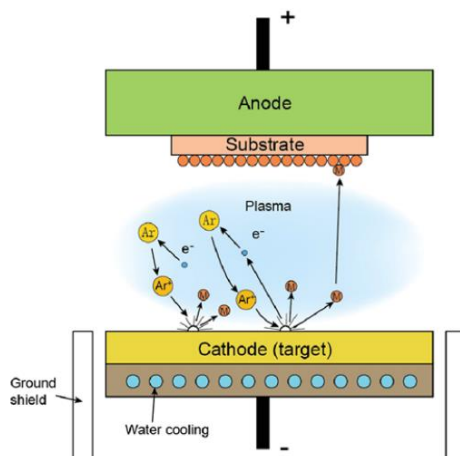


Figure 3-9 Schematic of DC sputtering process

The sputtering process for Si and AlN blades was carried out using DC Sputterer (ION Tech. Ltd., Teddington, UK). The target (Cr) and the substrate (Si or AlN blades) were placed in the chamber of the DC Sputterer, as shown in Figure 3-9. Argon (Ar) ions were used as the particles bombarding the target surface. Argon atoms were introduced into the chamber vacuumed to a pressure of 0.001 mbar. A DC voltage of 1000 V was applied between the Cr (cathode) and Si blades (anode), which ionized the argon atoms forming an ionized gas (plasma). The positively charged argon ions accelerated towards the cathode (Cr), bombarded its surface and broke the Cr atoms out. The Cr atoms travelled at various directions and settled on the substrate (Si blades) surface forming a deposited layer.

### Gold evaporation

Following the successful sputtering of Cr onto the blades, a thin film of Au was deposited using Edward Auto 306 Vacuum Coater (Edwards Ltd. UK). The schematic of the thermal evaporation process is shown in Figure 3-10 (a). Thermal evaporation is conducted in a vacuum chamber, to avoid reaction between the vapour and atmosphere. The Si and AlN blades (substrate) were mounted onto a disc over the material to be evaporated (gold wire). The gold wire was placed onto the Tungsten (W) evaporation boat clamped between two electrodes, as shown in Figure 3-10 (b). Current of 3.5A was applied across the two electrodes. Subsequently, the gold wire was heated up and finally

evaporated. The gold vapour finally condensed in form of thin film on the cold Si and AlN blades surface and on the vacuum chamber wall.

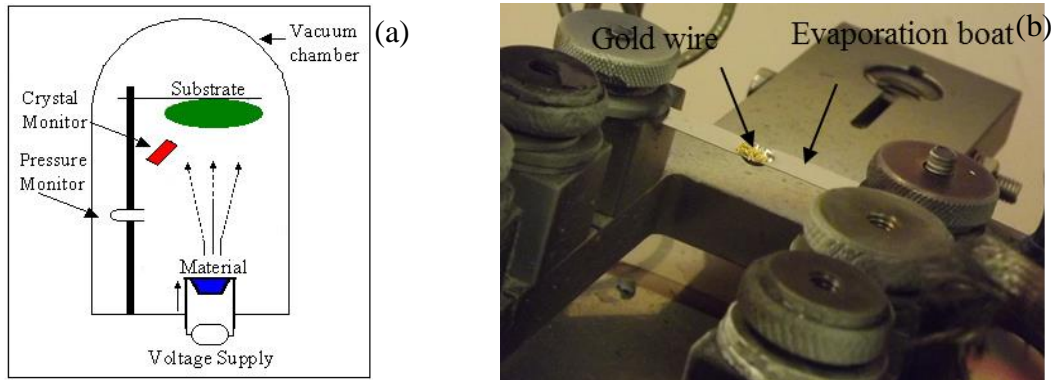


Figure 3-10 Gold evaporation process (a) schematic (b) gold wire mounted on evaporation boat

The process time depends on the desired thickness and deposition rate of Au while the thickness of the thin film depends on the distance between the blades and the boat. For Si and AlN blade, a film of 75 nm thick was deposited. The final Si and AlN blades with electrodes deposited are shown in Figure 3-11. Only the areas around the displacement node are deposited with Cr and Au. This is because only these areas will be used for electric connection and the other areas were covered by masks during the deposition process.

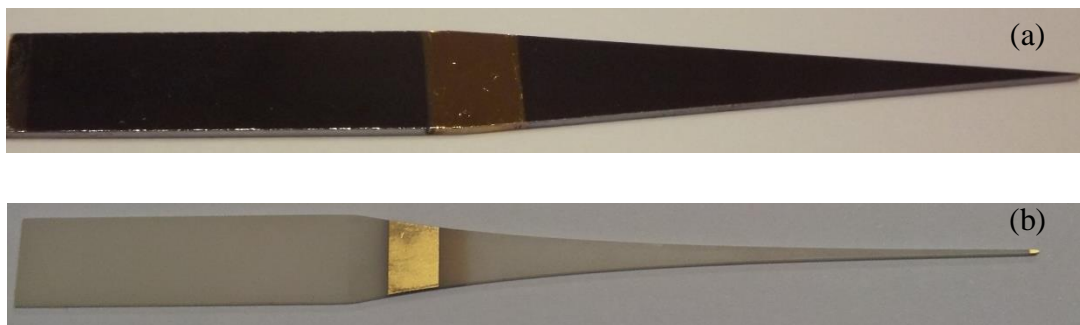


Figure 3-11 Blades with electrodes deposited (a) Si blade (b) AlN blade

### 3.3.2 Assemble the tools

As observed in finite element analysis, the mode shapes of the planar tools were quite sensitive to the position of the piezocrystal plates. To ensure accurate placement of the

piezocrystal plates, bespoke jigs were designed and fabricated by prototyping machine, shown in Figure 3-12. The jigs comprised two components where the bottom and top parts had provisions for the blade and the piezocrystal plates respectively.

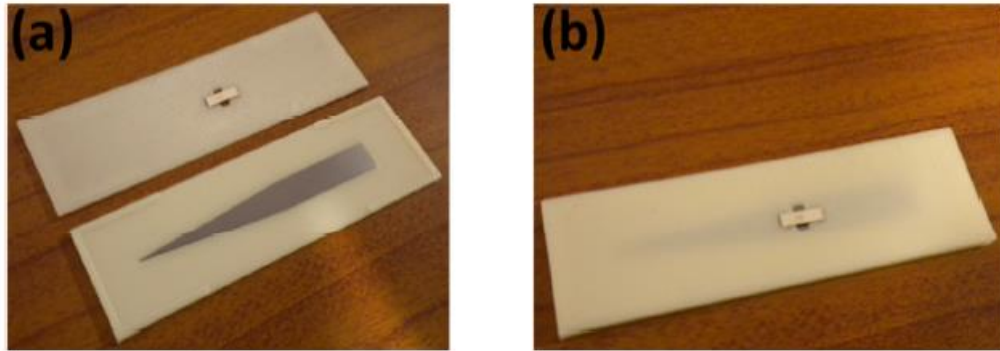


Figure 3-12 Bespoke jig for alignment (a) individual components (b) assembly

Silver-filled, two-component epoxy (EPO-TEK EJ2189, Epoxy Technology Inc., USA) was used to bond the piezocrystal plates onto the blades with high mechanical strength and high electrical conductivity. First of all, the two components of epoxy were mixed together by weight ratio of 10:1. Then a thin layer of mixed epoxy was applied to the piezocrystal plate. The piezocrystal was then bonded onto the blade with node planes aligned. Pressure was immediately applied to squeeze out the air and bubbles in the epoxy. Failing to squeeze out the air and bubbles in the epoxy results in poor adhesion, indicated by high electric impedance and low mechanical strength. Finally, the assembly was placed in an oven of 60 °C for 12 hours, allowing the epoxy to cure.

Coated copper wires in diameter of 0.5 mm were used for external electrical connections and silver loaded epoxy (Agar Scientific Ltd., Essex, UK) was used to secure these connections. Soldering was not applicable in this case because the high temperature ( $> 200^{\circ}\text{C}$ ) during soldering will damage the piezocrystal, considering the low Curie temperature of PMN-PT (130 °C). The positive connections were made on top of the PMN-PT plates while the negative connection on the blades. It was observed that both the positions of the wire connection and the amount of epoxy significantly affected the electrical impedance of the planar tool by introducing damping, since epoxy

is a material with high mechanical loss. To reduce this damping effect, the positive connections were secured at the node plane of the plates with small amount of epoxy.

Three of the fabricated planar tools with clamps are shown in Figure 3-13.

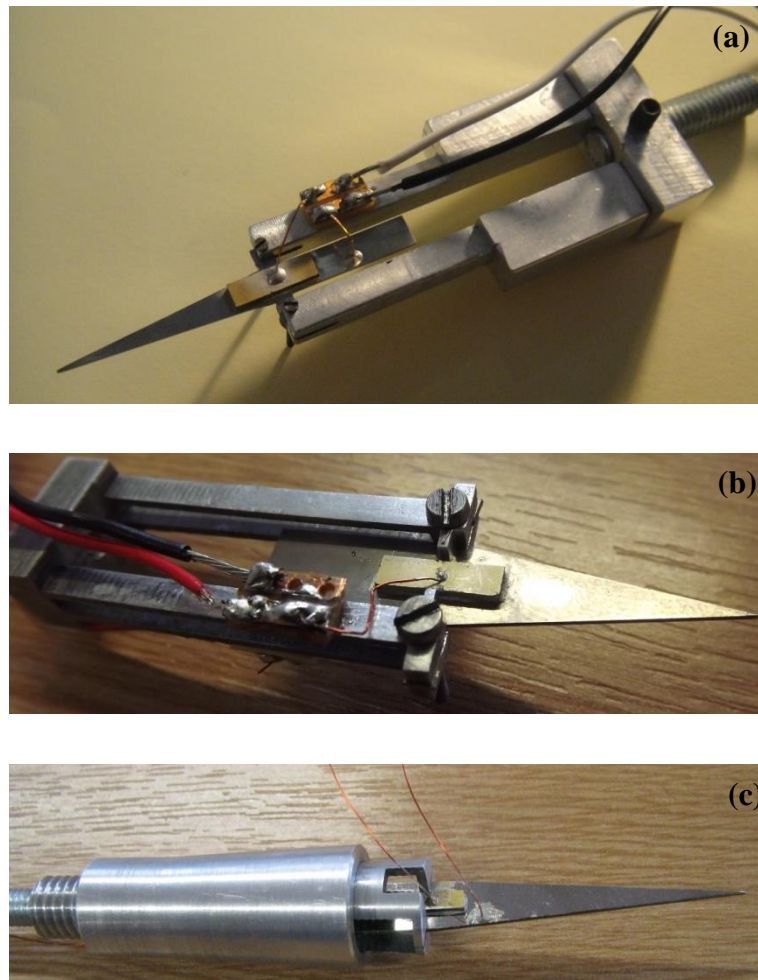


Figure 3-13 Fabricated planar tools (a) stainless steel tool (b) Ti tool (c) Si tool

### 3.4 Characterisation

#### 3.4.1 Methods

The performance of the ultrasonic planar tools was studied experimentally from the fabrication stage. The electrical input impedance was recorded by a HP 4194 impedance analyser. A Laser Doppler vibrometer (LDV) (OFV2571 & OFV 534, Polytec Ltd,







As stated in Section 3.2.2, the resonant frequency of the Ti blade matched to Pair III PMN-PT plates. Thus Sample 5 and Sample 6 were used to fabricate the Ti planar tool. First of all, Sample 5 was attached to the Ti blade by high strength epoxy. The electrical impedance of Sample 5 was measured before and after it was bonded onto the blade. The results are shown in Figure 3-15 with key properties listed in Table 3-6.

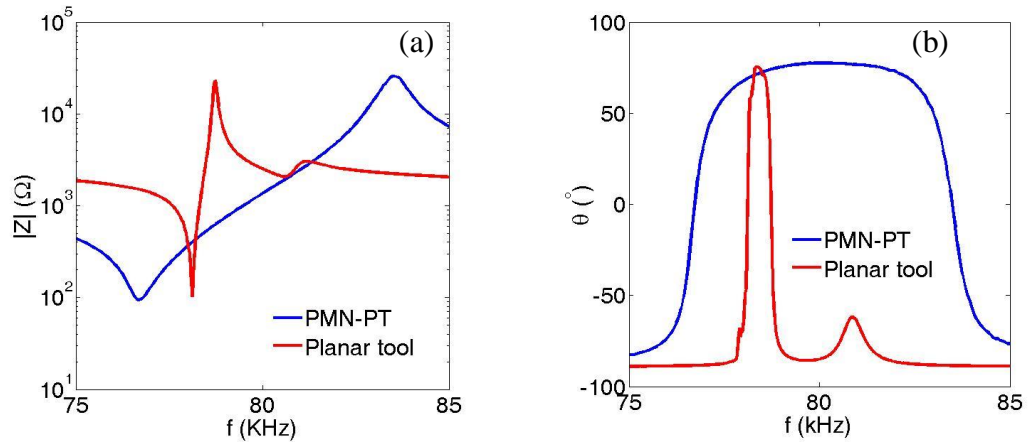


Figure 3-15 Electrical impedance of PMN-PT (Sample 5) and Ti planar tool with Sample 5 attached (a) magnitude (b) phase

Table 3-6 Properties of the Ti tool during fabrication

Properties	$f_s$	$ Z $	$k_{eff}$	$Q_M$
Devices	(kHz)	( $\Omega$ )		
PMN-PT (Sample 5)	76.68	94	0.39	115
Planar tool with Sample 5	78.97	120	0.12	850

The PMN-PT piezocrystal plate (Sample 5) itself is resonant at 76.68 kHz with electric impedance of 94  $\Omega$  and  $Q_M$  of 115. Increase in resonant frequency and electrical impedance are observed when Sample 5 is bonded onto the blade. The increase in electrical impedance to 120  $\Omega$  reflects the rise of mechanical losses, which results from both the Ti blade and the conductive epoxy. Even though the value of the mechanical losses rises, the ratio of the stored energy to the mechanical loss, indicated by  $Q_M$ , increases significantly from 115 to 850. This is because Ti blade holds a much higher

$Q_M$  than the PMN-PT piezocrystal. The planar tool exhibited a lower effective coupling factor ( $k_{eff}$ ) than the piezocrystal plate since  $Q_M$  is inversely proportional to  $k_{eff}$  [64].

After the successful characterisation of the planar tool with Sample 5, Sample 6 was attached to the blade symmetrically and the assembly of the planar tool was finished. Electrical impedance and vibration measurements were taken in three conditions: only Sample 5 excited; only Sample 6 excited; and both Sample 5 and 6 excited. Figure 3-16 shows the electrical impedance and displacement response (at voltage of 5V) of the Ti tool in these three conditions. The key properties of the Ti planar tool are summarized in Table 3-7.

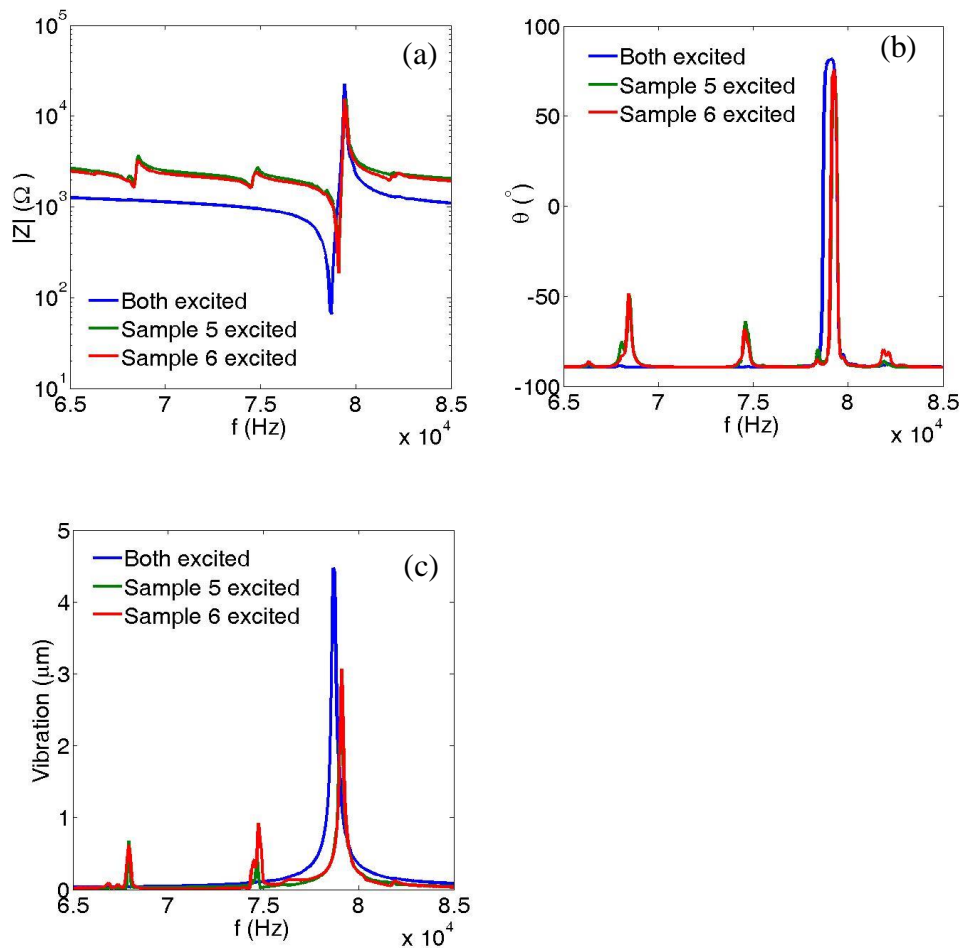


Figure 3-16 Electrical impedance and vibration response of the Ti tool (a) impedance magnitude (b) impedance phase (c) displacement response at 5 V

Table 3-7 Properties of the Ti tool

Properties	$f_s$ (kHz)	$ Z $ ( $\Omega$ )	$k_{eff}$	$Q_M$
Sample 5	79.02	231	0.11	658
Sample 6	79.13	257	0.12	660
Both Samples	78.60	55	0.16	697

When only Sample 5 or Sample 6 is excited, the planar tool is resonant longitudinally at around 79 kHz. However, other non-tuned modal frequencies exist in the close proximity of the longitudinal mode. They are 67.5 kHz, 75 kHz and 82 kHz, which can be identified from both the electric impedance curves and displacement response. When both Sample 5 and 6 are excited, these non-tuned modes disappear. The disappearance of the non-tuned modes improves the frequency separation of the longitudinal mode, which further improves the purity of the longitudinal mode and eliminates the possible modal interaction when the planar tool is driven at high power levels [144].

The electrical impedance magnitudes of the planar tool in only Sample 5 excited and only Sample 6 excited conditions are 231 and 257  $\Omega$ , respectively. A significant decrease is observed when both Sample 5 and 6 are excited. This is because the two piezocrystal plates, Sample 5 and Sample 6, were connected electrically in parallel and thus the overall impedance magnitude was much lower than either of the piezocrystal plates. This advantage of the multi-layer piezoelectric transducer was also confirmed by other studies [139, 145] and they demonstrated that the electrical impedance of an  $N$  layer multilayer transducer was  $1/N^2$  of that of a single layer transducer.

Figure 3-16 (c) also shows that the vibration amplitude in both Sample 5 and 6 excited conditions is higher than the condition either Sample 5 or 6 excited. This can be attributed to several reasons. First of all, when both piezoelectric plates were excited, the electric impedance was lower and thus more electric power was delivered into the planar tool under the same driving voltage. Furthermore, the disappearance of the non-

tuned modes and consequent improvement in purity of longitudinal motion reduced the vibration in unwanted modes and undesired directions.

Figure 3-17 shows the electrical impedance of the planar tools after fabrication and Table 3-8 summarizes the key properties.

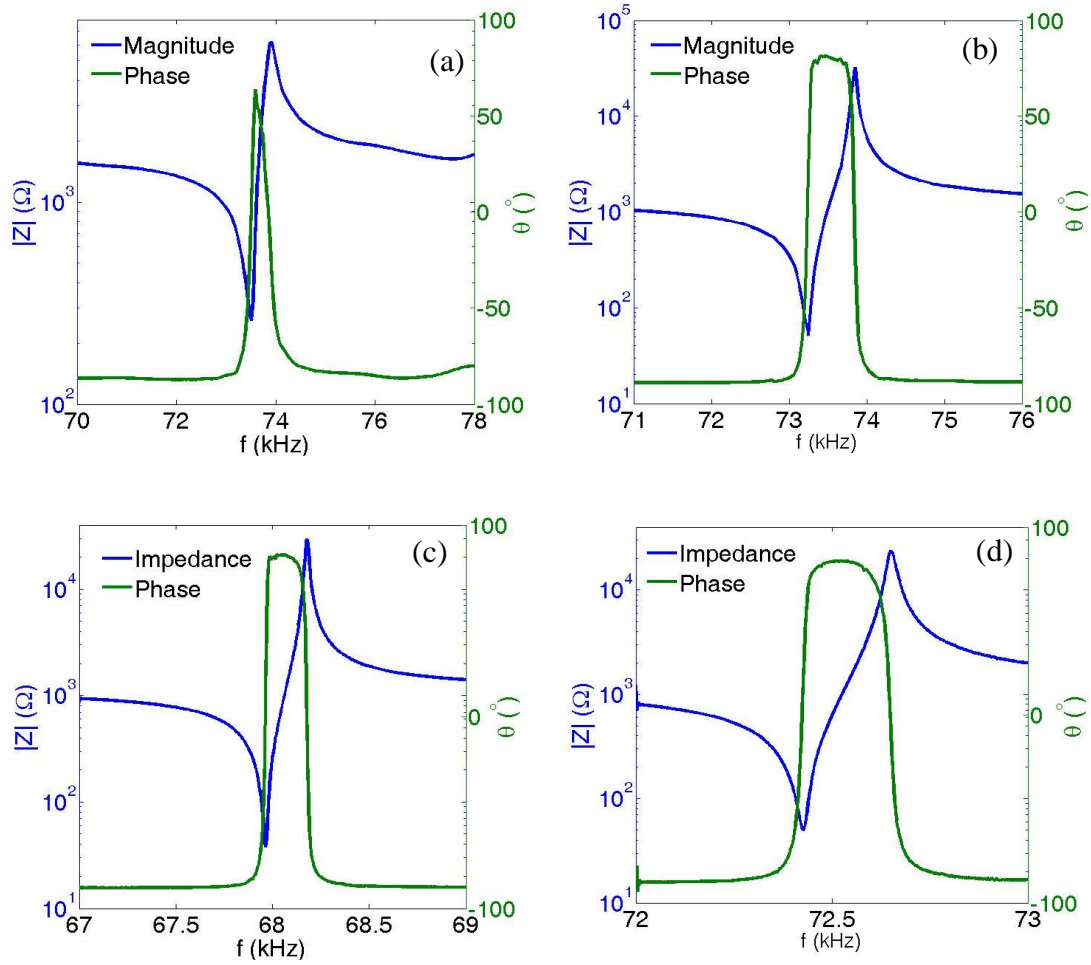


Figure 3-17 Electrical impedance of the planar tools (a) stainless steel tool (b) Si tool (c) AlN conical tool (d) AlN exponential tool

Table 3-8 Measured properties of the planar tools

Tools	Properties $f_s$ (kHz)	$ Z $ ( $\Omega$ )	$k_{eff}$	$Q_M$
Stainless steel	73.8	260	0.1	552
Ti	78.6	55	0.16	697
Si	73.3	37	0.13	2700
AlN conical	67.9	51	0.08	3340
AlN exponential	72.4	50	0.08	3218

$|Z|$  was found to be highly dependent on the strength of bond between the blade and the PMN-PT plates. Low strength of bond, associated with poor fabrication process, leads to high electric impedance, which is observed on stainless steel.

The AlN conical tool offers the highest  $Q_M$ , followed by AlN exponential tool, Si tool, Ti tool and Stainless steel tool, as presented in Table 3-8. This is associated with the acoustic loss of the materials. As discussed in Section 3.1.2, AlN has the lowest internal loss over the other materials used for the blades, and thus highest  $Q_M$  is expected on AlN tool. Si tool also shows a much higher  $Q_M$  than Ti tool and Stainless steel tool due to its low internal loss.

Figure 3-18 (a) shows the vibration velocity of the two AlN tools in different profiles. The exponential tool holds higher vibration velocity than the conical tool, even though its  $Q_M$  is lower. This is because exponential profile offers higher displacement amplification than conical profile, as presented in Section 3.2.2.

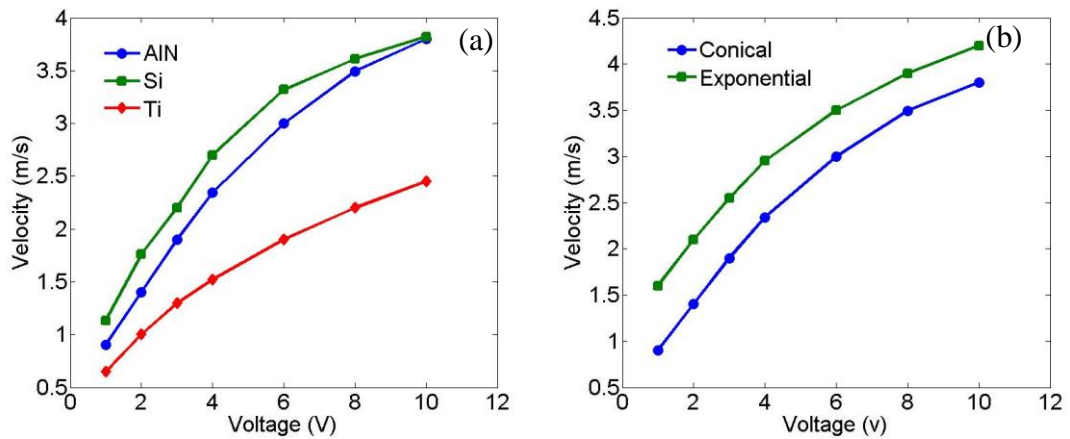


Figure 3-18 Vibration velocity of the ultrasonic planar tools at different voltage (a) AIN tools in conical and exponential profiles (b) conical profiles in different blade materials

Figure 3-18 (b) shows the vibration velocity of the three conical tools made of AlN, Si and Ti. The AlN and Si tools show much higher vibration velocity than the Ti tool because of the higher  $Q_M$ . However, it is also important to note that the Si tool offers a higher vibration velocity than the AlN conical tool at the same voltage (3320 mm/s versus 3000 mm/s at 6V) even though Si tool has a lower  $Q_M$ . Also, the vibration velocity for all the planar tools ceases to increase linearly with voltage when the voltage amplitude is above approximately 4V. Both phenomena are associated with the electrical impedance variation of the planar tools. The vibration velocity is expected to be proportional to current through the planar tool. Since Si tool has lower electrical impedance than AlN conical tool, the current generated at the same voltage is higher than the AlN conical tool. Consequently, higher vibration velocity is observed on Si tool. The electric impedance is believed to increase with voltage when the voltage is relatively high. In such a case, the current doesn't increase linearly with voltage. As a result, the vibration velocity doesn't increase linearly with voltage.

During the measurement of the vibration velocity, the resonant frequency was found to shift to lower values with power level. One typical example is shown in Figure 3-19, which was observed on the Ti tool. Compared with the resonant frequency at 1 V, which is 78.5 kHz, a frequency shift of 197 Hz is observed at 6 V. Although this is only 0.25% of its original frequency, it can significantly reduce the performance of the planar tool, since the bandwidth of the planar tool is only 112 Hz.

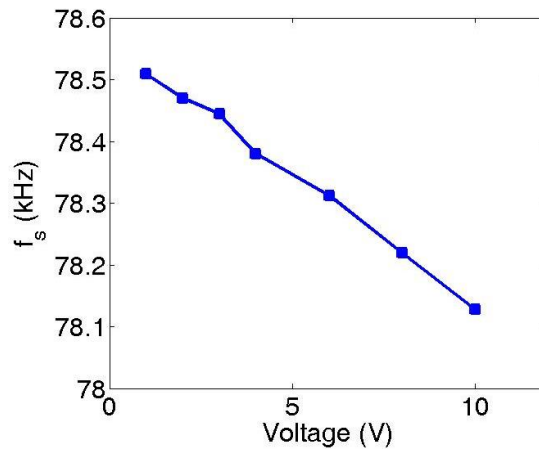


Figure 3-19 Resonant frequency of the Ti tool at different voltage

### 3.5 Discussion and Conclusion

Considering certain limitations of the conventional ultrasonic devices based on sandwich transducer, this chapter reported an alternative approach which has the potential to improve the existing ultrasonic surgical instruments. Five ultrasonic planar tools distinguished by the blade materials and profiles were fabricated. With the utilization of  $d_{31}$ -mode PMN-PT, this work can also be considered as a feasibility study to assess the performance of new piezocrystal for high power and actuator applications.

The use of two piezocrystal plates on both sides of the blade was found to be beneficial as it helped in reducing the electrical impedance. This is because the two piezocrystal plates were electrically connected in parallel. It also removed the non-tuned vibration modes in the close proximity of the longitudinal mode and reduced the flexural motion coupled in the longitudinal vibration. Subsequently, an increase in longitudinal vibration amplitude was observed.

Planar tool based on material with lower acoustic loss offered higher  $Q_M$  and consequently higher vibration velocity. AlN tools showed the highest  $Q_M$  (3398 for conical and 3218 for exponential), followed by Si tool (2700), Ti tool (697) and stainless steel tool (552). In contrast to the planar tools based on Si and PZT, reported by Lal and White [129, 130], which possessed  $Q_M=375$ , all the planar tools reported in this thesis exhibited higher  $Q_M$ . This is probably because in Lal's design, the tool was

clamped by a fixture on the top of the PZT, which damped it seriously and resulted in low  $Q_M$ . In contrast, in our design, the planar tool was fixed by a clamp on the displacement node of the blade without touching the PMN-PT, introducing minimum damp to the planar tool.

Planar tool with higher  $Q_M$  offered higher vibration velocity at the same voltage. However, the electrical impedance could also result in significant difference when comparing the vibration velocity at the same voltage. This is because the vibration velocity was proportional to current amplitude through the planar tool. Another factor that affected the vibration velocity of the planar tool was the amplification factor provided by the blade profile. Blade profile with higher amplification factor, exponential shape in this case, provided higher vibration velocity than conical shape.

Resonant frequency shift was observed on the planar tool. The value of the frequency shift was insignificant, compared with the resonant frequency itself. However, this frequency shift was still able to negatively affect the performance of the planar tool, considering the high  $Q_M$  and low bandwidth, and thus an adaptive driving system is needed.



## 4 ADAPTIVE DRIVING SYSTEM

During high power ultrasound procedures, it is necessary to drive the transducer at its resonant frequencies to maximise the power conversion and vibration amplitude. However, the resonant frequency of an ultrasonic transducer is subject to significant variations during operation, resulting from nonlinearities in piezoelectric material and external loads, as discussed in Chapter 2 and also observed on ultrasonic planar tools in Chapter 3 of this thesis.

This chapter presents an adaptive driving system designed for high power ultrasonic transducers, which can track transducer resonance and stabilise the vibration velocity amplitude at the same time. Section 4.1 presents the dynamic behaviour of piezoelectric transducers near resonance, based on which the strategies of resonance tracking and vibration stabilisation are analysed. The details of each module of the adaptive driving system are presented in Section 4.2. The calibration and validation of the system are provided in Section 4.3.

### 4.1 Dynamic behaviour of piezoelectric transducers

#### 4.1.1 Electrical model of the transducer

To analyse the performance of a piezoelectric transducer analytically, the BVD model discussed in Chapter 2 of this thesis is recalled, as shown in in Figure 4-1 [11].

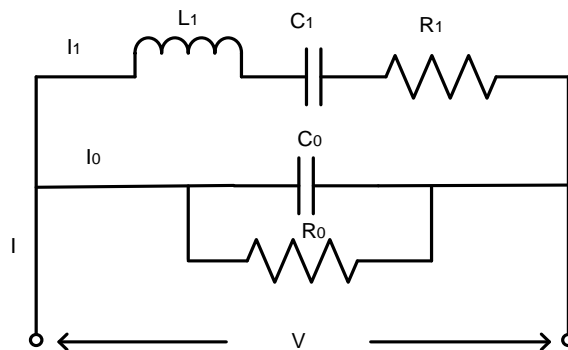


Figure 4-1 Electric model for an unloaded piezoelectric transducer operating near resonance

The electric circuit can be considered as two arms. The electric arm has two components,  $C_0$  and  $R_0$ , which are the capacitance of the clamped transducer and the dielectric loss resistance, respectively. As  $R_0$  generally has a much higher value than the other parallel components, it is neglected in this thesis. The mechanical arm consists of a mechanical compliance  $C_l$ , a mass component,  $L_l$  and a mechanical loss resistance  $R_l$ . All these parameters can be determined experimentally from the characteristic curves of the electric impedance of a transducer.

From Figure 4-1, the admittance of the ultrasonic transducer is [11]

$$Y = \frac{R_1}{R_1^2 + \left(2\pi f L_1 - \frac{1}{2\pi f C_1}\right)^2} + i \left[ 2\pi f C_0 - \frac{2\pi f L_1 - 1/2\pi f C_1}{R_1^2 + \left(2\pi f L_1 - \frac{1}{2\pi f C_1}\right)^2} \right] \quad (4-1)$$

in which  $f$  is the frequency. From equation (4-1), the conductance  $G$  and susceptance  $B$  can be deduced to be

$$G = \frac{R_1}{R_1^2 + \left(2\pi f L_1 - \frac{1}{2\pi f C_1}\right)^2} \quad (4-2)$$

$$B = 2\pi f C_0 - \frac{2\pi f L_1 - 1/2\pi f C_1}{R_1^2 + \left(2\pi f L_1 - \frac{1}{2\pi f C_1}\right)^2} \quad (4-3)$$

From equation (4-2) and (4-3), we obtain

$$\left(G - \frac{1}{2R_1}\right)^2 + (B - 2\pi f_s C_0)^2 = \left(\frac{1}{2R_1}\right)^2 \quad (4-4)$$

Where  $f_s$  is the mechanical resonant frequency

$$f_s = \frac{1}{2\pi\sqrt{L_1C_1}} \quad (4-5)$$

Equation (4-4) represents a circle with radius of  $1/2R_1$  and the centre locating at  $(\frac{1}{2R_1}, 2\pi f_s C_0)$ , shown in Figure 4-2.  $f_s$  is the mechanical resonant frequency characterised by maximum conductance.  $f_m$  is the frequency of maximum admittance (minimum impedance).  $f_r$  is zero phase frequency.

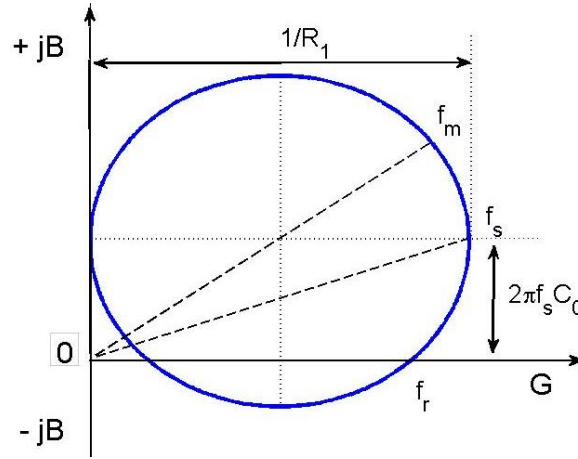


Figure 4-2 Locus diagram of admittance

The highest performance of the transducer can be obtained when these three resonant frequencies equal each other, as the impedance is lowest and purely resistive. However, because of the existence of  $C_0$ , the whole circle is moved upwards from the  $G$ -axis by  $B=2\pi f_s C_0$ . This makes  $f_s$ ,  $f_m$  and  $f_r$  differ from each other, with the difference increasing with frequency and  $C_0$ . For low loss transducers,  $f_s \approx f_m \approx f_r$  whereas for high loss transducer,  $f_m < f_s < f_r$ .

#### 4.1.2 Dynamic tuning of the transducer

Figure 4-3 (a) shows the admittance locus of Ti ultrasonic planar tool developed in Chapter 3. The admittance locus is slightly asymmetrical about the  $B=0$  axis. Because the mechanical resonant frequency  $f_s$  is relatively low (78 kHz) and the admittance of

the tool is high, the shift of the circle made by  $2\pi f_s C_0$  is small compared with the radius of the admittance locus ( $1/R_l$ ). The differences among  $f_s$ ,  $f_m$  and  $f_r$  are thus small (within 10 Hz). However, when planar tool was inserted into poultry breast tissue, the mechanical resistance of the planar tool  $R_l$  increased significantly. Consequently, the radius of the admittance locus decreased, as shown in (b). The difference between  $f_s$  and  $f_m$  increases significantly to 320 Hz.  $f_r$  does not exist any longer since there is no crosspoint between the admittance locus and  $B=0$ .

Thus, for an unloaded piezoelectric transducer with high  $Q_M$ , the clamped capacitance  $C_0$  introduces little influence to the transducer performance, where  $f_s \approx f_m \approx f_r$ . However, when the transducer is loaded, the increased loss can still result in low admittance and consequently large discrepancies among the three resonant frequencies.

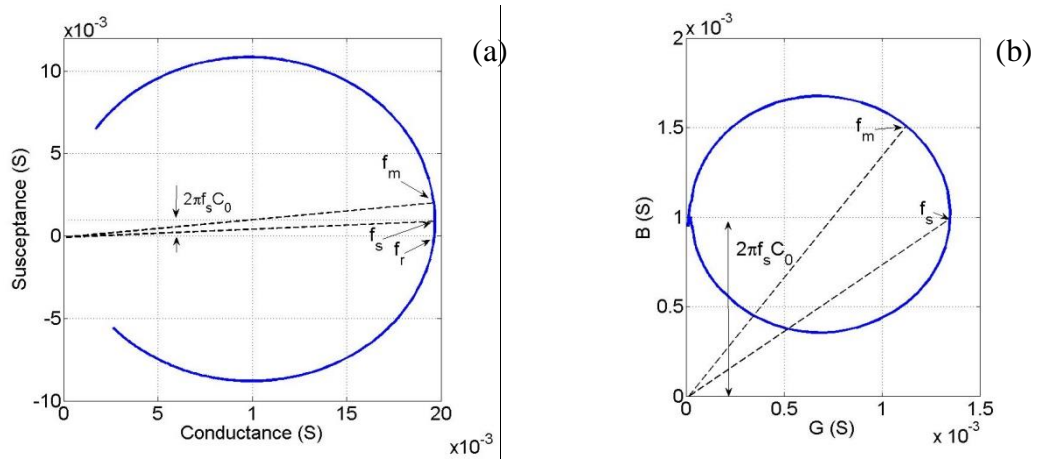


Figure 4-3 Admittance locus of Ti tool under loaded and unloaded conditions (a) unloaded (b) loaded by poultry breast tissue

Therefore, it is necessary to tune out the clamped capacitance  $C_0$ . One method is to shunt an inductor  $L_0$  to the transducer, as shown in Figure 4-4.  $L_0$  and  $C_0$  form a parallel LC circuit. By carefully selecting the inductance of  $L_0$ , it can cancel out  $C_0$  at the mechanical resonant frequency  $f_s$ . In such a case, the value of the inductance should be

$$L_0 = 1/4\pi^2 f_s^2 C_0 \quad (4-6)$$

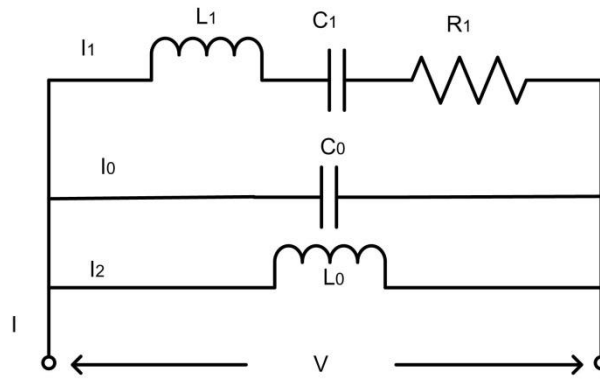


Figure 4-4 Electrical model of an unloaded transducer with a shunted inductor

For the Ti planar tool,  $C_0 = 2.024 \times 10^{-9}$  F and  $f_s = 78500$  Hz; thus  $L_0$  is 0.002 H. The admittance of the Ti planar tool with a shunted inductor of 0.002 H is shown as green curves in Figure 4-5. By using an inductor to tune out the capacitance  $C_0$ , the G-B circle is always symmetrical about the  $B=0$ , as shown in both (a) and (b). In such a case,  $f_m$ ,  $f_s$  and  $f_r$  merge into one frequency, at which lowest and purely resistive impedance is available.

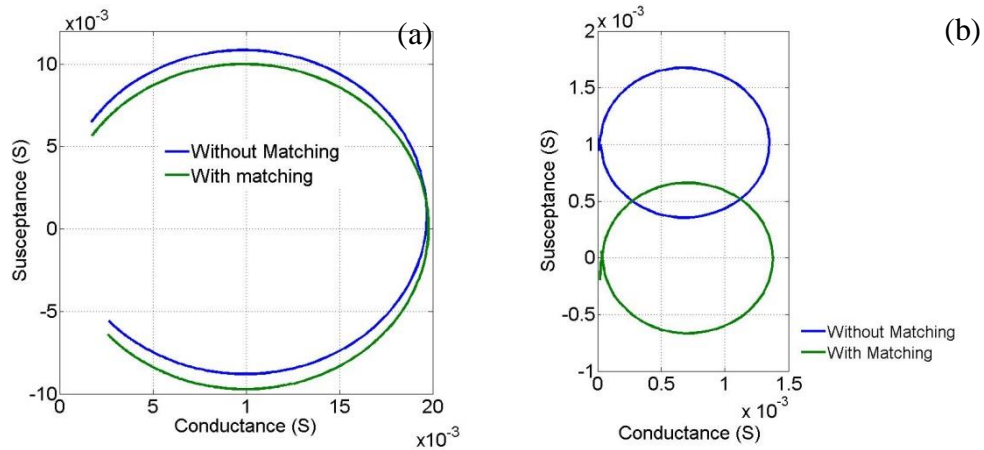


Figure 4-5 Admittance locus of Ti tool with and without electrical matching (a) unloaded (b) loaded by poultry breast tissue

Thus, to drive a transducer efficiently under both unloaded and loaded conditions, the tuning of the clamped capacitance is necessary. After this tuning, the resonant frequency of a transducer can be indicated by the zero value of impedance phase. This tuning procedure provides the basis of the resonance tracking in the adaptive driving system

developed in this thesis. At resonance, the vibration velocity is proportional to the current  $I_l$  in the mechanical arm [146]. Because the current  $I_2$  through  $L_0$  cancels out  $I_0$  through  $C_0$ , the vibration velocity is also proportional to the overall current,  $I$  through the transducer. Stable vibration velocity can be achieved by keeping the current  $I$  constant, which is the basis of the vibration stabilisation in the adaptive driving system.

## 4.2 Adaptive Driving System Configuration

### 4.2.1 Layout and hardware

The adaptive driving system is developed as a combined analogy-digital system. The control signal is processed by analogue devices. The parameters of the devices are controlled digitally by a LabVIEW program on a computer. The LabVIEW program also provides features for monitoring and displaying characteristics of the transducer in real time.

Figure 4-6 shows a schematic diagram of the adaptive driving system. The function generator (33220A, Agilent Technologies, Santa Clara, USA) is employed to produce a driving signal. The frequency and voltage amplitude of the driving signal is adjusted by the Control Module. The signal generated by the function generator is boosted by the power amplifier (1020L, Electronics & Innovation, Rochester, NY, USA) to high power level. The voltage across the ultrasonic transducer and the current in the circuit are detected by a voltage probe (N2862B, Agilent Technologies, Santa Clara, USA) and a current probe, respectively. The voltage and current signals are then sampled and digitized by a data acquisition device (PXIe 5122 on PXIe 1082 chassis, National Instruments, Newbury, UK). In the Impedance Calculation module, both the amplitude and phase of the digitized voltage and current are determined by cross-correlation method, which are further used to calculate the magnitude and phase of the electrical impedance. The current and voltage amplitude, impedance magnitude and phase are fed back to the Control Module.

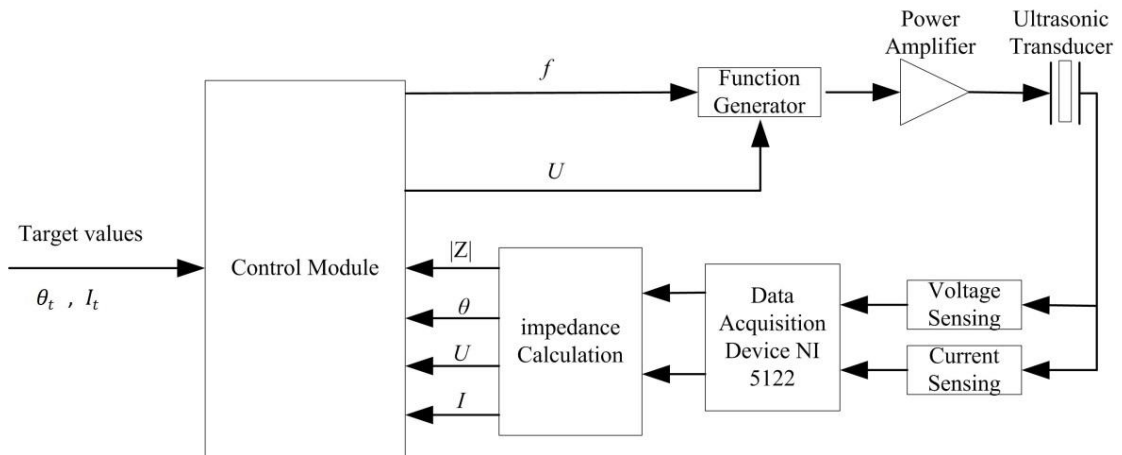


Figure 4-6 Schematic of the adaptive driving system for high power ultrasonic transducers

#### 4.2.2 Current measurement

As the electrical impedance of an ultrasound transducer varies from several ohms to thousands of ohms across the frequency range from serial resonance to parallel resonance, the current can change from several milliamperes to hundreds of milliamperes during an impedance measurement procedure. When a high power ultrasound transducer is working at serial resonance, the current value can be as high as several Amperes. So the current measurement circuit should have high sensitivity so that it can detect low current signals accurately. At the same time, it should be able to work at high power so that it can measure high level current safely.

To measure the alternating (AC) current through the ultrasonic transducers, initially, a circuit shown in Figure 4-7 was considered. The reference resistor with known resistance  $R_{ref}$  is connected in serial to the ultrasonic transducer. The current through the reference resistor equals to the current through the ultrasonic transducer. The current amplitude and phase through the transducer can be calculated by measuring the voltage across the reference resistor through NI 5122.

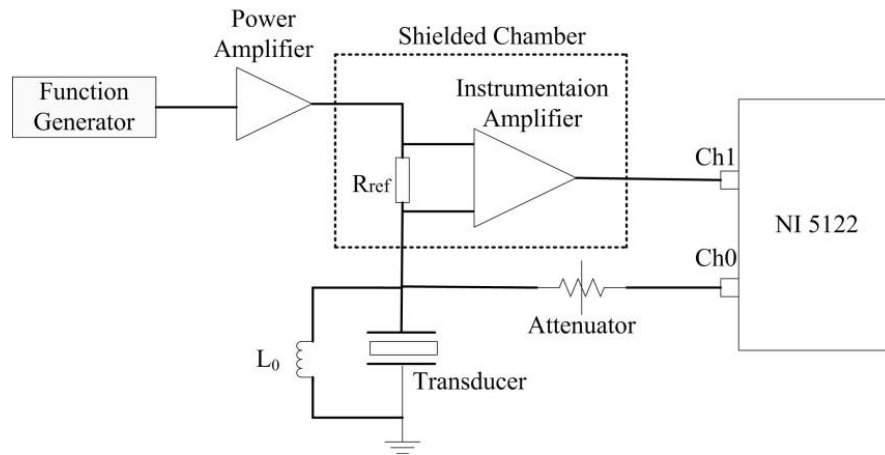


Figure 4-7 Current measurement circuit

Higher resistor value increases the sensitivity of the current measurement, but it also increases the power dissipated by the resistor. So the reference resistor value should be chosen to maximize the current signal while keeping the ratio of voltage across the reference resistor to the voltage across the transducer small. The reference resistor must also be in high precision with low reactive component so that the influence of the reactive component is small at a broad frequency range. Considering the impedance of an ultrasound transducer can be very low, a high precision resistor of  $1\ \Omega$  (CFR25 carbon film resistor, 1R 0.33W, TE Connectivity Ltd. Switzerland) was used, which resulted in a sensitivity of  $1\ \text{mA/mV}$ .

The signal sampled through the reference resistor suffered from serious noise, including high frequency harmonic noise and white noise. When the current signal is small, the signal-to-noise-ratio (SNR) is very low. To improve the SNR, an instrumentation amplifier INA 141 was used. The INA 141 is a low power general purpose instrumentation amplifier offering accurate signal amplification and effective noise reduce. So it can increase the signal level and reduce the noise at the same time.

Another method considered to measure the AC current was a commercial current probe (P6021, Tektronix, USA). The P6021 current probe converts an AC current waveform to a voltage waveform which can be measured by an oscilloscope. It provides a sensitivity of  $2\text{mA/mV}$  from  $450\ \text{Hz}$  to  $60\ \text{MHz}$ . The sensitivity can be further improved by increasing the conductor loops through the probe. Furthermore, it can measure AC current as high as  $6\ \text{A}$  continuously.



The bespoke current sample circuit is simple and cost-effective. The usage of high precision components allows it to cover the whole range of high power ultrasound. However, the high precision resistors are usually designed to work at low power (current less than 1A), which limits its application at higher power levels. Compared with the bespoke current sample circuit, the P6021 current probe offers broader frequency and power range. However, it is expensive. Even though both methods were tested in this work, the results reported in this thesis are based on the P6021 current probe for consistence.

#### 4.2.3 Impedance calculation

The measured complex impedance of the transducer can be calculated as

$$Z(j\omega) = |Z|e^{j\theta} = \frac{U}{I} e^{j(\theta_U - \theta_I)} \quad (4-7)$$

Where  $U$  and  $\theta_U$  are the amplitude and phase of the voltage across the transducer, and  $I$  and  $\theta_I$  are the amplitude and phase of the current through the transducer.

To calculate the impedance magnitude and phase,  $U$ ,  $\theta_U$ ,  $I$  and  $\theta_I$  should be determined first. In this adaptive driving system, this is achieved by the orthogonal correlation method, as it can detect weak signals accurately and reduce white noise effectively [147, 148]. A schematic of the method is shown in Figure 4-8.

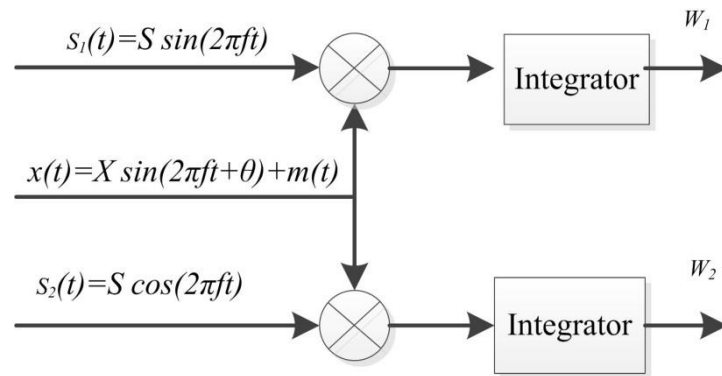


Figure 4-8 Schematic of the orthogonal correlation method

$S_1(t)$  and  $S_2(t)$  are quadrature sinusoidal reference signals with the same amplitude.  $x(t)$  contains the periodic signal of interest and additive white Gaussian noise,  $m(t)$ .

$W_n$  is the cross-correlation function of  $x(t)$  and  $S_n(t)$ ,  $n = 1, 2$ . Considering the non-correlation between the reference signal and the white noise,  $W_1$  and  $W_2$  can be formulated as:

$$W_1 = \lim_{T \rightarrow \infty} \frac{1}{T} \int_0^T x(t) S_1(t) dt = \frac{XS}{2} \cos \theta \quad (4-8)$$

$$W_2 = \lim_{T \rightarrow \infty} \frac{1}{T} \int_0^T x(t) S_2(t) dt = \frac{XS}{2} \sin \theta \quad (4-9)$$

The amplitude,  $X$ , and phase,  $\theta$ , of  $x(t)$  can then be calculated as

$$X = \frac{2}{S} \sqrt{W_1^2 + W_2^2} \quad (4-10)$$

$$\theta = \arctan\left(\frac{W_2}{W_1}\right) \quad (4-11)$$

To implement this algorithm, Equations (4-9) and (4-10) are expressed in discrete form as

$$W_1 = \frac{1}{N} \sum_{k=0}^{N-1} x\left(\frac{k}{M}\right) S_1\left(\frac{k}{M}\right) = \frac{XS}{2} \cos \theta \quad (4-12)$$

$$W_2 = \frac{1}{N} \sum_{k=0}^{N-1} x\left(\frac{k}{M}\right) S_2\left(\frac{k}{M}\right) = \frac{XS}{2} \sin \theta \quad (4-13)$$

Where  $M$  is the sampling rate and  $N$  is the number of samples used to obtain the values of  $W_1$  and  $W_2$ . Applying Equations (4-11) - (4-14) to the sampled voltage and current signals,  $U, \theta_U, I$  and  $\theta_I$  can be determined. Consequently, the impedance magnitude and phase can be calculated according to Equation (4-8).

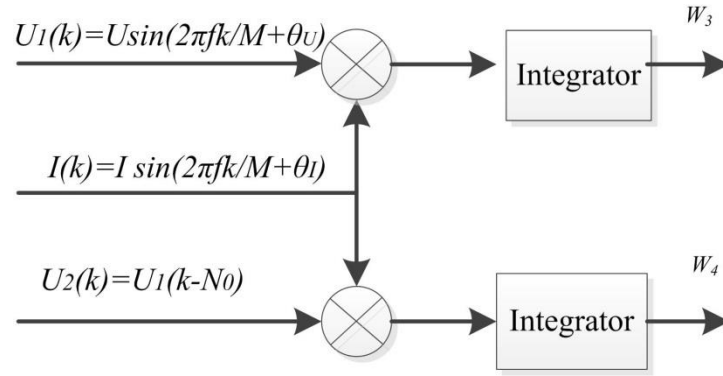


Figure 4-9 Schematic of the improved phase calculation algorithm

In practice, the phase calculated by Equation (4-11) usually suffers from wrapping, especially when the signal is low. To avoid the phase wrapping, an improved method has been adopted, which calculates the phase difference between voltage and current directly, as shown in Figure 4-9.  $U_1(k)$  is the discrete voltage across the transducer and  $I(k)$  is the discrete current through the transducer.  $U_2(k)$  is obtained by shifting  $U_1(k)$  to the right by  $N_0$  samples to obtain a delay equivalent to a quadrature phase shift, where

$$N_0 = [M/4f] \quad (4-14)$$

and  $[*]$  indicates rounding to the nearest integer. With a constant sampling rate  $M$ ,  $M/4f$  is not always an integer at different frequencies so the phase difference between  $U_1(k)$  and  $U_2(k)$  is not always  $90^\circ$ . Denoting the phase angle of  $U_2(k)$  as  $\theta_2$ , the phase difference between  $U_1(k)$  and  $U_2(k)$  is

$$\theta_U - \theta_2 = 90^\circ - \alpha \quad (4-15)$$

Where

$$\alpha = \frac{M/4f - N_0}{M/4f} \times 90^\circ \quad (4-16)$$

According to Equations (4-13) and (4-14),

$$W_3 = \frac{UI}{2} \cos(\theta_U - \theta_I) \quad (4-17)$$

$$W_4 = \frac{UI}{2} \cos(\theta_2 - \theta_1) = \frac{UI}{2} \sin(\theta_U - \theta_I + \alpha) \quad (4-18)$$

Therefore,

$$\frac{W_4}{W_3} = \tan(\theta_U - \theta_I) \cos \alpha + \sin \alpha \quad (4-19)$$

$\theta$  can then be obtained as

$$\theta = \theta_U - \theta_I = \arctan \frac{W_4/W_3 - \sin \alpha}{\cos \alpha} \quad (4-20)$$

#### 4.2.4 Control module

The control module determines the functions of the system. As a combined analogy-digital system, the control module was implemented as a virtual instrument in LabVIEW. This configuration enables the versatility and flexibility of the system. Functions can be included by modifying the algorithm of control module in LabVIEW. The current system covers two functions. One is to drive the transducers at tracked resonant frequency and stabilized vibration velocity. The other is to measure the electrical impedance of transducers at different power levels.

##### (1) Resonance tracking and vibration stabilization

To achieve resonance tracking and vibration stabilization, the control module adjusts the frequency and amplitude of signal generator by two proportional-integral-derivative (PID) controllers. Consequently, the impedance phase is kept at zero, and the current is stabilised.

A PID controller is a generic control loop feedback mechanism widely used in industrial control system [149]. A block diagram of a PID controller is shown in Figure 4-10. The controller calculates the error value,  $e(t)$ , as the difference between the measured process variable,  $y(t)$  and the desired setpoint,  $r(t)$ . The controller attempts to minimize the error by adjusting the process control inputs,  $u(t)$ :

$$u(t) = K_p e(t) + K_i \int_0^t e(\tau) d\tau + K_d \frac{d}{dt} e(t) \quad (4-21)$$

$K_p$ ,  $K_i$  and  $K_d$  are the proportional, integral and derivative constants, respectively.

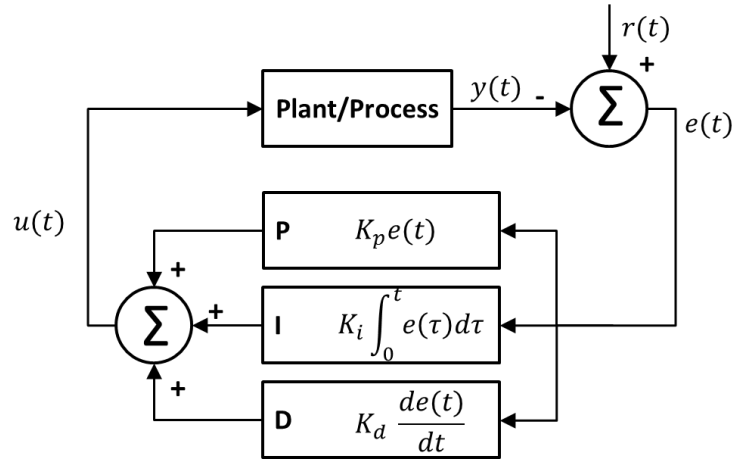


Figure 4-10 Block diagram of a PID controller

The proportional term produces an output value that is proportional to the current error value. The proportional gain  $K_p$  affects the system response speed and steady state error. However it can generate large overshoot, particularly when its value is too high. The contribution from the integral term is proportional to both the magnitude of the error and the duration of the error. It accelerates the movement of the process towards setpoint and eliminates the residual steady-state error that occurs with a pure proportional controller. However, since the integral term responds to the accumulated errors from the past, it can cause the present value to overshoot the setpoint. The derivative of the process error is calculated by determining the slope of the error over time and multiplying this rate of change by the derivative gain  $K_d$ . It is used to avoid system oscillation and improve stability [150]. These parameters can be determined both experimentally and theoretically to achieve desired performance [151].

However, the PID controller described by equation (4-22) cannot be applied directly to the resonance tracking for ultrasound transducers. The controller will search the zero phase frequency at the entire frequency range. However, an ultrasound transducer may have more than one vibration modes, and each vibration mode may have two zero phase resonant frequencies. This makes the tuning of the parameters difficult, and different

transducers with different resonant frequencies may require different controller parameters.

The PID controllers for the resonance tracking and vibration stabilization were modified from equation (4-22) and discretized, as illustrated in Figure 4-11. The Control Module consists of two control loops which are performed in parallel. The Resonance Tracking Loop is used to control the frequency output of the signal generator while the Vibration Stabilization Loop is used to adjust the voltage output.

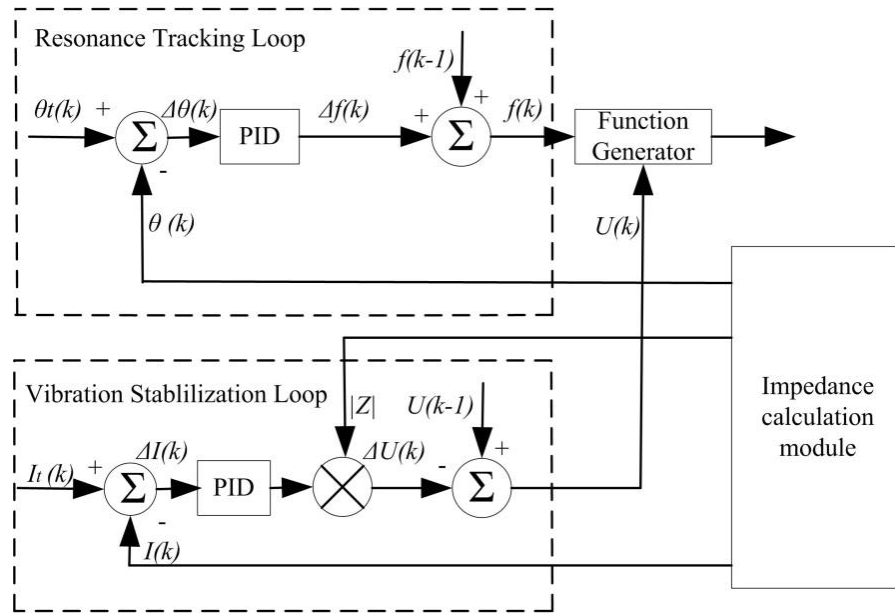


Figure 4-11 Schematic diagram of the control module

In the Resonance Tracking Loop, the phase error  $\Delta\theta(k)$  is calculated by comparing the target phase  $\theta_t(k) = 0$  and the measured phase  $\theta(k)$ .  $\Delta\theta(k)$  is then forwarded to the PID controller to calculate the frequency increment,  $\Delta f(k)$ . The frequency output of the function generator is adjusted by the controller to keep  $\Delta\theta(k)$  at zero according to

$$\begin{aligned}
 f(k) &= f(k-1) + \Delta f(k) \\
 &= f(k-1) + K_{pf} \Delta\theta(k) + K_{if} \sum_{j=0}^k \Delta\theta(j) \\
 &\quad + K_{df} [\Delta\theta(k) - \Delta\theta(k-1)]
 \end{aligned} \tag{4-22}$$

Where  $K_{pf}$ ,  $K_{if}$  and  $K_{df}$  are the proportional, integral and derivative gains of the PID controller, respectively.

In equation (4-22), the controller adjusts the frequency increment  $\Delta f(k)$ , which is added to the frequency output in the last loop,  $f(k-1)$ , to form the frequency output in the current loop,  $f(k)$ . By choosing the initial frequency  $f(0)$  roughly near the desired resonant frequency of the transducer, the controller will search the zero phase frequency near  $f(0)$ . So the tracked resonant frequency is always the desired resonance.

In the Vibration Stabilization Loop, the current error,  $\Delta I(k)$  is calculated as the difference between the target current,  $I_t(k)$ , and the measured current,  $I(k)$ . The PID controller is used to adjust the amplitude of the driving voltage to keep the current through the transducer at desired value. The relationship between the voltage output,  $U(k)$  and  $\Delta I(k)$  is

$$\begin{aligned} U(k) &= U(k-1) + \Delta U(k) \\ &= U(k-1) + |Z| [K_{pl} \Delta I(k) + K_{il} \sum_{j=0}^k \Delta I(j) \\ &\quad + K_{dl} [\Delta I(k) - \Delta I(k-1)]] \end{aligned} \quad (4-23)$$

Where  $K_{pl}$ ,  $K_{il}$  and  $K_{dl}$  are the proportional, integral and derivative gains of the PID controller, respectively.

In equation (4-23), the controller adjusts the voltage increment  $\Delta U(k)$ , which is added to the voltage output of last loop,  $U(k-1)$  to create the voltage output of the current loop,  $U(k)$ . Because the voltage output is incremental, the malfunction of the system has little effect on the output [150], preventing the transducer from unwanted high voltage during a system malfunction. The vibration stabilization loop operates only when  $|\Delta\theta| \leq 5^\circ$  for safety reasons: when the phase is far from zero, the impedance of the transducer will increase dramatically, requiring a very high voltage to maintain the current value, which could damage the transducer.

## (2) Impedance measurement

For the Resonance Tracking Loop, it is necessary to choose an initial frequency near the desired resonance of the transducer. Therefore, an impedance measurement function was included into the adaptive driving system to measure the impedance versus frequency characteristics of transducers. The impedance measurement was conducted by sweeping the frequency of the sine voltage applied to the transducer and measuring the impedance at each frequency point at the same time.

To perform the frequency sweep, the control module controls the frequency output of the signal generation,  $f(k)$  according to

$$f(k) = f(k - 1) + \Delta f(k) \quad (4-24)$$

Where

$$\Delta f(k) = \frac{f_{stop} - f_{start}}{N_{point} - 1} \quad (4-25)$$

The frequency range is specified by the starting frequency  $f_{start}$  and stopping frequency  $f_{stop}$ .  $N_{point}$  is the number of frequency points to measure in the frequency range of interest.  $k=1, 2, 3 \dots N_{point}$  and  $f(0) = f_{start}$ .

At each frequency  $f(k)$ , the voltage, current, impedance magnitude and phase are recorded. Thus, the variations of these parameters against frequency are obtained. The voltage output of the signal generator can be any desired values. So the adaptive driving system can characterise the performance of the ultrasound transducers at both low and high power levels.

During the impedance measurement, if a LDV is used to measure the vibration amplitude, the vibration against frequency can also be obtained. Measuring the vibration response during a frequency sweep was conducted in Chapter 3 without using the adaptive driving system. However, without the adaptive driving system, the current and impedance against frequency are not available.



#### 4.2.5 Software programming

LabVIEW, Laboratory Virtual Instrument Engineering Workbench, is a system-design platform and development environment for a visual programming language from National Instruments. It is a graphical, dataflow programming language. The reason to choose LabVIEW as the platform for the system here is its extensive support for accessing instrumentation hardware. Drivers and abstraction layers for many different types of instruments and buses are included or available for inclusion, providing convenience for the adaptive driving system to communicate with the signal generator. Furthermore, LabVIEW is an inherently concurrent language, so it is very easy to program multiple tasks by means of multithreading. Multithreading is beneficial for the adaptive driving system since two controllers are required to run in parallel.

##### (1) Resonance tracking and vibration stabilization

The programming flow chart of the system for resonance tracking and vibration stabilization and the program code are listed in Appendix A. The system works in the following sequence:

1. Start the program.
2. The LabVIEW program communicates with the signal generator and controls it to output an initial voltage of  $U(0)$  at initial frequency of  $f(0)$  to an ultrasound transducer.
3. If not stop, go to step 4. Otherwise, go to step 10.
4. The LabVIEW program orders the NI 5122 to sample the voltage and current, and save the waveforms to the memory.
5. Calculates  $U$ ,  $I$ ,  $\theta_U$ ,  $\theta_I$ ,  $|Z|$  and  $\theta$ . The algorithm was described in Section 4.2.3. The results are displayed in real time.
6. According to the measured impedance phase  $\theta$  and the pre-set parameters of the controller, frequency increment in the current loop  $\Delta f(k)$  is calculated. At the

same time, voltage increment in the current loop  $U(k)$  is also computed according to the measured current  $I$  and the pre-set parameters of the controller.

7. The frequency increment  $\Delta f(k)$  is added to  $f(k-1)$  to form the frequency output in the current loop,  $f(k)$ . At the same time, the voltage increment  $\Delta U(k)$  is added to  $U(k-1)$  to form the voltage output in the current loop,  $U(k)$ .
8. The LabVIEW program communicates with the signal generator and orders it to output voltage of  $U(k)$  at frequency of  $f(k)$ .
9. If not stop, go to step 4. Otherwise, go to step 10.
10. Stop the program.

The program runs on the PC core installed on NI PXIe 1082 chassis. The NI 5122 data acquisition card is installed on the PXI Express slot of the NI 1082 chassis and NI-DAQmx provides interfaces for LabVIEW program to visit and control it. The communication between the NI PXIe 1082 and the signal generator is enabled by a USB cable while the interfaces for LabVIEW program is provided by a driver developed by National Instruments.

## (2) Impedance measurement

The programming flowchart of the system for impedance measurement and the LabView code are listed in Appendix B. The system works in the following sequences:

1. Start the program.
2. Calculate the frequency output of the signal generator,  $f(k)$ , according to equations (4-30) and (4-31).
3. Communicate with the signal generator and control it to output voltage of  $U$  at frequency of  $f(k)$ .
4. The program orders the NI 5122 to sample the voltage and current, and then saves the waveform in the memory.

5. Calculate  $U$ ,  $I$ ,  $\theta_U$ ,  $\theta_I$ ,  $|Z|$  and  $\theta$ . The algorithm was described in Section 4.2.3. The results are displayed in real time.
6. If the all the frequency points are measured, go to step 7. Otherwise, go to step 2.
7. Stop the program.

### **4.3 Experimental validation**

The adaptive driving system was tested to validate its accuracy in measuring electric impedance of the transducer. Following that, the effectiveness in resonance tracking and vibration stabilisation was studied. Figure 4-12 illustrates the driving system developed. The digitizer NI 5122 installed on the PXIe 1082 has two input channels: Ch0 and Ch1. The voltage signal from the voltage probe is routed to Ch0 whereas the current signal from the current probe is routed to Ch1. The LDV used to measure the vibration amplitude of the transducer is optional for the system. The signal from LDV is connected to the input channel of digitizer NI 6124, which is also installed on PXIe 1082. The experimental results are displayed on the monitor in real time.

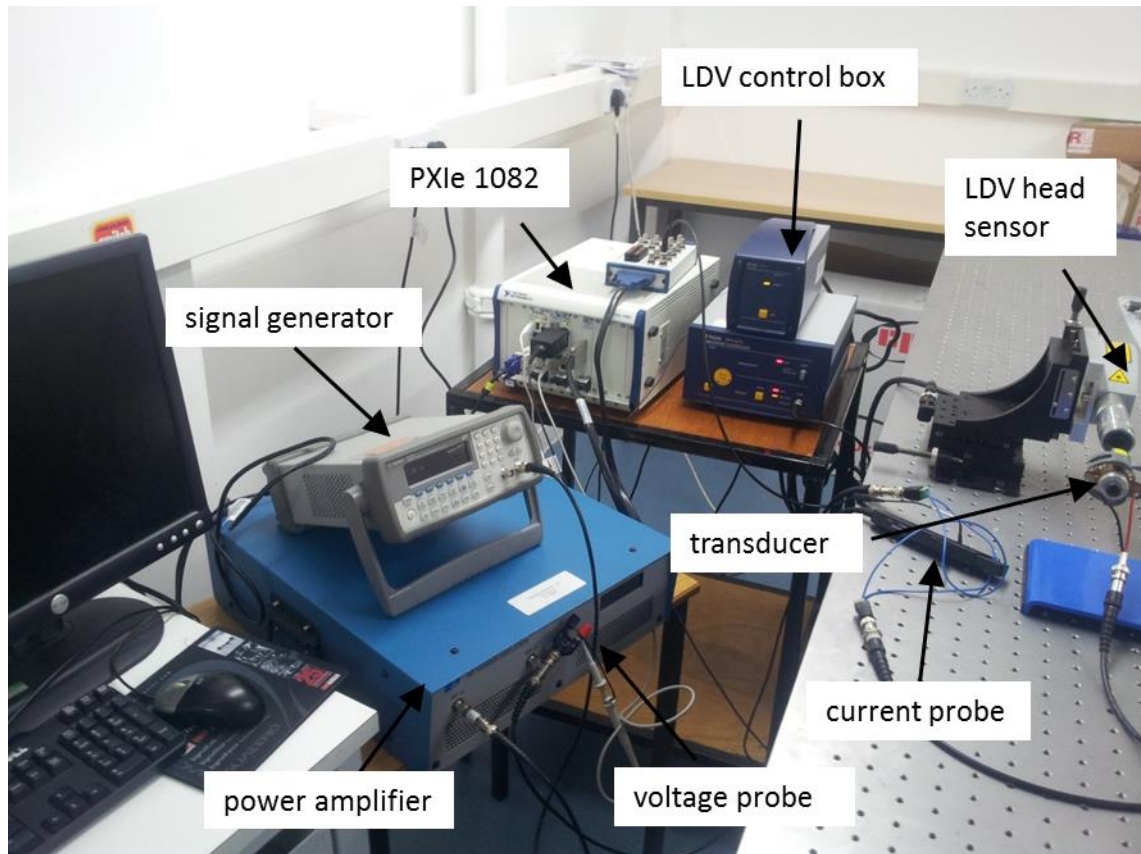


Figure 4-12 The adaptive driving system with LDV

#### 4.3.1 Impedance measurement

The controllers for resonance tracking and vibration stabilization function calculates the outputs of the signal generator based on the impedance measurement results. The accuracy of the impedance measurement will affect the effectiveness of the resonance tracking and vibration stabilization. Therefore, the impedance measurement function of the system was tested before the experiment on resonance tracking and vibration stabilization.

A 50  $\Omega$  Cantenna RF load resistor (HN-31, Heath Co., Benton Harbor, USA) was used to calibrate the impedance measurement function. The impedance amplitude and phase of the resistor was measured with the calibrated HP 4194A impedance analyser and the adaptive driving system from 20 kHz to 5 MHz. The results obtained from HP 4194 served as a reference. When measuring the impedance with the adaptive driving system, the system was controlled by the LabVIEW program described in Section 4.2.4 (2) to

output a frequency sequence. The current probe P6021 was used to transform AC current to AC voltage. Three conductor loops were wound through the probe, resulting in a sensitivity of 2/3 mA/mV. The impedance measurement results are shown in Figure 4-13.

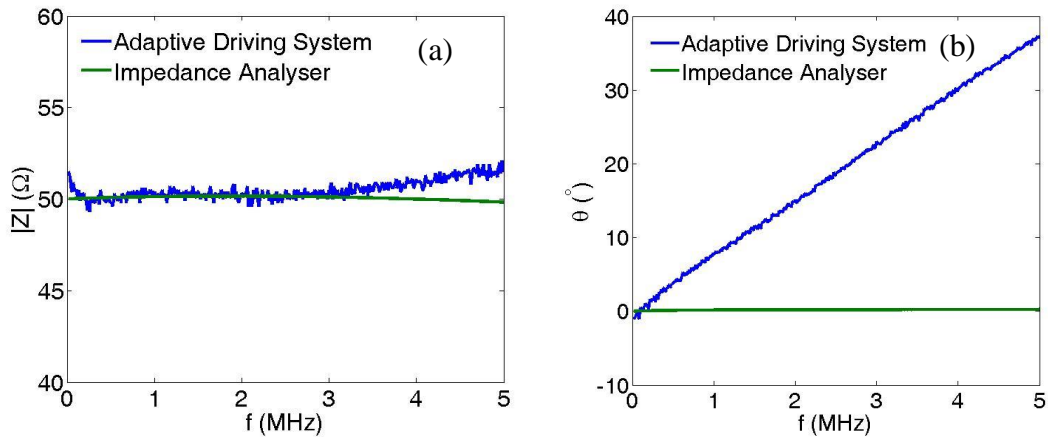


Figure 4-13 Impedance of a standard resistor measured by HP 4194A impedance analyser and the adaptive driving system from 20 kHz to 5 MHz (a) magnitude (b) phase

The magnitude measured by the adaptive driving system showed high accuracy, especially at frequency up to 3 MHz, where the magnitude error is within  $\pm 2\%$ . At frequency higher than 3 MHz, the magnitude error increases gradually with frequency. However, the maximum error is still within  $\pm 5\%$ . The increasing error at high frequency results from the current probe, which induced impedance into the circuit measured. The effects of the insertion impedance to the overall impedance are negligible at low frequency but become significant at high frequency range.

The phase of the resistor measured by the impedance analyser is almost zero from 20 kHz to 5 MHz, as shown in Figure 4-13 (b). The phase measured by the adaptive driving system shows significant error, which increases with frequency. However, it was found that the phase error at the low frequency range is low. Figure 4-14 shows the phase measurement results from 20 to 100 kHz. 20-100 kHz is the typical frequency range of high power piezoelectric transducers. The phase measured by the adaptive driving system is within  $\pm 1^{\circ}$ .

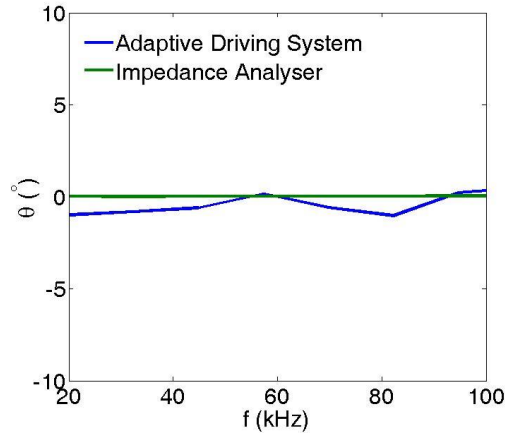


Figure 4-14 Impedance phase between 20 and 100 kHz measured by the adaptive driving system and the commercial impedance analyser

So, for high power ultrasound applications in frequency range of 20-100 kHz, the adaptive driving system provides accurate impedance and phase measurement. However, for applications at high frequency range, for example High Intensity Focused Ultrasound (HIFU), which works between 0.5-2 MHz, the adaptive driving system has to be calibrated in phase measurement. The phase error shows a linear relationship with frequency; this can be modelled as

$$\theta_e(f) = \theta - \theta_{imp} = 2\pi f * a - b \quad (4-26)$$

Where  $\theta$  and  $\theta_{imp}$  are the values measured by the adaptive driving system and the HP 4194A impedance analyser, respectively.  $a$  and  $b$  are the slope and intercept of the error curve,  $\theta_e(f)$ , respectively. The phase error is probably associated with two causes: the time delay difference between the voltage and current sensing probes, and the insertion impedance induced by the current probe. Both causes can results in a phase error increasing with frequency.  $a$  and  $b$  can be calculated by the least-square fitting method to be  $a = 1.2 \times 10^{-6}s$  and  $b = -0.123^\circ$ , with a mean square error of 0.084. The phase calculation equation is thus calibrated as

$$\theta_c = \theta - \theta_e(f) = \theta - 7.536f \times 10^{-6} + 0.123 \quad (4-27)$$

After calibration, the phase error is within  $\pm 1^\circ$ .

Following the calibration, the electric impedance of a commercial ultrasound transducer was measured by the HP 4194A impedance analyser and the adaptive driving system. The results are shown in Figure 4-15. The curves characterised by the adaptive driving system follow the results measured by the HP 4194A impedance analyser precisely.

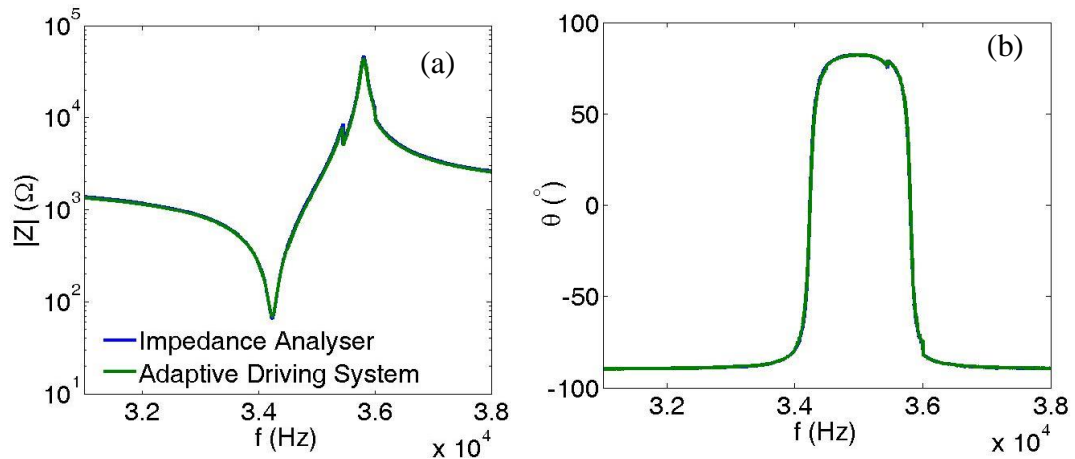


Figure 4-15 Electrical impedance of a commercial transducer measured by HP 4194A impedance analyser and the adaptive driving system: (a) magnitude (b) phase

#### 4.3.2 Resonance tracking and vibration stabilization

Following the successful validation of the impedance measurement function, the resonance tracking and vibration stabilization function of the adaptive driving system was tested. The controller parameters were tuned manually. They were set to be:  $K_{pf} = 0.8$ ,  $K_{if} = 0.001$  minute and  $K_{df} = 0$ ;  $K_{pi} = 0.5$ ,  $K_{ii} = 0.001$  minute and  $K_{di} = 0$ . During the tuning procedure, it was found the system oscillation was not significant, so the derivative term was not included by specifying the constants  $K_{di}$  and  $K_{df}$  to be zero. The controllers finally used were PI controllers.

#### Optimise the performance of Ti planar tool

The Ti ultrasonic planar tool was driven by the adaptive driving system at 0.03, 0.05 and 0.07A. The parameters of the planar tool monitored in real time during the driving process are presented Figure 4-16.

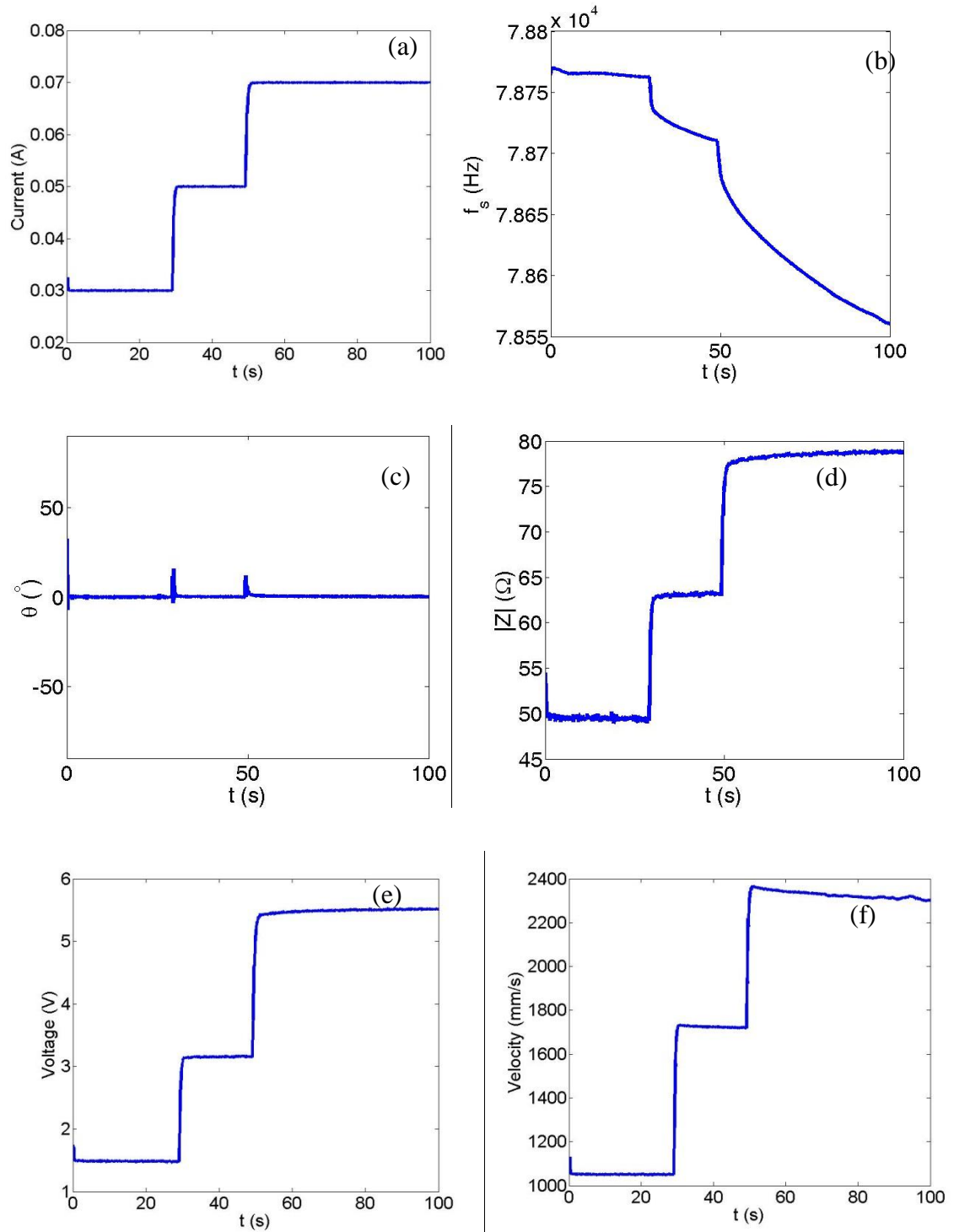


Figure 4-16 Parameters of the Ti planar tool driven by the adaptive driving system: (a) current; (b) resonant frequency; (c) impedance phase; (d) impedance magnitude; (e) voltage; and (f) vibration velocity

The measured currents through the transducer are stabilised at the desired levels, as shown in Figure 4-16 (a). The resonant frequency, Figure 4-16 (b), shifts to lower



values with time, the rate of change increasing with increasing driving current. The success of the resonance tracking can be verified by the impedance phase, Figure 4-16 (c), which stays at zero. The steady state error of the phase lock is within  $\pm 1^\circ$  and this error decreases with the driving current due to improvement in signal to noise ratio.

Fluctuation of the phase angle is observed when the current increases suddenly. This fluctuation cannot be fully eliminated because of the unavoidable delay between the frequency tracking and frequency shifting. However, the magnitude of this disturbance can be minimized by increasing the speed of the resonance tracking loop. The impedance magnitude of the planar tool, Figure 4-16 (d), increases with driving signal amplitude. As shown in Figure 4-16 (e), the driving system adjusts the driving voltage automatically, so that the current and, therefore the vibration amplitude of the transducer maintain constant values during operation, without influence from the increased impedance and frequency shifts.

The results above suggest that the adaptive driving system successfully tracked the resonant frequency and stabilised the vibration velocity of the planar tool. However, it is still unclear whether the maximum vibration velocity of the planar tool is achieved. To verify this, two experiments were conducted: frequency sweep test and driving test.

In the frequency sweep test, the impedance measurement function of the adaptive driving system was used. The adaptive driving system controlled the signal generator to sweep the frequency of the voltage applied to the planar tool. At the same time, the LDV recorded the vibration response of the planar tool so that the vibration against frequency curve was obtained. From this curve, the maximum vibration amplitude, i.e. the optimal performance of the planar tool was identified.

In the driving test, the planar tool was driven by the resonance tracking and vibration stabilisation function of the adaptive driving system for 5s. The vibration velocity was recorded by the LDV. The reason to choose a short driving time is to avoid the performance degradation of piezoelectric material due to long driving time and temperature increase, which will be discussed in Chapter 5 of this thesis.

Figure 4-17 compares the vibration velocities of the Ti planar tool obtained in the two experiments at different current values. In both cases, the vibration velocity is linearly proportional to the current amplitude. The velocity from the driving test is about the same as that from the swept-sine test, suggesting that the optimal performance of the planar tool is attained in the driving test.

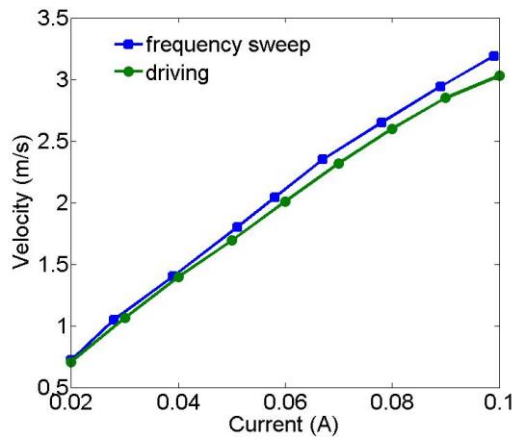


Figure 4-17 Vibration velocity of the Ti planar tool during a swept-sine test and a continuous driving test at different current amplitudes

### Comparison with commercial and non-adaptive systems

The effectiveness of the adaptive driving system was compared with two other driving systems: Vibra cell VCX 735 (SONICS & MATERIALS INC, USA) and a non-adaptive driving circuit. Vibra cell VCX 735 is a commercial driving system for high power ultrasonic transducers, which can track the resonant frequency and provide stable vibration amplitude at a 35-35.5 kHz. The non-adaptive circuit consists of a function generator (33220A) and a power amplifier (1020L) only. The driving frequency of the non-adaptive system was fixed at the resonant frequency indicated by HP 4194A impedance analyser.

The three driving systems were used to drive two unloaded piezoelectric transducers (shown in Figure 4-18). They are both sandwich transducers for high power ultrasonic applications and resonant at 35.5 kHz and 34.25 kHz respectively. The vibration velocity at the front face of the transducers was measured by the LDV. No impedance

tuning was conducted because the differences among  $f_m$ ,  $f_s$  and  $f_r$  are small when they are unloaded.

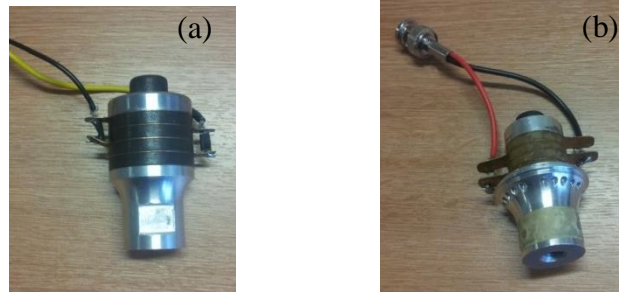


Figure 4-18 Two piezoelectric sandwich transducers used in the experiment (a) 35.3 kHz (b) 34.25 kHz

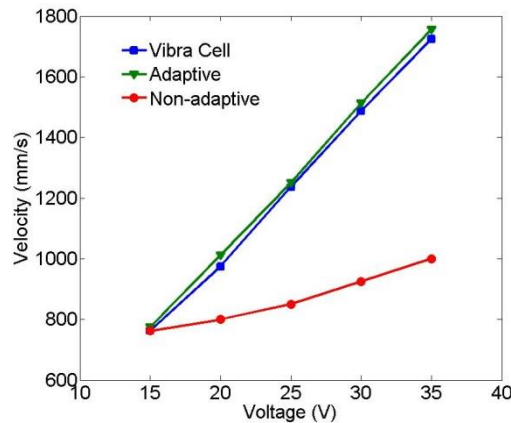


Figure 4-19 Vibration velocity of the 35.3 kHz transducer driven by the three driving systems

The vibration velocity of the 35.3 kHz transducer at different voltage is shown in Figure 4-19. At 15V, the three systems offer the same vibration velocity because there is little frequency shift at low power level. At 35 V, the vibration velocities obtained from the Vibra cell, the adaptive driving system and the non-adaptive driving circuit are 1750, 1700 and 950 mm/s, respectively. So both the adaptive driving system and the Vibra cell improve the transducer's vibration amplitude significantly at high power levels, compared with results from the non-adaptive driving circuit. They hold about the same performance. However, the working frequency range of Vibra cell is narrow. If the

resonant frequency of the transducer shifts out of this range or if another transducer with slightly different resonant frequency is used, the Vibra cell may not work properly.

The performance of the 34.25 kHz ultrasonic transducer driven by the adaptive driving system and the Vibra Cell is shown in Figure 4-20 (a). To achieve the same vibration velocity as the adaptive driving system, the Vibra cell requires much higher voltage, because the resonant frequency of the transducer was out of the working range of Vibra cell, and the Vibra cell failed to track the resonance. The excitation frequency of Vibra cell was between 35 kHz and 35.5 kHz, resulting in high electrical impedance and consequently low current and low vibration velocity. In contrast, the adaptive driving system tracked the resonance of the transducer correctly and thus improvement in performance was observed, compared with the results from the non-adaptive circuit, as shown in Figure (b).

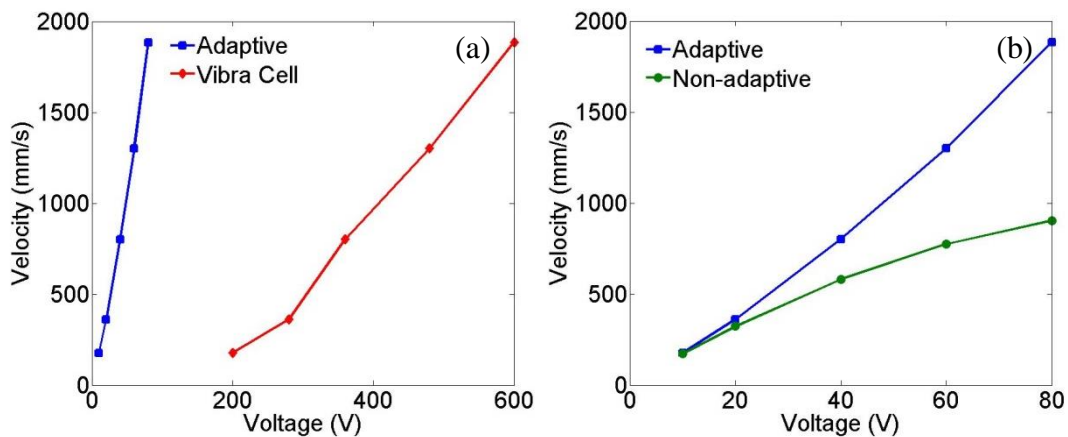


Figure 4-20 Vibration velocity of the 34.25 kHz transducer (a) comparison between the adaptive driving system and the Vibra Cell (b) comparison between the adaptive driving system and the non-adaptive circuit

#### 4.4 Discussion and Conclusions

An adaptive and flexible driving system to address issue of resonant frequency shift and electrical impedance variation of high power ultrasonic transducers was developed and validated.

The electric model and dynamic behaviour of high power ultrasonic transducers were analysed first. The transducer could be regarded as a serial RLC circuit shunted by a

capacitance  $C_0$ . After the capacitance  $C_0$  was tuned out, the mechanical resonance, zero-phase frequency and maximum admittance frequency of the transducer merged to one frequency. In such a case, the resonance of the transducer could be indicated by zero impedance phase value. The adaptive driving system tracked the transducers' resonant frequency based on this principal.

The accuracy of the impedance measurement directly affects the performance of the adaptive driving system because the controller adjusts the frequency and voltage according to the measurement results. High power ultrasound transducers usually work in the frequency range of 20-100 kHz. At this frequency range, the adaptive driving system showed high accuracy in impedance measurement: magnitude error within  $\pm 2\%$  and phase error within  $\pm 1^\circ$ . To measure the transducers in MHz range, calibration of the phase measurement results is required.

An incremental algorithm was introduced to both PID controllers for resonance tracking loop and vibration stabilisation loop. For the resonance tracking loop, an initial frequency was specified at the targeted resonance vicinity. Then the PID controller searched the resonant frequency by changing the frequency increments. This method prevented the systems from locking the frequency at unwanted resonance mode. Also, by choosing the initial frequency, the system was able to work with transducers in a broad frequency range. In principal, the adaptive system can track the resonant frequency of a transducer as soon as the impedance phase can be accurately measured. The frequency range of the system thus is up to 5 MHz. The power range is up to 300 W. Both are currently limited by the power amplifier.

The adaptive driving system successfully worked with transducers in 34.25 and 35.3 kHz, and Ti planar tool at 78.5 kHz without changing the controller parameters. The results obtained from the planar tool suggested that the optimal performance be achieved by using the adaptive driving system. The commercial driving system, Vibra Cell showed about the same performance as the adaptive driving system when working with the 35.3 kHz transducer. However, its working range is limited. It failed to work with the 34.25 kHz transducer.

In conclusion, the adaptive driving system developed in this chapter exhibited several features that offer advantages over the conventional driving circuits for high power ultrasound transducers. These features include:

1. Combined analogue-digital configuration. The parameters of the components in the system were controlled digitally in LabVIEW program. Due to this configuration, the function of the system can be changed and extended conveniently by modifying the program codes. The performance of the transducers can be monitored and displayed in real time.
2. Employing commercial components. All the components employed in this system are commercially available. They are connected by either power cables or USB cables and controlled by a computer. This makes the development process easy and time-saving.
3. Incremental PID controllers. The controllers calculate the output increment and add it to the last output to create the new output value. The system can lock the resonant frequency of the transducer at any desired resonant mode within the frequency range of the hardware without changing the controller parameters.

## 5 EFFECTS OF POWER LEVELS AND SOFT TISSUE LOADS

Ultrasonic surgical instruments usually work at high power levels and under external loads placed by target tissues. High driving power leads to high electrical field and high strain in piezoelectric material, which results in nonlinearities [8]. External loads also vary the resonant frequency and electrical impedance [9, 10]. As a result, it is important to have an adaptive driving system, which can track the resonant frequency and stabilise the vibration velocity of ultrasonic surgical instruments under a combined influence of both high power levels and external loads.

This chapter first investigates the performance variation of ultrasonic planar tools resulting from high power levels and external soft tissue loads by using the adaptive driving system, presented as high power characterisation in Section 5.1. This allows identifying the working limit and optimal working condition of the ultrasonic planar tools. Following this characterisation, the ultrasonic planar tool is used to penetrate soft animal tissue, as presented in Section 5.2. The ability of the adaptive driving system to improve the performance of the ultrasonic planar tools is studied in the tissue penetrating tests. For all the experiments in this Chapter, the Ti planar tool was used. The reason to choose the Ti tool rather than Si and AlN tools is because the Si and AlN are very brittle. Without depositing tough material on the surfaces, the Si and AlN tools can be easily broken during the cutting experiment.

### 5.1 High Power Characterisation

Even though the high power characterisation of piezoelectric material and transducers have been widely reported, as discussed in Chapter 2, most of these studies are based on PZT or sandwich transducers with PZT stack. The high power characterisation of transducers based on piezocrystals in  $d_{31}$  mode has not been reported. Attention must be paid to the PMN-PT piezocrystal in high power usage. Although PMN-PT piezocrystal has shown high charge coefficient and high coupling factor, however, it exhibits a low

Curie temperature point and low morphotropic phase boundary (MPB)[92]. The temperature increase during high power driving can potentially degrade its performance.

In addition to high power level, external load is also a key factor that affects the operative performance of ultrasonic instruments. During operation, the tissue acts as a load onto the blade thus changes the characteristics of ultrasonic instruments. Chen [9] measured the load characteristics of different *ex vivo* animal tissue on an ultrasonic surgery scalpel. However, the characterization was carried out in the small signal region.

This section reports the high power characterisation of Ti planar tool developed in Chapter 3 of this thesis to study the variations of the performance variables, including self-heating effect, resonant frequency, electric impedance and vibration velocity. The characterisation was first conducted under unloaded condition. This characterisation allows identifying the performance variation of the planar tool caused by the high power level. Then the characterisation was carried out under loaded condition, which measured the performance variation of the planar tool caused by both high power level and the external loads.

### 5.1.1 Experimental Arrangements

In both unloaded and loaded conditions, the Ti planar tool developed in Chapter 3 was used. The capacitance  $C_0$  of the Ti tool was tuned out by an inductor, as described in Chapter 4. The adaptive driving system developed in Chapter 4 was used to drive the planar tool and record the performance parameters.

#### (1) Unloaded condition characterisation

During unloaded condition characterisation, the planar tool was fixed by a clamp. An infrared camera (TIM 160, Micro-Epsilon, UK) was used to monitor the temperature of the PMN-PT plates, and the LDV was used to measure the vibration velocity at the tool tip, as shown in Figure 5-1.



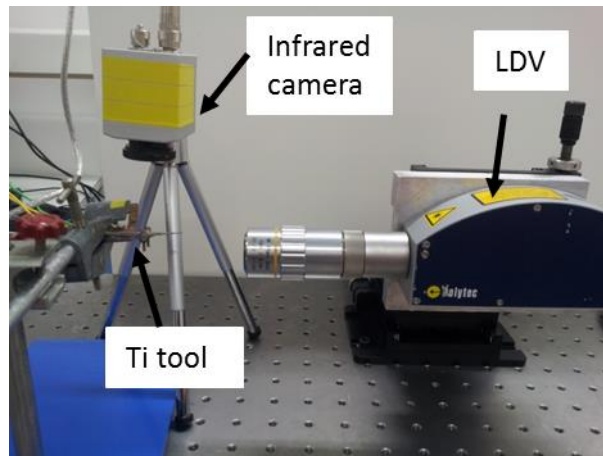


Figure 5-1 LDV and infrared camera used to characterise the Ti planar tool in unloaded characterisation

At a range of current amplitudes from 0.02A to 0.15A, the planar tool was driven continuously by the adaptive driving system until it achieved the steady state, where the resonant frequency and temperature of the PMN-PT piezocrystal ceased to change. A time delay of 10 minutes was included between two driving processes to allow the planar tool cooling down. During each driving process, the electric impedance and resonant frequency were recorded by the adaptive driving system in real time. The temperature increase of the PMN-PT piezocrystal and the vibration velocity of the planar tool were also recorded.

### (2) Loaded condition characterisation

In loaded condition characterisation, the ultrasonic planar tool is fixed on the moving crosshead of a material testing machine (H5KS, Tinius Olsen Inc., Horsham, USA), as shown in Figure 5-2 (a). The moving cross head provides a controlled downward motion at a constant speed so that the planar tool can insert into the specimen to desired depth,  $d$ , as shown in Figure 5-2 (b). Fresh poultry breast tissue obtained fresh from a local butcher was used as a specimen and placed on the specimen holder.

The planar tool was inserted into the specimen to 1, 5, 7 and 10 mm. After the desired depth was reached, the planar tool stopped inserting. Then, the planar tool was driven by the adaptive driving system at constant current amplitude until it achieved the steady state, where the resonant frequency and temperature of the PMN-PT piezocrystal ceased

to change. A time delay of 10 minutes was included between two consecutive driving processes to allow the planar tool to cool down. During each driving process, the electric impedance and resonant frequency were recorded by the adaptive driving system in real time. The infrared camera was used to measure the temperature of the PMN-PT. However, the LDV was not used because the tool tip was not accessible to the laser beam.

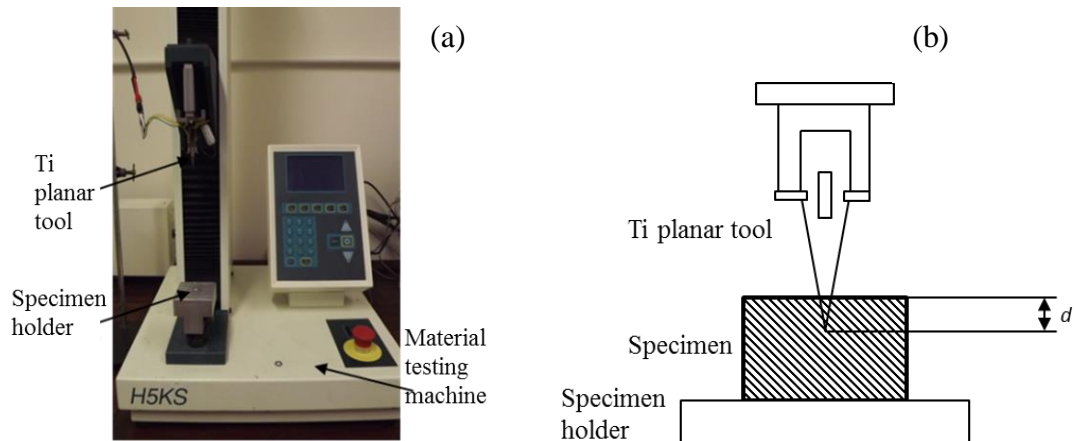


Figure 5-2 (a) Experimental setup for loaded characterisation (b) a diagram of the loaded characterisation

### 5.1.2 Experimental Results

#### (1) Unloaded characterisation

When the planar tool was driven continuously, the temperature of the PMN-PT piezocrystal increased quickly. A typical thermograph of the planar tool captured by the infrared camera is shown in Figure 5-3 (a), which illustrates the temperature increase from a baseline room temperature of 24°C. Apparently, the temperature distribution is not uniform and shown as location dependant.

Figure 5-3 (b) shows the original picture of the planar tool around the PMN-PT, where three areas are identified: Bottom epoxy, Top epoxy and the PMN-PT surface. The ‘Bottom epoxy’ is high strength conductive epoxy used to bond the blade and the PMN-PT plates. Some of conductive epoxy was squeezed out during fabrication. The ‘Top

epoxy’ was used to secure the wire connection to the upper electrode on the PMN-PT plate.

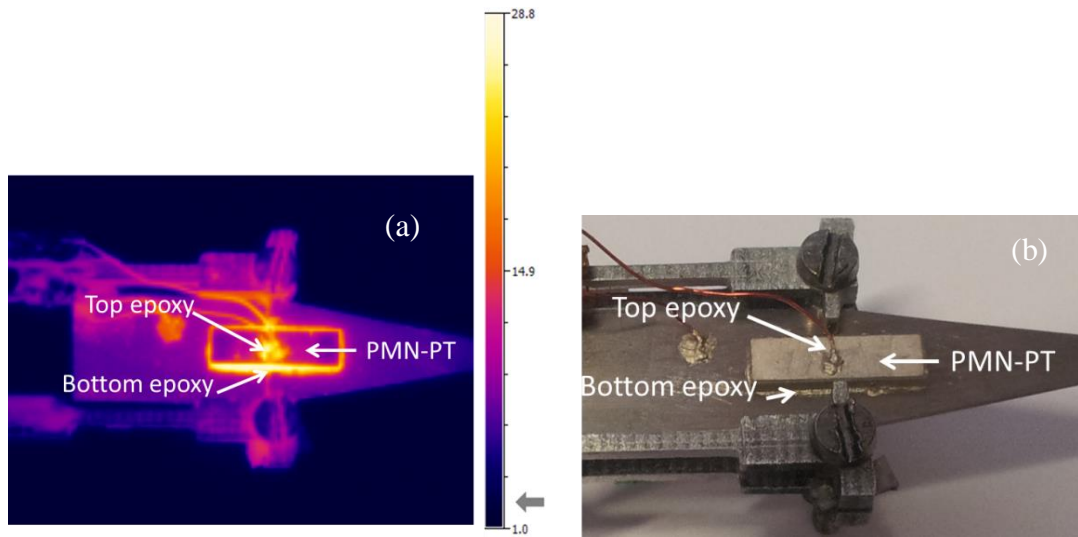


Figure 5-3 (a) Typical thermograph of the Ti tool captured by the infrared camera (b) detailed view of the Ti tool

As shown in Figure 5-3 (a), the ‘Bottom epoxy’ suffers from the highest temperature increase, followed by the ‘Top epoxy’. The upper surface of PMN-PT plate shows the smallest temperature change. The steady state temperature of the ‘Bottom epoxy’, ‘Top epoxy’ and PMN-PT surface at different current amplitudes is presented in Figure 5-4.

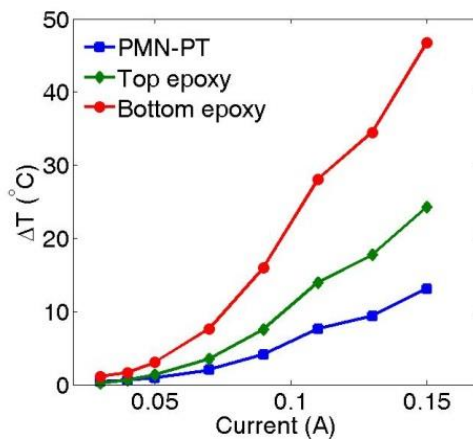


Figure 5-4 Steady state temperature of the Ti tool at different current amplitudes

The temperature in the three areas increases with current amplitude. At low current levels, the temperature increase of the three areas is insignificant and approximately the same. However, after 0.05A, the temperature increases rapidly, and the discrepancies between the three traces go up quickly with current amplitude. Highest temperature is always observed on the 'Bottom epoxy'. Although the temperature increase on the PMN-PT surface is within 13°C (0.15A), higher temperature is believed to be present inside the PMN-PT, because the infrared camera only measures the surface temperature. In the 'Bottom epoxy', the temperature increase is as high as 47 °C (0.15A), resulting in an absolute temperature of 71 °C. During the experiment, when increasing the current further ( $> 0.15\text{A}$ ), the maximum temperature on the bottom epoxy exceeded 75°C, and the planar tool failed to work properly. It lost the zero phase frequency, and the electrical impedance decreased. However it recovered after the temperature decreased. The behaviour of PMN-PT at temperature higher than  $\sim 75^\circ\text{C}$  is because the piezoelectric material enters into the phase transition zone at high temperature, where the piezoelectric behaviour of the PMN-PT deteriorates significantly and becomes unstable. Even though the Curie point of PMN-PT is  $\sim 130^\circ\text{C}$ , the phase transition point is  $\sim 80^\circ\text{C}$ . The usage range for PMN-PT is thus below  $80^\circ\text{C}$  [152].

When the piezoelectric material is driven at high power levels, both mechanical and dielectric losses will increase. Part of the increased losses is dissipated into heat, resulting in temperature increase [153]. The high temperature in the 'Bottom epoxy' may be partly because two heating sources were located quite close to each other since two PMN-PT plates were driven at the same time. However, even when only one PMN-PT plate was driven, the highest temperature was still observed in the region of 'Bottom epoxy'. Furthermore, even the 'Top epoxy', which had the same heat dissipation condition as PMN-PT surface, always exhibited higher temperature than the PMN-PT surface. This suggests in addition to the heat resulting from the mechanical and dielectric losses of the PMN-PT plates, there was intensive heat in the area where the epoxy was used.

Hu [154] has found that the highest temperature was always located at the area adjacent to the solder points, which were used to secure lead wires on the electrodes of PZT actuators. He contributed this to the contact resistance between the solder and electrode

probably caused by the non-intimate contact and interfusion between the solder and the electrode. However, in case of the planar tool, even a dummy epoxy bump on the top of PMN-PT shows a higher temperature than the PMN-PT, as shown in Figure 5-5.

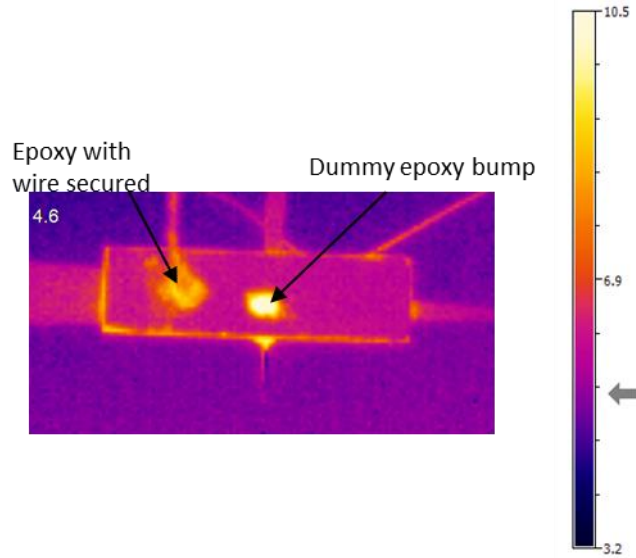


Figure 5-5 Thermal graph of PMN-PT piezocrystal with a dummy epoxy bump under continuous driving

The epoxy on the left of the PMN-PT is used to secure the electrode connection and the epoxy located at the middle of the PMN-PT is a dummy epoxy bump without lead wire connection. The dummy epoxy bump is in open circuit; thus no contact resistance should be considered. However, the dummy epoxy bump still exhibits higher temperature than the PMN-PT surface. Even though this phenomenon cannot exclude the contribution of the contact resistance to the self-heating in epoxy, it suggests the contact resistance is not necessarily related. The high temperature in epoxy is mainly caused by the very high mechanical loss because of high damping coefficient [95, 155].

When the planar tool was driven at different high power (constant current) levels, the resonant frequency shifted. The magnitude of frequency shift,  $\Delta f$  was calculated as

$$\Delta f = f_0 - f_{high} \quad (5-1)$$

$f_{high}$  is the resonant frequency characterised in the high power measurement. So the positive value of  $\Delta f$  indicates that the resonant frequency shifts down.

A representative time profile of the frequency shift measured on the Ti tool at 0.07A is shown in Figure 5-6 (a). In the figure, the frequency shift  $\Delta f$  starts from 270 Hz and then increases gradually until a constant value of 680 Hz is achieved. Denote  $\Delta f$  at the beginning as  $\Delta f_0$  and at the steady state as  $\Delta f_{max}$ . The comparison of  $\Delta f_0$  and  $\Delta f_{max}$  at different current amplitudes is shown in (b).

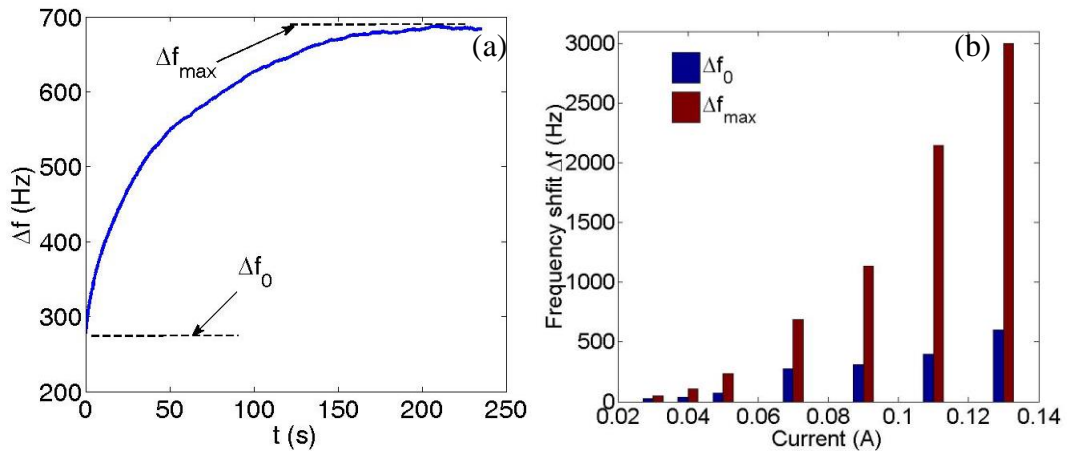


Figure 5-6 Resonant frequency shift of the planar tool (a) time profile at 0.07A (b) resonant frequency shift measured at the beginning and the steady state of the driving processes

During the driving process, there are mainly two factors contributed to the shift of the resonant frequency: vibration velocity/strain and temperature rise of the piezoelectric material [80, 108]. At the beginning of driving, as soon as the electric field is established in the PMN-PT, high vibration velocity is attained, but the temperature rise of the PMN-PT at this stage can be neglected since it takes time for the PMN-PT to heat up, as shown in Figure 5-7. So  $\Delta f_0$  is mainly caused by the high vibration velocity of the PMN-PT and increases with current amplitude.

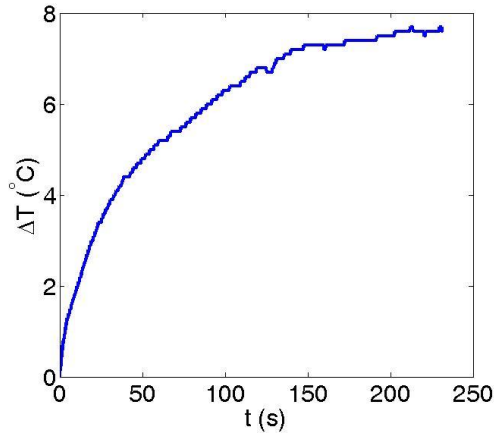


Figure 5-7 Profile of  $\Delta T$  in the ‘bottom epoxy’ when the planar tool is driven at 0.07A

After the initial increase at the beginning,  $\Delta f$  increases gradually with time until the steady state is achieved. The differences between  $\Delta f_0$  and  $\Delta f_{max}$  are believed to be the contribution of temperature rise because the time profile of  $\Delta f$  follows the same trend as that of  $\Delta T$ , as shown in Figure 5-8 (a). Both values increase rapidly at the beginning, and then gradually plateau under steady state conditions. Because it takes time for the planar tool to set up a thermal gradient and achieve thermal equilibrium, the resonant frequency requires a long time to reach a stable value.

The time profiles of  $\Delta f$  and  $\Delta T$  can be modelled as Equation (5-1) and (5-2) respectively.

$$\Delta f(t) = (\Delta f_{max} - \Delta f_0) \left( 1 - e^{-\frac{t}{\tau_f}} \right) + \Delta f_0 \quad (5-1)$$

$$\Delta T(t) = \Delta T_{max} (1 - e^{-\frac{t}{\tau_T}}) \quad (5-2)$$

By applying the least-square fitting technology, the time constants  $\tau_f$  and  $\tau_T$  can be calculated, as shown in Figure 5-8 (b).

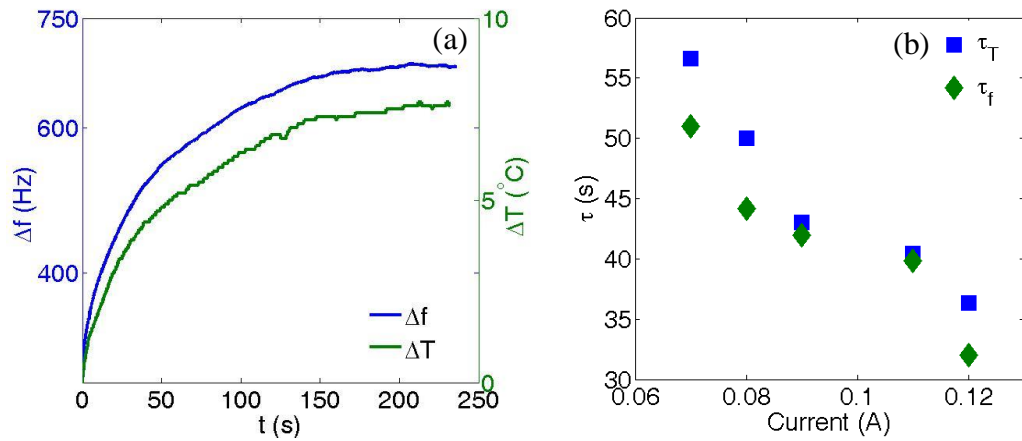


Figure 5-8 (a) Time profiles of  $\Delta T$  and  $\Delta f$  measured at 0.07A (b) Estimated time constants  $\tau_f$  and  $\tau_T$

$\tau_f$  and  $\tau_T$  are close to each other at different current amplitudes with a maximum difference of 6s at 0.05A. This suggests the strong dependence of  $\Delta f$  on  $\Delta T$  during the driving process. In addition, both  $\tau_f$  and  $\tau_T$  are dependent on the current amplitude. They decrease with increasing current amplitude. As time constant is the time that a system required to achieve 63.2% of the steady state response, the reduction of time constant with current amplitude suggests that the planar tool takes a shorter time to achieve the steady state at higher current amplitudes, which is caused by the increase in heat transfer coefficient of the planar tool. Heat convection is believed to increase at high vibration levels, resulted in an increase in heat transfer coefficient [89, 153]. The increase in heat transfer coefficient with vibration velocity makes the  $\tau_T$  decrease with the current amplitude.

The increase in mechanical loss was evidenced by the increase in electric impedance  $|Z|$ , as shown in Figure 5-9, where the values of  $|Z|$  at the beginning and the steady state of the driving process are illustrated.  $|Z|$  increases linearly with current amplitude. At the beginning of driving, the temperature increase can be neglected. Thus,  $|Z|$  measured at the beginning of driving are mainly caused by vibration velocity, which is proportional to the current amplitude, as shown in Figure 5-10. The increase in  $|Z|$  reflects the increase in the mechanical loss of the planar tool. The increase in mechanical loss is attributed to the increasing dynamic stress undergoing in the piezoelectric material under high vibration velocity [83]. In the steady state, a slight increase in mechanical



losses is observed because of the long duration of the driving and the temperature increase. However, the dependence of the mechanical losses on temperature is insignificant.

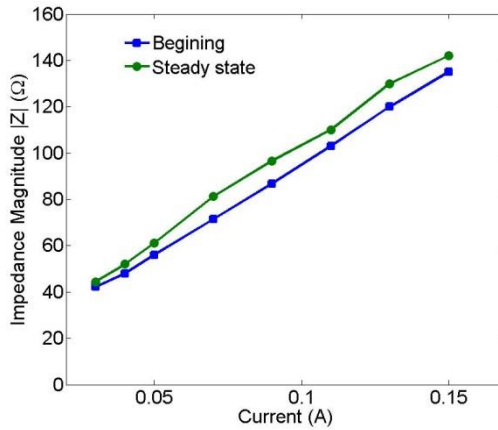


Figure 5-9 Electric impedance of the planar tool at different current amplitudes

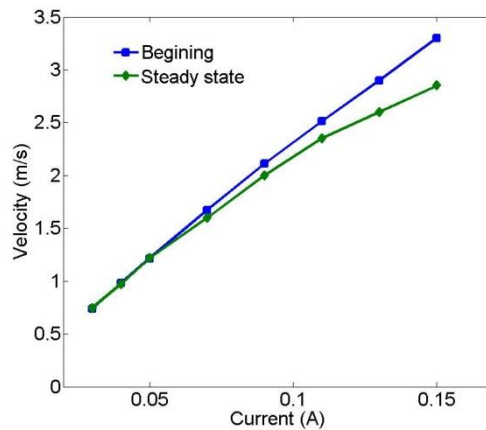


Figure 5-10 Vibration velocity of the planar tool at different current amplitudes

Despite the increasing electric impedance, the vibration velocity is linearly proportional to the current levels at the beginning but exhibits some degradation at high current levels in the steady state. A drop of 21% is observed at 0.15 A. This is attributed to changes in material properties and degradation caused by sustained high temperatures of the planar tool because of long duration of driving.

(2) Loaded characterisation

The electrical impedance  $|Z|$  and resonant frequency  $f_s$  of the planar tool in loaded condition measured at the beginning of driving are presented in Figure 5-11.  $|Z|$  and  $f_s$  in unloaded condition are served as control results.  $|Z|$  increases linearly with current levels at depths of 1 and 5 mm, with decreasing slopes. However, at depths of 7 and 10 mm,  $|Z|$  becomes inversely proportional to the current amplitude. Moreover, higher  $|Z|$  is always observed at larger depth at the same current amplitude. The resonant frequency in soft tissue loaded condition decreases with current amplitude. However, the resonant frequencies under loaded condition are higher than the resonant frequency under unloaded condition, when the same current amplitude was applied. This means that the poultry breast tissue increased the resonant frequency of the planar tool.

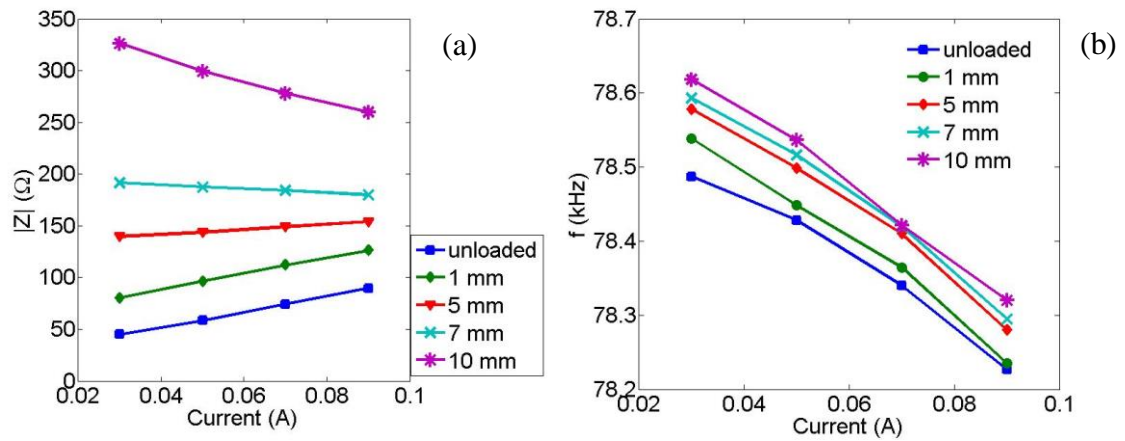


Figure 5-11 Electrical impedance and resonant frequency of the planar tool in soft tissue loaded condition (a) electrical impedance (b) resonant frequency

To analyse the results, the BVD model of the loaded planar tool was used, as presented in Figure 5-12.  $C_0$  is the capacitance of the planar tool, which is tuned out by a shunted inductance  $L_0$ .  $L_1$ ,  $C_1$  and  $R_1$  are the inductor, capacitor and resistor, which represent the mechanical compliance, effective mass and internal mechanical resistance of the planar tool, respectively.  $X_r$  and  $R_r$  are the radiation reactance and radiation resistance caused by external loads, respectively.

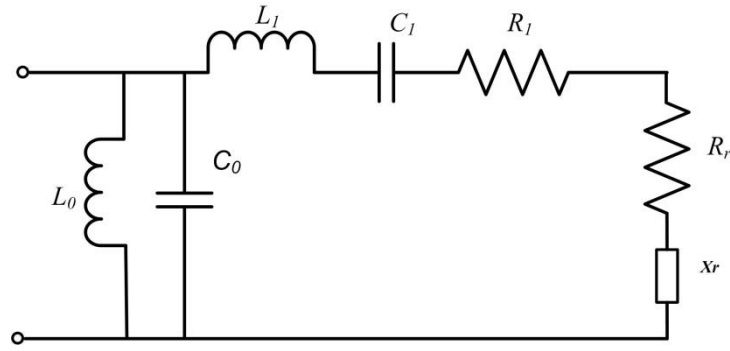


Figure 5-12 BVD model for the loaded ultrasonic planar tool operating near resonance

The resonant frequency  $f_s$  of the planar tool thus should satisfy the following equation

$$2\pi f_s L_1 - \frac{1}{2\pi f_s C_1} + X_r = 0 \quad (5-3)$$

The electric impedance at the resonant frequency is

$$|Z| = R_1 + R_r \quad (5-4)$$

When the planar tool is unloaded,  $X_r$  and  $R_r$  are close to zero because of the mismatched acoustic impedance between the air and the blade.  $|Z|$  measured in the unloaded condition is the internal loss  $R_1$ . Assuming that  $R_1$  is not affected by the change in resonant frequency and the external loads, the radiation resistance,  $R_r$  of the planar tool at different insertion depth and current amplitudes can be calculated according to Equation (5-4). Results are shown in Figure 5-13.

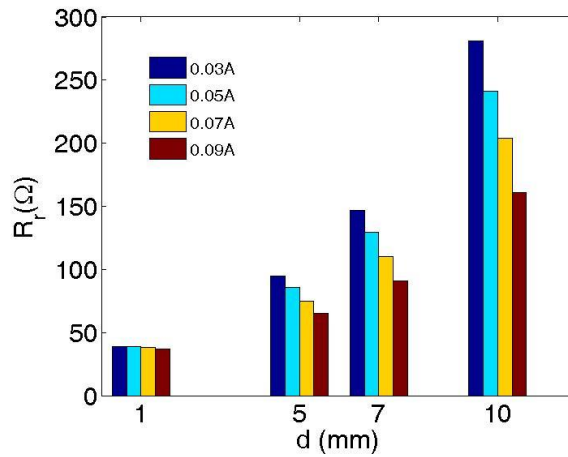


Figure 5-13 Radiation resistance of the planar tool at different insertion depths and different current amplitudes

$R_r$  always increases with the insertion depth. This is because with larger depths, a larger area of the planar tool is coupled into the tissue, thus allowing more energy to be transmitted into the tissue. However,  $R_r$  decreases as the current amplitude increases, i.e. vibration velocity increases, at each depth. The decrease of  $R_r$  with vibration velocity is attributed to the reduced contact and interaction force between the tissue and the blade at high vibration velocities. At small depth, even though  $R_r$  decreases with increasing current amplitude, the magnitude of the decrease is small, compared with the increase in  $R_l$ . As a result, the electrical impedance  $|Z|$  still increases with increasing current amplitude. However, at large depths, the decrease in  $R_r$  outweighs the increase of  $R_l$ , so  $|Z|$  decreases with the increasing current amplitude.

When the planar tool is inserted into soft tissue, the soft tissue manifests itself as a mass to the planar tool and also changes its stiffness, leading to variation in  $X_r$  and consequently a shift in  $f_s$ . A negative value of  $X_r$  shifts the resonant frequency upward while a positive value of  $X_r$  shift the resonant frequency downwards. In this case, the soft tissue results in an increase in the resonant frequency of the planar tool. However, the study conducted by Ying [9] observed that soft tissue decreased while hard tissue increased resonant frequency of an ultrasonic scalpel based on sandwich transducer. This difference in change of  $f_s$  is caused by the difference in  $X_r$  due to the transducer configuration and loading condition.

The planar tool in soft tissue loaded condition showed much higher electrical impedance magnitude than the unloaded condition. Therefore, to maintain the same current amplitude, the planar tool in soft tissue loaded condition required higher voltage and electrical power. However, this increase in electrical voltage and electric power did not increase the self-heating effect, as shown in Figure 5-14.

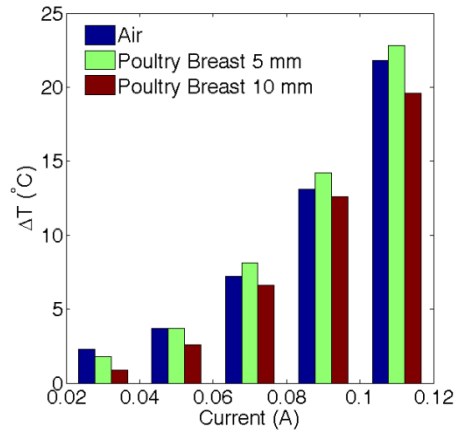


Figure 5-14 Temperature rise of the planar tool in soft tissue loaded condition

The temperature increase of the planar tool in soft tissue load condition is approximately the same as the unloaded condition. This is because the main heating source of the planar tool is the mechanical loss of the epoxy, which is proportional to the vibration velocity of the planar tool.

## 5.2 Soft Tissue Penetrating Test

Following the high power characterisation, the Ti planar tool was used to penetrate soft tissue. During the penetrating tests, the resonant frequency and the impedance of the Ti tool was affected by the power level and external loads at the same time. The ability of the adaptive driving system to improve the performance of the planar tool is investigated.

### 5.2.1 Experimental Arrangements

In the penetrating test, the material testing machine in Figure 5-2 (a) was used. A load cell was installed on the moving crosshead and the planar tool was fixed on the sensitive

area of the load cell. A diagram is shown in Figure 5-15. Fresh poultry breast tissue obtained fresh from a local butcher was used as a specimen and placed on the specimen holder. The ultrasonic planar tool was inserted into 20 mm of the specimen. During the insertion procedure, it was driven by the adaptive driving system with the resonance tracking and vibration stabilisation function.

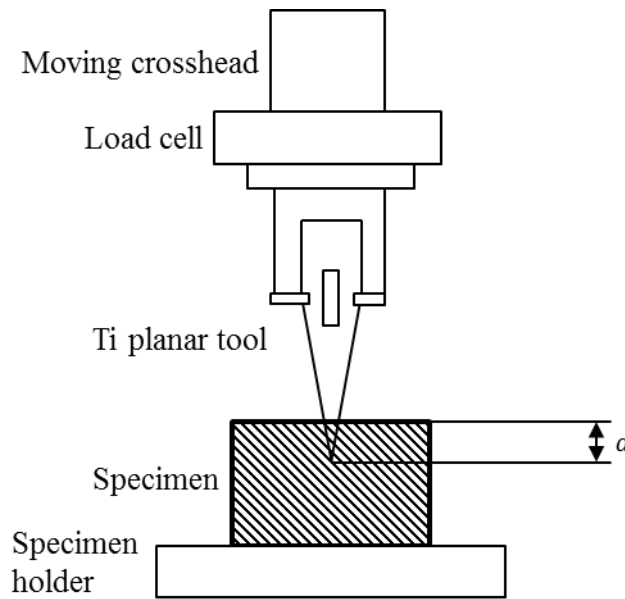


Figure 5-15 A diagram of the soft tissue penetrating experiment

Prior to cutting, the vertical cutting velocity was set to be 25, 50, 100 or 200 mm min<sup>-1</sup> by adjusting the crosshead speed. For each cutting velocity, experiments without ultrasonic excitation ( $I=0A$ ,  $v=0$  mm/s) were also carried out and served as controls. During the cutting procedures with ultrasonic excitation, the current value through the planar tool was kept at 0.02, 0.05 or 0.1 A. The resonant frequency, electrical impedance, current and voltage were recorded by the adaptive driving system. The cutting force and depth were monitored by the material testing machine. All the experiments were performed at room temperature in five replicates.

The overall work ( $W$ ) and maximum penetrating force ( $F_{max}$ ) required to penetrate the planar tool into the specimen by 20 mm were studied. The overall cutting work was calculated by integrating the actual cutting force ( $F$ ) over the cutting depth ( $d$ ).  $W$  and  $F_{max}$  obtained in experiments with ultrasonic excitation were compared with the results

in the control tests at the same vertical velocity without ultrasonic excitation. The reductions of  $W$  and  $F_{max}$  in percentage specify the relative impact of ultrasonic assistance on the cutting process and higher reduction is desirable for an efficient application of ultrasonic cutting [156, 157].

### 5.2.3 Experimental Results

Figure 5-16 depicts the typical cutting force versus cutting depth at different current amplitudes and vibration velocities. The vertical cutting velocity was  $25 \text{ mm min}^{-1}$ . The control test result without ultrasonic excitation in each graph was obtained in an adjacent area of the cutting test with ultrasonic excitation to avoid significant variation in force profiles due to the inhomogeneous property of tissue.

As expected, the force required to penetrate through the poultry breast tissue was reduced by the aid of ultrasonic excitation, the averaged force and work reduction are summarized in Table 5-1. Both the work reduction and the force reduction increases with the current amplitude, which means the impact of ultrasonic excitation increases with the vibration velocity of the planar tool. At current amplitude of 0.1 A, i.e. vibration velocity of 2.5 m/s (Figure (c)), the maximum force required with ultrasonic excitation is 4.14 N whereas the overall work is 0.04 J, compared with  $F_{max}$  of 9.59 N and  $W$  of 0.09 J in the control test. The force and work reduction averaged in 5 tests at 0.1A are 47.1% and 53.5%, respectively.

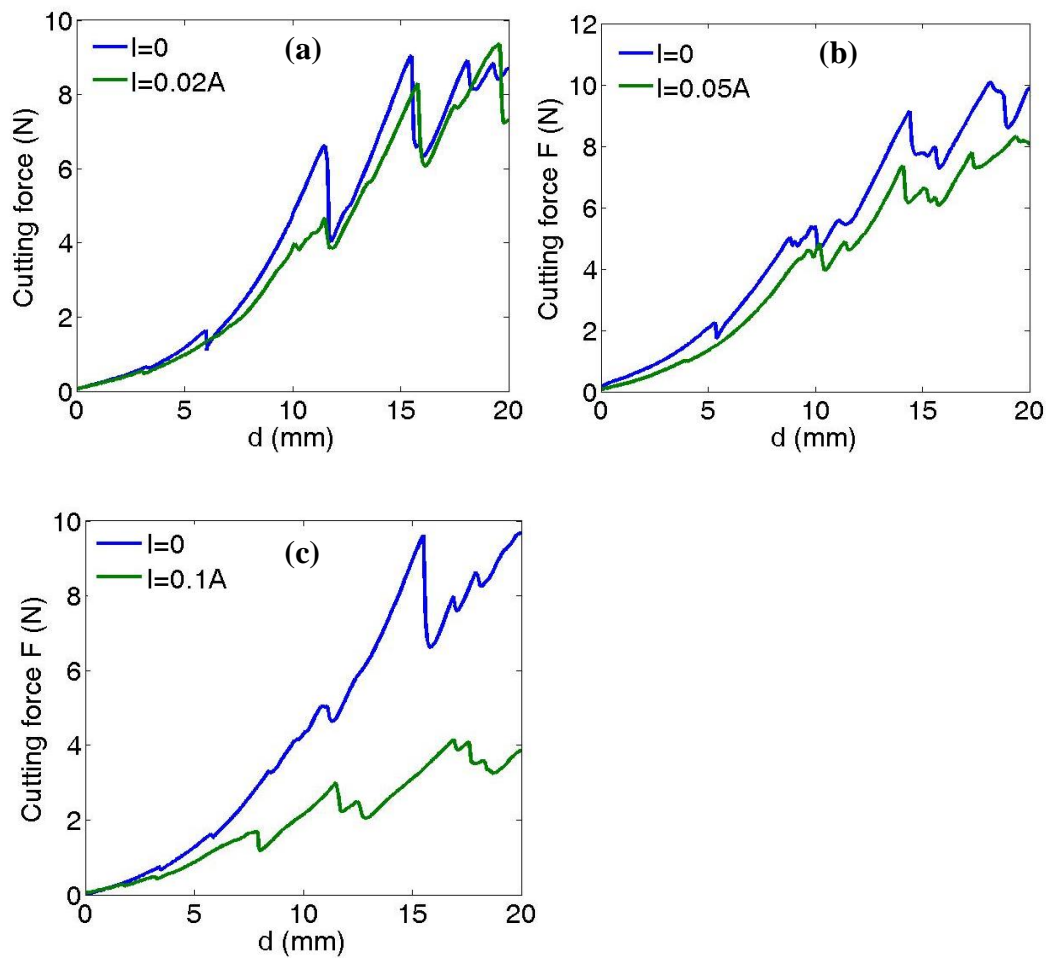


Figure 5-16 Cutting force versus cutting depth at different power level and vibration velocity (a) 0.02A & 0.5 m/s (b) 0.05A & 1.25 m/s (c) 0.1 A & 2.500 m/s

Table 5-1 Averaged force and work reduction at different current amplitudes

Current (A)	$F_{max}$ reduction	$W$ reduction
0.02	9.2%	9.3%
0.05	17.6%	18.7%
0.1	47.1%	53.5%

Figure 5-17 shows the parameters of the planar tool versus cutting depth during a penetrating procedure, monitored by the adaptive driving system. The current amplitude was 0.1A. The force profile for this penetrating test was presented previously in Figure 5-16 (c).



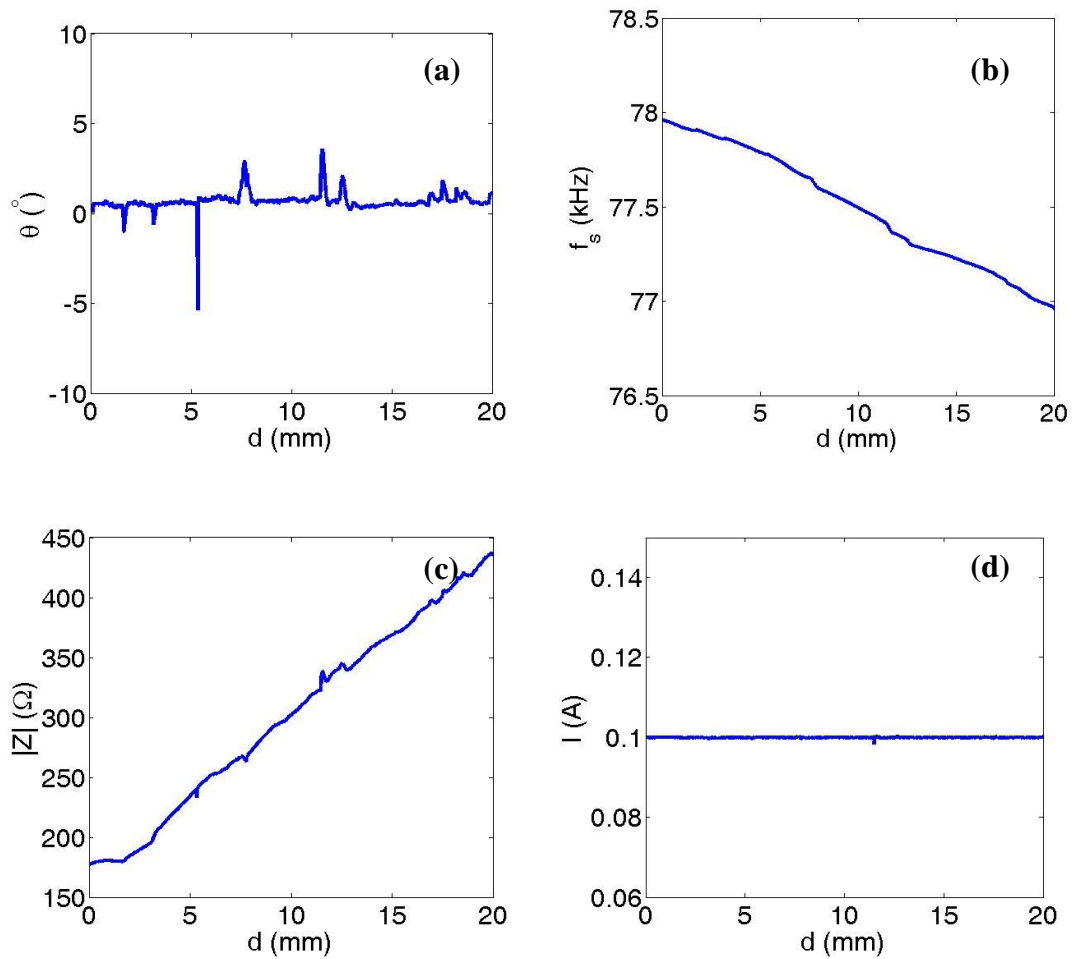


Figure 5-17 Parameters of the planar tool monitored during an penetrating test at 0.1A  
(a) impedance phase (b) resonant frequency (c) impedance magnitude (d) current

The resonance of the planar tool was maintained during the cutting procedure, indicated by the zero phase value, as shown in Figure 5-17 (a). The fluctuations observed in phase are caused by the puncturing of different tissue layers, which can be identified from the force profile (Figure 5-16 (a), blue curve) by the sudden drops of cutting force. The sudden change in cutting force and entering into a new layer of tissue changes the loading condition of the planar tool violently and consequently causes the abrupt shift in resonant frequency. As there is an unavoidable delay between frequency shift and frequency tracking, these fluctuations cannot be eliminated. However, the fluctuations are within  $5^\circ$ , and the resonance is regained immediately.

To keep the impedance phase at zero value, the adaptive driving system adjusted the excitation frequency continuously, as shown in Figure 5-17 (b). The frequency

decreases by about 1 kHz when the cutting depth changes from 0 to 20 mm. Although the electric impedance of the planar tool increases with the cutting depth, as shown in (c), the current through the planar tool is kept constant precisely.

Thus, although the working characteristics of the planar tool changed due the combined effect of power levels and external loads, the adaptive driving system tracked the resonant frequency correctly and stabilised the current amplitude successfully. Because the vibration velocity is proportional to current amplitude, as shown in Figure 5-10 in Section 5.1.2, the vibration velocity of the planar tool was stabilised.

Figure 5-18 shows the cutting force profiles with and without using the adaptive driving system. The cutting force profile without ultrasonic excitation is used as a control variable. The three force profiles were obtained in an adjacent region on the poultry breast tissue. For the ‘without tracking’, the planar tool was driven at 20 V 78.5 kHz; for the ‘with tracking’, the planar tool was driven at 20 V, and the resonant frequency was tracked by the adaptive driving system.

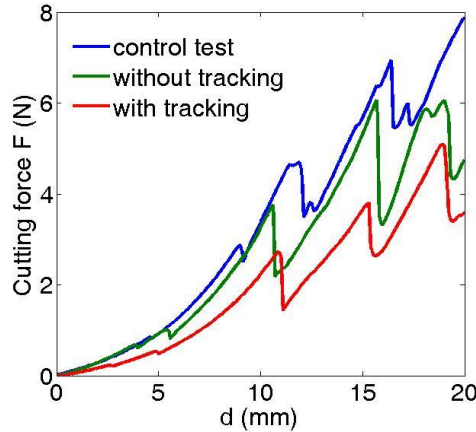


Figure 5-18 Cutting force versus cutting depth with and without using adaptive driving system

When the cutting was assisted by the ultrasonic excitation but without the adaptive driving system, the  $F_{max}$  required to penetrate through the poultry breast tissue was 6 N. This leads to a force reduction of 23%, compared with the value of 7.8 N observed in the control test. The  $W$  required is also reduced by 15%. In contrast, when the planar

tool is driven by the adaptive driving system, the maximum force and overall work are reduced by 35% and 42% compared with the control test, respectively.

The higher efficiency with the adaptive driving system than without is because the adaptive driving system tracked the resonance of the planar tool during the test. Figure 5-19 shows the impedance phase of the planar tool with and without using the adaptive driving system during the tests. In the figure, the planar tool starts to cut the tissue from  $d=0$ . When the planar tool is controlled by the adaptive driving system, the phase is kept at zero values with limited distributions, suggesting that the planar tool is driven at the resonant frequency. When the adaptive driving system is driven at 78.5 kHz without using the adaptive driving system, the phase is close to zero at  $d= -2$  mm. However, the phase increases quickly and reaches  $58^\circ$  when the cutting process starts ( $d=0$ ). This phase rise to positive values is because the resonant frequency shifts downward, resulting from the high driving power. The phase decreases after the planar tool cut into the tissue because the soft tissue increases the resonant frequency, as discussed in Section 5.1.2. However, during the whole cutting procedure, the phase is always above  $20^\circ$ , suggesting that the planar tool is not driven at the resonant frequency.

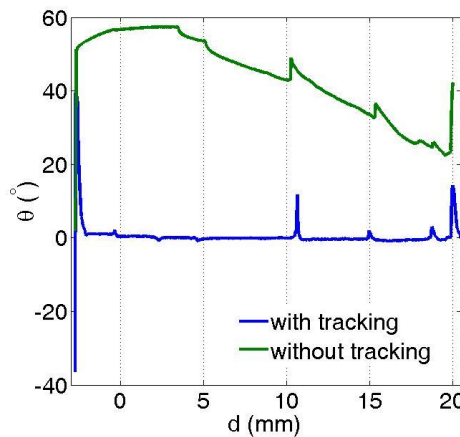


Figure 5-19 impedance phase of the planar tool with and without using the adaptive driving system during the soft tissue penetrating test

It was also found the vertical cutting velocity affected cutting efficiency of the planar tool. Figure 5-20 shows of both  $F_{max}$  and  $W$  at different vertical cutting velocities while using ultrasonic excitation. The results were obtained at current amplitude of 0.1 A. The

force and work reduction diminished with increasing vertical cutting velocity. At 25 mm/min, the reduction of  $F_{max}$  and  $W$  required to penetrate through tissue are 47.1% and 53.5%, respectively. These are reduced to 24% and 20%, respectively at 200 mm/min. These results are consistent with finds from other studies [156-158].

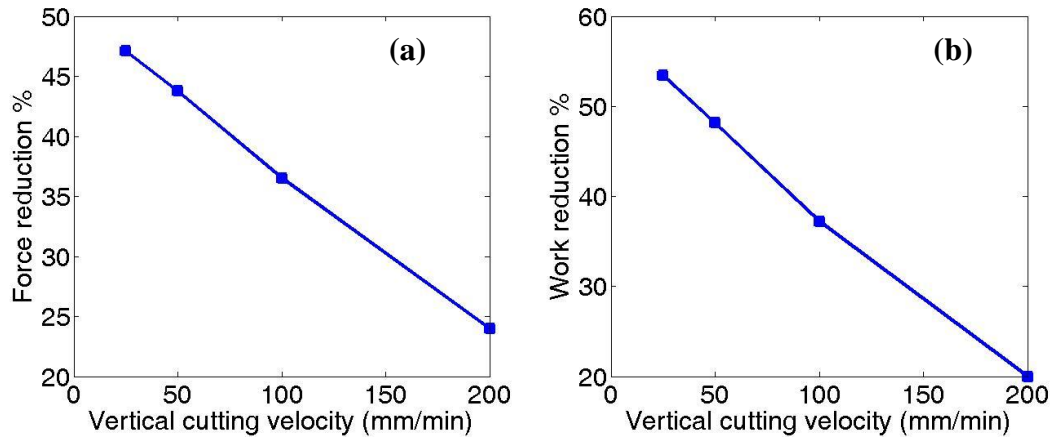


Figure 5-20 Effects of vertical cutting velocity on the cutting force and work required (a) force reduction in percentage (b) work reduction in percentage

### 5.3 Discussion and conclusion

This chapter first investigated the performance variation of an unloaded ultrasonic planar tool under high power levels. When the unloaded planar tool was driven continuously, significant self-heating was observed, particularly in and around the epoxy because of the high mechanical loss in epoxy. The serious self-heating in the epoxy prevented the planar tool from working at current amplitude higher than 0.15A because the maximum temperature in the epoxy was close to the phase transition temperature of PMN-PT Piezocrystal.

The mechanical loss of the planar tool increased with the current amplitude and temperature increase, reflected by the increase in electric impedance and drop in  $Q_M$ . A sudden frequency shift occurred as soon as the power was applied to the planar tool. After that, the resonant frequency gradually shifted to lower values with time and finally reached a plateau. This process was dominated by the temperature increase of the PMN-PT piezocrystal.

Under soft tissue loaded condition, the tissue imposed radiation impedance to the planar tool, which increased with insertion depth. The radiation resistance decreased with the current amplitude and vibration velocity because of the reduced contact between the blade and tissue. Even though the planar tool in loaded condition exhibited much higher electric impedance than that in unloaded condition, the difference in temperature increase was small at the same current amplitude.

Despite the variation of the planar tool's working characteristics, the adaptive driving system tracked the resonant frequency correctly and stabilised the current amplitude successfully during the soft tissue penetrating tests. Consequently, the cutting efficiency of the planar tool, measured by the  $F_{max}$  and  $W$  reductions, was improved, compared with tests without using the adaptive driving system.

More significant force and work reduction were observed at higher current amplitudes and vibration velocities. The vertical cutting velocity also affected the cutting efficiency. Higher force and work reduction were expected at lower vertical cutting velocity. The reduction in force and work is believed to be associated with the diminishing separation force and friction forces with the use of ultrasonic vibration during cutting [156].

The overall conclusion that can be drawn from this chapter is that the adaptive driving system can track the resonant frequency of the planar tool and stabilise the current amplitude. As a result, optimal performance of the planar tool can be achieved. The planar tool configuration together with PMN-PT piezocrystals shows the ability to work at high power levels and reduce the penetration force during soft tissue penetration. However, higher performance of this design concept is limited by the intensive mechanical loss in the joint between the piezoelectric material and blade, and the relatively low Curie point of PMN-PT.

## 6 CASE STUDY-NEEDLE ACTUATING DEVICE

Clear visualisation of needle is important in ultrasound imaging guided percutaneous needle procedures such as tissue biopsy and regional anaesthesia. However, the needle is poorly visualised under ultrasound imaging due to its smooth surface. To improve the needle visibility, this chapter presents a needle actuating device, which uses a piezoelectric transducer to actuate a standard medical needle to vibrate longitudinally. This work follows the methodology developed in Chapter 3 in designing ultrasonic devices and uses the adaptive driving system developed in Chapter 4 to control and optimise the performance of the needle actuating device. The device is designed based on a sandwich piezoelectric transducer, which actuates standard medical needles to oscillate longitudinally to enhance the needle visibility in ultrasound imaging guided percutaneous procedures.

The unmet medical need and technical background of ultrasound guided percutaneous procedures are reported in Section 6.1. The design, FEA, fabrication and characterisation of the device are detailed in sections 6.2- 6.5 respectively. The *ex vivo* needle insertion experiment is presented in Section 6.6. Discussion and conclusion are provided in Section 6.7.

### 6.1 Percutaneous Needle Procedures

Percutaneous needle procedures are common clinical operations nowadays for diagnosis and local therapies. The most widespread applications are regional anaesthesia [159] and tissue biopsy [160]. A survey of the American Society of Regional Anesthesia and Pain Medicine shows that approximately 50% of surgeons perform more than 100 spinal and epidural nerve blocks each year [161]. Tissue biopsy under regional anaesthesia is an important method to diagnose cancers. In USA, about 1 million needle biopsies are performed each year [160].

In these procedures, needles are inserted deep into soft tissue to reach the targets. The effectiveness of treatments and the success or precision of diagnosis is highly dependent on the accuracy of percutaneous needle insertion [162]. To place the needle within the

desired region, it is crucial to visualise the needle shaft and especially the needle tip for an effective intervention [163]. Ultrasound imaging has been historically used as guidance for such procedures to visualise both anatomical structures of interest as well as the advancing needle. While the identification of relevant anatomical structures can become relatively easy with practice and development of a trained eye, keeping the needle tip in view as the needle is advanced toward the target is much more difficult. Without accurate identification of the position of the needle, damage to the collateral structure or inadequate biopsy may occur even if the target structure has been visualised correctly. Percutaneous needle insertion without adequate needle visibility may result in serious subsequent complications and failed procedures. This problem cannot be totally solved by training because even experienced practitioners can face difficulty in keeping the needle visualised [164]. In ultrasound guided peripheral nerve block, persistent failure to visualize the needle tip was even reported by experienced surgeon, who had performed more than 100 such operations [165]. According to Liberman [166], 9-18% of biopsies performed by experienced operators are inadequate, through poor visualisation.

Poor needle visibility under ultrasound imaging is mainly because of its mismatched acoustic impedance and smooth surface [167]. The acoustic impedance of tissue and needle is significantly different. Therefore, most of the ultrasound waves are reflected. Because of the smooth surface of the needle, specular reflections usually occur. In such a case, the ultrasound waves are reflected away, instead of back to the transducer, resulting in a loss of information and inaccurate representation the needle in the ultrasound imaging. This problem is further exacerbated when the needle is inserted in steep angles [168]. Other factors that also contribute to the poor needle visibility including difficulty in alignment needle and beam, gauge of needles, acoustic background, etc. [167, 168].

Percutaneous procedures without adequate needle visualisation may results in failed or inaccurate diagnosis and serious complications such as vascular, neural or visceral injury [169, 170]. Because of these risks, a number of techniques have been attempted to address the problem of poor needle visibility in ultrasound imaging. These include advanced imaging technologies such as beam steering, 3D ultrasound to improve

imaging quality [171]; echogenic needles to increase the ultrasound echoes reflected back towards the transducer [172]; ColorMark [173, 174] clipping onto the needle and inducing minute vibration at the needle tip etc. However, these technologies have significant limitations; none can be recommended fully to increase needle visibility, especially at deep target locations and steep insertion angles.

This Chapter proposes a needle actuating device, which actuates a standard needle to vibrate in the longitudinal mode to increase its visibility under colour Doppler imaging.

### 6.2 Needle Actuating Device Design

A schematic CAD model of the needle actuating device designed is shown in Figure 6-1. This device was proposed and prototyped by M. Sadiq [152]. It comprises of a standard needle, a piezoelectric transducer and an outer collar. The needle is clamped by the transducer through assembling the outer collar to the front mass. When the piezoelectric transducer is excited, it actuates the needle to oscillate longitudinally.

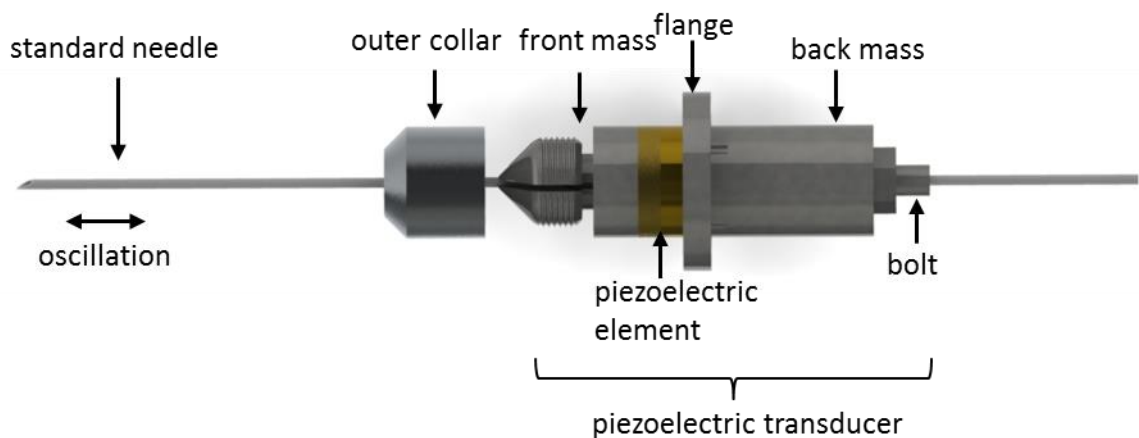


Figure 6-1 Schematic CAD model of the needle actuating device

In the piezoelectric transducer, the piezoelectric element is sandwiched between the front mass and the back mass by a bolt. The front mass is specially designed with a collet to clamp the needle. The collet forms a collar around the needle and exerts a strong clamping force when it is tightened by the outer collar through threads. The piezoelectric element consists of two PZ 26 rings (outer diameter 10 mm; inner



diameter 5 mm; thickness 2 mm) (Meggit-Ferroperm, Kvistgaard, Denmark). They are polarized in the opposite direction and electrically connected in parallel. A flange is created on the back mass for device packaging. The bolt applies a pre-stress force to the piezoelectric element to prevent dynamic tensile forces in the piezoelectric material [175]. A hollow is created on the bolt and the front mass so that the needle can pass through.

### 6.3 Finite Element Analysis of the Needle Actuating Device

Based on the schematic design of the needle actuating devices, dimensions of the piezoelectric transducer were predicted using Abaqus. The lengths of back mass and the front mass were controlled to place the displacement node at the position of the flange. The modal behaviour of standard needles and needle actuating devices were studied following the successful design of piezoelectric transducers.

#### 6.3.1 Piezoelectric Transducers

The transducer was designed to be resonant in longitudinal mode with the flange located at its nodal plane. To determine the dimensions of the front and back masses, frequency analysis was conducted followed the procedures described in Chapter 3 of this thesis.

Considering the geometrical complexity of the transducer, 3D models of the transducers were created in Solidworks. The 3D models were then saved as ASCIS SAT files and imported into Abaqus/CAE as the physical models. In a sandwich piezoelectric transducer, metal electrodes are used to supply the external exciting electrical signal. As the thickness of the metal electrodes, 0.1 mm of brass shim in this case, was much less than the thickness of the PZ 26 ring, the effect of the electrode was ignored. All the threads were not included. In practice, the prestress is necessary to avoid depolarization and cracking of the piezoelectric material, however, as pre-stress has only small effect in the theoretical analysis [176], it was ignored in this FE analysis.

The contact areas between different components were constrained by 'Tie constraint'. Opposite polling directions were specified to the two PZ 26 rings, and all the electrodes were specified with zero potential. For the front and back masses, which were made of aluminium and stainless steel respectively, the material properties required to

implement frequency analysis are Young's modulus, Poisson's ratio and density, as listed in Table 6-1. The material properties of PZ 26 are listed in Table 6-2.

Table 6-1 Mechanical properties of aluminium and stainless steel

Material	Young's Modulus (GPa)	Density (kg/m <sup>3</sup> )	Poisson's Ratio
Aluminium	71.7	2800	0.33
stainless steel	210	7850	0.3

Table 6-2 Material properties of PZ 26

Elastic constants (GPa)	Stress constants (C/m <sup>2</sup> )	Permittivity (F/m)	Density (kg/m <sup>3</sup> )
D <sub>1111</sub> = 168	e <sub>311</sub> = -2.8	K <sub>11</sub> = 7.33E-9	7700
D <sub>1122</sub> = 110	e <sub>322</sub> = -2.8	K <sub>22</sub> = 7.33E-9	
D <sub>1133</sub> = 99.9	e <sub>333</sub> = 14.7	K <sub>33</sub> = 6.19E-9	
D <sub>2222</sub> = 168	e <sub>212</sub> = 9.86		
D <sub>2233</sub> = 99.9	e <sub>113</sub> = 9.86		
D <sub>3333</sub> = 123			
D <sub>1212</sub> = 28.8			
D <sub>1313</sub> = 30.1			
D <sub>2323</sub> = 30.1			

Frequency was first conducted on the piezoelectric transducer without assembling the outer collar. The length of the back mass was carefully adjusted so that the nodal plane was around the flange. The finalized lengths of back mass and front mass were 17 and 13 mm, respectively. This led to a total length of 34 mm for the whole transducer. The longitudinal vibration mode of the transducer was found at 71.2 kHz as shown in Figure 6-2.

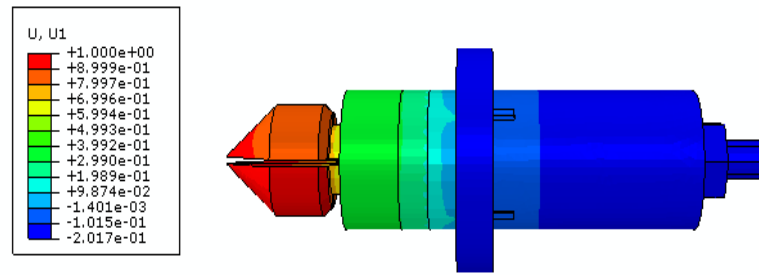


Figure 6-2 Longitudinal vibration mode of the transducer

Then the outer collet was assembled to the piezoelectric transducer and frequency analysis was conducted. After assembling the outer collar to the transducer, the transducer still holds longitudinal resonant mode, as shown in Figure 6-3. However, the resonant frequency was found at 52.1 kHz. Compared with the resonant frequency before assembling the outer collar, a shift of 19.1 kHz was observed.

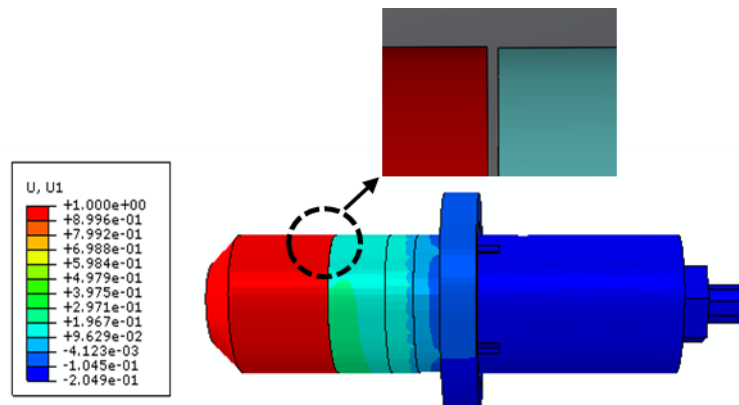


Figure 6-3 Longitudinal vibration mode of the transducer with the outer collet assembled

The resonant frequency variation results from two causes: the mass added by the outer collar and the limited contact between the outer collar and the front mass. The masses added by the outer collars lowered the resonant frequencies of transducers, since  $f = 2\pi\sqrt{k/m}$ , where  $k$  is the stiffness and  $m$  is the mass. This resonant frequency was further reduced by the limited contact between the front mass and the outer collet because of the small space between them, as shown in Figure 6-3.

### 6.3.2 Standard Needles

Commercial needles used for percutaneous procedures vary in length and diameter, depending on the specific operation. The piezoelectric transducer in this thesis was designed for needles from 20 to 22-gauge. Figure 6-4 shows the 3D model of a standard regional anaesthesia needle of 21-gauge and 100 mm in length (G21×100 mm), featuring in bevel of 30°. The model was created in Solidworks. The needle hub and the cartridge end were not included in the FEA. In this thesis, the term ‘tip’ refers to the sharp tip of the needle whereas ‘end’ refers to the distal end of the needle, as illustrated in Figure 6-4.

The 3D model of the needle created in Solidworks was imported into Abaqus for FE analysis. The material for the regional anaesthesia needles is surgical stainless steel, with mechanical properties listed in Table 6-3 and specified in Abaqus.



Figure 6-4 3D model of a standard needle

Table 6-3 Mechanical properties of surgical stainless steel

Young's Modulus (GPa)	Density (kg/m <sup>3</sup> )	Poisson's Ratio
200	7900	0.29

The natural frequencies of the G21×100 mm needle and their corresponding vibration modes were calculated by using frequency analysis. Typical vibration modes of the needle predicted by the FEA are shown in Figure 6-5. They are the first flexural mode at 10.4 kHz, the first torsional mode at 15.9 kHz and the first longitudinal mode at 25.2

kHz. The needle actuating device was designed to work at the longitudinal mode. The excitation of flexural and torsional mode should be avoided.

Higher orders of these vibration modes exist at higher frequencies. The second longitudinal mode of the needle is at 50.7 kHz, which is about twice of the first longitudinal frequency. The longitudinal displacement profiles in the first and second longitudinal modes of the G21×100 mm needle are shown in Figure 6-6.

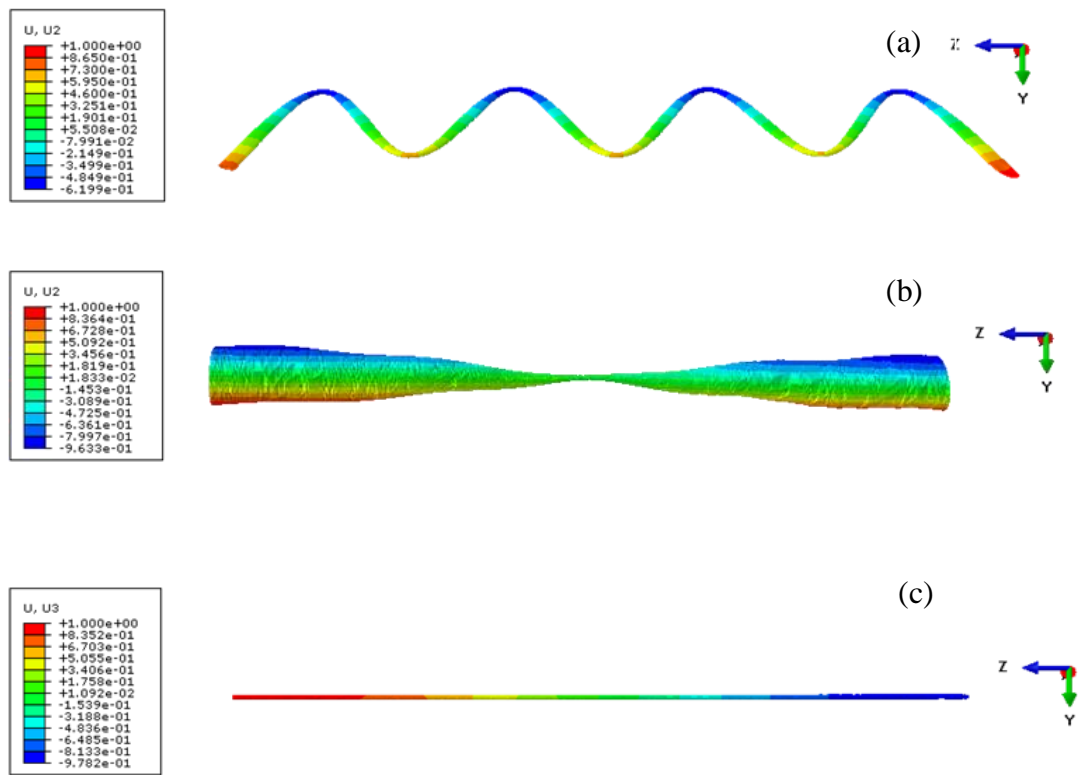


Figure 6-5 Typical vibration modes of a needle (a) flexural mode at 10.4 kHz (b) torsional mode at 15.9 kHz (c) longitudinal mode at 25.2 kHz

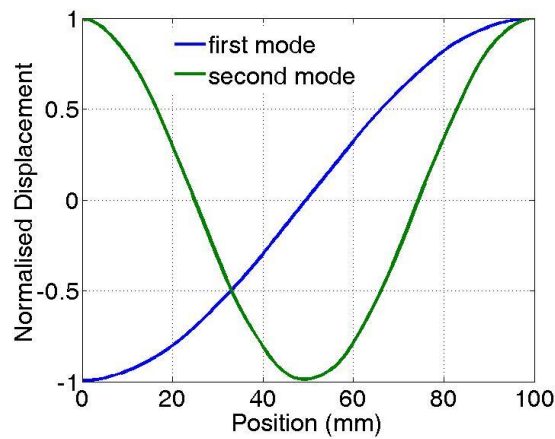


Figure 6-6 Longitudinal displacement along the G21×100 mm needle in the first and second longitudinal vibration modes

The longitudinal resonant frequencies of the 21-gauge needle varying in length between 40 and 120 mm were simulated and compared, as shown in Figure 6-7. The longitudinal resonant frequencies decrease as the needle length increases. The second resonant frequency at each length is always twice of the first one, as expected. It was also observed that the diameter and bevel tip of the needle made little difference to its resonant frequency and mode shape. The resonant frequency was mainly determined by the total needle length.

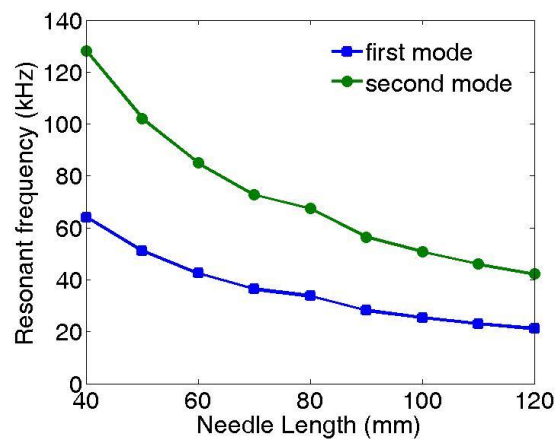


Figure 6-7 Longitudinal resonant frequencies of standard needle of different lengths

### 6.3.3 Needle Actuating Device

The needle actuating devices were obtained by assembling the piezoelectric transducer and standard needles together. The contact areas between the front mass of the transducer and the needle were bonded by the ‘tie constraint’.

A G21×100 mm needle was assembled to the transducer at 45 mm from the needle tip in Abaqus. The needle in 100 mm was chosen because its second longitudinal frequency is 50.7 kHz, which is close to the resonant frequency of the piezoelectric transducer. Zero potential was assigned to each electrode and frequency analysis was conducted. The first three longitudinal vibration modes of the needle actuating device are shown in Figure 6-8.

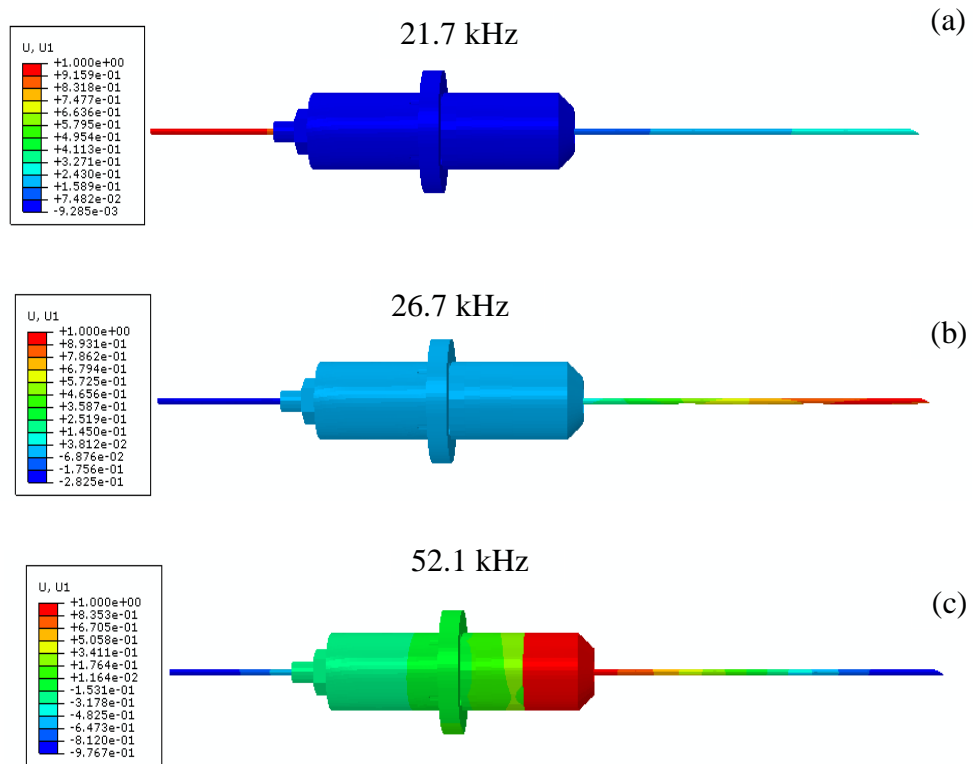


Figure 6-8 Longitudinal vibration modes of Needle Actuating Device: (a) 21.7 kHz (b) 26.7 kHz (c) 52.1 kHz

The longitudinal vibration modes of the needle actuating device are categorised into two groups. One is needle's resonant modes, including the 21.7 and 26.7 kHz modes. The other is the transducer's resonant mode, which is the 52.1 kHz mode.

#### (1) Needle's resonant modes

At both 21.7 kHz and 26.7 kHz modes, the transducer is not at resonant and provides small vibration amplitudes. These longitudinal modes exist because the needle is resonant, and are termed as 'needle's resonant modes' of the needle actuating device in this thesis. The part of the needle from needle end to the clamping position is defined as 'end part' whereas the part of needle from needle tip to the clamping position is defined as 'tip part'. The longitudinal displacement profiles of the needle in 21.7 kHz and 26.7 kHz modes are presented in Figure 6-9.

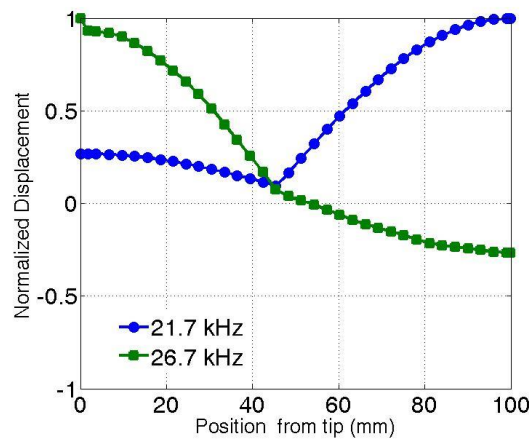


Figure 6-9 Displacement profile on the G21×100 mm needle at the needle's resonance modes: the needle is clamped by the transducer at 45 mm from needle tip

The 21.7 kHz mode is associated with the end part of the needle. At this mode, the needle end offers the highest vibration amplitude whereas the needle tip offers relatively low vibration. The 26.7 kHz mode is associated with the tip part of the needle. At this mode, the needle tip shows the highest vibration amplitude and the needle end shows relatively low vibration. So at the needle's resonant mode, only one part of the needle, either the tip part or the end part is resonant. In the application of needle actuating device, high vibration amplitude at the needle tip is desired. So only the vibration



modes associated with the needle tip are selected in this thesis. The needle's resonant mode refers to the mode associated with the tip part unless specified.

The needle's resonance modes at different tip part lengths were computed in Abaqus. Two needles in different lengths were used: one is a G21×100 mm needle and the other G21×120 mm needle. They were assembled to the piezoelectric transducer with different clamping positions to obtain different tip part lengths. At each clamping position, frequency analysis was conducted to obtain the longitudinal resonant frequency associated with tip part. The first longitudinal resonant frequencies are presented in Table 6-4.

Table 6-4 The first longitudinal resonant frequencies of the needle's resonance modes at different tip part lengths

Tip part length (mm)	G21×100 mm needle (kHz)	G21×120 mm needle (kHz)
40	29.6	30.0
45	26.7	28.2
50	22.8	23.5
60	20.0	20.9
70	17.3	18.0
80	15.3	15.3

As the tip part length increases from 40 mm to 80 mm, the resonant frequency of the needle actuating device with the G21×100 mm needle decreases from 29.6 kHz to 15.3 kHz, meanwhile, the resonant frequency of the needle actuating device with the G21×120 mm needle decreases from 30 kHz to 15.3 kHz. At the same tip part length, the needle actuating device with the G21×100 mm offers about the same resonant frequency as that with the G21×120 mm. The resonant frequency decreases as the tip part length increases.

The results suggest that the resonant frequency of the needle's resonance mode is determined by the tip part length and independent on the total needle length. In other

words, the resonant frequency of the needle's resonance mode is only determined by the clamping position. It should be noted the second longitudinal resonant frequency of the needle's resonant mode is about three times of the first longitudinal resonant frequency because of the boundary conditions that the transducer applies to the needle.

Figure 6-10 shows the displacement profiles of the G21×100 mm needle when it is clamped by the transducer at positions ranging from 40 to 80 mm from the tip. The displacement profiles are normalized to the displacement at the needle end, i.e. the displacement at the needle end is unity.

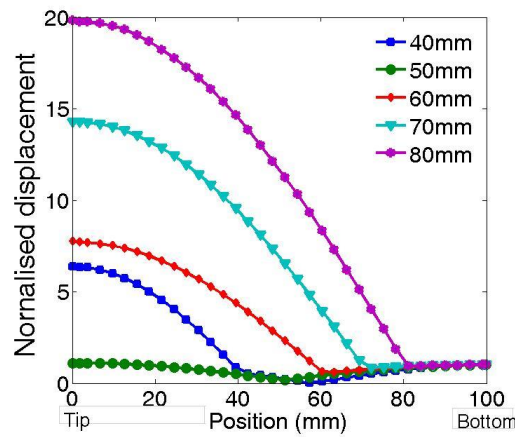


Figure 6-10 Displacement profiles of the needle actuating device at different clamping positions

When the needle is clamped at 50 mm, i.e. at the middle, the needle tip and the end hold about the same vibration amplitude. When the needle is clamped at positions other than the middle, such as 40, 60, 70 and 80 mm, the needle tip provide higher vibration amplitude than the needle end. When the clamping position is at the middle of the needle, the tip part and the end part are in the same length. Consequently, the resonant frequency associated with the tip part is the same as that associated with the end part. In such a case, the tip part and the end part are resonant at the same frequency. In contrast, when the clamping position is not at the middle, the tip part and the end part are different in length. As a result, they are different in resonant frequency. At the resonant frequency associated with tip part, only the tip part is resonant.

When the needle is clamped at the middle, the ratio of vibration amplitude at tip to vibration amplitude at the end is unity. In contrast, when the needle is clamped at other positions, the ratio of vibration amplitude at the tip to the vibration at the end is higher than one. Thus, clamping the needle at positions other than the middle leads to higher tip vibration amplitude than clamping the needle at the middle.

## (2) Transducer's resonant mode

The 52.1 kHz mode is referred to as transducer's resonant mode because the piezoelectric transducer is at resonance at this mode. The displacement profile on the needle is shown in Figure 6-11. It is compared with the second longitudinal resonant mode of a G21×100 mm needle in free vibration, which was presented previously in Section 6.3.2.

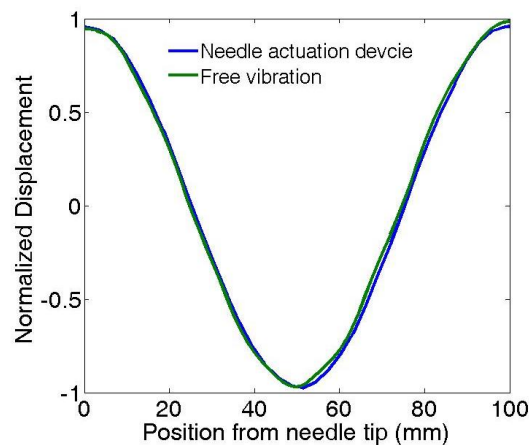


Figure 6-11 Comparison of displacement profiles: the transducer's resonant mode of the needle actuating device and the second longitudinal vibration mode of a free vibration needle

The displacement profile of the needle at the transducer's resonant mode is the same as that of a free vibrating needle at its second longitudinal mode. This is because the second longitudinal resonant frequency of the G21×100 mm is 50.7 kHz, which approximately matches the frequency of the transducer. It is important to note that the needle tip and needle end offer about the same vibration amplitude at this mode.

Simulation was conducted to study the effects of clamping position and needle length on the resonant frequency and mode shape. It was found that the resonant frequency of

the transducer's mode is independent of the both clamping position and needle length. The clamping position makes little differences on the longitudinal displacement profile along the needle. However, the mode shape is highly dependent on the needle length. If the longitudinal resonant frequency of the needle in free vibration matches the transducer's frequency, the vibration mode at the transducer's mode is longitudinal. Otherwise, the vibration mode is flexural, torsional, or a combination of both.

Figure 6-12 shows the transducer's mode of the needle actuating device with a G21×120 mm needle. The resonant frequency is at 52 kHz. Because the second longitudinal natural frequency of the G21×120 mm needle is 40 kHz, which doesn't match the transducer's frequency, the vibration mode on needle is flexural.

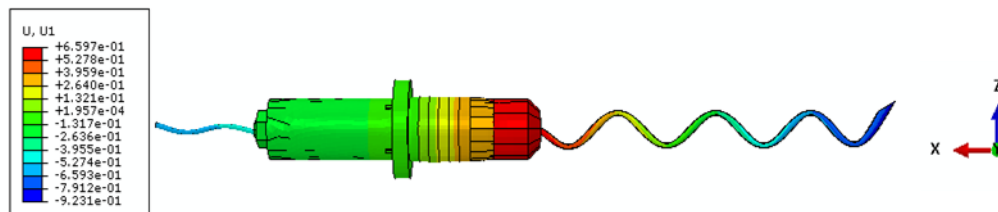


Figure 6-12 Transducer's resonant mode of the needle actuating device working with a G21×120 mm needle

## 6.4 Fabrication

The fabrication of needle actuating device was straightforward. The prepared components are shown in Figure 6-13. Firstly, the bolt with a hollow was screwed into the front mass. A part of the bolt was covered by an insulating tube to insulate it from the piezoelectric rings and electrodes. Then the PZ26 rings were slid down the bolt to rest on the front mass. The brass electrodes were placed between rings for electric connections. The back mass was then slid down the bolt so that the rings were sandwiched between the front and back masses. Lead wires were soldered on the brass electrodes and prestress was applied by torquing the nut on the bolt. Finally the transducers were packed by the housings. The fabricated transducer is shown in Figure 6-14 (a). The needle actuating device was obtained by assembling the needle to the transducer, as shown in Figure 6-14 (b).

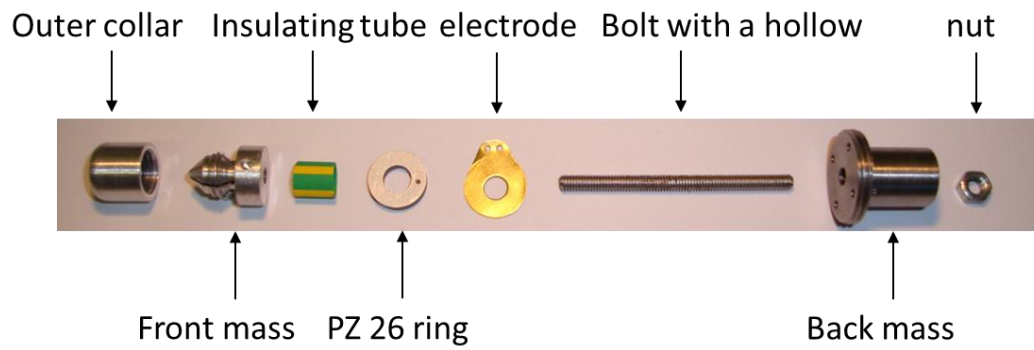


Figure 6-13 Components prepared for transducer fabrication

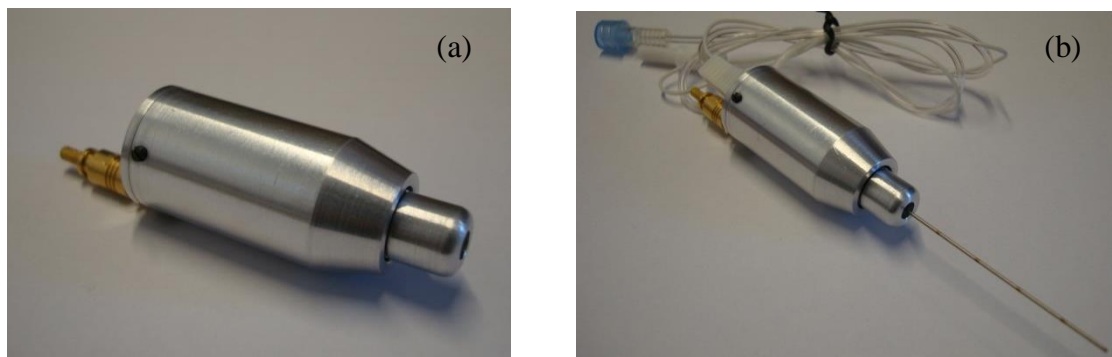


Figure 6-14 (a) fabricated piezoelectric transducer (b) needle actuating device

## 6.5 Characterisation

### 6.5.1 Piezoelectric Transducers

The electric impedance of the transducer was measured by the HP4149 impedance analyser before and after the outer collar was assembled. The results are shown in Figure 6-15. Before the outer collar is assembled to the transducer, the transducer is resonant longitudinally at 70 kHz with electric impedance of 532  $\Omega$ , which is quite close to the simulation result (71.2 kHz).

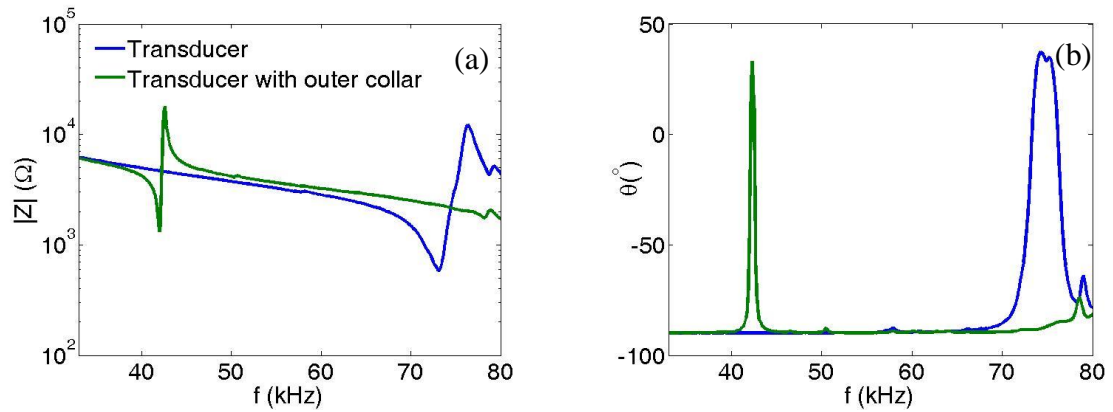


Figure 6-15 Electric impedance of the piezoelectric transducer (a) magnitude (b) phase

After the outer collar is assembled to the transducer, the resonant frequency shifts to a lower value, as expected. However, the resonant frequency is 42 kHz with electric impedance of 1200  $\Omega$ . Compared with the simulation result (51.1 kHz), there is a difference of 9.1 kHz in resonant frequency.

The discrepancy between the experimental and theoretical values is attributed to the torque level applied to the outer collar during assembly. Higher torque level leads to higher resonant frequency and lower electric impedance because higher torque increases the effective matching area between the outer collar and the collet. The increasing effective matching area reduces the electric impedance and increase resonant frequency [175, 177]. In FEA, threads were ignored, and the bonding between outer collars and collets was ideal, resulting in a maximum effective matching area. However, in practice, the torque applied to the outer collars was limited to avoid the mechanical failure of the collets. So the measured resonant frequency was lower than the simulation.

### 6.5.2 Needle Actuating Device

As the resonant frequency of the transducer with outer collar was 40 kHz, the needle that matched the transducer's frequency was G21  $\times$ 120 mm. Thus, a G21  $\times$ 120 mm needle was assembled to the transducer to form the needle actuating device. The clamping position was 45 mm from the needle tip.

The impedance measurement function of the adaptive driving system was used to measure the electric impedance of the needle actuating device. During the measurement,

the LDV was used to record the vibration amplitude at both needle tip and end. Figure 6-16 shows the vibration amplitude and electric impedance when the needle actuating device was driven at 5V. The needle actuating device shows three vibration modes, which can be identified from the displacement response curves: 16.5 kHz, 27.6 kHz and 42.2 kHz.

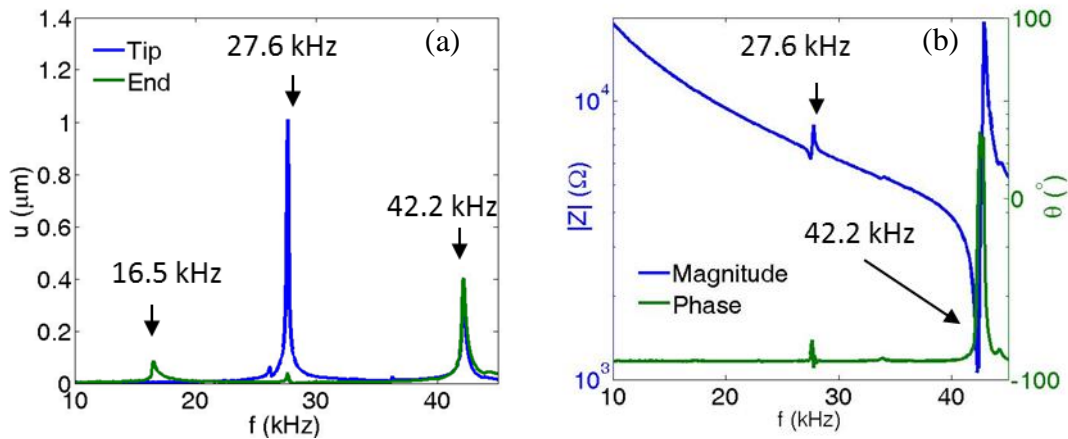


Figure 6-16 (a) Longitudinal displacement response and (b) electric impedance of the needle actuating device: a G21  $\times$ 120 mm needle is clamped by the transducer at 45 mm from tip

The 16.5 kHz mode is the first needle's resonant modes associated with the end part. It offers high vibration amplitude at needle end and low response at needle tip. The 27.6 kHz is the first needle's resonant mode associated with tip part, which agrees well with the simulation result (26.7 kHz) in Section 6.3.3. It offers high vibration amplitude at needle tip but low response at needle end. All the needle's resonance modes exhibit high electrical impedance because the transducer is off resonance. The 16.5 kHz mode cannot even be identified from the impedance curve because it is located too far away from the transducer's resonance.

The 42.2 kHz mode is the transducer's resonant mode. At this mode, the electric impedance is low because the transducer is at resonance. The needle tip and needle end hold about the same vibration amplitude, as predicted in FEA in Section 6.3.3.

To study the effects of clamping position and needle length on the resonant frequencies of the needle's resonant mode and transducer's mode, a G21  $\times$ 120 mm needle and G21

×100 mm needle were clamped by the transducer at different positions. At each clamping position, both the electric impedance and vibration against frequency characteristics were measured by the adaptive driving system with the LDV. Then the resonant frequencies were identified from the impedance and vibration against frequency curves.

Figure 6-17 (a) shows the resonant frequencies of the needle's resonant mode at different clamping positions. The resonant frequency decreases as the tip part length increases. At each tip part length, the G21 ×120 mm needle and G21 ×100 mm needle holds about the same resonant frequency. This confirms the conclusion we drew from the simulation that the resonant frequency of the needle's resonant mode is determined by the tip part length and is independent on the total needle length. Figure 6-17 (b) compares the experimental results with the FEA results. The FEA predicted the resonant frequencies of the needle's resonant mode accurately.

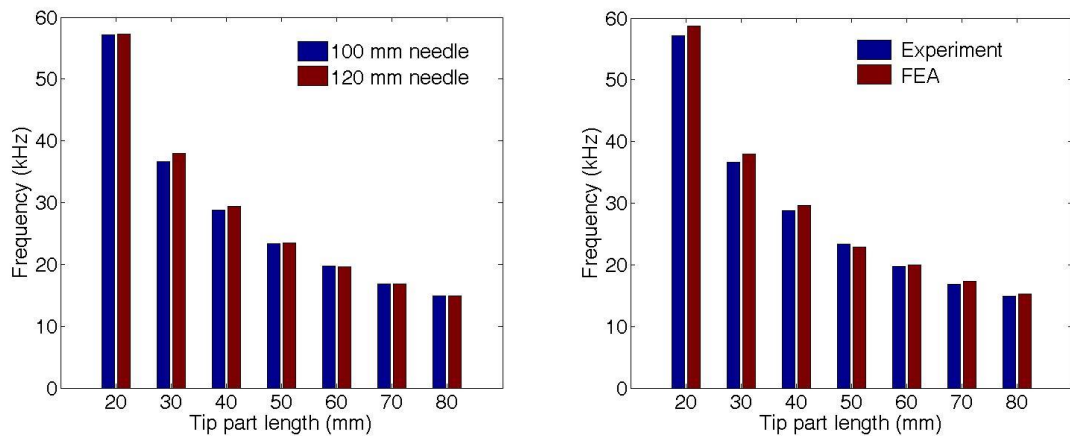


Figure 6-17 Resonant frequencies of needle's resonant mode: (a) resonant frequencies of a G21 ×120 mm needle and a G21 ×100 mm needle at different clamping positions (b) comparison of the experiment results with the FEA results on a G21 ×100 mm needle

Figure 6-18 shows the resonant frequencies of the transducer's mode with the two needles at different clamping positions. The resonant frequency keeps almost constantly with both needles at different clamping positions. The small variations in some positions are attributed to the different torques applied when tightening the outer collar to the transducer. So the needle length and the clamping position make little difference to the resonant frequency of the transducer's mode.



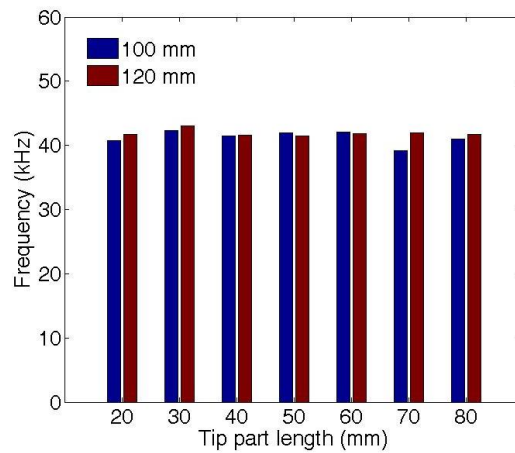


Figure 6-18 Resonant frequencies of the transducer's mode with a G21  $\times$ 120 mm needle and a G21  $\times$ 100 mm needle at different clamping positions

However, as predicted in FEA, needle length affected the mode shape of the transducer's mode. The resonant frequency of the G21  $\times$ 100 needle is 50.7 kHz, which doesn't match the frequency of the transducer in practice. The transducer's mode with the G21  $\times$ 100 needle is thus not longitudinal. This can be verified by comparing the vibration amplitude of the needle in the longitudinal direction with the lateral direction, as shown in Figure 6-19. The G21  $\times$ 100 needle was clamped by the transducer at 45 mm from the tip. The vibration against frequency at the transducer's mode was measured at needle tip in both longitudinal direction and lateral direction. The lateral vibration amplitude at 42 kHz is 0.49  $\mu$ m, which is higher than the longitudinal vibration (0.15  $\mu$ m). So the vibration mode is a lateral mode.

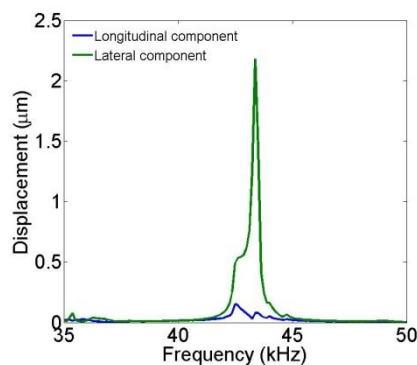


Figure 6-19 Longitudinal and lateral vibration at the tip of a G21  $\times$ 100 needle clamped by the transducer at 45 mm

The needle actuating device always holds both needle's resonant modes and transducer's modes. The advantage of using the transducer's resonant mode to actuate the needle is that the resonant frequency and vibration mode are independent of the clamping position. This offers convenience in practice. The electric impedance at this mode is low, which ensures high power conversion efficiency. The existence of zero phase frequency makes it possible to use the adaptive driving system to track the resonant frequency in operation. The negative side of the transducer's mode is that it requires needles in specific lengths to match the transducer's frequency to obtain a longitudinal vibration mode. This places constraints in the choice of needles for a transducer. Furthermore, the vibration amplitude at both needle tip and needle end offers approximately the same vibration amplitude. Thus, the vibration amplitude at transducer's mode is lower than that at needle's resonance mode.

The benefit of employing needle's resonant mode to actuate the needle is that the resonant frequency and vibration mode are independent of the total needle length. The independence of resonant frequency of total needle length eliminates the requirement of needles in specific total length to match the transducer. Longitudinal vibration mode is available at each clamping position. However, the clamping position still needs to be carefully selected since it affects the resonant frequency of the longitudinal mode. The negative side of the needle's resonant mode is that the electric impedance is very high, and the zero phase frequency doesn't exist because the resonant frequency is away from the transducer's resonance. In such a case, it is not possible to track the resonance of the device by the adaptive driving system, since the adaptive driving system always works at zero phase frequency. Even if the impedance is tuned out by a transformer as described in Chapter 4 of this thesis, which makes the resonance tracking possible, the needle's resonant mode is still not robust enough. It was found that the needle's resonant mode might disappear from the electric impedance curve as soon as the needle was inserted into the tissue, leading to the resonance tracking impossible.

A feasible solution to the high impedance of the needle's resonance mode found in practice is to adjust the clamping position to make sure that the resonant frequency of the needle's resonant mode is close to the transducer's resonant mode. Then a transformer can be used to match the impedance, as shown in Figure 6-20.

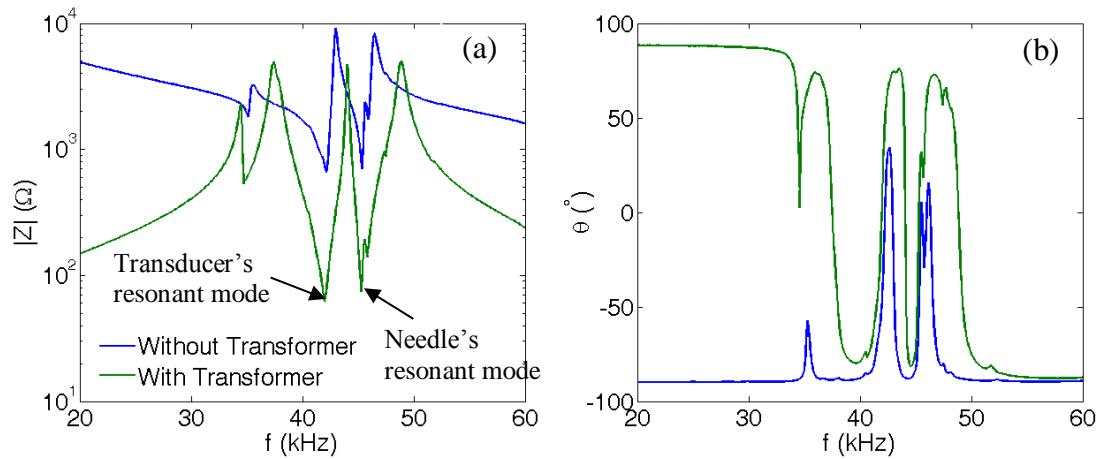


Figure 6-20 Electric impedance of the needle actuating device working with a G21×120 mm needle before and after impedance matching (a) magnitude (b) phase

A G21×120 mm needle was clamped by the transducer at 80 mm from the tip. The transducer's and needle's resonance modes were at 42 and 45 kHz, respectively. The impedance at the needle's resonant mode is about the same as the transducer's mode. Zero phase value at the needle's resonant mode is available after using the transformer, and therefore can be tracked by the adaptive driving system. This zero phase was even available after the needle was inserted into soft tissue, as shown in Figure 6-21.

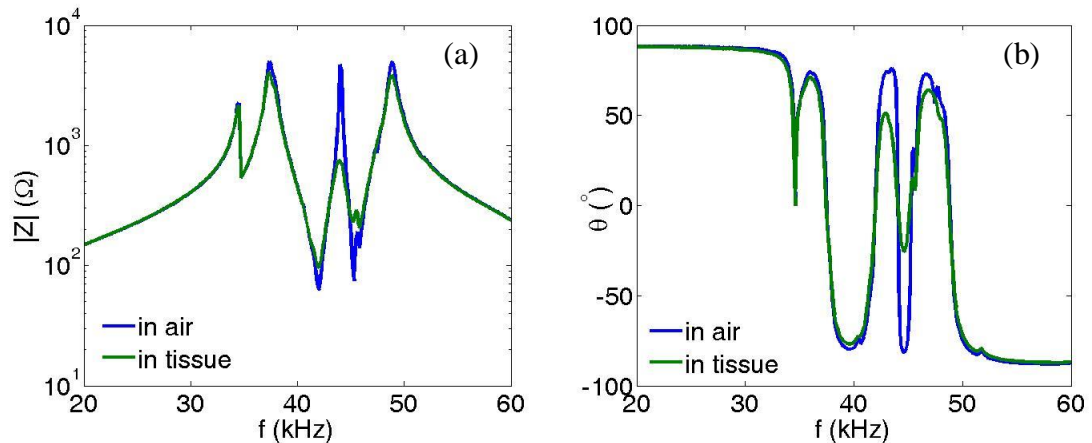


Figure 6-21 Electric impedance of the needle actuating device measured in air and in tissue (a) magnitude (b) phase

However, it can be observed that the needle's resonance mode is still more sensitive to the loading condition than the transducer's mode. The electric impedance increases

from  $74\ \Omega$  to  $234\ \Omega$  for the needle's resonance mode. In contrast for the transducer's mode, the impedance increases from  $62\ \Omega$  to  $97\ \Omega$ .

The longitudinal vibration velocity of the needle actuating device was measured by the LDV at the needle tip, as shown in Figure 6-22. The needle was clamped by the transducer at 80 mm from the needle tip, corresponding to the impedance curve in Figure 6-20. The transformer was used, and the needle actuating device was free of loads. The vibration velocity increases linearly with current amplitude. The device in the needle's resonance mode provides higher vibration velocity than the transducer's mode at the same current amplitude, as expected. At 0.1A, the vibration velocity measured in the needle's mode is 1628 mm/s whereas in the transducer's mode 580 mm/s.

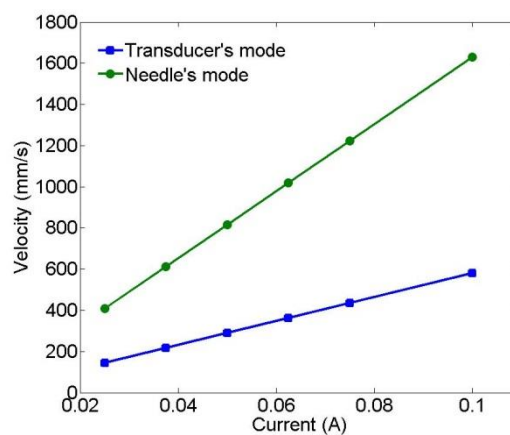


Figure 6-22 Vibration velocity of the needle actuating device at needle tip

### 6.6 Needle Visibility Test

Following the successful design and characterisation of the needle actuating device, its ability to enhance the needle visibility in ultrasound imaging was tested.

#### 6.6.1 Experimental arrangement

##### (1) Setup

To obtain repeatable experimental results, the needle actuating device was installed on a motorized translation stage (MTS50-Z8, THORLABS Ltd. UK), as shown in Figure

6-23. The translation stage can provide a maximum displacement of 50 mm at a maximum velocity of 3 mm/s. It was installed on a rotational stage which could control the angle of the translation stage. With the help of the two stages, the insertion angle and insertion depth of the needle could be precisely controlled and repeated.

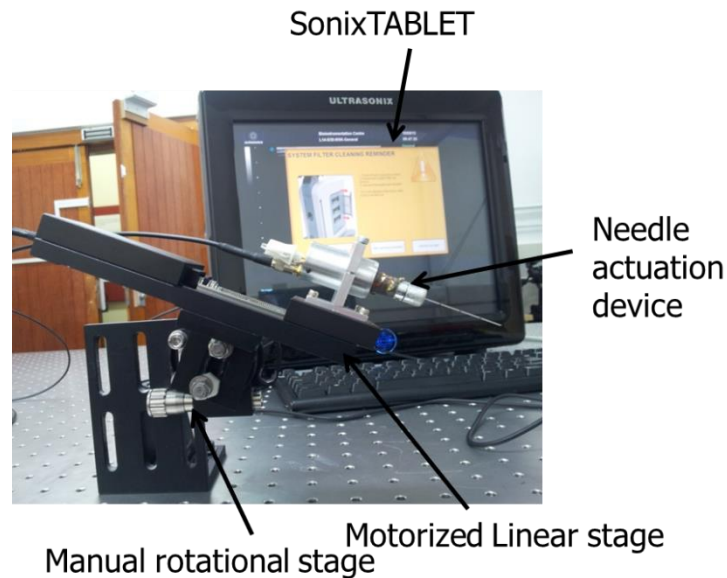


Figure 6-23 Experimental setup

A state of the art ultrasound imaging system, SonixTablet (Ultrasonics, Richmond, Canada), together with a 5 MHz linear ultrasound imaging probe was used to visualise the needle inside the test specimens.

### (2) Specimen

Porcine tissue obtained freshly from a local butcher was used as a specimen to study the effects of different factors on the performance of the needle actuating device. The reason to choose porcine tissue is that pig is the most commonly used animal for biomedical research due to its biological similarities with human tissue [178].

### (3) Methods

The study was carried out by using both in plane and out of plane needle approaches, which are both employed during ultrasound guided regional anesthesia [179]. In the in plane approach, the needle is inserted in the same plane as the ultrasound beam and is

visible as a bright hyperechoic line. In this approach, the needle-beam alignment is critical to visualise the shaft of the needle [165]. In the out of plane approach, the longitudinal axis of the needle is inserted in a plane perpendicular to that of the ultrasound beam. Visualizing the needle tip in this approach can be difficult, as only a cross-sectional area of the needle is imaged[165].

The insertion depth was 30 mm in all cases. Experiments were conducted to access the effects of various factors on the performance of needle actuating devices. These factors include excitation power level, insertion angle, and resonance modes. During each insertion procedure, the needle was inserted into the porcine tissue automatically by the translation stage at a velocity of 3 mm/s. The adaptive driving system was used to track the resonant frequency of the device and control the input current amplitude.

### 6.6.2 Experimental results

Prior to observing the needle actuating device under colour Doppler imaging, the grey scale ultrasound imaging of the actuated needle was captured, as Figure 6-24 (a). The needle can be visualised as a pale and grey line. The shaft of the needle is not very clear, but still distinguishable. However, it is very difficult to determine the position of the needle tip. The visibility of the actuated needle was significantly improved by observing it under colour Doppler imaging, as presented in Figure 6-24 (b). The needle actuating device was working at its transducer's resonance mode, and the adaptive driving system was used to track the resonant frequency. The needle is delineated as a coloured line. The whole needle including both the shaft and tip is visible.

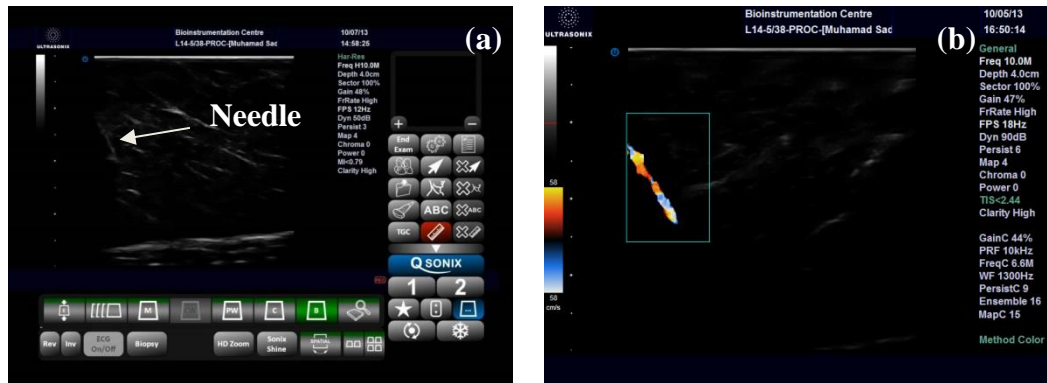


Figure 6-24 Comparison of the needle actuating device observed under grey scale ultrasound imaging and colour Doppler imaging (a) grey scale (b) colour Doppler

Resonant frequency change was noted during the needle insertion procedure due to the loads from tissue, as expected. The resonant frequency was precisely tracked, and the resonance was always achieved by the adaptive driving system. When the adaptive driving system was absent, the frequency output of the signal generator had to be tuned manually to maintain the resonance. Otherwise, the needle was not visible. Figure 6-25 shows the imaging of the needle actuating device when the adaptive driving system was not used and the frequency was tuned manually to attain resonance. The visibility of the needle is still enhanced.

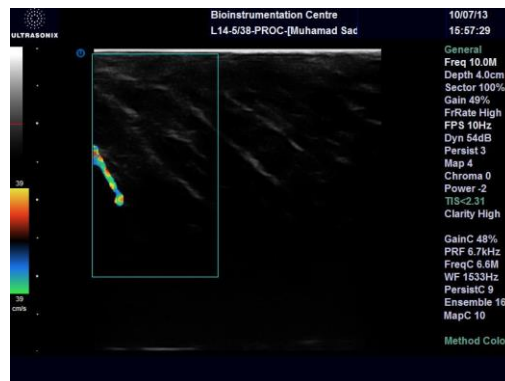


Figure 6-25 Colour Doppler imaging of the needle actuating device by tuning the frequency manually

However, tuning the frequency manually is a tricky task since the frequency shift cannot be predicted precisely because biological tissues are not homogeneous structures and individual tissues presents unique and different loads to the needle. Also, a surgeon cannot perform the surgery and tune the frequency at the same time. Furthermore,

tuning the frequency manually is only effective when the needle stops advancing. When the needle is advancing, the loads imposed by the tissue changes continuously, and so does the resonant frequency. In other words, keeping the needle visible during the advancing procedure is difficult by tuning the frequency manually.

In contrast, by using the adaptive driving system, the resonant frequency shift was tracked automatically even when the needle was advancing. The needle was visualized during the whole insertion procedure, as presented in Figure 6-26. The images were captured at an interval of 2s from a video, which recorded the colour Doppler imaging of the needle during an insertion procedure.



## CASE STUDY- NEEDLE ACTUATING DEVICE

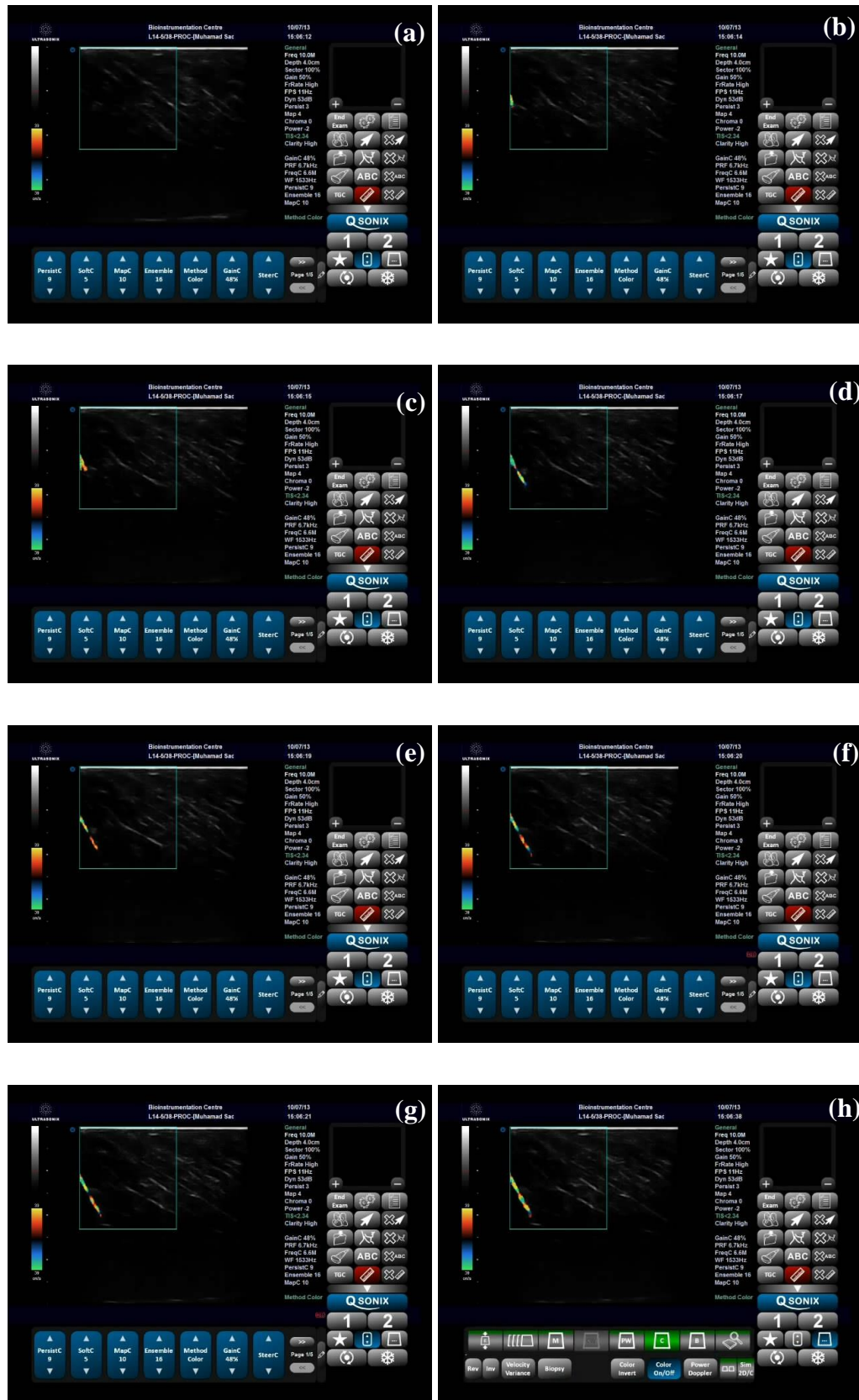


Figure 6-26 Colour Doppler imaging of the needle actuating device during needle advancing (a) 0 s (b) 2s (c) 4s (d) 6s (e) 8s (f) 10s (g) 12s (h) 14s

In Figure 6-26 (a), the needle was not inserted yet, so no imaging was observed. A coloured line appeared as soon as the needle was inserted into the visual field of the ultrasound probe. The clear visualisation of the needle being advanced is quite beneficial and essential to clinical application as the surgeon can monitor the position of the needle in real time.

The effects of the excitation power level on the performance of the needle actuating device during the in plane approach are presented in Figure 6-27. The needle insertion angle was  $60^\circ$  at a depth of 30 mm. At 0.025A (2V), the needle is hardly seen except a small highlighted dot, as shown in Figure 6-27 (a). More parts of the needle become visible at 0.0375A (3V) but the coloured line is still not continuous. The minimum current amplitude required to visualise the whole needle is 0.05A (4V). By increasing the voltage further to 0.0625, this line delineating the needle becomes brighter and wider.

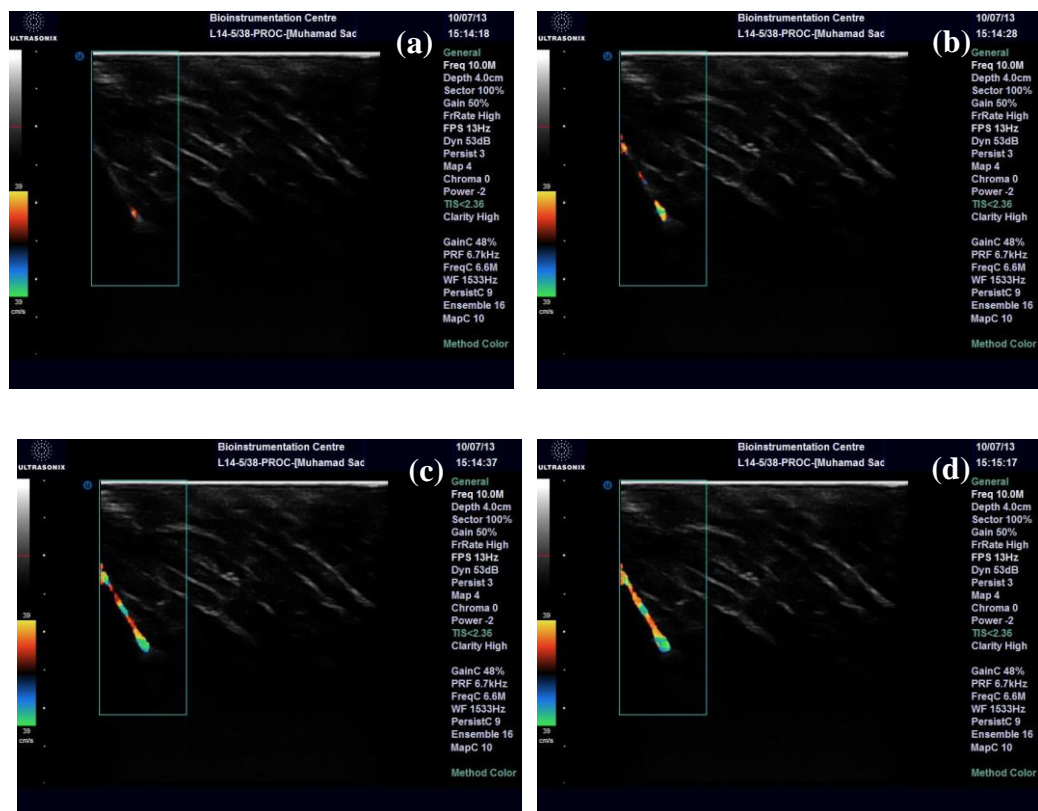


Figure 6-27 Colour Doppler images of the needle actuating device under different excitation current: in plane approach (a) 0.025A (b) 0.0375A (c) 0.05A (d) 0.0625A

The colour Doppler images of the actuated needle during an out of plane procedure are shown in Figure 6-28. The same device and resonance mode with the in-plane approach study was used. The needle insertion angle was  $30^\circ$  at a depth of 30 mm. At 0.0125A (1V), a small coloured dot representing the needle is visualised. This dot becomes brighter and bigger as the driving current increases.

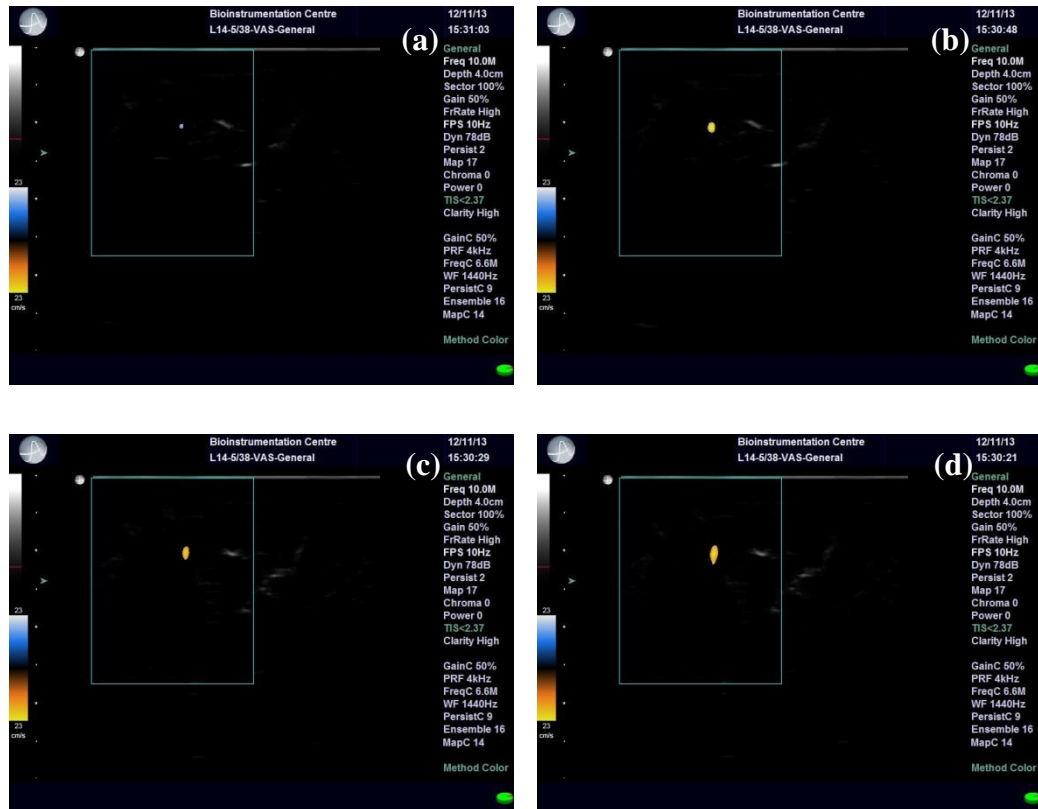


Figure 6-28 Colour Doppler images of the needle actuating device under different driving voltage: out of plane approach (a) 0.0125A (b) 0.025A (c) 0.0375A (d) 0.05A

In both in plane and out of plane approaches, the hyperechoic line or dot delineating the needle spreads to larger areas at higher excitation levels, because the observed colour Doppler images in the experiment were not the direct image of the needle itself, but the image of the tissue that was surrounding the needle and actuated to oscillate by the vibrating needle. If the excitation power delivered to the needle actuating device increases, the vibration amplitude in the needle will grow as well. Consequently, larger area of tissue will be actuated by the needle to oscillate and detected by the ultrasound imaging. When the vibration amplitude of the needle is too small, it might not be able to drive enough surrounding tissue to move and thus only part of the needle is visible.

When the vibration amplitude is too high, too much tissue will be vibrating, resulting in a needle image spreading to a large area and thus difficulties in determining the accurate needle position. So to drive the needle actuating device, the power should be chosen to maximize the visibility of the needle while maintaining the coloured areas as small as possible.

Figure 6-29 shows the effect of the insertion angle on the visibility of the needle. The needle actuating device was driven at 0.05A, and inserted at 30°, 40°, 50° and 60°. The needle shaft is visible at all the four insertion angles. However, for the shallow insertion angles, the hyperechoic region tends to expand to too large area, particularly near tip of the needle. This problem was not solved by decreasing the actuating current. Reducing the actuating current resulted in the discontinuity of hyperechoic region with little artefacts reduced. Obviously, better performance is achieved at steep insertion angles since the hyperechoic line becomes thinner. This is opposite to grey scale ultrasound imaging where better images are obtained in small insertion angles [180]. The better performance of the needle actuating device at larger insertion angles is attributed to the principle of Doppler imaging. As the angle between the incident ultrasound beam and the axis of movement decreases, the Doppler shifts increase and are greatest when the movement is along the same axis as that of the beam [181].

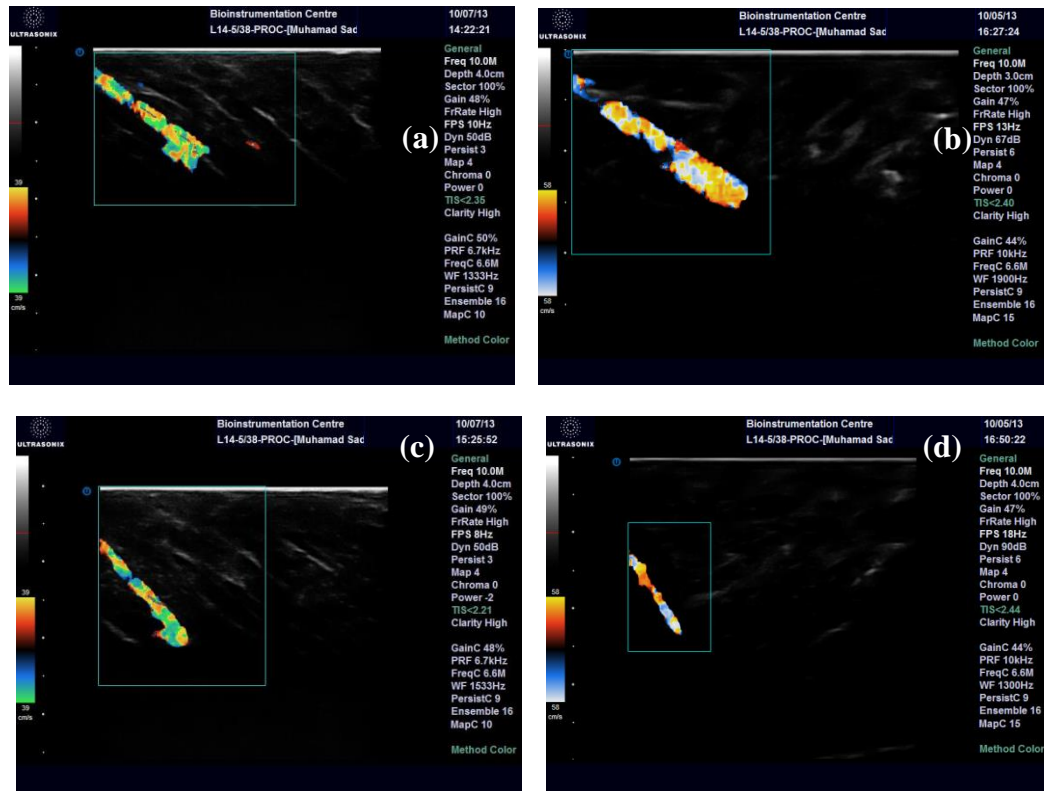


Figure 6-29 Colour Doppler imaging of the needle at different insertion angles: (a) 30° (b) 40° (c) 50° (d) 60°

The results reported above were obtained by using the transducer's resonant mode of the needle actuating device. The needle actuating device working at needle's resonance mode can also increase the needle visibility, as shown in Figure 6-30.

The minimum current amplitude required to obtain a clearly needle image in the needle's resonant mode is 0.05A. This is the same as the transducer's resonant mode. However, the input voltage at 0.05A for the needle's resonant mode is 12.5 V, compared with 4 V in the transducer's resonant mode. The higher voltage required in the needle's resonant mode is because the electric impedance in the needle's resonant mode is more sensitive to loads and increases more significantly than the transducer's resonant mode.

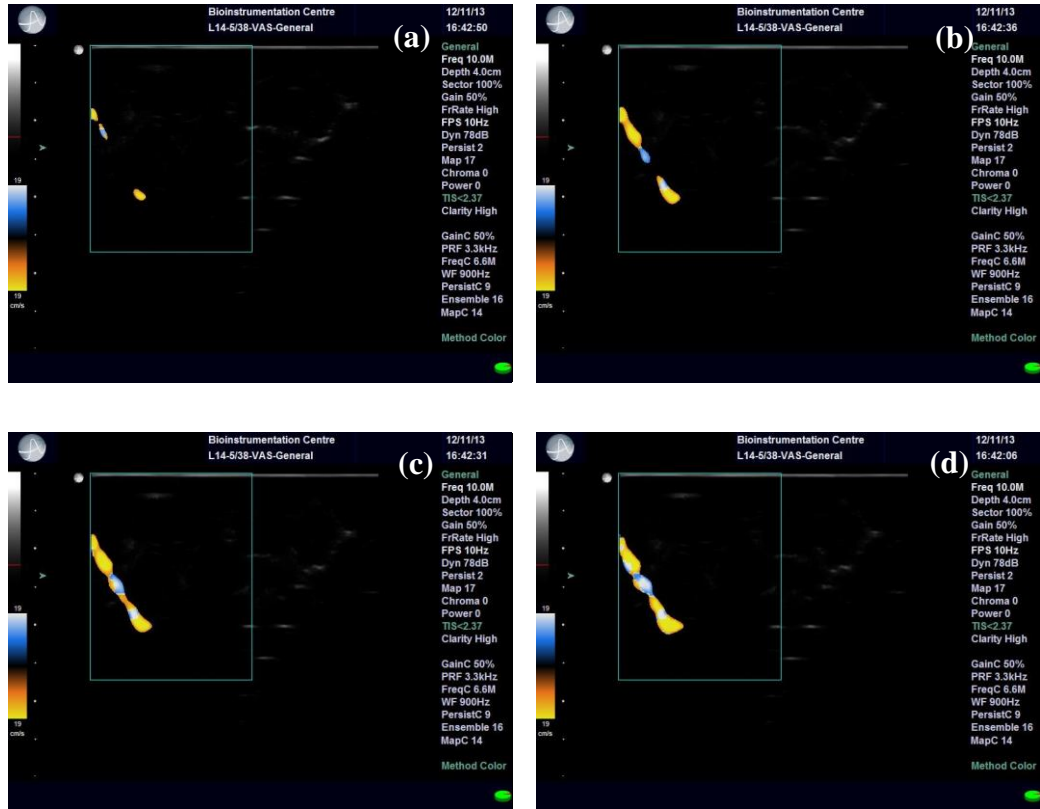


Figure 6-30 Colour Doppler imaging of the needle actuating device working at its needle's resonance mode at different current amplitudes: (a) 0.025A (b) 0.0375A (c) 0.05A (d) 0.0625A

## 6.7 Discussion and conclusion

In this chapter, the design, fabrication and characterisation of a needle actuating device based on piezoelectric sandwich transducer were reported. Its effectiveness in improving needle visibility under colour Doppler imaging has been tested in *ex vivo* animal tissue. The capacity of the adaptive driving system to optimize the device's performance was studied.

The performance of the device was analysed through FEA in Abaqus and then validated by experimental characterisation. The experimental results are in agreement with FEA. For the piezoelectric transducer, caution should be taken on the outer collet. The outer collet was observed to lower the resonant frequency of the transducer significantly by additional mass and reduced effective matching area.

The needle actuation device holds two kinds of vibration modes: needle's resonant mode and transducer's resonant mode. At the needle's resonant mode, part of the needle is resonant whereas the transducer is not resonant and shows small vibration. In both simulation and experimental characterisation, the resonant frequency of the needle's resonant mode was found to decrease with the tip part length. The resonant frequency was independent of the total needle length. At the transducer's mode, the transducer is resonant, and it actuates the needle to vibrate at the transducer's resonant frequency. The vibration of the needle is longitudinal only if the longitudinal resonant frequency of the needle matches the transducer.

The needle's resonant mode showed a higher vibration amplitude than the transducer's mode. The high vibration amplitude in the needle's resonant mode is associated with the high displacement amplification of the vibration modes. At needle's mode, the vibration was mainly focused on the tip part of the needle so high displacement amplification was expected. However, at transducer's mode, the needle showed the same vibration amplitude at the needle tip and the end, so the displacement amplification was unity.

Based on the results in the needle visibility tests, it can be concluded that the needle actuating device coupled with colour Doppler imaging modality showed significant effectiveness in improving needle visibility in both in plane and out of plane approaches. Under in plane approach, the whole needle, including the shaft and tip, was visible as a thin coloured line, whereas under out of plane approach, the needle was also identified as a highlighted dot.

Resonant frequency shift negatively affected the performance of the needle actuating device. However, with the use of the adaptive driving system, optimized performance was always obtained without involving tuning the frequency output of the signal generator manually. The adaptive driving system brings in an improved imaging quality and high convenience in practice. Furthermore, attributed to the adaptive driving system, the needle was also visible when it was advancing, which was very difficult in previous studies without an adaptive driving system [152].

The excitation power applied to the needle actuating device should be carefully selected. When the power is too low, the vibration generated on the needle may not be high

enough to actuate enough surrounding tissue to oscillate. In such a case, only part of the needle is visible. When the power is too high, the vibration generated on the needle may be too high and too much surround tissue is actuated. In such a case, the hyperechoic area tends to spread to a large area, resulting in difficulty in determining the accurate needle position. Thus, the power should be chosen to maximize the visibility of the needle while maintaining the colourful areas as small as possible.

Both the needle's resonant mode and the transducer's resonant mode were able to increase the needle visibility. They needed the same current level to visualise the whole needle. However, the needle's resonant mode required higher electric power than the transducer's mode because its electric impedance was more sensitive to external loads.

The overall conclusion which can be drawn from this chapter is that the needle actuating device driven by the adaptive driving system can produce colourised images of standard medical needles with significant improvement in visualisation, compared with the situation without using adaptive driving system. The successful track of the resonant frequency helps the needle actuating device to maintain optimized performance under varying load conditions.



## 7 CONCLUSIONS AND FUTURE WORK

### 7.1 Conclusions

The work presented in this thesis has focused on improving the performance of ultrasonic surgical instruments through an adaptive driving system. The adaptive driving system developed has shown ability to track the resonant frequency and stabilise the vibration velocity of ultrasonic devices under both loaded and unloaded conditions. Its high flexibility has allowed it to work with different devices at different frequency ranges. It has been witnessed that the performance of an ultrasonic planar tool and a needle actuating device was optimised by using the adaptive driving system. The key findings in this thesis are presented in the following.

Chapter 3 reported the design, fabrication and characterisation of ultrasonic planar tools, which are alternatives to the traditional piezoelectric sandwich transducers. The ultrasonic planar tools operate in  $d_{31}$  mode as opposed to  $d_{33}$  mode of the piezoelectric sandwich transducers. Moreover, the piezoelectric element of the planar tools is a relatively new piezoelectric single crystal: PMN-PT, which holds higher coupling coefficient and piezoelectric constants than PZT. So the work reported on the planar tools can also be considered as a feasibility study to assess the performance of new piezocrystal for high power actuator applications. Various materials were chosen for the blades: stainless steel, titanium alloy, and silicon wafer and aluminium nitride, which hold decreasing acoustic loss.

Through characterisation, it was found that both blade material and blade profile affected the vibration amplitude. Blade material with lower acoustic loss offered a higher mechanical quality factor, leading to a higher vibration amplitude at constant voltage. Exponential profile held higher displacement amplification than the linear profile, thus offering higher vibration amplitude. Planar tool with double piezoelectric plates bonded symmetrically was beneficial. Electrically, the two plates were connected in parallel, resulting in lower electric impedance than any single plate. Mechanically,

the two plates distributed the mass symmetrically on the blade, resulting in minimum vibration on the lateral directions.

When characterising the planar tool, resonant frequency shift with power level was found. The impedance at the resonant frequency also varied, leading to a nonlinear relationship between voltage and vibration velocity. To address the issue of resonant frequency change and impedance variation, an adaptive driving system is required.

Chapter 4 presented the development of the adaptive driving system. The adaptive driving system designed tracked the resonant frequency of the transducer by locking the phase value at zero and stabilised the vibration velocity by keeping the current through the transducer constant. This control strategy was proposed based on the BVD electric model of piezoelectric transducers. The system was configured as a combined analogue-digital system to increase its flexibility and tuneable range. The control signals were processed in the signal generator and power amplifier whereas the impedance calculation and the control algorithms were implemented in LabVIEW programs. The system was able to drive piezoelectric transducers at a frequency range up to 5 MHz and a power limit up to 300 W, currently limited by the power amplifier.

The adaptive driving system was carefully calibrated. After calibration, it was able to measure electric impedance of transducers up to 5 MHz with magnitude error less than 5% and phase error less than  $1^\circ$ . The capacity of the adaptive driving system was validated on three air-loaded (free loaded) transducers (resonant frequencies at 34.5 kHz, 35.2 kHz and 78.5 kHz respectively) for high power applications. Its performance was also compared with a commercial adaptive driving system for high power piezoelectric transducers. The results demonstrated that the adaptive driving system was able to track the resonant frequency and stabilise the vibration velocity of piezoelectric transducers in a broad frequency range. The optimal performance of the transducers can be achieved by using the adaptive driving system.

Chapter 5 first reported the high power characterisation of the planar tool by using the adaptive driving system. This work was to study the performance variation of the planar tool under both high power level and external loads to access the ability of the planar tool and the PMN-PT piezocrystal for high power applications. The performance

variables of the planar tool underwent significant variations under high power levels. The  $Q_M$  was reduced by 90% at 0.15A whereas the electric impedance increased by 250%. The vibration velocity dropped by 21% and frequency change up to 3 kHz was observed. The serious temperature rise in the epoxy prevented the planar tool from working at current level above 0.15A because the performance of the piezocrystal degraded quickly after the temperature enters the phase transition point (80°C for PMN-PT). The poultry breast tissue was found to increase both the loss and the resonant frequency of the planar tool. However, the additional loss did not cause further temperature increase of the planar tool.

Following the high power characterisation of the planar tool, Chapter 5 reported soft tissue penetrating test using the Ti planar tool, which was penetrated into poultry breast tissue by 20 mm at constant feed rate. Results showed that the ultrasonic planar tool was able to reduce the force and work needed to penetrate through tissue. The adaptive driving system successfully tracked the resonant frequency of the planar tool and stabilised the current amplitude. When the planar tool was driven by the adaptive driving system, the work reduction was 42%, compared with the work reduction of 23% when the planar tool was driven by a non-adaptive driving circuit. So, the performance of the planar tool was improved by the adaptive driving system.

Chapter 6 presented a case study of using the adaptive driving system to optimise the performance of a needle actuating device. The device was designed to increase the visibility of medical needles under colour Doppler imaging for a range of percutaneous needle procedures including regional anaesthesia and cancer biopsy. It is composed of a sandwich piezoelectric transducer with specially designed front mass, which actuates a standard medical needle to vibrate in the longitudinal direction. Both simulation and experimental characterisation showed that the needle actuating device could be resonant at either the needle's resonant mode or the transducer's mode. Both modes had several promises and challenges and were potentially useful for needle actuating.

The needle visibility tests demonstrated that the needle actuating device coupled with colour Doppler was effective in increasing the needle visibility, particularly at large insertion angles. Resonant frequency shift negatively affected the performance of the

needle actuating device. The needle was not visible unless the needle actuating device was excited at the resonant frequencies. With the help of the adaptive driving system, the resonant frequency of the device was successfully tracked, and the needle was always clearly visible.

The overall conclusions that can be drawn from this thesis are:

- (1) The adaptive driving system can optimise the performance of ultrasonic devices through continuous resonance tracking and vibration stabilisation.
- (2) The ultrasonic planar tool actuated by piezocrystal PMN-PT can generate vibration velocity up to 3 m/s. It is feasible for soft tissue cutting to reduce the loading force.
- (3) The PMN-PT can be used for high power ultrasonic actuation. However, the low Curie point restricts the power level.
- (4) The needle actuating device can produce colourised images of standard medical needles with significant improvement in visualisation.

### 7.2 Future Work

#### 7.2.1 Adaptive Driving System

The adaptive driving system developed has shown ability to track the resonant frequency and stabilise the vibration velocity of a range of ultrasonic devices. It consists of a 33220A signal generator and a 1020L power amplifier, which are controlled by a PC with data acquisition cards installed. Future work will be focused on developing an adaptive driving system based on embedded chips and circuits. The PC will be replaced by a microcontroller. Bespoke circuits for signal generation and power amplifier will also be developed. The adaptive driving system in such a configuration will be more compact and portable than the current one.

#### 7.2.2 Ultrasonic Planar Tool

PMN-PT piezocrystals in  $d_{31}$  mode have shown feasibility to work with blades in different materials and shapes. Further work will explore blade shapes, device

packaging and medical compatibility for specific surgical operations. The temperature increase resulting from the high mechanical loss of epoxy limited the maximum power applied to the planar tool, and thus the maximum vibration amplitude at the tip. Further studies are demanded to address this problem, either by reducing the heat production or by increasing the Curie point of the piezoelectric material.

### 7.2.3 Needle Actuating Device

The needle actuating device increased the needle visibility in colour Doppler imaging. However, to make it for clinical applications, additional work is required to improve the design and the performance characteristics. Moreover, clinicians normally prefer the B-scan (grey-scale) imaging mode during the ultrasound imaging guided percutaneous procedures. To address this, an image processing algorithm is required, which calculates a best-fit mathematical line representing the needle based on the colour Doppler imaging and then superimposes this line onto the B-scan image, showing the exact location of the needle.

## REFERENCES

1. Labanca, M., et al., *Piezoelectric surgery: Twenty years of use*. British Journal of Oral and Maxillofacial Surgery, 2008. **46**(4): p. 265-269.
2. O'Daly, B.J., et al., *High Power, Low Frequency Ultrasound: Meniscal Tissue Interaction and Ablation Characteristics*. Ultrasound in Medicine and Biology, 2011. **37**(4): p. 556-567.
3. Bond, L.J. and W.W. Cimino, *Physics of ultrasonic surgery using tissue fragmentation*. Ultrasonics, 1996. **34**(2-5): p. 579-585.
4. Schmidbauer, S., et al., *Experience With Ultrasound Scissors and Blades (UltraCision) in Open and Laparoscopic Liver Resection*. Annals of surgery, 2002. **235**(1): p. 4.
5. Lucas, M., A. Cardoni, and A. MacBeath, *Temperature effects in ultrasonic cutting of natural materials*. CIRP Annals - Manufacturing Technology, 2005. **54**(1): p. 195-198.
6. Lucas, M., et al., *Design and Characterisation of Ultrasonic Cutting Tools*. CIRP Annals - Manufacturing Technology, 2001. **50**(1): p. 149-152.
7. O'Daly, B.J., et al., *High-power low-frequency ultrasound: A review of tissue dissection and ablation in medicine and surgery*. Journal of Materials Processing Technology, 2008. **200**(1-3): p. 38-58.
8. Albareda, A., et al., *Characterization of the mechanical nonlinear behavior of piezoelectric ceramics*. Ultrasonics, Ferroelectrics and Frequency Control, IEEE Transactions on, 2000. **47**(4): p. 844-853.
9. Ying, C., Z.Y. Zhou, and G.H. Zhang, *Effects of different tissue loads on high power ultrasonic surgery scalpel*. Ultrasound in Medicine and Biology, 2006. **32**(3): p. 415-420.
10. Shuyu, L., *Load characteristics of high power sandwich piezoelectric ultrasonic transducers*. Ultrasonics, 2005. **43**(5): p. 365-373.
11. Ramos-Fernandez, A., J.A. Gallego-Juarez, and F. Montoya-Vitini, *Automatic system for dynamic control of resonance in high power and high Q ultrasonic transducers*. Ultrasonics, 1985. **23**(4): p. 151-156.
12. Babitsky, V.I., V.K. Astashev, and A.N. Kalashnikov, *Autoresonant control of nonlinear mode in ultrasonic transducer for machining applications*. Ultrasonics, 2004. **42**(1-9): p. 29-35.
13. Wang, Y., et al. *Control scheme evaluation for Class-D amplifiers in a power-ultrasonic system*. in *Power Electronics, Machines and Drives (PEMD 2012), 6th IET International Conference on*. 2012.
14. Mortimer, B., et al., *High power resonant tracking amplifier using admittance locking*. Ultrasonics, 2001. **39**(4): p. 257-261.
15. Lucas, M., A. Gachagan, and A. Cardoni, *Research applications and opportunities in power ultrasonics*. Proceedings of the Institution of Mechanical Engineers, Part C: Journal of Mechanical Engineering Science, 2009. **223**(12): p. 2949-2965.

16. Gill, R., *The Physics and Technology of Diagnostic Ultrasound: a practitioner's guide*. 2012, Sydney: High Frequency Publishing.
17. Kennedy, J.E., G.R. Ter Haar, and D. Cranston, *High intensity focused ultrasound: surgery of the future?* Br J Radiol, 2003. **76**(909): p. 590-9.
18. Koch, C., et al., *Determination of temperature elevation in tissue during the application of the harmonic scalpel*. Ultrasound in Medicine & Biology, 2003. **29**(2): p. 301-309.
19. Gossot, D., et al., *Ultrasonic dissection for endoscopic surgery*. Surgical Endoscopy, 1999. **13**(4): p. 412-417.
20. Lee, S.J. and K.H. Park, *Ultrasonic Energy in Endoscopic Surgery* Yonsei Medical Journal, 1999. **40**(6): p. 5.
21. Emam, T.A. and A. Cuschien, *How safe is high-power ultrasonic dissection?* Annals of surgery, 2003. **237**(2): p. 6.
22. Amaral, J.F., *The Experimental Development of an Ultrasonically Activated Scalpel for Laparoscopic Use*. Surgical Laparoscopy Endoscopy & Percutaneous Techniques, 1994. **4**(2): p. 92-99.
23. Amaral, J., *Ultrasonic dissection*. Endoscopic surgery and allied technologies, 1993. **2**(3-4): p. 181-185.
24. Amaral, J. and C. Chrostek, *Experimental comparison of the ultrasonically-activated scalpel to electrosurgery and laser surgery for laparoscopic use*. Minimally Invasive Therapy & Allied Technologies, 1997. **6**(4): p. 324-331.
25. Sherman, J.A. and H.T. Davies, *Ultracision®: the harmonic scalpel and its possible uses in maxillofacial surgery*. British Journal of Oral and Maxillofacial Surgery, 2000. **38**(5): p. 530-532.
26. Lyons, S.D. and K.S. Law, *Laparoscopic Vessel Sealing Technologies*. Journal of minimally invasive gynecology, 2013. **20**(3): p. 301-307.
27. Noble, E., et al., *Experimental comparison of mesenteric vessel sealing and thermal damage between one bipolar and two ultrasonic shears devices*. British Journal of Surgery, 2011. **98**(6): p. 797-800.
28. Awwad, J.T. and K. Isaacson, *The harmonic scalpel: an intraoperative complication*. Obstetrics & Gynecology, 1996. **88**(4, Part 2): p. 718-720.
29. Kadesky, K., et al., *Proximity injury by the ultrasonically activated scalpel during dissection*. Journal of pediatric surgery, 1997. **32**(6): p. 878-879.
30. Abbasoglu, O. and I. Sayek, *Parenchymal transection with ultrasonic scalpel in liver resection*. Hpb, 2003. **5**(3): p. 167-169.
31. Vercellotti, T., *Technological characteristics and clinical indications of piezoelectric bone surgery*. Minerva stomatologica, 2004. **53**(5): p. 207-214.
32. Gleizal, A., et al., *Piezoelectric osteotomy: a new technique for bone surgery—advantages in craniofacial surgery*. Child's Nervous System, 2007. **23**(5): p. 509-513.
33. Salami, A., et al., *Piezosurgery in otologic surgery: four years of experience*. Otolaryngology-Head and Neck Surgery, 2009. **140**(3): p. 412-418.

34. Salami, A., et al., *Piezosurgery in the excision of middle-ear tumors: effects on mineralized and non-mineralized tissues*. Medical science monitor: international medical journal of experimental and clinical research, 2007. **13**(12): p. PI25-9.
35. Khambay, B.S. and A.D. Walmsley, *Investigations into the use of an ultrasonic chisel to cut bone. Part I: forces applied by clinicians*. Journal of Dentistry, 2000. **28**(1): p. 31-37.
36. Schaeren, S., et al., *Assessment of nerve damage using a novel ultrasonic device for bone cutting*. Journal of Oral and Maxillofacial Surgery, 2008. **66**(3): p. 593-596.
37. Beziat, J.-L., et al., *Ultrasonic osteotomy as a new technique in craniomaxillofacial surgery*. International Journal of Oral and Maxillofacial Surgery, 2007. **36**(6): p. 493-500.
38. Cardoni, A., A. MacBeath, and M. Lucas, *Methods for reducing cutting temperature in ultrasonic cutting of bone*. Ultrasonics, 2006. **44**(Supplement 1): p. e37-e42.
39. MacBeath, A., *Ultrasonic Bone Cutting*. 2006, University of Glasgow: Glasgow.
40. Eggers, G., et al., *Piezosurgery®: an ultrasound device for cutting bone and its use and limitations in maxillofacial surgery*. British Journal of Oral and Maxillofacial Surgery, 2004. **42**(5): p. 451-453.
41. Cimino, W. and L. Bond, *Physics of ultrasonic surgery using tissue fragmentation: Part I*. Ultrasound in Medicine & Biology, 1996. **22**(1): p. 89-100.
42. Sadick, N.S. *Overview of ultrasound-assisted liposuction, and body contouring with cellulite reduction*. in *Seminars in cutaneous medicine and surgery*. 2009. Elsevier.
43. Cooter, R., et al., *Ultrasound assisted lipoplasty*. ANZ journal of surgery, 2001. **71**(5): p. 309-317.
44. Aro, H., et al., *Ultrasonic device in bone cutting: A histological and scanning electron microscopical study*. Acta Orthopaedica, 1981. **52**(1): p. 5-10.
45. Abramov, O.V., *High-Intensity Ultraonics Theory and Industrial Application*. 1998, Amsterdam: Gordon and Breach Science Publisher. 446.
46. Claeysen, F., N. Lhermet, and T. Maillard. *Magnetostrictive actuators compared to piezoelectric actuators*. in *European Workshop on Smart Structures in Engineering and Technology*. 2003. International Society for Optics and Photonics.
47. Tsujino, J., et al., *Transverse and torsional complex vibration systems for ultrasonic seam welding of metal plates*. Ultrasonics, 2000. **38**(1-8): p. 67-71.
48. Zhu, X., *Piezoelectric Ceramic Materials: Processing, Properties, Characterization, and Applications*. 2010, New York: Nova Science Publishers.
49. Coobbold, R.S.C., *Foundations of Biomedical Ultrasound*. 2007, Oxford: Oxford University Press.
50. Oakley, C.G. and M.J. Zipparo. *Single crystal piezoelectrics: a revolutionary development for transducers*. in *Ultrasonics Symposium, 2000 IEEE*. 2000.
51. Park, S.-E.E. and W. Hackenberger, *High performance single crystal piezoelectrics: applications and issues*. Current Opinion in Solid State and Materials Science, 2002. **6**(1): p. 11-18.



52. Jun Kuwata, K. Uchino, and S. Nomura, *Dielectric and Piezoelectric Properties of  $0.91\text{Pb}(\text{Zn}_{1/3}\text{Nb}_{2/3})\text{O}_3\text{-}0.09\text{PbTiO}_3$  Single Crystals*. Jpn. J. Appl. Phys, 1982. **21**: p. 5.
53. Hashimoto, S., et al., *Ultrasonic probe*. 1994, Google Patents.
54. Zipparo, M.J. and C.G. Oakley. *Finite element modeling of PZN-PT and PMN-PT single crystal materials*. in *Ultrasonics Symposium, 2001 IEEE*. 2001.
55. Park, S.-E. and T.R. Shrout, *Ultrahigh strain and piezoelectric behavior in relaxor based ferroelectric single crystals*. Journal of Applied Physics, 1997. **82**(4): p. 1804-1811.
56. Shuyu, L., *Optimization of the performance of the sandwich piezoelectric ultrasonic transducer*. The Journal of the Acoustical Society of America, 2003. **115**(1): p. 182-186.
57. Sherit, S., et al. *Comparison of the Mason and KLM equivalent circuits for piezoelectric resonators in the thickness mode*. in *Ultrasonics Symposium, 1999. Proceedings. 1999 IEEE*. 1999. IEEE.
58. *IEEE Standard Definitions and Methods of Measurement for piezoelectric vibrators*. 1966(177).
59. Sherman, C.H. and J.L. Butler, *Transducers and Arrays for Underwater Sound*. 2006, New York: Springer Science+Business Media.
60. Haiying, H. and D. Paramo, *Broadband electrical impedance matching for piezoelectric ultrasound transducers*. Ultrasonics, Ferroelectrics and Frequency Control, IEEE Transactions on, 2011. **58**(12): p. 2699-2707.
61. Arnau, A., T. Sogorb, and Y. Jimenez, *A new method for continuous monitoring of series resonance frequency and simple determination of motional impedance parameters for loaded quartz-crystal resonators*. Ultrasonics, Ferroelectrics and Frequency Control, IEEE Transactions on, 2001. **48**(2): p. 617-623.
62. Mezheritsky, A.V., *Elastic, dielectric, and piezoelectric losses in piezoceramics: how it works all together*. Ultrasonics, Ferroelectrics and Frequency Control, IEEE Transactions on, 2004. **51**(6): p. 695-707.
63. Jordan, T. and Z. Ounaies, *Piezoelectric ceramics characterization*. 2001, DTIC Document.
64. Chen, Q. and Q.-M. Wang, *The effective electromechanical coupling coefficient of piezoelectric thin-film resonators*. Applied Physics Letters, 2005. **86**(2): p. -.
65. Peshkovsky, S.L. and A.S. Peshkovsky, *Matching a transducer to water at cavitation: Acoustic horn design principles*. Ultrasonics Sonochemistry, 2007. **14**(3): p. 314-322.
66. Lin, S., *Study on the longitudinal-torsional composite mode exponential ultrasonic horns*. Ultrasonics, 1996. **34**(7): p. 757-762.
67. Zhou, G. and M. Li, *A study on ultrasonic solid horns for flexural mode*. The Journal of the Acoustical Society of America, 2000. **107**(3): p. 1358-1362.
68. Wang, D.-A. and H.-D. Nguyen, *A planar Bézier profiled horn for reducing penetration force in ultrasonic cutting*. Ultrasonics, 2014. **54**(1): p. 375-384.
69. Chung-Hoon, L. and A. Lal. *Silicon ultrasonic horns for thin film accelerated stress testing*. in *Ultrasonics Symposium, 2001 IEEE*. 2001.

- 
70. Nagarkar, B.N. and R.D. Finch, *Sinusoidal Horns*. The Journal of the Acoustical Society of America, 1971. **50**(1A): p. 23-31.
  71. Ensminger, D., ed. *Ultrasonics: Fundamentals, Technology, Applications*. 1988, Marcel Dekker, INC: New York.
  72. M.Cartmell, *Introduction to linear, parametric and nonlinear vibrations*. 1st ed. 1990, London: Chapman and Hall.
  73. Takahashi, S., et al. *Electro-mechanical characteristics of lead-zirconate-titanate ceramics under vibration-level change*. in *Applications of Ferroelectrics, 1994.ISAF '94., Proceedings of the Ninth IEEE International Symposium on*. 1994.
  74. Negishi, K., *Jump phenomenon in resonance curve of ferroelectric ceramics*. Journal of the Physical Society of Japan, 1960. **15**(3): p. 534-534.
  75. Damjanovic, D., *Contributions to the piezoelectric effect in ferroelectric single crystals and ceramics*. Journal of the American Ceramic Society, 2005. **88**(10): p. 2663-2676.
  76. Li, S., W. Cao, and L. Cross, *The extrinsic nature of nonlinear behavior observed in lead zirconate titanate ferroelectric ceramic*. Journal of Applied Physics, 1991. **69**(10): p. 7219-7224.
  77. Omori, M., T. Mishima, and T. Fujimoto, *Modes of Domain Wall Motion and Polarization of Lead Zirconate Titanate Polycrystals*. Japanese Journal of Applied Physics, 2011. **50**(9).
  78. Trolier-McKinstry, S., N.B. Gharb, and D. Damjanovic, *Piezoelectric nonlinearity due to motion of 180 domain walls in ferroelectric materials at subcoercive fields: A dynamic poling model*. Applied Physics Letters, 2006. **88**(20): p. 202901.
  79. Xu, F., et al., *Domain wall motion and its contribution to the dielectric and piezoelectric properties of lead zirconate titanate films*. Journal of Applied Physics, 2001. **89**(2): p. 1336-1348.
  80. Hall, D.A., *Review Nonlinearity in piezoelectric ceramics*. Journal of Materials Science, 2001. **36**(19): p. 4575-4601.
  81. Guyomar, D., B. Ducharne, and G. Sebald, *High nonlinearities in Langevin transducer: A comprehensive model*. Ultrasonics, 2011. **51**(8): p. 1006-1013.
  82. Albareda, A., et al., *Optimization of Elastic Nonlinear Behavior Measurements of Ceramic Piezoelectric Resonators with Burst Excitation*. Ultrasonics, Ferroelectrics and Frequency Control, IEEE Transactions on, 2007. **54**(10): p. 2175-2188.
  83. Li, T., Y.H. Chen, and J. Ma, *Frequency dependence of piezoelectric vibration velocity*. Sensors and Actuators A: Physical, 2007. **138**(2): p. 404-410.
  84. Uchino, K., et al., *High Power Characterization of Piezoelectric Materials*. Journal of Electroceramics, 1998. **2**(1): p. 33-40.
  85. Sadayuki, T., *Vibration-Level Characteristics of Lead-Zirconate-Titanate Ceramics*. Japanese Journal of Applied Physics, 1992. **31**(1): p. 3.
  86. Sherrit, S., et al. *Characterization of transducers and resonators under high drive levels*. in *Ultrasonics Symposium, 2001 IEEE*. 2001.
  87. Albareda, A. and R. Pérez, *Non-Linear Behaviour of Piezoelectric Ceramics*, in *Multifunctional Polycrystalline Ferroelectric Materials*. 2011, Springer. p. 681-726.

88. Uchino, K. and S. Hirose, *Loss mechanisms in piezoelectrics: how to measure different losses separately*. Ultrasonics, Ferroelectrics and Frequency Control, IEEE Transactions on, 2001. **48**(1): p. 307-321.
89. Zheng, J., et al., *Heat Generation in Multilayer Piezoelectric Actuators*. Journal of the American Ceramic Society, 1996. **79**(12): p. 3193-3198.
90. Senousy, M.S., et al., *Self-heat generation in piezoelectric stack actuators used in fuel injectors*. Smart Materials and Structures, 2009. **18**(4): p. 045008.
91. Kielczyński, P. and W. Pajewski, *Analysis of temperature fields in ultrasonic transducers of high power*. Sensors and Actuators A: Physical, 1993. **36**(2): p. 97-103.
92. Lebrun, L., et al., *Investigations on ferroelectric PMN-PT and PZN-PT single crystals ability for power or resonant actuators*. Ultrasonics, 2004. **42**(1-9): p. 501-505.
93. Uchino, K., et al., *Loss mechanisms and high power piezoelectrics*, in *Frontiers of Ferroelectricity*. 2007, Springer. p. 217-228.
94. Tashiro, S., M. Ikehiro, and H. Igarashi, *Influence of temperature rise and vibration level on electromechanical properties of high-power piezoelectric ceramics*. Japanese Journal of Applied Physics, 1997. **36**(part 1): p. 3004-3009.
95. Stewart, M. and M.G. Cain, *Measurement and Modelling of Self-heating in Piezoelectric Materials and Devices*. Measurement Good Practice Guide No. 84 2006.
96. Hu, J., *Analyses of the temperature field in a bar-shaped piezoelectric transformer operating in longitudinal vibration mode*. Ultrasonics, Ferroelectrics and Frequency Control, IEEE Transactions on, 2003. **50**(6): p. 594-600.
97. Kanayama, K. *Thermal analysis of a piezoelectric transformer*. in *Ultrasonics Symposium, 1998. Proceedings., 1998 IEEE*. 1998. IEEE.
98. Hirose, S., et al. *Measuring methods for high-power characteristics of piezoelectric materials*. in *MATERIALS RESEARCH SOCIETY SYMPOSIUM PROCEEDINGS*. 1995. Cambridge Univ Press.
99. Takahashi, S., et al. *Nonlinear behavior in piezoelectric ceramic transducers*. in *Applications of Ferroelectrics, 2000. ISAF 2000. Proceedings of the 2000 12th IEEE International Symposium on*. 2000. IEEE.
100. Pérez, R. and A. Albareda, *Analysis of nonlinear effects in a piezoelectric resonator*. Journal of the Acoustical Society of America, 1996. **100**(6): p. 9.
101. Mikio, U., et al., *An Analysis of Jumping and Dropping Phenomena of Piezoelectric Transducers using the Electrical Equivalent Circuit Constants at High Vibration Amplitude Levels*. Japanese Journal of Applied Physics, 2000. **39**(9B): p. 5623.
102. Tamura, H., et al., *Software-Controlled Measurement System for Large Vibrational Amplitude Piezoelectric Resonator Using Continuous Driving Method with Numerical Equivalent Model*. Japanese Journal of Applied Physics, 2011. **50**(7).
103. Astashev, V. and V. Babitsky, *Ultrasonic cutting as a nonlinear (vibro-impact) process*. Ultrasonics, 1998. **36**(1): p. 89-96.
104. Aurelle, N., et al., *Nonlinear behavior of an ultrasonic transducer*. Ultrasonics, 1996. **34**(2): p. 187-191.

105. Mathieson, A., *Nonlinear characterisation of power ultrasonic devices used in bone surgery*. PhD thesis, Univerisyt of Glasgow, 2012.
106. Mathieson, A., et al., *The influence of piezoceramic stack location on nonlinear behavior of langevin transducers*. Ultrasonics, Ferroelectrics and Frequency Control, IEEE Transactions on, 2013. **60**(6).
107. Noumura, Y., et al., *High-Power Piezoelectric Characteristics at Continuous Driving of Bi4Ti3O12-SrBi4Ti4O15-Based Ferroelectric Ceramics*. Japanese Journal of Applied Physics, 2011. **50**(7).
108. Aurelle, N., et al., *Nonlinear behavior of an ultrasonic transducer*. Ultrasonics, 1996. **34**(2–5): p. 187-191.
109. Priya, S., et al., *High-power resonant measurements of piezoelectric materials: Importance of elastic nonlinearities*. Journal of Applied Physics, 2001. **90**(3): p. 1469-1479.
110. Perez, R. and A. Albareda, *Analysis of nonlinear effects in a piezoelectric resonator*. The Journal of the Acoustical Society of America, 1996. **100**(6): p. 3561-3569.
111. Umeda, M., K. Nakamura, and S. Ueha, *The measurement of high-power characteristics for a piezoelectric transducer based on the electrical transient response*. Japanese Journal of Applied Physics Part 1-Regular Papers Short Notes & Review Papers, 1998. **37**(9B): p. 5322-5325.
112. Umeda, M., K. Nakamura, and S. Ueha, *Effects of vibration stress and temperature on the characteristics of piezoelectric ceramics under high vibration amplitude levels measured by electrical transient responses*. Japanese Journal of Applied Physics, 1999. **38**(9S): p. 5581.
113. Sasaki, Y., et al., *High-Power Characteristics of Multilayer Piezoelectric Ceramic Transducers*. Japanese Journal of Applied Physics Part 1-Regular Papers Short Notes & Review Papers, 2001. **40**(Part 1, No. 9B): p. 4.
114. Umeda, M., K. Nakamura, and S. Ueha, *The Measurement of High-Power Characteristics for a Piezoelectric Transducer Based on the Electrical Transient Response*. Japanese Journal of Applied Physics 1998. **37**(Part 1, No. 9B): p. 4.
115. Albareda, A., et al. *Nonlinear measurements of piezocomposite transducers with burst excitation*. in *Applications of Ferroelectrics, 2000. ISAF 2000. Proceedings of the 2000 12th IEEE International Symposium on*. 2000. IEEE.
116. Albareda, A., et al., *Nonlinear measurements of high power 1-3 piezo-air-transducers with burst excitation*. Ferroelectrics, 2002. **273**(1): p. 47-52.
117. Casals, J.A., et al., *Nonlinear characterization with burst excitation of 1-3 piezocomposite transducers*. Ultrasonics, 2003. **41**(4): p. 307-311.
118. Voronina, S. and V. Babitsky, *Autoresonant control strategies of loaded ultrasonic transducer for machining applications*. Journal of Sound and Vibration, 2008. **313**(3): p. 395-417.
119. Babitsky, V., A. Kalashnikov, and F. Molodtsov, *Autoresonant control of ultrasonically assisted cutting*. Mechatronics, 2004. **14**(1): p. 91-114.
120. Sokolov, I. and V. Babitsky, *Phase control of self-sustained vibration*. Journal of Sound and Vibration, 2001. **248**(4): p. 725-744.
121. Hui-juan, D., et al., *Automatic stablization of velocity for ultrasonic vibration system*. Journal of Harbin Institue of Technology, 2001. **8**(1): p. 5.

122. Wang, Y., et al. *Power converters for power-ultrasonic transducers*. in *Universities' Power Engineering Conference (UPEC), Proceedings of 2011 46th International*. 2011. VDE.
123. Ishikawa, J., et al. *High-frequency drive-power and frequency control for ultrasonic transducer operating at 3 MHz*. in *Industry Applications Conference, 1997. Thirty-Second IAS Annual Meeting, IAS '97., Conference Record of the 1997 IEEE*. 1997.
124. Dong, H., et al., *A Novel Method of Stabilizing the Vibration Velocity at the End of Piezoelectric Transducers*  
*Advanced Research on Computer Education, Simulation and Modeling*, S. Lin and X. Huang, Editors. 2011, Springer Berlin Heidelberg. p. 39-46.
125. Svilainis, L. and G. Motiejūnas, *Power amplifier for ultrasonic transducer excitation*. *Ultragarsas (Ultrasound)*. Kaunas: Technologija, 2006. **58**: p. 30-36.
126. Martin, R.W., et al., *Water-cooled, high-intensity ultrasound surgical applicators with frequency tracking*. *Ultrasonics, Ferroelectrics and Frequency Control*, IEEE Transactions on, 2003. **50**(10): p. 1305-1317.
127. Babitsky, V., *Autoresonant mechatronic systems*. *Mechatronics*, 1995. **5**(5): p. 483-495.
128. Lin, S. and H. Tian, *Study on the sandwich piezoelectric ceramic ultrasonic transducer in thickness vibration*. *Smart Materials and Structures*, 2008. **17**(1): p. 015034.
129. Lal, A. and R.M. White. *Silicon micromachined ultrasonic micro-cutter*. in *Ultrasonics Symposium, 1994. Proceedings., 1994 IEEE*. 1994.
130. Lal, A. and R.M. White, *Silicon microfabricated horns for power ultrasonics*. *Sensors and Actuators A: Physical*, 1996. **54**(1-3): p. 542-546.
131. Friedrich, F., et al. *Silicon micromachined ultrasonic transducer with improved power transfer for cutting application*. in *Ultrasonics Symposium (IUS), 2012 IEEE International*. 2012. Dresden, Germany.
132. Tsai, S.C., et al., *High-frequency, silicon-based ultrasonic nozzles using multiple Fourier horns*. *Ultrasonics, Ferroelectrics and Frequency Control*, IEEE Transactions on, 2004. **51**(3): p. 277-285.
133. Tsai, S.C., et al., *Silicon-based megahertz ultrasonic nozzles for production of monodisperse micrometer-sized droplets*. *Ultrasonics, Ferroelectrics and Frequency Control*, IEEE Transactions on, 2009. **56**(9): p. 1968-1979.
134. Chen, X. and A. Lal. *Integrated pressure and flow sensor in silicon-based ultrasonic surgical actuator*. 2001. Atlanta, GA.
135. Chih-Ming, L., et al. *Quality factor enhancement in lamb wave resonators utilizing AlN plates with convex edges*. in *Solid-State Sensors, Actuators and Microsystems Conference (TRANSDUCERS), 2011 16th International*. 2011.
136. Vladimir, B., et al., *Improving aluminum nitride plasma etch process for MEMS applications*. *Journal of Micromechanics and Microengineering*, 2013. **23**(11): p. 117001.
137. Lal, A. and R.M. White. *Micromachined silicon needle for ultrasonic surgery*. 1995. Seattle, WA, USA: IEEE.

138. Meyer, R.J., T.C. Montgomery, and W.J. Hughes. *Tonpilz transducers designed using single crystal piezoelectrics*. in *OCEANS '02 MTS/IEEE*. 2002.
139. Sung Min, R., J. Ho, and L. Ki-Jong. *Multilayer PMN-PT single crystal transducer for medical application*. in *Ultrasonics Symposium, 2004 IEEE*. 2004.
140. Shujun, Z., et al., *Relaxor-PbTiO<sub>3</sub> single crystals for various applications*. Ultrasonics, Ferroelectrics and Frequency Control, IEEE Transactions on, 2013. **60**(8): p. 1572-1580.
141. Z.Qiu, et al., *Characterisation of Piezocrystals for Practical Configurations with Temperature- and Pressure-Dependent Electrical Impedance Spectroscopy*. Ieee Transactions on Ultrasonics Ferroelectrics and Frequency Control, 2011. **58**(9): p. 10.
142. Hopcroft, M.A., W.D. Nix, and T.W. Kenny, *What is the Young's Modulus of Silicon?* Microelectromechanical Systems, Journal of, 2010. **19**(2): p. 229-238.
143. Petersen, K.E., *Silicon as a mechanical material*. Proceedings of the Ieee, 1982. **70**(5): p. 420-457.
144. Gallego-Juarez, J.A., E. Riera, and V.M. Acosta-Aparicio, *Modal Interactions in High-Power Ultrasonic Processing Transducers*. AIP Conference Proceedings, 2008. **1022**(1): p. 595-604.
145. Greenstein, M. and U. Kumar, *Multilayer piezoelectric resonators for medical ultrasound transducers*. Ultrasonics, Ferroelectrics and Frequency Control, IEEE Transactions on, 1996. **43**(4): p. 620-622.
146. Kinsler, L.E., et al., *Fundamentals of Acoustics*. John Wiley & Sons, Inc., 1982.
147. Jiang, S., et al., *Weak signal detection method of adaptive digital lock-in amplifier based on particle swarm optimization algorithm*. The Ninth International Conference on Electronic Measurement & Instruments, 2009. **2**: p. 6.
148. Moe, A.E., et al. *A miniaturized lock-in amplifier design suitable for impedance measurements in cells [biological cells]*. in *Sensors, 2004. Proceedings of IEEE*. 2004.
149. Bennett, S., *Development of the PID controller*. Control Systems, IEEE, 1993. **13**(6): p. 58-62.
150. Heping, S., et al. *Design of a new high accuracy incremental PID controller with dual temperature sensors*. in *Control and Decision Conference (CCDC), 2012 24th Chinese*. 2012.
151. Lee, Y., et al., *PID controller tuning for desired closed-loop responses for SI/SO systems*. AIChE Journal, 1998. **44**(1): p. 106-115.
152. Sadiq, M.R., *Enhanced Biopsy and Regional Anaesthesia through Ultrasound Actuation of a Standard Needle*, in *School of Engineering, Physics and Mathematics 2013*, University of Dundee: Dundee.
153. Pritchard, J., R. Ramesh, and C.R. Bowen, *Time-temperature profiles of multi-layer actuators*. Sensors and Actuators A: Physical, 2004. **115**(1): p. 140-145.
154. Hu, J., et al., *An experimental investigation of the temperature field in small piezoelectric vibrators*. Ultrasonics, 2004. **41**(9): p. 731-735.
155. Richard, C., et al., *Selecting passive and active materials for 1.3 composite power transducers*. Ultrasonics, 2002. **40**(1-8): p. 895-901.

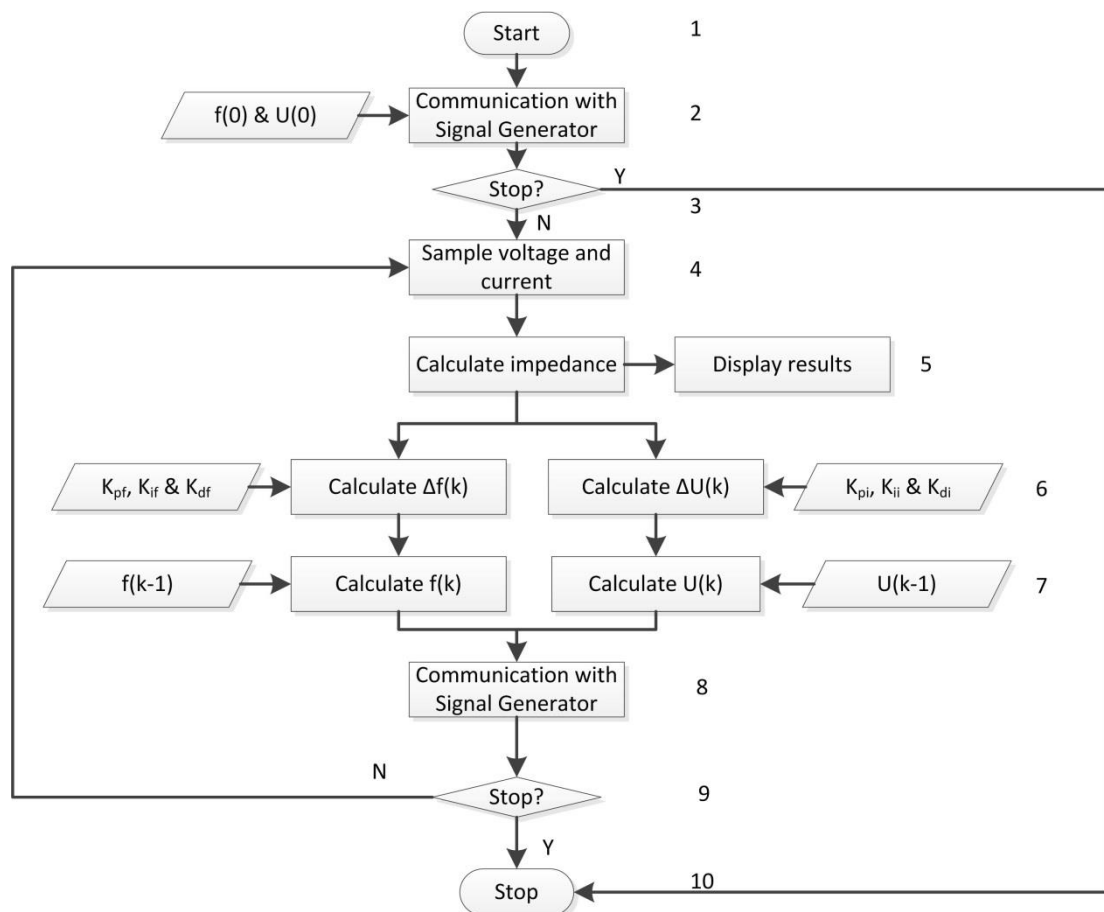
- 
156. Zahn, S., Y. Schneider, and H. Rohm, *Ultrasonic cutting of foods: Effects of excitation magnitude and cutting velocity on the reduction of cutting work*. Innovative Food Science and Emerging Technologies, 2006. **7**(4): p. 288-293.
157. Schneider, Y., S. Zahn, and L. Linke, *Qualitative Process Evaluation for Ultrasonic Cutting of Food*. Engineering in Life Sciences, 2002. **2**(6): p. 153-157.
158. Arnold, G., et al., *Ultrasonic cutting of cheese: Composition affects cutting work reduction and energy demand*. International Dairy Journal, 2009. **19**(5): p. 314-320.
159. Kehlet, H. and J.B. Dahl, *Anaesthesia, surgery, and challenges in postoperative recovery*. The Lancet, 2003. **362**(9399): p. 1921-1928.
160. Hoorntje, L.E., et al., *Vacuum-assisted breast biopsy: a critical review*. European Journal of Cancer, 2003. **39**(12): p. 1676-1683.
161. Brull, R., et al., *Practice patterns related to block selection, nerve localization and risk disclosure: a survey of the American Society of Regional Anesthesia and Pain Medicine*. Regional Anesthesia and Pain Medicine, 2008. **33**(5): p. 395-403.
162. Youk, J.H., et al., *Sonographically Guided 14-Gauge Core Needle Biopsy of Breast Masses: A Review of 2,420 Cases with Long-Term Follow-Up*. American Journal of Roentgenology, 2008. **190**(1): p. 202-207.
163. Hebard, S., G. Hocking, and K. Murray, *Two-dimensional mapping to assess direction and magnitude of needle tip error in ultrasound-guided regional anaesthesia*. Anaesth Intensive Care, 2011. **39**(6): p. 1076-81.
164. Sites, B.D., et al., *Characterizing Novice Behavior Associated With Learning Ultrasound - Guided Peripheral Regional Anesthesia*. Regional Anesthesia and Pain Medicine, 2007. **32**(2): p. 107-115.
165. Chin, K.J., et al., *Needle Visualization in Ultrasound-Guided Regional Anesthesia: Challenges and Solutions*. Regional Anesthesia and Pain Medicine, 2008. **33**(6): p. 532-544.
166. Liberman, L., *Percutaneous imaging-guided core breast biopsy: state of the art at the millennium*. American Journal of Roentgenology, 2000. **174**(5): p. 1191-1199.
167. Chapman, G.A., D. Johnson, and A.R. Bodenham, *Visualisation of needle position using ultrasonography*. Anaesthesia, 2006. **61**(2): p. 148-158.
168. Marhofer, P., M. Greher, and S. Kapral, *Ultrasound guidance in regional anaesthesia*. Br J Anaesth, 2005. **94**(1): p. 7-17.
169. Dillane, D. and B. Finucane, *Local anesthetic systemic toxicity*. Canadian Journal of Anesthesia/Journal canadien d'anesthésie, 2010. **57**(4): p. 368-380.
170. Brull, R., et al., *Neurological complications after regional anesthesia: contemporary estimates of risk*. Anesth Analg, 2007. **104**(4): p. 965-74.
171. Cheung, S. and R. Rohling, *Enhancement of needle visibility in ultrasound-guided percutaneous procedures*. Ultrasound in Medicine & Biology, 2004. **30**(5): p. 617-624.
172. Hebard, S. and G. Hocking, *Echogenic Technology Can Improve Needle Visibility During Ultrasound-Guided Regional Anesthesia*. Regional Anesthesia and Pain Medicine, 2011. **36**(2): p. 185-189 10.1097/AAP.0b013e31820d4349.

173. Fronheiser, M.P. and S.W. Smith, *Analysis of a Vibrating Interventional Device to Improve 3-D Colormark Tracking*. Ultrasonics, Ferroelectrics and Frequency Control, IEEE Transactions on, 2007. **54**(8): p. 1700-1707.
174. Klein, S.M., et al., *Piezoelectric Vibrating Needle and Catheter for Enhancing Ultrasound-Guided Peripheral Nerve Blocks*. Anesthesia & Analgesia, 2007. **105**(6): p. 1858-1860.
175. Arnold, F.J. and S.S. Mühlen, *The mechanical pre-stressing in ultrasonic piezotransducers*. Ultrasonics, 2001. **39**(1): p. 7-11.
176. Hawkins, D.W. and P.T. Gough, *Multiresonance design of a Tonpilz transducer using the finite element method*. Ultrasonics, Ferroelectrics and Frequency Control, IEEE Transactions on, 1996. **43**(5): p. 782-790.
177. Arnold, F.J. and S.S. Mühlen, *The resonance frequencies on mechanically pre-stressed ultrasonic piezotransducers*. Ultrasonics, 2001. **39**(1): p. 1-5.
178. Kuzmuk, K.N. and L.B. Schook, *Pig as a Model for Biomedical Sciences*. The Genetics of the Pig, ed. M.F. Rothschild and A. Ruvinsky. 2011, Oxfordshire: CAB International.
179. Gray, A.T., *Ultrasound Guided Regional Anesthesia: Current State of the Art*. Anesthesiology 2006. **104**(2): p. 6.
180. Souzdalnitski, D., I. Lerman, and T. Halaszynski, *How to Improve Needle Visibility*, in *Atlas of Ultrasound-Guided Procedures in Interventional Pain Management*, S.N. Narouze, Editor. 2011, Springer New York. p. 35-75.
181. Longo, J.M., et al., *Percutaneous vascular and nonvascular puncture under US guidance: role of color Doppler imaging*. Radiographics, 1994. **14**(5): p. 959-72.

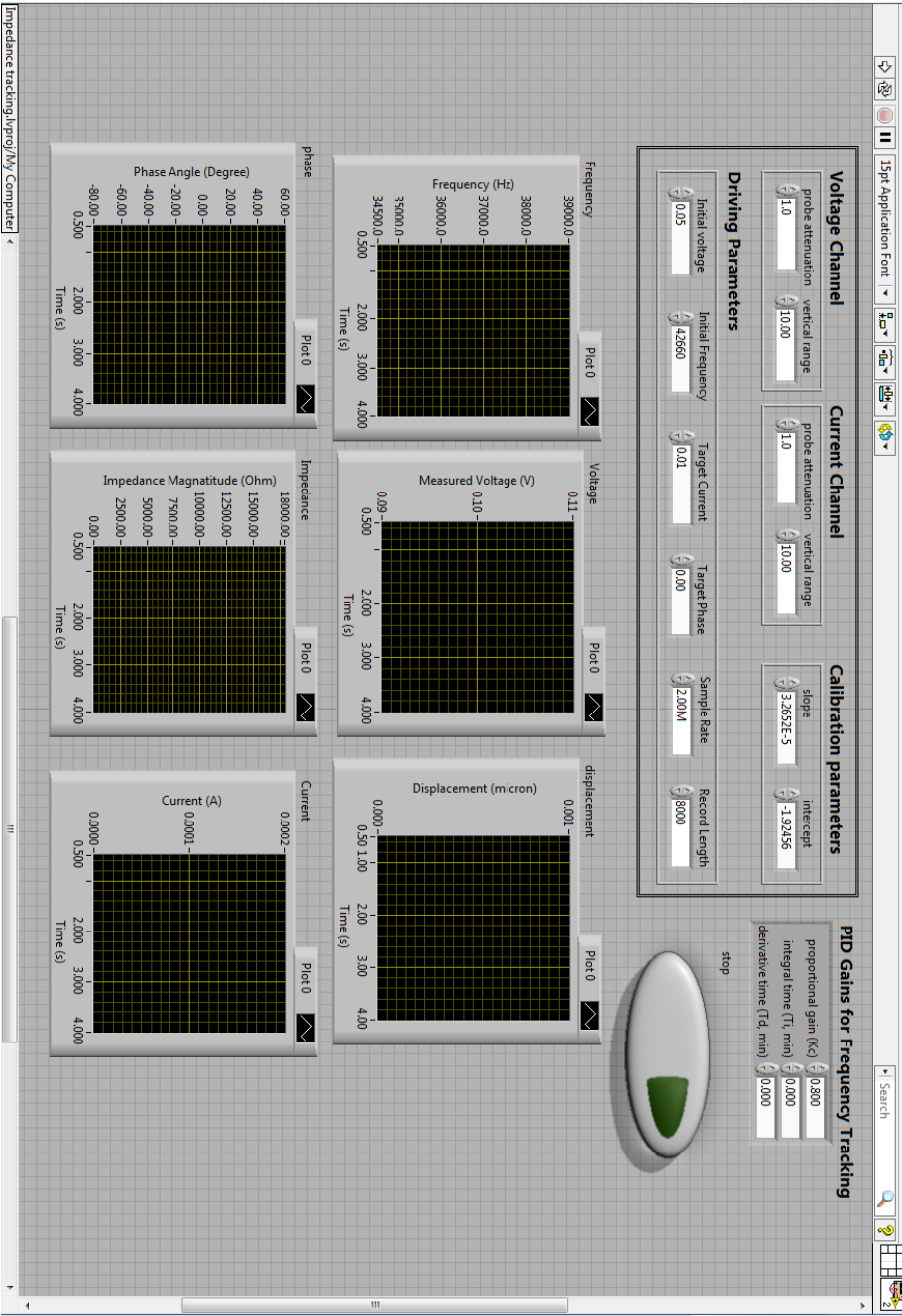


# APPENDIX A- LABVIEW PROGRAM FOR RESONANCE TRACKING AND VIBRATION STABLISATION

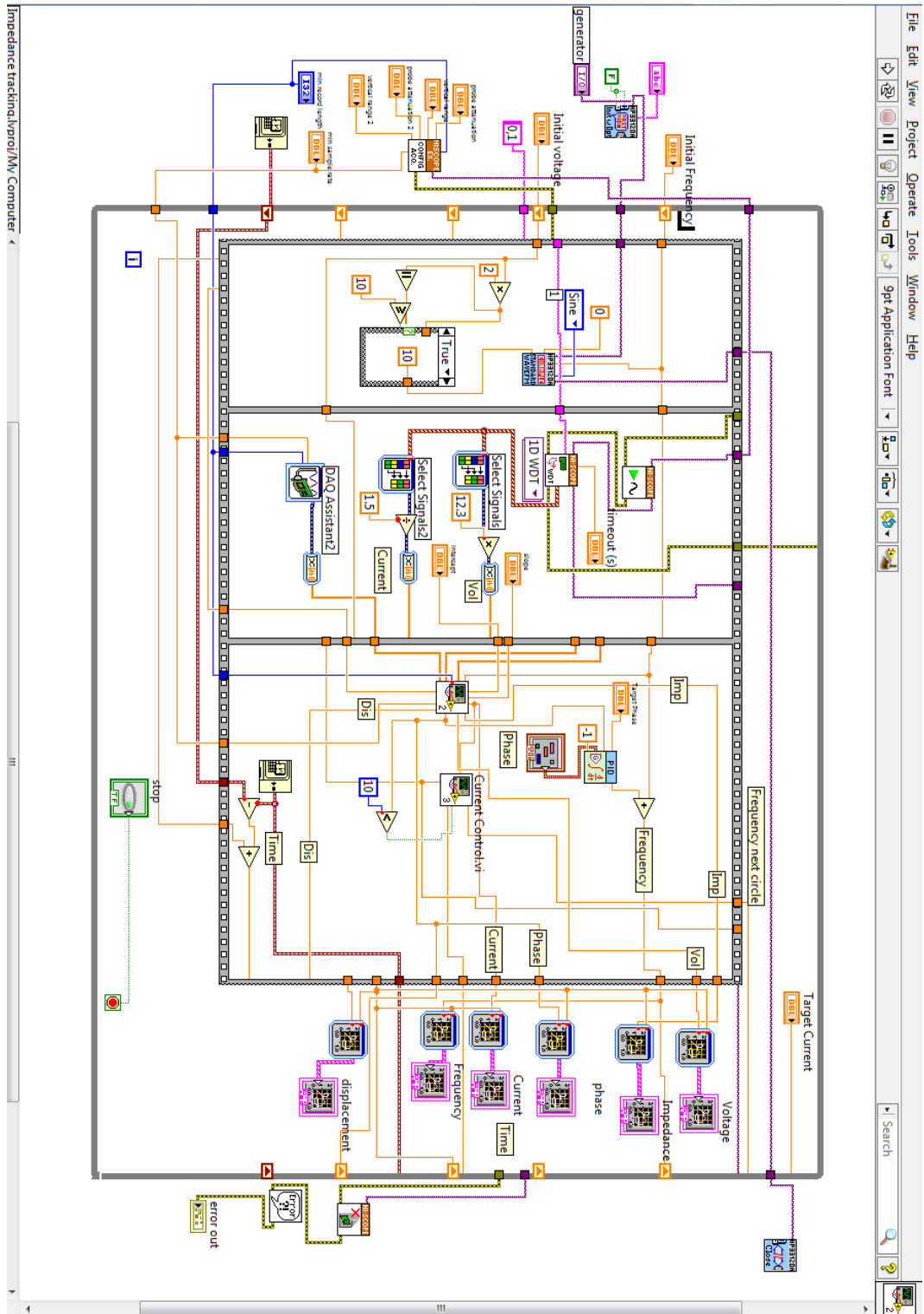
Flow chart



Front panel

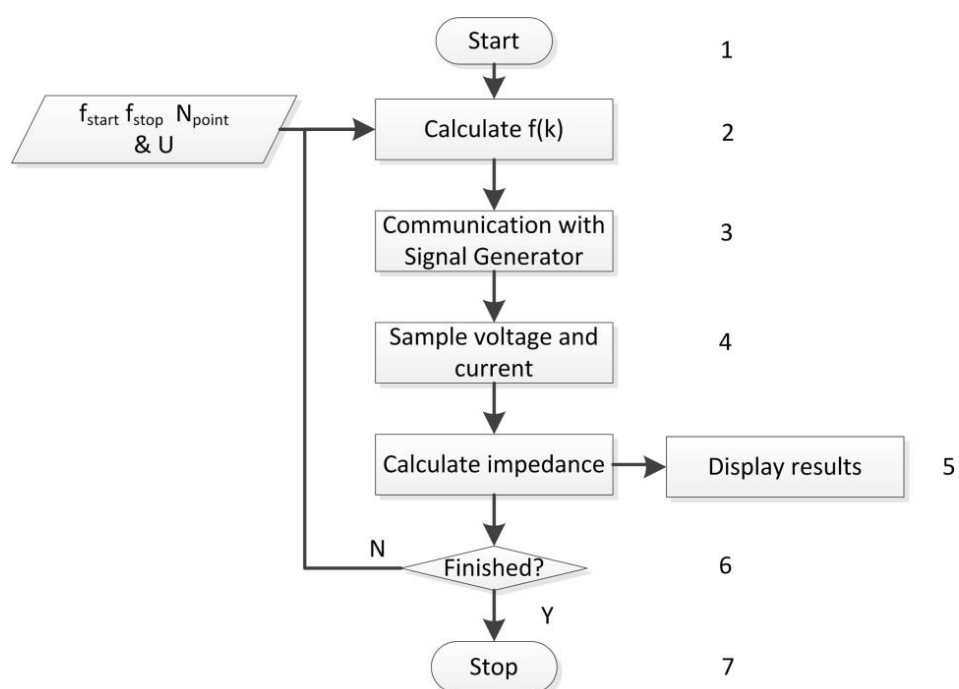


Block diagram

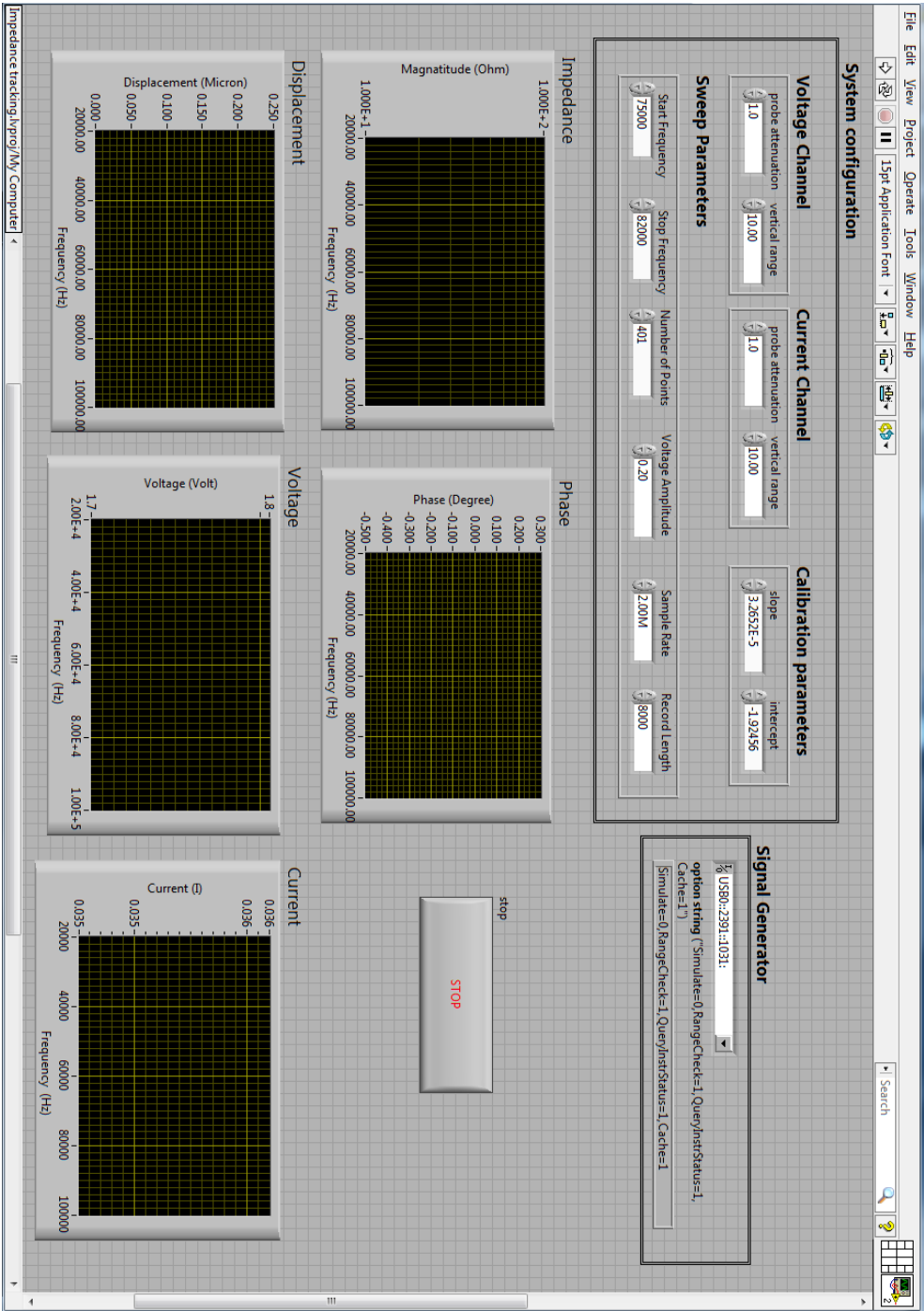


## APPENDIX B- LABVIEW PROGRAM FOR IMPEDANCE MEASUREMENT

Flow chart



Front panel



Block diagram

